The Role of Boundary Layer Dynamics in Tropical Cyclone Intensification

A DISSERTATION SUBMITTED TO THE GRADUATE DIVISION OF

THE UNIVERSITY OF HAWAIʻI AT MĀNOA

IN PARTIAL FULFILLMENT OF THE REQUIREMENTS FOR THE DEGREE OF

DOCTOR OF PHILOSOPHY

IN

METEOROLOGY

NOVEMBER 2018

By

Tsung-Han Li

Dissertation Committee:

Yuqing Wang, Chairperson

Michael M. Bell

Steven Businger

Yi-Leng Chen

Niklas Schneider

ACKNOWLEDGEMENT

I would like to thank my advisor, Prof. Yuqing Wang, for his excellent mentoring and personal concerns during these years. Also thanks to my committee, Prof. Michael M. Bell, Prof. Steven Businger, Prof. Yi-Leng Chen, and Prof. Niklas Schneider, for their guidance and patience. Thank you so much for your reading and time.

This study has been supported in part by the National Basic Research and Development Project (973 program) of China under contract no. 2015CB452805 and in part by National Natural Science Foundation of China under grant 41730960 and NSF grant AGS-1326524 and Basic Research Fund of CAMS 2016Z003.

ABSTRACT

This study examines the role of boundary layer dynamics in tropical cyclone (TC) intensification. The hypothesis is that although surface friction has a negative effect on TC intensification by the frictional dissipation (dissipation effect), it contributes positively to TC intensification by modifying the strength and radial location of eyewall updrafts/convection and also enhancing eyewall contraction (indirect effect). To test the hypothesis and isolate the direct dissipation effect and indirect effect, three models with different complexities are used to conduct idealized experiments with a varying surface drag coefficient (C_D) and TC vortex structure. Results from a simplified dynamical framework, which includes three layers: a multi-level boundary layer model below, a shallow-water-equation model as the middle layer, and an upper layer, are discussed first. In this framework, the mass sink in the middle layer is parameterized by a mass-flux at the top of the boundary layer to mimic eyewall heating such that the indirect effect of boundary layer dynamics on TC intensification can be evaluated. Namely, the frictional boundary layer in response to gradient wind distribution above the boundary layer controls the strength and radial location of eyewall convection, which in turn contributes to eyewall contraction and intensification of the gradient wind. Results show that through the indirect effect of surface friction, TCs with larger surface drag coefficient, smaller radius of gale wind (RGW), and higher intensity display faster eyewall contraction and more rapid intensification, and that the fastest intensification occurs for TCs with the initial radius of maximum wind (RMW) at around 80 km.

Results from full-physics model simulations using the Tropical Cyclone Model version 4 (TCM4) are discussed with the focus on the relative importance and the combined direct dissipation and indirect effect of boundary layer dynamics due to the presence of surface friction on TC intensification. Results show that the intensification rate of a TC during the primary

intensification stage is insensitive to C_D (including the surface wind-dependent C_D), suggesting that the positive contribution due to the indirect effect of surface friction to TC intensification is almost offset by the negative contribution resulting from the direct dissipation effect of surface friction. However, greater surface friction can significantly shorten the initial spin-up stage (the onset of the primary intensification stage) through faster moistening of the inner core of the TC vortex but would lead to a weaker storm in the mature stage. The results thus strongly suggest that the boundary layer dynamics contributes significantly to the onset of the primary intensification while has important but dual opposite effects on the subsequent intensification rate during the primary intensification stage. Results from further sensitivity experiments demonstrate that the TC vortex initially with a smaller RMW or a smaller RGW has a shorter initial spin-up stage and intensifies more rapidly during the primary intensification stage through the indirect effect of the boundary layer dynamics discussed in the simplified framework.

TABLE OF CONTENTS

ACKNOWLEDGEMENT I

ABSTRACT II

TABLE OF CONTENTS IV

LIST OF TABLES VII

LIST OF FIGURES VIII

CHAPTER 1. INTRODUCTION 1

1.1 Tropical cyclones and their intensity change 1

1.2 The role of the boundary layer in tropical cyclone intensification 2

1.2.1. Overview of the tropical cyclone boundary layer 2

1.2.2. Overview of surface drag coefficient under tropical cyclones 5

1.2.3. Review of tropical cyclone boundary layer model 8

1.2.4. The boundary layer spin-up mechanism 10

1.2.5. Sensitivity of tropical cyclone intensification to surface drag coefficient in numerical models 13

1.3 Eyewall convection and its impact on tropical cyclone intensification 15

1.4 The influence of tropical cyclone structure and intensity on storm intensification 17

1.5 The link between tropical cyclone boundary layer dynamics and eyewall convection 21

1.6 Objectives and approaches 23

CHAPTER 2. MODEL DESCRIPTION AND EXPERIMENTAL DESIGN 26

2.1 The multi-level boundary layer model 26

2.2 The interactive model 29

2.3 Tropical Cyclone Model version 4 (TCM4) 35

CHAPTER 3. RESULTS FROM A SIMPLIFIED DYNAMICAL FRAMEWORK 41

3.1 Results from the simple boundary layer model 41

3.1.1 Overview of the boundary layer responses 41

3.1.2 Sensitivity to surface drag coefficient 43

3.1.3 Sensitivity to the initial tropical cyclone vortex structure and intensity 44

3.1.4 Dependence of the boundary layer response to various parameter spaces 47

3.2 Results from the interactive model 48

3.2.1 Overview of the boundary layer response and gradient wind evolution 48

3.2.2 Sensitivity to surface drag coefficient 49

3.2.3 Sensitivity to the initial tropical cyclone vortex structure and intensity 50

3.2.4 Dependence of intensification rate on various parameter spaces 52

3.3 Concluding remarks on results from the two simplified models 55

CHAPTER 4. RESULTS FROM A FULL-PHYSICS MODEL 57

4.1 Overview of the control experiment 57

4.2 Sensitivity to surface drag coefficient 59

4.3 Sensitivity to surface drag coefficient after the eyewall convection well organized 63

4.4 Sensitivity to surface wind dependent surface drag coefficient 69

CHAPTER 5. THE INFLUENCE OF INITIAL VORTEX STRUCTURE ON TROPICAL CYCLONE INTENSIFICATION 74

5.1 Sensitivity to the initial vortex radius of maximum wind 75

5.2 Sensitivity to the initial vortex radius of gale wind 80

CHAPTER 6. CONCLUSIONS 87

6.1 Key findings 87

6.2 Summary and discussion 88

6.3 Some remaining issues and future work 95

REFERENCES.....100

LIST OF TABLES

Table 1.1. Results of the role of surface friction in TC formation and subsequent intensification in previous studies using numerical models. 110

Table 1.2. Summary of the main purpose of each model in this study. 111

Table 2.1. Values of the parameters used in the interactive model. 112

Table 2.2. Summary of the model physical processes in TCM4. 113

Table 2.3. Summary of numerical sensitivity experiments for C_D performed using TCM4. The maximum tangential wind speed V_m is 15 m s^{-1} at the radius of maximum wind R_m of 75 km with the decaying parameter b = 1 for the initial TC vortex in all experiments. 114

Table 2.4. Summary of numerical sensitivity experiments for the initial TC structure performed using TCM4. 115

Table 6.1. Summary of ensemble numerical sensitivity experiments of surface friction performed using TCM4. The maximum tangential wind speed V_m is 15 m s^{-1} at the radius of maximum wind R_m of 75 km with the decaying parameter b = 1 for the initial TC vortex in all experiments. 116

Table 6.2. Summary of numerical experiments performed using TCM4. The maximum tangential wind speed V_m is 15 m s^{-1} at the radius of maximum wind R_m of 75 km with the decaying parameter b = 1 for the initial TC vortex in all experiments. 117

LIST OF FIGURES

Figure 1.1. Schematic diagram illustrating the agradient force imbalance in the friction layer of a tropical cyclone and the secondary circulation that it generates (quoted from Montgomery and Smith 2014). 118

Figure 1.2. Vertical cross section of the mean radial wind (m s^{-1}). The zero contour (vertically interpolated, then radially smoothed) corresponds to the top of the inflow layer. Other contours were drawn subjectively. Also shown is the V_r = 0 level at R = 2° (222 km) from Frank's (1977) composite analysis of typhoons. The arrow on the abscissa denotes the radius of maximum winds and mean upward motion at 560 m; the other arrows illustrate the flow (quoted from Frank 1984). 119

Figure 1.3. The aircraft data from an inbound leg in the southwest quadrant (red, 434 m average height) and an outbound leg in the northeast quadrant (blue, 2682 m average height) of Hurricane Hugo on 15 September 1989. The solid curves show the tangential wind component, while the dotted curves show the radial wind component (top). The vertical component of the velocity (bottom) (quoted from William et al. 2013). 120

Figure 1.4. The variation of C_D with 10-m height wind speed from Gopalakrishnan (2013) (gray), Black et al. (2007) (blue), Large and Pond (1981) (green), Donelan et al. (2004) (red), and Powell et al. (2003) (pink) (quoted from Gopalakrishnan 2013). 121

Figure 1.5. Schematic of the axisymmetric view of tropical cyclone intensification in the new paradigm. Above the boundary layer, spinup of the vortex occurs as air parcels are drawn inward by the inner-core convection at levels where absolute angular momentum is approximately conserved. Air parcels spiraling inward in the boundary layer may reach small radii quickly (minimizing the loss of absolute angular momentum during spiral circuits) and acquire a larger tangential wind speed than that above the boundary layer (quoted from Smith

and Montgomery 2015). 122

Figure 2.1. Radial profiles of the initial tangential wind speed used in the sensitivity experiments in the simple boundary layer model for (a) storm RGW [b = 1 (black) and b = 0.4 (yellow)], (b) storm RMW [R_m = 20 km (black) and R_m = 100 km (green)], and (c) storm intensity [V_m = 15 m s^{-1} (black) and V_m = 30 m s^{-1} (red)]. 123

Figure 2.2. As in Figure 2.1, but for geopotential field. 124

Figure 2.3. Schematic showing the design of the interactive model. 125

Figure 2.4. Typical stratification of the tropical atmosphere (after Jordan, 1958) where θ is the potential temperature, θ_e the equivalent potential temperature, θ_e^* the equivalent potential temperature of the hypothetically saturated air of the same temperature at each level. Correspondence between the sea surface temperature T_s and the saturated equivalent potential temperature, $(\theta_e^*)_s$ at the sea surface, is shown on the additional scale below the diagram (quoted from Ooyama 1969). 126

Figure 2.5. Modeled (with Reynolds number dependent sheltering coefficient) and observed surface drag coefficients versus wind speed. Note the fetch dependence of the modeled surface drag coefficient between 30 and 55 m s^{-1} (quoted from Donelan 2018). 127

Figure 2.6. The dependence of surface drag coefficients (10^{-3}) on surface wind speed (m s^{-1}) in the interactive model (red), TCM4 (black), Donelan (2018) (magenta), and modified Donelan (blue). 128

Figure 3.1. Radius-height cross-sections of tangential wind speed (shaded; m s^{-1}) and radial velocity (contours; m s^{-1}) for (a) 50% C_D and (b) 200% C_D; vertical vorticity (shaded; 10^{-4} s^{-2}) and vertical velocity (contours; m s^{-1}) for (c) 50% C_D and (d) 200% C_D; agradient force (shaded; m s^{-2}) for (e) 50% C_D and (f) 200% C_D in the steady-state response in the simple boundary layer model. 130

Figure 3.2. As in Figure 3.1, but (a), (c), (e) for the storm with a smaller RGW (b = 1) and (b), (d), (f) for the storm with a larger RGW (b = 0.4). 132

Figure 3.3. As in Figure 3.1, but (a), (c), (e) for the storm with a smaller RMW (R_m = 40 km) and (b), (d), (f) for the storm with a larger RMW (R_m = 60 km). 134

Figure 3.4. As in Figure 3.1, but (a), (c), (e) for the storm with a lower intensity (V_m = 15 m s^{-1}) and (b), (d), (f) for the storm with a higher intensity (V_m = 30 m s^{-1}). 136

Figure 3.5. Dependence of the maximum radial wind speed (solid, left ordinate, m s^{-1}) and the maximum vertical velocity (dashed, right ordinate, m s^{-1}) near the top of the boundary layer (at the 866-m height) on (a) surface drag coefficient, (b) the initial RGW inferred from the decaying parameter b, (c) the initial RMW (km), and (d) the initial storm intensity (m s^{-1}) in the steady-state response in the simple boundary layer model. 137

Figure 3.6. Radius-time cross-sections of vertical velocity at the top of the boundary layer (944 m) (m s^{-1}, shaded) and gradient wind speed at the middle layer (m s^{-1}, contours) in the experiment with (a) 100% C_D and initial b = 1.0, the initial RMW = 40 km, and V_m = 15 m s^{-1}, (b) as in (a) but with 50% C_D, (c) as in (a) but with 200% C_D, (d) as in (a) but for initial b = 0.4, (e) as in (a) but with an initial RMW of 60 km, and (f) as in (a) but with an initially V_m = 30 m s^{-1}. The red dots represent the radius of maximum gradient wind in the middle layer. 138

Figure 3.7. Dependence of the averaged intensification rates [solid, left ordinate, m s^{-1} $(12\ hr)^{-1}$] and the contraction rates of the RMW [dashed, right ordinate, km $(12\ hr)^{-1}$] on (a) surface drag coefficient, (b) the initial RGW inferred from the decaying parameter b, (c) the initial RMW (km), and (d) the initial storm intensity (m s^{-1}), all are averaged between 0 h and 18 h of integration in the interactive model. 140

Figure 3.8. Schematic diagram summarizing the role of boundary layer dynamics in TC

intensification. The direction of the arrow represents the cause and effect. The thick yellow curve denotes the radial profile of axisymmetric vertical vorticity. The blue dashed line denotes the RMW. The blue scalloped area denotes the predominant radial location of eyewall convection. There are four sequential interactive processes: (1) the boundary layer inflow in response to the given radial distribution of gradient wind above the boundary layer in the presence of surface friction; (2) the boundary layer inflow, as a function of surface friction and radial distribution of gradient wind above the boundary layer, determines the strength and radial location of the boundary layer mass convergence and thus the eyewall updraft; (3) the upward mass-flux at the top of the boundary layer determines both the strength and radial location of diabatic heating in the eyewall; and (4) the contraction of the RMW and intensification of the TC vortex in response to diabatic heating in the eyewall, which is in turn a response to gradient wind above the boundary layer through the boundary layer dynamics. 141

Figure 4.1. The total wind speed (m s^{-1}) at the 2320-m height at every 12-h interval from 24 h to 108 h in CTRL. 142

Figure 4.2. Time evolution of (a) the maximum 10-m height tangential wind speed (m s^{-1}) and (b) the radius of maximum wind (km) in CTRL. 143

Figure 4.3. Radius-height cross-sections of the azimuthal mean radial wind speed (shaded; m s^{-1}) and tangential wind speed (contours; m s^{-1}) at every 12-h interval from 24 h to 108 h in CTRL. 145

Figure 4.4. As in Figure 4.3, but for the azimuthal mean relative humidity (shaded; %) and vertical velocity (contours; m s^{-1}). 147

Figure 4.5. As in Figure 4.3, but for the azimuthal mean vertical vorticity (shaded; 10^{-4} s^{-1}) and condensational heating rate (contours; K hr^{-1}). 149

Figure 4.6. Time evolution of (a) the maximum 10-m height tangential wind speed (m s^{-1}) in the control experiment (CTRL, black), 50% C_D experiment (CT05, blue), 70% C_D experiment (CT07, cyan), 130% C_D experiment (CT13, magenta), and 200% C_D experiment (CT20, red). (b) the 12-h intensification rates (m s^{-1} 12 hr^{-1}) with 5-h running mean in CT05 (blue), CTRL (black), and CT20 (red). 150

Figure 4.7. Scatter diagrams of the subsequent 12-h intensification rate (m s^{-1} 12 hr^{-1}) against instantaneous maximum tangential wind speed (m s^{-1}) during the intensification stage with 5-h running mean in CT05, CTRL, and CT20. 151

Figure 4.8. Radius-height cross-sections of the azimuthal mean relative humidity (shaded, %) and vertical velocity (contours, cm s^{-1}), both averaged in the first 6-h simulation in (a) CT05 and (b) CT20 respectively. 152

Figure 4.9. Radius-time cross-sections of the azimuthal mean relative humidity (%) at the 1331-m height in (a) CT05, (b) CT20. The black dots represent the radius of maximum tangential wind at the same level. 153

Figure 4.10. Time evolution of relative humidity (%) at the 1331-m height averaged within the RMW in CT05 (blue) and CT20 (red). The blue (red) dashed line denotes the time when the storm starts to intensify in CT05 (CT20). 154

Figure 4.11. (a) Time evolution of the maximum 10-m height tangential wind speed (m s^{-1}) in CTRL (black), 50% C_D experiment but with C_D changed after 36 h (CT05-R, dashed blue) and 200% C_D experiment but with C_D changed after 36 h (CT20-R, dashed red). (b) Time evolution of the 12-h intensification rate (m s^{-1} 12 hr^{-1}) in CTRL (black), CT05-R (dashed blue), and CT20-R (dashed red). 155

Figure 4.12. The total wind speed (m s^{-1}) at the 2320-m height at every 6-h interval from 42 h to 60 h in CT05-R (left) and CT20-R (right). 156

Figure 4.13. Radius-height cross-sections of the azimuthal mean radial wind speed (m s^{-1}) and vertical velocity (contours, m s^{-1}) at (a) 37 h, (c) 38 h, (e) 39 h, and (g) 40 h in CT05-R and (b) 37 h, (d) 38 h, (f) 39 h, and (h) 40 h in CT20-R. C_D was modified after the first 36 h of integration in CTRL in both CT05-R and CT20-R. 158

Figure 4.14. As in Figure 4.13, but for condensational heating rate (K hr^{-1}). 159

Figure 4.15. Radius-time cross-sections of the azimuthal mean condensational heating rate (shaded, K hr^{-1}) and tangential wind speed (contours, m s^{-1}) at the 1781-m height in (a) CT05-R and (b) CT20-R from 36 h. The red dots represent the radius of maximum tangential wind at the same level. 160

Figure 4.16. Time evolution of (a) the vertically integrated condensational heating rate (K hr^{-1}) averaged within 1.5 times of the RMW (K hr^{-1}) and (b) surface wind stress at the RMW (m s^{-2}) in CT05-R (blue) and CT20-R (red) from 36-h of simulation after C_D was modified in the two experiments. The black (green) slashed area can be considered as the difference in the indirect (dissipation) effect of surface friction. 161

Figure 4.17. Time evolution of (a) the maximum 10-m height tangential wind speed (m s^{-1}) in the control experiment (CTRL, black), the experiment with new dependence of surface drag coefficient on surface wind speed (CTDO, magenta), and the experiment with modified dependence of surface drag coefficient on surface wind speed (CTD1, blue). (b) the 12-h intensification rate (m s^{-1} 12 hr^{-1}) with 5-h running mean in CTRL (black), CTDO (magenta), and CTD1 (blue). 162

Figure 4.18. Time-height cross-sections of relative humidity (shaded, %) and the vertical velocity (contours, cm s^{-1}), both averaged within the radius of 1.5 times of the RMW in (a) CTRL, (b) CTDO, and (c) CTD1, respectively. The vertical green dashed line in each panel shows the time when the initial spin-up stage ends in the corresponding experiments. 164

Figure 4.19. Radius-height cross-sections of azimuthal mean radial wind (left shaded, m s^{-1}) and vertical velocity (left contours, m s^{-1}), together with the condensational heating rate (right shaded, K hr^{-1}) and inertial stability (right contours, 10^{-4} s^{-1}) for (a), (b) CTRL and (c), (d) CTDO, all averaged 3-h interval when the intensity is over 20 m s^{-1}, respectively. The red solid curve shows the radius of maximum wind in the corresponding experiments.....165

Figure 4.20. Time evolution of (a) the vertically integrated condensational heating rate (K hr^{-1}) averaged within 1.5 times of the RMW and (b) surface wind stress at the RMW (m s^{-2}) in CTRL (black) and CTDO (magenta) from 46 h and 53 h when the intensity is over 20 m s^{-1}, respectively.....166

Figure 4.21. As in Figure 4.19, but for (a), (b) CTDO and (c), (d) CTD1, all averaged in 3-h interval when the intensity is over 48 m s^{-1} respectively. 167

Figure 4.22. As in Figure 4.20, but for CTDO (magenta) and CTD1 (blue) from 72 h to 96 h.168

Figure 5.1. Radial distribution of (a) initial tangential wind speed (m s^{-1}) and (b) inertial stability (10^{-4} s^{-2}) in R041 (R_m = 40 km, red), R061 (R_m = 60 km, blue), and R101 (R_m = 40 km, magenta). 169

Figure 5.2. The total wind speed (m s^{-1}) at the 2320-m height at every 12-h interval from 24 h to 108 h in R041. 171

Figure 5.3. As in Figure 5.2, but for R061. 172

Figure 5.4. As in Figure 5.2, but for R101. 173

Figure 5.5. Time evolution of (a) the maximum 10-m height tangential wind speed (m s^{-1}) and (b) the radius of maximum wind (km) in R041 (R_m = 40 km, red), R061 (R_m = 60 km, blue), and R101 (R_m = 100 km, magenta). 174

Figure 5.6. Time evolution of the intensification rate (m s^{-1} 12 hr^{-1}) with 5-h running mean in R041 (R_m = 40 km, red), R061 (R_m = 60 km, blue), and R101 (R_m = 100 km, magenta). .175

Figure 5.7. Time-height cross-sections of relative humidity (shaded, %) and vertical velocity (contours, cm s^{-1}), both averaged within the radius of 1.5 times of the RMW, together with the time evolution of the RMW (km) shown at the bottom of each panel in (a) R041 (R_m = 40 km), (b) R061 (R_m = 60 km), and (c) R101 (R_m = 100 km). The vertical green dashed line in each panel shows the time when the initial spin-up stage ends in the corresponding experiment. 177

Figure 5.8. Radius-height cross-sections of the azimuthal mean radial wind (left shaded, m s^{-1}) and vertical velocity (left contours, m s^{-1}), together with the condensational heating rate (right shaded, K hr^{-1}) and inertial stability (right contours, 10^{-4} s^{-1}) for (a), (b) R041 (R_m = 40 km), (c), (d) R061 (R_m = 60 km), and (e), (f) R101 (R_m = 100 km), all averaged in 3-h interval prior to the corresponding primary intensification stage. The red solid curve shows the radius of maximum wind in the corresponding experiment..... 178

Figure 5.9. As in Figure 5.8, but for 3-h average when the intensity is over 30 m s^{-1} respectively. 180

Figure 5.10. Radial distribution of the azimuthal mean rain rate (mm day^{-1}) in R041 (R_m = 40 km, red), R061 (R_m = 60 km, blue), and R101 (R_m = 100 km, magenta), all averaged in 3-h interval when the intensity is over 30 m s^{-1} respectively..... 181

Figure 5.11. Radial distribution of (a) initial tangential wind speed (m s^{-1}) and (b) inertial stability (10^{-4} s^{-2}) in b055 (b = 0.5, magenta), b075 (b = 0.7, blue), and b105 (b = 1, red). 182

Figure 5.12. The total wind speed (m s^{-1}) at the 2320-m height at every 12-h interval from 24 h to 108 h in b055. 183

Figure 5.13. As in Figure 5.12, but for b075. 184

Figure 5.14. As in Figure 5.12, but for b105. 185

Figure 5.15. Time evolution of (a) the maximum 10-m height tangential wind speed (m s^{-1}) and

(b) the radius of maximum wind (km) in b055 (b = 0.5, magenta), b075 (b = 0.7, blue), and b105 (b = 1, red). 186

Figure 5.16. Time evolution of the intensification rate (m s^{-1} 12 hr^{-1}) with 5-h running mean in b055 (b = 0.5, magenta), b075 (b = 0.7, blue), and b105 (b = 1, red). 187

Figure 5.17. As in Figure 5.11, but at 10 h of simulation before the primary intensification stage. 188

Figure 5.18. Time-height cross-sections of relative humidity (shaded, %) and vertical velocity (contours, cm s^{-1}), both averaged within the radius of 1.5 times of the RMW, together with the time evolution of the RMW (km) shown at the bottom of each panel in (a) b055 (b = 0.5), (b) b075 (b = 0.7), and (c) b105 (b = 1). The vertical green dashed line in each panel shows the time when the initial spin-up stage ends in the corresponding experiment. 190

Figure 5.19. Radius-height cross-sections of the azimuthal mean radial wind speed (left shaded, m s^{-1}) and vertical velocity (left contours, m s^{-1}), together with the condensational heating rate (right shaded, K hr^{-1}) and inertial stability (right contours, 10^{-4} s^{-1}) for (a), (b) b055 (b = 0.5), (c), (d) b075 (b = 0.7), and (e), (f) b105 (b = 1), all averaged in 3-h interval prior to the corresponding primary intensification stage. The red solid curve shows the RMW in the corresponding experiment. 191

Figure 5.20. As in Figure 5.19, but for 3-h average when the intensity is over 35 m s^{-1} respectively. 193

Figure 5.21. Radial distribution of the azimuthal mean rain rate (mm day^{-1}) in b055 (b = 0.5, magenta), b075 (b = 0.7, blue), and b105 (b = 1, red), all averaged in 3-h interval when the intensity is over 35 m s^{-1} respectively. 194

Figure 6.1. Schematic diagram showing the indirect effect and the direct dissipation effect of boundary layer dynamics in the presence of surface friction to the TC intensification rate.

The plus (minus) sign denotes the positive (negative) contribution to TC intensification. 195

Figure 6.2. Time evolution of the maximum 10-m height tangential wind speed (m s^{-1}) for (a) CT05 and its ensemble members (b) CTRL and its ensemble members (c) CT20 and its ensemble members. 197

Figure 6.3. (a) Time evolution of the maximum 10-m height tangential wind speed (m s^{-1}) of the ensemble means (eight members) in CT05-E (blue), CTRL-E (black), and CT20-E (red). (b) Time evolution of the 12-h intensification rate (m s^{-1} 12 hr^{-1}) with 5-h running mean of ensemble means (eight members) in CT05-E (blue), CTRL-E (black), and CT20-E (red). 198

Figure 6.4. Time evolution of the maximum 10-m height tangential wind speed (m s^{-1}) in the control experiment (CTRL, black) and the experiment with 90% initial moisture in CTRL (Q090, cyan). 199

Figure 6.5. Hovmoller plots of the azimuthal mean relative humidity (%) at the 1781-m height in (a) CTRL and (b) Q090. 200

Figure 6.6. As in Figure 6.4, but for the control experiment (CTRL, black), 5% C_D experiment (C005-R, yellow), 10% C_D experiment (C010-R, cyan), 20% C_D experiment (C020-R, blue), 30% C_D experiment (C030-R, magenta), and 40% C_D experiment (C040, red). 201

Figure 6.7. As in Figure 6.4, but for the control experiment (CTRL, black), the experiment C_D = 0 (CC0-R, cyan), the experiment $C_D = 1.5\times10^{-5}$ (CC5-R, blue), and 1% C_D experiment (C001-R, magenta). 202

CHAPTER 1. INTRODUCTION

1.1 Tropical cyclones and their intensity change

Tropical cyclones (TCs) can have major impacts on human life and property of billions of people living near the coastlines in the tropics. How to accurately predict TC intensity and structure is an urgent and important issue. Tropical cyclone intensification has been studied extensively, but the dominant processes are still under debate in the literature. Observations show that TCs tend to develop and intensify over the ocean with higher enthalpy flux potential, plenty of moisture, and higher conditionally convective instability in the mid-lower troposphere. Based on observations, several mechanisms have been proposed in earlier studies to explain TC intensification. One possible mechanism is the positive feedback between boundary layer moisture convergence due to Ekman pumping and convective activity in the core region of a TC vortex, namely the so-called convective instability of the second kind (CISK) (Charney and Eliassen 1964; Ogura 1964; Ooyama 1969). By this mechanism, the secondary circulation induced by surface friction can lead to moisture convergence in the frictional boundary layer and the Ekman pumping can transport moisture into the troposphere. This supports moist convection in the inner core region and releases latent heating that further lowers the central sea level pressure, leading to the intensification of tangential wind and the primary circulation. The second

mechanism is known as the wind-induced surface heat exchange (WISHE), elaborated on by a series of studies (Riehl 1950; Kleinschmidt 1951; Malkus and Riehl 1960; Emanuel 1986, 1995, 1997). The wind-induced surface heat exchange describes a positive feedback between surface winds, heat, and moisture fluxes at the air-sea interface. As inferred from the bulk aerodynamic formula of surface entropy flux, higher tangential wind near the radius of maximum wind (RMW) can induce more surface entropy flux from the ocean under the eyewall, thus increasing equivalent potential temperature and supporting stronger eyewall updrafts and enhancing eyewall convection. This also lowers the central sea level pressure, thus accelerating surface tangential winds and causing more surface entropy flux. The major difference between the two mechanisms lies in how important the surface friction is and whether the positive feedback is a local process under the eyewall or involves the storm-scale structure. On the other hand, the TC structure may considerably affect the intensification rate of a TC as found from observation (Carrasco et al. 2014; Xu and Wang 2015, 2018a, b). The accurate forecasting of TC intensity change continues to be an active research topic.

1.2 The role of the boundary layer in tropical cyclone intensification

1.2.1. Overview of the tropical cyclone boundary layer

Many previous studies have particularly emphasized the importance of the boundary layer

dynamics to TC structure and intensification due to the presence of surface friction. A TC can be considered as a quasi-axisymmetric system. Above the boundary layer, the motion is nearly in the gradient wind balance, which means the pressure gradient force ($\partial p/\rho\partial r$) is balanced by the centrifugal force (v^2/r) and the Coriolis force (fv), as given in:

$$\frac{v^2}{r} + fv = \frac{1}{\rho}\frac{\partial p}{\partial r}, \tag{1}$$

where v is the tangential wind speed, r the radius, f the Coriolis parameter, ρ the air density, and p the pressure. However, surface friction is an important feature in the boundary layer. The wind speed in the boundary layer is often reduced by surface friction, leading to the reduction of both centrifugal force and Coriolis force, and creates an unbalanced situation. This unbalance drives the air-parcel to accelerate toward the storm center, and leading to the frictionally induced boundary layer inflow (Figure 1.1).

Since the flow converges cyclonically inward in the TC boundary layer, the TC boundary layer is also often called the inflow boundary layer. Figure 1.2 presents the vertical cross-section of the mean radial wind in Hurricane Frederic (1979). It is demonstrated that both the depth of the inflow layer and the inflow speed increase with radius in the inner core, and an outflow layer appears above the inflow layer near the storm center. The momentum equation for radial wind in an axisymmetric vortex can be written as:

$$\frac{du}{dt} - \left(\frac{V_\theta^2}{r} + fV_\theta\right) = -\frac{1}{\rho}\frac{\partial p}{\partial r}. \tag{2}$$

For a quasi-steady and quasi-horizontal motion, the term du/dt can be approximated by

$$\frac{du}{dt} = \frac{\partial u}{\partial t} + u\frac{\partial u}{\partial r} + w\frac{\partial u}{\partial z} \sim \frac{\partial}{\partial \mathrm{r}}\left(\frac{1}{2}u^2\right), \tag{3}$$

so that the equation (2) becomes:

$$\left(\frac{V_\theta^2}{r} + fV_\theta\right) = \frac{1}{\rho}\frac{\partial p}{\partial r} + \frac{\partial}{\partial \mathrm{r}}\left(\frac{1}{2}u^2\right). \tag{4}$$

Based on the definitions of supergradient/subgradient wind, that is, wind of greater/lesser speed than the gradient wind speed, the deceleration (acceleration) of radial wind implies the existence of supergradient (subgradient) wind:

$$\begin{cases} \frac{\partial}{\partial \mathrm{r}}\left(\frac{1}{2}u^2\right) > 0, & supergradient\ wind \\ \frac{\partial}{\partial \mathrm{r}}\left(\frac{1}{2}u^2\right) < 0. & subgradient\ wind \end{cases} \tag{5}$$

Therefore, from Figure 1.2 it would be expected that the flow is mostly supergradient near the top of the inflow boundary layer and subgradient above the inflow boundary layer in the eyewall region.

The observed tangential wind, radial wind, and vertical motion distributions with radius from the aircraft data on Hurricane Hugo (1989) are shown in Figure 1.3. The red curve is observed at a height of 434 m, which can be regarded as the TC boundary layer. The blue curve, at a height of 2682 m, represents the free atmosphere above the boundary layer. In the boundary layer of the eye region, both tangential wind and radial wind are weak, and the vertical motion also weak. Nevertheless, all of them sharply increase within several hundred meters of the RMW. Outside

the RMW, both tangential wind and radial wind gradually decrease, while the vertical motion decreases suddenly. The maximum upward motion appears at the radius where the tangential wind and radial wind have a sharp difference. However, this sharp contrast of wind does not appear above the boundary layer (the blue curve in Figure 1.3), and the associated vertical motion is relatively weak. The blue tangential wind curve can be regarded as a gradient balanced flow, while the red tangential wind curve is the flow in the frictional boundary layer. Since both red and blue curves are driven by the similar radial pressure gradient, the flow in the interior boundary layer is supergradient inside r ~ 13 km and subgradient outside this radius.

1.2.2. Overview of surface drag coefficient under tropical cyclones

A better understanding of the parameterization of surface drag coefficient (C_D) is essential for forecasting TC intensity and improving numerical simulation. The boundary layer can be regarded as a medium that communicates between the free atmosphere above and the ocean below. The energy from the ocean, in terms of surface enthalpy flux, determines the development and maximum intensity of a TC. Therefore, this quality has received a great deal of attention in previous studies (e.g., Malkus and Riehl 1960; Rosenthal 1962; Smith 1968; Ooyama 1969; Kurihara and Tuleya 1974; Anthes and Chang 1978; Tuleya and Kurihara 1978; Emanuel 1986, 1995). In numerical simulations, the boundary layer vertical turbulent mixing is often parameterized based on several key parameters, such as surface exchange coefficient for enthalpy

flux C_K, surface drag coefficient for momentum C_D, eddy diffusivities for enthalpy K_h, and momentum K_m. The turbulent momentum flux or wind stress (τ) at the surface is usually calculated using a bulk aerodynamic formula, which is equal to the product of C_D and the square of the 10-meter-height wind speed (U_{10}), given by:

$$\tau = \rho U_*^2 = \rho C_D U_{10}^2, \tag{6}$$

where ρ is the air density, and U_* is the friction velocity. For the neutral surface condition, the length scale height z only depends on the boundary layer shear (Garratt 1992), namely:

$$\frac{z}{U_*}\frac{\partial \mathrm{u}}{\partial \mathrm{z}} = \text{constant} = \frac{1}{k}, \tag{7}$$

where k is the von Karman constant (= 0.4 empirically). Integration of the equation yields

$$\frac{kU}{U_*} = \ln\frac{z}{z_0} \quad (\mathrm{z}/z_0 \gg 1), \tag{8}$$

where z_0 is the so-called roughness length. Substituting (8) into the bulk aerodynamic formula (6) gives

$$C_D = \left(\frac{k}{\ln\frac{z}{z_0}}\right)^2. \tag{9}$$

For the non-neutral surface conditioner, on the other hand, based on the Monin-Obukhov theory (Monin and Obukhov 1954), the general gradient form of the wind profile can be written as a function of stability parameter ζ:

$$\frac{kz}{U_*}\frac{\partial \mathrm{u}}{\partial \mathrm{z}} = \Phi(\zeta), \tag{10}$$

where $\Phi(\zeta) = 1$ in the neutral condition, $\Phi(\zeta) < 0$ in unstable conditions, and $\Phi(\zeta) > 0$ in stable

condition. The integration of (10) yields

$$\begin{aligned}\frac{kU}{U_*} &= \int (\zeta')^{-1}\,\Phi(\zeta')\mathrm{d}\zeta' \\ &= \ln\frac{z}{z_0} - \int [1-\Phi(\zeta')]\mathrm{d}(\ln\zeta') \\ &\approx \ln\frac{z}{z_0} - \Psi(\zeta). \end{aligned} \tag{11}$$

In this approximation, the effects of stability conditions can be interpreted as a deviation of the wind speed from the neutral case. In unstable conditions, $\Psi(\zeta) > 0$, while in stable conditions, $\Psi(\zeta) < 0$ (Garratt 1992). Therefore,

$$C_D = \left(\frac{k}{\ln\frac{z}{z_0} - \Psi(\zeta)}\right)^2. \tag{12}$$

Observations show that C_D is approximately in an order of 1.5×10^{-3} over the ocean. Nevertheless, estimates of C_D have a large degree of uncertainty. Previous studies have focused on the variation of C_D given 10-m height wind speed based on observations (Large and Pond 1981; Powell et al. 2003; Black et al. 2007), laboratory experiments (Donelan et al. 2004), and numerical simulations (Moon et al. 2004a, b; Gopalakrishnan 2013). These studies suggested that C_D increases linearly with a 10-m height wind speed in the low-wind regime (less than 30 m s^{-1}) while flatting off or even decreasing with 10-m height wind speed in the high-wind regime (Figure 1.4). Some researchers have made several attempts to explain these phenomena (Stogryn 1972; Monahan and O'Muircheartaigh 1980; Monahan and Woolf 1989; Newell and Zakharov 1992; Reul and Chapron 2003; Makin 2005; Callaghan et al. 2007; Soloviev et al. 2014; Golbraikh and

Shtemler 2016; Donelan 2018). The role of the air-sea foam layer was first illustrated by Newell and Zakharov (1992). Later, Makin (2005) suggested that a suspension layer is formed above the marine atmospheric surface layer resulting from the spray droplets due to intensive wave breaking at wind speeds above about 33 m s^{-1}. This suspension layer is a stable layer that damps the turbulence and hence reduces C_D. Similarly, in a laboratory experiment and numerical simulation, Soloviev et al. (2014) found that a foam layer is generated at the air-water interface. The foam layer invokes the Kelvin-Helmholtz shear instability between two fluids with a large density difference, and so reduces C_D by suppressing short gravity-capillary waves. The existing coverage of the foam layer was confirmed by Golbraikh and Shtemler (2016), who proposed a physical model for the prediction of C_D variation with wind speed by optical and radiometric measurements. More recently, Donelan (2018) used the laboratory measurements of wind stress and waves and found that C_D is not only a function of surface wind speed but also a function of the Reynolds number. He further proposed a modeled C_D variation using a surface wind speed with a Reynolds number dependent, which better resembles the observation.

1.2.3. Review of tropical cyclone boundary layer model

A tropical cyclone boundary layer model is an effective tool for examining the character of boundary layer flow under a TC, and has also been used to study the role of boundary layer dynamics in TC intensification. Rosenthal (1962) and Eliassen and Lystad (1977) used Ekman-

like models to simulate the boundary layer structure of a stationary TC vortex. Using linear models, they successfully simulated a supergradient flow at the top of the boundary layer, though it was rather weak. Shapiro (1983) found supergradient winds inside the RMW in a stationary storm by using a simple slab boundary layer model with a constant boundary layer depth. However, the simple model could not adequately describe the detail of the boundary layer structure, especially near the eyewall region. More recent studies, including Kepert (2001) and Kepert and Wang (2001), conducted two models of the tropical cyclone boundary layer to study frictional responses to a prescribed gradient flow in a TC. These models did not include the total feedback from boundary layer processes acting on a TC. They suggested that vertical advection played an important role in producing the stronger supergradient flow in the non-linear model, as the linear model showed only a weak supergradient flow. It was also shown that a TC with a weaker tangential wind in the outer radius can induce stronger inflow in the boundary layer. Furthermore, Kepert (2010a, b) compared two different boundary layer models – slab and height-resolving models of tropical cyclone boundary layers – and argued that the slab boundary layer model may overestimate the inflow as a result of excessive surface drag and thus show an overestimated supergradient wind. Therefore, he argued that the height-resolving boundary layer model should be used rather than the slab boundary layer model. In summary, results from the literature suggest that boundary layer dynamics can produce supergradient winds near the top of

the inflow boundary layer.

1.2.4. The boundary layer spin-up mechanism

Previous studies based on balanced vortex dynamics have demonstrated that the radial inflow induced by diabatic heating in eyewall convection can bring significant absolute angular momentum (AAM) inward in the mid-lower troposphere (including the boundary layer) to spin up the tangential wind, thus leading to the intensification of a TC (Schubert and Hack 1982; Shapiro and Willoughby 1982; Pendergrass and Willoughby 2009; Fudeyasu and Wang 2011; Molinari and Vollaro 1990; Molinari et al. 1993; Möller and Shapiro 2002; Persing et al. 2002; Hendricks et al. 2004; Montgomery et al. 2006). Smith et al. (2009) proposed two intensification processes. The first is the spin-up of the TC outer circulation or the increase of the TC size above the boundary layer due to the convergence of AAM where AAM is conserved. The second process is called the boundary layer spin-up mechanism, which spins up the inner core of the storm in the boundary layer, where the AAM is not conserved. They argued that although AAM is not conserved due to dissipation from surface friction in the boundary layer, the tangential wind tendency can be still positive when the reduction of AAM due to surface friction is less than the inward transport of AAM by the frictionally induced radial inflow (Figure 1.5). Namely, the storm can spin up when the positive tangential wind tendency induced by the inward AAM transport is large enough to offset the negative tangential wind tendency resulting from surface friction. Smith

et al. (2009) also emphasized that the second spin-up mechanism is mainly related to unbalanced boundary layer dynamics in the inner-core region. Since the unbalanced dynamics directly results from surface friction, this implies that surface friction and its related unbalanced dynamics chiefly contribute to the spin-up of the inner core of the TC boundary layer.

This boundary layer spin-up mechanism described by Smith et al. (2009) was evaluated in several subsequent studies. Stern et al. (2015) calculated the tangential wind tendency due to surface friction and diabatic heating in a numerically simulated TC in the Weather Research and Forecasting (WRF) model using the linearized vortex model (Three-Dimensional Vortex Perturbation Analysis and Simulation – 3DVPAS). They suggested that the tangential wind tendency from diabatic heating is positive near the RMW, while the net frictionally induced tangential wind tendency is negative near the RMW in the boundary layer. This means that the net contribution of surface friction to TC intensification is negative. In a latter study, Smith and Montgomery (2015) argued that since the spin-up processes proposed by Smith et al. (2009) are intrinsically nonlinear, the linearized diagnostic model used in Stern et al. (2015) cannot be utilized to verify the boundary layer spin-up mechanism.

Heng and Wang (2016a) carried out two experiments, one with and one without surface friction, with prescribed eyewall heating in the nonlinear TC model version 4 (TCM4). They showed that surface friction could enhance inflow and vertical motion in the boundary layer and

also contribute to the contraction of the RMW of a model TC. However, they found that the positive tangential wind tendency due to the frictionally induced inward AAM transport is not large enough to offset the negative tangential wind tendency due to the frictional loss of AAM. This is consistent with the results of Stern et al. (2015), but contradicts the mechanism proposed by Smith et al. (2009). Heng and Wang (2016a) suggested that condensational heating in the eyewall should be the primary driving force of TC intensification, and that surface friction could contribute to TC intensification indirectly by modifying the strength and radial location of eyewall updrafts or convection and the contraction of the RMW. However, since the diabatic heating rate in the numerical experiments was prescribed in Heng and Wang (2016a), the possible feedback between the eyewall convection and boundary layer inflow resulting from the presence of surface friction and eyewall heating was not considered. In a follow up study, Heng et al. (2017) revisited the balanced and unbalanced aspects of TC intensification in a full-physics model simulation using the Sawyer-Eliassen balanced vortex model and found that the balanced dynamics can largely reproduce the secondary circulation in the full-physics model simulation and thus can capture the simulated TC intensification. In addition, they found that unbalanced dynamics plays a role in preventing agradient winds from further intensification, a process related to gradient wind adjustment. As a result, Heng et al. (2017) argued that the spin-up mechanism of supergradient winds in the interior of the boundary layer do not likely contribute significantly to

the overall TC intensification because the supergradient flow exists in the lifetime of a TC from its developing stage to weakening stage. They also further emphasized that condensational heating in the eyewall is the main driving force of TC intensification, and that surface friction and the related unbalanced dynamics can contribute to TC intensification through their modification to strength and radial location of eyewall updrafts and thus condensational heating in the eyewall. Heng et al. (2017) called this the indirect effect of surface friction on TC intensification.

1.2.5. Sensitivity of tropical cyclone intensification to surface drag coefficient in numerical models

Several studies (Craig and Gray 1996; Thomsen et al. 2014; Peng et al. 2018) have shown that the intensification rate of a TC vortex in state-of-the-art high-resolution numerical models is often insensitive to C_D (in the reasonable range) during its primary intensification stage. Since the indirect effect of boundary layer dynamics, namely surface friction, can contribute to TC intensification through modification to convection and diabatic heating in the eyewall, in the presence of surface friction may have a positive (indirect) effect on TC intensification (Kepert 2017; Li and Wang 2018a, b), while the mechanical dissipation (direct) effect of surface friction has a negative effect on TC intensification (Stern et al. 2015; Heng and Wang 2016a, b; Heng et al. 2017). It seems that in a reasonable parameter space, the positive and negative effects largely offset each other, giving rise to the insensitivity of the simulated TC intensification rate to changes

in C_D (a point that will be verified in the present study).

However, other studies have suggested that TC intensification is considerably sensitive to C_D. For instance, Rosenthal (1971) investigated the sensitivity of TC intensification to C_D in an axisymmetric hydrostatic primitive equation model with a modified Kuo-type cumulus parameterization scheme. He showed that the intensification rate of the simulated TC increased with the increasing C_D, while the steady-state intensity of the TC decreased as C_D increased and no TC intensification occurred when C_D was set to zero. He suggested that the low-level frictional convergence of water vapor is key to convection in the inner core and thus the intensification of a TC. In a more recent study, Montgomery et al. (2010) examined the sensitivity of the intensification rate of a simulated TC to C_D using a three-dimensional, nonhydrostatic, cloud-resolving model. They found that both the intensification rate and the mature intensity of the simulated TC increased slightly with an increase in C_D when the C_D was less than 2.0×10^{-3}, but that the mature intensity decreased for both larger or zero C_D (see their Fig. 1). However, in a later following-up numerical modeling study, Thomsen et al. (2014) showed that the simulated TC intensification rate and mature intensity were insensitive to randomly perturbed C_D with changes of as large as 60%, even when the same numerical model and similar experimental design were adopted. Schecter (2011) studied TC formation and intensification using the Regional Atmospheric Modeling System (RAMS) and found that there was no TC formation with zero C_D.

Although these studies seem to have turned up inconsistent results, caution needs to be taken. This particularly applies for the work of Rosenthal (1971), who used a cumulus parameterization scheme that connected convection in the inner core with frictional convergence in the boundary layer. In addition, it is noted that in Montgomery et al. (2010), if the initial spin-up stage of the TC were to be excluded, the dependence of the resulting intensification rate on C_D during the primary intensification stage would become quite weak as well.

In brief, Table 1.1 summarizes the main results in the literature and suggests that all previous studies have demonstrated that surface friction is indispensable to the formation and subsequent intensification of TCs, although the TC intensification rate during its primary intensification stage is still under debate. Therefore, the physical reasoning behind such sensitivity or insensitivity in numerical simulations should be carefully investigated.

1.3 Eyewall convection and its impact on tropical cyclone intensification

The eyewall convection plays a significant role in TC intensification. Convection is commonly accompanied with high moist content and thus a greater virtual temperature and includes plenty of moist static energy. The positive localized temperature tendency leads to a decrease in central sea level pressure (Emanuel 1997). However, the efficiency of diabatic heating being converted to kinetic energy of the storm can determine whether a TC will intensify or not (Schubert and

Hack 1982, Nolan et al. 2007). Regarding the relationship between the location of eyewall convection and TC intensification, Vigh and Schubert (2009) suggested based on results from a balanced model that storms with eyewall convection inside the RMW have more rapid intensification. They emphasized that diabatic heating in the high-inertial-stability region (i.e., inside the RMW) is able to generate a temperature tendency associated with storm intensification. In short, the more heating that occurs inside the RMW, the higher intensification rate the storm has. In a similar study, Pendergrass and Willoughby (2009), using the Sawyer-Eliassen equation, demonstrated that the intensification rate of a TC vortex is sensitive to the radial location of heating source, and is also dependent on the storm structure and the associated secondary circulation.

Rogers et al. (2013) compared two groups of TCs using data from National Oceanic and Atmospheric Administration (NOAA) WP-3D aircraft missions. The first group included the intensifying storms, and the other included the steady-state storms. Based on a composite analysis, they found that the tangential wind was stronger in the outer core region in the steady-state group than in the intensifying group, which means that the storms in the steady-state group had larger the radius of gale form wind (RGW) (i.e., the radial decay rate of the tangential wind outside the RMW) as measured by the tangential wind outside the inner core. A storm with a larger RGW indicates a slower radial decay rate of tangential wind. They also found that more convective

bursts are located inside of the RMW for the intensifying group, whereas more convective bursts are located outside of the RMW for the steady-state group. As a result, they suggested that the radial location of convection and the tangential wind profile outside the RMW are key to determining whether or not a TC will intensify. However, this raises questions as to what determines the radial location of eyewall convection and whether the vortex structure plays an important role in affecting the strength and radial location of eyewall convection.

1.4 The influence of tropical cyclone structure and intensity on storm intensification

In addition to environmental forcing, the TC structure, such as the RMW, RGW, and intensity can significantly affect the intensification rate of a storm. From a theoretical point of view, several studies have shown that the TC intensity and inner-core size play an important role in TC intensification (Shapiro and Willoughby 1982; Schubert and Hack 1982; DeMaria et al. 2005; DeMaria (2009); Pendergrass and Willoughby 2009; Kaplan et al. 2010). The results from one of these studies, conducted by Shapiro and Willoughby (1982), suggested that the tangential wind tendency (namely the intensification rate) is maximum inside the RMW given diabatic heating in the eyewall (near the RMW) in an idealized barotropic TC vortex. This leads to the contraction of the eyewall as the TC vortex intensifies. In a latter study, Schubert and Hack (1982) showed that the inertial stability in the inner-core can determine the efficiency of latent heat release to

enable local temperature change and tangential wind change, which increase as the TC vortex intensifies. Specifically, local warming caused by diabatic heating in the eyewall is substantially greater in a region of relatively high inertial stability. Since the inertial stability in the inner core is a function of both TC intensity and structure (such as the RMW), the results from the balanced dynamics also imply that the intensification rate of the TC could depend on TC structure and intensity. In addition, results from DeMaria et al. (2005), DeMaria (2009), and Kaplan et al. (2010) have suggested that the intensification rate substantially depends on the initial TC intensity.

Both observational and numerical studies have focused on the impact of TC structure and intensity on TC intensification. Observational studies (Kimball and Mulekar 2004; Chen et al. 2011; Rogers et al. 2013; Carrasco et al. 2014; Xu and Wang 2015; Xu and Wang 2018a, b) have assessed the statistical behavior of the dependence of the intensification rate on TC structure and intensity. For instance, Kimball and Mulekar (2004) examined 6-hourly best-track data of Atlantic TCs during the period of 1988-2002 and stratified the dataset by intensifying, steady-state, and weakening TCs over the next six hours. They found that the percentage of smaller RMW in weakening storms is higher than the percentage of smaller RMW in intensifying storms. However, Chen et al. (2011), by comparing the 24-h intensification for western North Pacific TCs, showed that higher intensification rates are favorable for compact TCs (either small RMW, or smaller average 34-kt wind radius, or both). Compact TCs with strong convection concentrated near their

centers also show more frequent occurrences of rapid intensification relative to incompact storms over the western North Pacific.

Similar to the results in Chen et al. (2011), Carrasco et al. (2014) investigated TCs and their 24-h intensification from 1990 to 2010, using data from the second-generation North Atlantic hurricane database (HURDAT2). They concluded that the rapid intensification of TCs shows a significant dependence on the initial size (RMW and average 34-kt wind radius) of the TCs. Comparisons between rapid intensification and non-rapid intensification TCs suggested that TCs that undergo rapid intensification tend to be smaller initially than the non-rapidly intensifying TCs. Based on the same database, Xu and Wang (2015) also examined the dependence of subsequent 24-h intensification rates on both TC initial structure and intensity for a total of 341 TCs in North Atlantic basin occurring during 1988-2012. They found that the intensification rate of a TC is positively correlated with TC intensity when the maximum wind speed is below 80 knots, and is negatively correlated with TC intensity when the maximum wind speed is above 80 knots. This cut-off point for the maximum wind speed was interpreted as a balance between the potential intensification due to the increase of inertial stability in the inner-core as the storm intensifies and the approaching to the maximum potential intensity (MPI). The increasing efficiency of the intensification to eyewall heating leads the increasing trend of intensification rate when the TC intensity is below 80 knots. On the other hand, energy dissipation due to surface friction offsets

the increasing heating efficiency when the maximum wind speed becomes greater than 80 knots. In addition, results showed that the intensification rate of TCs increases with decreasing RMW due to the higher inertial stability for those TCs, given their intensity. Similar to the results of Rogers et al. (2013), Xu and Wang also found that storms with larger RGW are unfavorable to rapid intensification. More recently, as a follow-up study, Xu and Wang (2018a) extended the statistical analysis in Xu and Wang (2015) to the western North Pacific in the period from 1982 to 2015. The overall results were considerably similar to those from the TCs in the North Atlantic basin.

The earliest numerical simulation study on the dependence on storm size was Rotunno and Emanuel (1987), who carried out numerical simulations with a non-hydrostatic primitive-equation model. By performing the sensitivity experiments with different initial TC vortex sizes, it was found that a larger initial RMW TC vortex leads to a slower intensification. In a recent numerical study, Xu and Wang (2018b) used the non-hydrostatic, axisymmetric, full-physics model CM1, developed by Bryan and Fritsch (2002), to conduct idealized sensitivity experiments to understand the impact of the initial TC vortex structure on the spin-up stage and the primary intensification stage of the simulated TC vortex. They found that the spin-up stage is shorter and the primary intensification rate is higher for an initially smaller RMW TC vortex or an initially smaller RGW TC vortex. The weaker Ekman pumping of a larger RMW vortex and the higher inertial stability

outside the RMW of a large RGW TC lead to a longer spin-up stage and a lower intensification rate during the primary intensification stage. In short, previous studies have suggested that TCs with higher intensities, smaller RMWs, and smaller RGWs have shorter spin-up stages and subsequent higher intensification rate. However, understanding why the intensification rate of a TC depends strongly on TC structure still needs to be improved.

1.5 The link between tropical cyclone boundary layer dynamics and eyewall convection

Convection in the eyewall of a TC is always rooted in the boundary layer where mass and moisture convergence and large surface enthalpy flux are located. Therefore, in most early successful numerical simulations of TCs, moist convection was often parameterized based on mass-flux (vertical motion) at the top of the boundary layer or moisture convergence in the boundary layer (e.g., Ooyama 1969; Yamasaki 1968; DeMaria and Schubert 1984). All of these studies demonstrated the importance of boundary layer dynamics in controlling the organization of convection and diabatic heating in the eyewall, and thus the intensification of a TC. Kepert (2017) recently studied the boundary layer control of the radial location of eyewall updraft (and thus convection). He found that frictional eyewall updraft is often displaced to the inward side of the RMW by a distance scaled by $-u_{10}/I$ (where $-u_{10}$ is the 10-m height frictional inflow and I is the inertial stability parameter). This results from the nonlinear overshooting of the inflowing air

as it crosses the relatively sharp increase in *I* inside the RMW. This inward displacement of eyewall updraft relative to the RMW favors eyewall contraction, particularly when the RMW is relatively large (due to smaller *I*) or in the early development stage of a TC with rapid eyewall contraction. Kepert (2017) also suggested that the dependence of the inward displacement may partially explain why observed RMWs are rarely less than 20 km and why storms with relatively peaked radial profiles of tangential wind speed can intensify more rapidly. However, these conclusions are based on only a simple TC boundary layer model. The gradient wind distribution at the top of the boundary layer was specified in Kepert's study (2017).

The aforementioned studies suggest two opposing effects of boundary layer dynamics due to the presence of surface friction on TC intensification. On one hand, surface friction can cause a reduction in maximum tangential wind speed through the turbulent stress at the surface in a TC, or a "dissipation effect." On the other hand, the nonlinear boundary layer dynamics in the presence of surface friction may largely control the strength and radial location of mass and moisture convergences in the boundary layer and the upward mass-flux at the top of the boundary layer regarding to the TC structure, and thus the eyewall updraft and convection, contributing positively to TC intensification. This perspective could be framed in terms of an "indirect effect" of surface friction on TC intensification. It is needed to distinguish both direct dissipation and indirect effects of surface friction and the related boundary layer dynamics on TC intensification. Meanwhile,

based on the results in Rogers et al. (2013) and Kepert (2017), it could be concluded that the TC structure such as RMW and RGW may have a significant impact on determining the intensification rate of the TC through affecting the strength and radial location of eyewall convection.

1.6 Objectives and approaches

The purpose of this study is to understand and quantify not only the direct dissipation effect and the indirect effect of the boundary layer dynamics on TC intensification, but also the effect of TC structure, including RMW and RGW, on TC intensification through both effects of surface friction and the associated boundary layer dynamics. As opposed to the approach of most previous studies, in which the gradient wind at the top of the boundary layer is specified, this study allows the gradient wind above the boundary layer to evolve as a response to the boundary layer dynamics through the eyewall convection and diabatic heating. In turn, this allows the changes in gradient wind above the boundary layer to further modify the boundary layer response and feedback to gradient wind above the boundary layer again. This coupled process is studied using three models with different complexities, and without and with the dissipation effect of surface friction. The first model is a multi-level simple boundary layer model, which is used to understand how the boundary layer responds to surface friction given a radial distribution of gradient wind above the

boundary layer. The second model is a simplified dynamical framework – an interactive model that includes three layers: a multi-level boundary layer model that is the same as in the first model, a middle layer above the boundary layer, and an upper layer. The middle layer interacts with the boundary layer model through the mass sink term, which mimics diabatic heating in the TC eyewall. Since the dissipation effect of surface friction on motion is roughly included in the middle layer, the results from the second model can thus help distinctly evaluate the indirect effect of boundary layer dynamics on TC intensification. The third model is the full-physics TC model: TCM4, which is used to perform sensitivity experiments to evaluate the combined indirect effect and dissipation effect of boundary layer dynamics on TC intensification. In addition, the sensitivity to TC structure of TC intensification is investigated by the TCM4. The effect of initial TC structure on TC intensification through boundary layer dynamics introduced above is examined. A brief description of the three models, experimental design, and data are given in Chapter 2 and summarized in Table 1.2. Results from the simple boundary layer model and those from the interactive model are discussed in Chapter 3, and results of the sensitivity experiments regarding surface friction and the interpretation from the full-physics model are described in Chapter 4. Then, the sensitivity experiments regarding TC structure from the full-physics model are explained in Chapter 5. The main conclusions from this study are summarized in Chapter 6. The following scientific questions will be addressed in this study:

1. What is the tangential wind tendency in the boundary layer of a tropical cyclone induced by surface friction?
2. How do the feedbacks proceed between the boundary layer response and the radial gradient wind distribution above the boundary layer?
3. What is the net effect of surface friction on tropical cyclone intensification in terms of dissipation and indirect processes?
4. How important is the initial radial distribution of gradient wind above the boundary layer in the subsequent evaluation of the above feedback processes?
5. Whether is the surface wind speed dependence of surface drag coefficient important to the tropical cyclone intensification?
6. How does the initial TC structure determine the intensification rate through the boundary layer dynamics?

CHAPTER 2. MODEL DESCRIPTION AND EXPERIMENTAL DESIGN

2.1 The multi-level boundary layer model

The multi-level axisymmetric TC boundary layer model used in this study is a simplified version of the TC boundary layer model of Kepert and Wang (2001) and similar to the one used in Kepert (2017). The air in this model is assumed to be incompressible and homogeneous. For the governing equations, two momentum equations and a mass continuity equation are given below:

$$\frac{\partial u}{\partial \mathrm{t}} + u\frac{\partial u}{\partial r} + w\frac{\partial u}{\partial z} = -\frac{1}{\rho}\frac{\partial p}{\partial r} + v\left(f + \frac{v}{r}\right) + F_u + D_u, \tag{13}$$

$$\frac{\partial v}{\partial \mathrm{t}} + u\frac{\partial v}{\partial r} + w\frac{\partial v}{\partial z} = -u\left(f + \frac{v}{r}\right) + F_v + D_v, \tag{14}$$

$$\frac{1}{r}\frac{\partial ru}{\partial r} + \frac{\partial w}{\partial z} = 0, \tag{15}$$

where u and v are the radial and tangential wind components respectively, w is the vertical velocity, r is the radius, z is the height, and f is the Coriolis parameter. $\frac{1}{\rho}\frac{\partial p}{\partial r} = v_p\left(f + \frac{v_p}{r}\right)$ is the pressure gradient force in gradient wind balance, where v_p is the gradient (tangential) wind immediately above the boundary layer. F_u and F_v are the vertical diffusions of u and v components, and D_u and D_v are the horizontal diffusions of u and v components.

The horizontal diffusion terms are calculated with the Laplacian operator in cylindrical coordinates as given below (Rotunno and Emanuel 1987):

$$D_u = \frac{1}{r}\left[\frac{\partial}{\partial r}\left(2K_H\frac{\partial u}{\partial r}\right) - 2K_H\frac{u}{r}\right], \tag{16}$$

$$D_v = \frac{1}{r^2}\frac{\partial}{\partial r}\left[r^2 K_H r \frac{\partial}{\partial r}\left(\frac{v}{r}\right)\right], \quad (17)$$

where K_H is the horizontal diffusion coefficient and is a function of horizontal mixing length l_H and deformation field S, namely,

$$K_H = K_{H0} + l_H^2 S, \quad (18)$$

$$S^2 = 2\left[\left(\frac{\partial u}{\partial r}\right)^2 + \left(\frac{u}{r}\right)^2\right] + \left(\frac{\partial v}{\partial r} - \frac{v}{r}\right)^2, \quad (19)$$

where a small background horizontal diffusion coefficient K_{H0} (= $0.5\triangle r$, where $\triangle r$ is the grid spacing in the radial direction, namely 1000 m) is added to reduce noise in the outer region of the model where the horizontal deformation is weak. The horizontal mixing length l_H is taken to be $0.5\triangle r$, a value similar to that recommended by Zhang and Montgomery (2012) based on observations in TCs.

The vertical diffusion term is given by

$$F_A = \frac{\partial F^A}{\partial z} = \frac{\partial}{\partial z}\left(K_m \frac{\partial A}{\partial z}\right), \quad (20)$$

where F^A is the vertical flux of A (u or v). K_m is the vertical diffusion coefficient and is given by

$$K_m = l_V^2 \max(0.0, 1 - \alpha R_i)\left|\frac{\partial \vec{V}}{\partial z}\right|, \quad (21)$$

where $\vec{V}$ is the total wind vector, l_V is the vertical mixing length defined as $l_V = \frac{\kappa z}{1+\kappa z/l_0}$ with l_0 (= 80 m) being the asymptotic mixing length, κ (0.4) is the von Karmen constant, α =1.12, and R_i is the Richardson number defined as $Ri = \frac{N}{\left|\frac{\partial \vec{V}}{\partial z}\right|^2}$. In this study, the Vaisaila frequency $N = 10^{-5}$ s^{-1} is fixed. The momentum flux (stress) at the surface is calculated using the bulk formula

$$F^A = C_D\left|\vec{V}\right|A, \tag{22}$$

where the surface drag coefficient (C_D) is given as

$$C_D = \max(1.0, \min\left(2.4,\ 1.0 + 0.07 * \left(\left|\vec{V}\right| - 5.0\right)\right)) * 10^{-3}. \tag{23}$$

In this boundary layer model, the pressure gradient force is calculated based on the gradient wind at the top of the boundary layer. The modified parametric TC tangential wind profile (Wood and White 2011; Wood et al. 2013) is used to define the gradient wind at the top of the boundary layer, namely,

$$V_p(r) = V_m\left(\frac{r}{R_m}\right)\left\{1 + \frac{1}{1+b}\left[\left(\frac{r}{R_m}\right)^{\frac{1+b}{0.2}} - 1\right]\right\}^{-0.2}, \qquad r \le R_o, \tag{24}$$

$$V_p^M(r) = V_p(r)e^{\left(-\frac{r-R_o}{R_d}\right)}, \qquad r > R_o, \tag{25}$$

where b is the decaying parameter for the outer tangential wind speed, V_m is the maximum tangential wind speed, R_m is the RMW, and R_o (= 600 km) and R_d (= 800 km) are two specific radii to force the tangential wind to vanish in the environment of the TC vortex. These were used as the initial conditions of the boundary layer model and independent of time at the model top (z = 2500 m). The boundary layer was unevenly discretized into 24 layers between the surface and 2500 m, with the lowest model level of u, v being at a height of 10 m.

To understand the effects of surface friction and the given gradient wind distribution at the model top on the boundary layer response, four groups of sensitivity experiments with varying

surface friction, RMW, RGW, and intensity of TC vortices at the model top were conducted. The sensitivity to surface friction was examined by modifying C_D multiplied by a factor from 0.5 to 2 of the default value given in equation (23) with an interval of 0.05 (31 cases in total). The sensitivity to the storm RGW was examined by varying the shape parameter *b* from 0.4 to 1 with an interval of 0.05 (13 cases in total). The sensitivity to the storm RMW was examined by varying RMW (R_m) from 20 km to 100 km with an interval of 1 km (81 cases in total). Finally, the sensitivity to the storm intensity was examined by varying V_m from 15 m s^{-1} to 35 m s^{-1} with an interval of 0.5 m s^{-1} (41 cases in total). Note that in these experiments, although the boundary layer response was often faster (around two hours in most cases), all experiments were integrated for eight hours until a steady state was nearly reached. Several examples of the radial distribution of the initial tangential wind speed and the geopotential height are shown in Figure 2.1 and Figure 2.2.

2.2 The interactive model

The interactive model consists of three layers lying on top of each other, including the multi-level boundary layer model described in Section 2.1 in the bottom layer, a shallow water equation in the middle layer, and an upper layer with a lower density, sketched in Figure 2.3. This model is similar to the one used in Frisius and Lee (2016), which was modified from the Ooyama model

(Ooyama 1969). The lowest layer in the bottom layer is adjacent to the sea surface, where the surface turbulent entropy flux and stress are parameterized based on the bulk scheme. The interface between the bottom and the middle layers is fixed in height but permeable, while both the interface between the middle and the upper layers and the top of the upper layer are assumed to be a free material surface. A constant value is assumed for the thickness of the bottom layer H_b (1000 m), while the thicknesses of the middle and the upper layers, h_1 and h_2, are both variable and functions of time and radius. A major simplification of the system used in this study is that the ratio of the upper layer to the middle layer perturbation depths is assumed to be a constant -α, namely a baroclinic vertical structure

$$h_2 - H_2 = -\alpha(h_1 - H_1), \tag{26}$$

and the density ratio of the upper layer to the middle layer ε ($\varepsilon < 1$) is used to represent the stable stratification of the troposphere as in Ooyama (1969), that is,

$$\rho_2 = \varepsilon\rho_0 \; and \; \rho_1 = \rho_0. \tag{27}$$

In contrast with the boundary layer model described in Section 2.1, both the radial distribution of gradient wind and the pressure gradient force above the boundary layer (i.e., in the middle layer here) are not fixed in time, but evolve with time and are governed by the shallow water equations given below:

$$\frac{\partial u_1}{\partial \mathrm{t}} + u_1 \frac{\partial u_1}{\partial r} = -\frac{\partial \phi_1}{\partial r} + v_1 \left(f + \frac{v_1}{r}\right) + D_{u1} + S_{u_1}, \tag{28}$$

$$\frac{\partial v_1}{\partial \mathrm{t}} + u_1 \frac{\partial v_1}{\partial r} = -u_1 \left(f + \frac{v_1}{r} \right) + D_{v1} + S_{v_1}, \tag{29}$$

$$\frac{\partial h_1}{\partial t} + \frac{\partial r u_1 h_1}{r \partial r} = S_h, \tag{30}$$

where u_1 and v_1 are the radial wind and tangential wind components in the middle layer respectively, r is the radius, $\partial \phi_1 / \partial r$ is the pressure gradient force, and h_1 is the height of the interface between the middle layer and upper layer with a mean depth of 5000 m (the results are not sensitive to the mean depth and thus the same value was used in all experiments). D_{u1} and D_{v1} are the horizontal diffusion of u_1 and v_1 components as used in the boundary layer model described in Section 2.1, and S_{v_1} and S_{v_2} are the radial and tangential momentum sources related to the cumulus vertical transport and vertical mixing (see below). The perturbation geopotentials in the middle layer and upper layer are, respectively,

$$\phi_1 = g(h_1 - H_1) + \varepsilon g(h_2 - H_2), \text{ and} \tag{31}$$

$$\phi_2 = g(h_1 - H_1) + g(h_2 - H_2), \tag{32}$$

where g is gravity and H_1 and H_2 are the mean depths of the middle layer and upper layer, respectively. Both are taken as 5000 m as in the original Ooyama model. Note that although the wind and pressure gradient force do not explicitly appear in the prognostic system, the perturbation geopotential ϕ_2 is needed to determine the thickness of the middle and upper layers so that the warm core can be roughly estimated in the simplified system (see below). S_h is the mass sink representing diabatic heating, and is parameterized as follows:

$$S = (1-\eta)w_p, \quad w_p > 0, \tag{33}$$

where w_p is the vertical velocity at the top of the bottom boundary layer. A constant of 1000 m is used in the interactive model. This term can be regarded as a representative of convective heating in the eyewall of a TC, similar to the CISK-type cumulus parameterization following Ooyama (1969). The nondimensional entrainment parameter η is a function of the radius and the equivalent potential temperature profile, namely the vertical thermal and moisture stratification (Ooyama 1969):

$$\eta = 1 + \frac{\theta_{eb} - \theta^*_{e2}}{\theta^*_{e2} - \theta_{e1}}, \tag{34}$$

where θ^*_{e2} is the saturation equivalent potential temperature in the upper layer and θ_{eb} and θ_{e1} are the equivalent potential temperatures in the boundary layer and in the middle layer respectively. A constant value of 332 is given for θ_{e1} as used in Ooyama (1069), while θ^*_{e2} is given by

$$\theta^*_{e2} = \overline{\theta^*_{e2}} + \frac{a}{C_p}(\phi_2 - \phi_1), \tag{35}$$

where $\overline{\theta^*_{e2}}$ is the initial ambient value of θ^*_{e2} and a is a positive constant that was readily estimated as 10.0 by Ooyama (1069). C_P is the heat capacity at constant pressure. The boundary layer θ^*_{eb} is predicted using the following prognostic equation:

$$\frac{\partial \theta_{eb}}{\partial t} = -u_b \frac{\partial \theta_{eb}}{\partial r} + w_{p-} \frac{\theta_{e1} - \theta_{eb}}{H_b} + C_E \left|\overrightarrow{V_{10}}\right| \frac{\theta^*_{es} - \theta_{eb}}{H_b} + D_{\theta_{eb}}, \tag{36}$$

where u_b is the vertically average radial wind obtained from the multi-level boundary layer model,

w_{p-} is zero for positive w_p at the top of the boundary layer, C_E is the surface exchange coefficient taken as a constant of 1.2×10^{-3}, $\left|\overrightarrow{V_{10}}\right|$ is the wind speed at 10-m height above the sea surface from the multi-level boundary layer, and $D_{\theta_{eb}}$ is the horizontal diffusion of θ_{eb}. The first term on the right hand side is the radial advection, the second term is the downward flux of the middle layer θ_{e1} into the boundary layer due to downward motion, and the third term is surface flux. The local saturation equivalent potential temperature at the sea surface θ^*_{es} is assumed to vary linearly with the hydrostatic surface pressure anomaly as in Ooyama (1069), and is given by

$$\theta^*_{es} = \overline{\theta^*_{es}} - \frac{b}{C_p}\phi_1, \tag{37}$$

where $\overline{\theta^*_{es}}$ defines the ambient surface saturation equivalent potential temperature. A constant value of 372 K is used in all of numerical experiments, which is equivalent to SST of 29 ^{o}C in the mean tropical conditions. The initial value of θ_{eb} is set to be 10 K higher than the middle layer θ_{e1} based on the typical stratification of the tropical atmosphere (Jordan 1958) (Figure 2.4).

In addition to the mass sink, the middle layer and the boundary layer also exchange momentum through vertical advection and the simply parameterized cumulus transport and vertical mixing. This is different from the multi-level boundary layer model discussed in Section 2.1, where the no-shear assumption had been used as the top boundary condition for both radial and tangential winds at the model top. In the interactive model, the middle layer radial and tangential winds are used as the top boundary condition in the multi-level boundary layer. In this

case, the upwind scheme is used to calculate vertical advection at the top of the multi-level boundary layer where the downward motion is allowed to advect both tangential and radial winds from the middle layer to the upper boundary layer. The momentum sources in the middle layer have the following form

$$S_{u_1} = \frac{1}{2}[(1-\eta) + |(1-\eta)|]w_{p+}\frac{(u_{944}-u_1)}{h_1}, \quad (38)$$

$$S_{v_1} = \frac{1}{2}[(1-\eta) + |(1-\eta)|]w_{p+}\frac{(v_{944}-v_1)}{h_1}, \quad (39)$$

where the subscript 944 means the value at the 944-m height, namely the top (u_1, v_1) level in the boundary layer model. w_{p+} is the upward motion (zero if w_p is less than zero). The shear in the middle layer is assumed to be zero. The right hand side is related to cumulus momentum transport as in Ooyama (1969). Note that the vertical mixing across the interface of the boundary layer and the middle layer is not included in the momentum equation.

In this interactive model, the mass sink will modify the pressure field and thus the gradient wind distribution in the middle layer. The gradient wind distribution in turn affects the boundary layer response and vertical motion at the top of the boundary layer. Therefore, how the boundary layer dynamics contributes to diabatic heating and spins up the TC can be addressed, as well as how the TC vortex structure above the boundary layer may affect the vertical motion at the top of the boundary layer and thus the strength and radial location of diabatic heating in the eyewall of the TC. Note that although the exchange of momentum between the multi-level boundary layer

and the middle layer is considered, but is treated very crudely. As a result, it is best to keep in mind that the effect of surface friction on the middle layer motion is not accurately represented.

Similar to the experiments designed in Section 2.1, the sensitivity of the intensification rate of the TC vortex to surface friction, RMW, RGW and intensity of the TC vortex were studied using the interactive model. All experiments were run for 18 h. As noted above, since the dissipation effect of surface friction on motion was roughly included in the middle layer above the boundary layer, this interactive model was mainly used to illustrate the indirect effect of surface friction on TC intensification rate through modulating the radial location and strength of eyewall heating. The model parameters used in all experiments are listed in Table 2.1.

2.3 Tropical Cyclone Model version 4 (TCM4)

The Tropical Cyclone Model version 4 (TCM4) developed by Wang (2007) was used in this study, which is a quadruply nested, fully compressible, and nonhydrostatic primitive equation model. The lower boundary is a flat surface with the unperturbed surface pressure of 1010 hPa. The upper boundary is set at about 38 km with a sponge-type layer above about 20 km to absorb the upward-propagating gravity and sound waves as in Durran and Klemp (1983). The model domain has four meshes that are two-way interactively nested, with horizontal grid spacings of 67.5, 22.5, 7.5, and 2.5 km and domain sizes of 281×241, 181×181, 217×217, and 271×271 grid

points respectively. The model has 32 vertical levels with relatively higher resolutions in the boundary layer and near the tropopause.

The model physics include a modified Monin-Obukhov scheme for surface flux calculation (Fairall et al. 2003), an E-ε turbulence closure scheme for subgrid-scale vertical turbulent mixing (Langland and Liou 1996), an explicit treatment of mixed-phase bulk cloud microphysics (Wang 1999, 2001), a Newtonian cooling term that is added to the potential temperature equation to mimic longwave radiative cooling as used in Rotunno and Emanuel (1987), a nonlinear fourth-order horizontal diffusion term with the deformation-dependent diffusion coefficient for all prognostic variables except for that related to the mass conservation equation, and a turbulent kinetic energy dissipation rate ε that is added to the thermodynamic equation to take into account the dissipative heating due to turbulent motion (Table 2.2). Cumulus parameterization was not employed even in the outermost domain, because in an environment at rest convection and spiral rainbands are mainly active within a radius of around 300 km from the TC center and thus can be covered by the innermost mesh. More complete descriptions and the application of TCM4 to TC studies can be found in Wang (2007, 2008a, b, 2009), Wang and Xu (2010), Xu and Wang (2010a, b), Wang and Heng (2016), and Heng and Wang (2016a; 2017).

The model was initialized with an idealized axisymmetric cyclonic vortex, which has a surface radial tangential wind distribution given below:

$$V_t(r) = \begin{cases} \frac{V_m}{R_m} r, & r \le R_m \\ \frac{V_m}{R_m} r \left[exp \frac{1}{b} (1 - (r/R_m)^b) - \frac{|r - R_m|}{R_0 - R_m} exp \frac{1}{b} (1 - (R_0/R_m)^b) \right], & r > R_m \end{cases} \quad (40)$$

where r is the radius, V_m is the maximum tangential wind at the surface, R_m is the radius of maximum tangential wind, R_0 is the radius outside which the tangential wind becomes zero, and b is a parameter that determines the radial decay rate of the tangential wind outside R_m. The tangential wind speed decreases sinusoidally with pressure to zero at 100 hPa, as in Wang (2007). A western Pacific clear-sky environment presented in Gray et al. (1975) was utilized as the reference state for the thermodynamic structure of the unperturbed model atmosphere. All numerical experiments were performed on an *f*-plane of 18 °N in a quiescent environment over the ocean with a constant sea surface temperature (SST) of 29 °C. The thermodynamic and mass fields were obtained by solving the nonlinear balance equation [see Wang (2001) for more details].

The surface drag coefficient is given as

$$C_D = (\frac{U_*}{U_{10}})^2, \quad (41)$$

where U_* is friction velocity = $(\tau/\rho)^2$ m s^{-1}, U_{10} is the 10-m height wind speed. The variation of C_D with U_{10} is approximated by a quadratic relation given below:

$$C_D = 1 \times 10^{-3} \times (-0.0002 \times U_{10}^2 + 0.369 \times U_{10} + 1.2231). \quad (42)$$

In total, two groups of numerical experiments were conducted (listed in Table 2.3 and Table 2.4). In the control experiment (CTRL), the initial vortex had the maximum tangential wind speed

V_m = 15.0 m s^{-1} at R_m = 75 km with b = 1.0. In the sensitivity experiments to surface friction, the C_D was multiplied by a factor from 0.5 to 2 of the default value used in CTRL. In experiments CT05, CT07, CT13, and CT20, the multiplications of C_D were, respectively, 50%, 70%, 130%, and 200% of that in CTRL. To isolate the impact of changing C_D on the initial spin-up of the TC vortex before the primary intensification stage, the experiments CT05 and CT20 but with C_D being multiplied by, respectively, 50% (CT05-R) and 200% (CT20-R) after 36 h of simulation in CTRL were carried out for a comparison.

To understand the effects of the dependence of C_D on surface wind speed, a new surface wind speed dependent C_D (Figure 2.5) modeled with 50 km fetch in Donelan (2018) was used. The new surface drag coefficient is given as:

$$C_D = 1 \times 10^{-3} \times$$

$$\begin{cases} \max(1.0, -0.0001779|\vec{V}|^3 + 0.008435|\vec{V}|^2 - 0.0246917|\vec{V}| + 0.8928661), |\vec{V}| \le 30 \\ \max(1.0, 0.0000644|\vec{V}|^3 - 0.0090905|\vec{V}|^2 + 0.3555079|\vec{V}| - 1.2816667), 30 < |\vec{V}| < 60 \cdot \\ \max\left(1.0, min(1.5, 0.00625|\vec{V}| + 0.875)\right), |\vec{V}| \ge 60 \end{cases} \quad (43)$$

There are three turbulent flow regimes: wind speeds below 30 m s^{-1} where C_D increases with 10-m height wind speed, wind speeds between 30 and 60 m s^{-1} where C_D decreases with 10-m height wind speed, and wind speeds above 60 m s^{-1} where C_D slightly increases with 10-m height wind speed. Based on previous studies, C_D is always greater than 1×10^{-3}. In addition, another

surface wind speed dependent C_D modified from Donelan (2018) is given as:

$$C_D = 1 \times 10^{-3} \times$$

$$\begin{cases} \max\left(1.0, -0.0001779\left|\vec{V}\right|^3 + 0.008435\left|\vec{V}\right|^2 - 0.0246917\left|\vec{V}\right| + 0.8928661\right), \left|\vec{V}\right| \le 30 \\ 2.9409\,, \left|\vec{V}\right| > 30 \end{cases} . \quad (44)$$

In this case, there are two turbulent flow regimes: wind speeds below 30 m s^{-1} where C_D increase with 10-m height wind speed, and wind speeds above 30 m s^{-1} where C_D is a constant, independent of surface wind speed. As shown from Figure 2.6, C_Ds calculated using equations (23), (42), (43), and (44) are all wind speed dependent. The two new surface wind speed dependent C_Ds given in equations (43) and (44) were used respectively, in experiments CTDO and CTD1 to replace C_D used CTRL given in the equation (42) to understand the effect of various surface wind speed dependent C_D on TC intensification.

In addition, to address how the structure of the initial TC vortex may affect the intensification rate of the simulated storm through the boundary layer dynamics, a series of sensitivity experiments with varying RMW were conducted. The RMWs of the initial TC vortex were set to be 40 (R041), 60 (R061), and 100 (R101) km. Meanwhile, in the sensitivity experiments with varying vortex RGW, specifically the radial decay rate of tangential wind of the initial TC vortex, the radial decaying parameter *b* in equation (40) was set to be 0.5 (b055), 0.7 (b075), and 1.0 (b105). A larger RGW TC vortex indicates a slower radial decay rate of tangential wind outside

the RMW, and therefore a smaller decaying parameter *b*. All experiments were integrated for 180 h, but the following analyses will focus on the initial spin-up stage and the primary intensification stage. Here, the initial spin-up stage refers to the initial period prior to, or say the onset of, the primary intensification stage.

CHAPTER 3. RESULTS FROM A SIMPLIFIED DYNAMICAL FRAMEWORK

Based on the scientific objectives outlined in Chapter 1, the results are given in three parts. First, results from the 2-D simple boundary layer model demonstrate how the boundary layer response to a given radial distribution of gradient wind at the model top depends on surface drag coefficient (C_D) and both the intensity and structure of the initial TC vortex. Second, results from the interactive model show how the boundary layer response may lead to changes in the gradient wind distribution above the boundary layer and thus the intensification of the TC vortex. In this chapter, the indirect effect of surface friction on TC intensification is evaluated using these two models. In the next chapter, results from the full-physics model TCM4 will shed some lights on the indirect effect of surface friction and the direct dissipation effect of surface friction on TC intensification. Also, mechanisms corresponding to the net contribution of boundary layer dynamics to TC intensification based on results from this chapter will be discussed.

3.1 Results from the simple boundary layer model

3.1.1 Overview of the boundary layer responses

In this subsection, the dependences of the boundary layer response to the given/fixed radial gradient wind distribution at the model top on C_D and the initial radial gradient wind distribution, are investigated using the simple boundary layer model. Given a time-independent radial

distribution of (gradient) tangential wind speed at the top of the boundary layer, the boundary layer response would achieve a steady state after about two-hour model integration. In this regard, the boundary layer response can be considered as a rapid adjustment process compared to the lifecycle of a TC. The overall boundary layer responses in these experiments are generally similar to a typical azimuthal mean vertical profile of the observed TC boundary layer. For instance, Figure 3.1a shows that the radial inflow suddenly increases with the radius from the TC center until a specific radius outside, which the inflow decreases with radius. In the vertical direction, the radial inflow decreases with height, and the outflow appears slightly inside the radius of maximum radial inflow above the inflow boundary layer. Both maximum tangential wind and maximum vertical velocity are located inside of the radius of maximum radial inflow (i.e., the radius where the radial wind speed has a sharp radial convergence). The vertical vorticity distribution shows a ring structure (below 1500 m) and is located at the radius where the maximum tangential wind gradient occurs, which is considerably contributed by the shear vorticity (Figure 3.1c). Figure 3.1e also gives the agradient force, which shows subgradient tangential wind (negative area) region outside the maximum radial inflow below 200 m and a supergradient tangential wind (positive area) region inside the maximum radial inflow between 100-m and 700-m heights. The supergradient wind region mostly is overlapped with both maximum tangential wind and maximum vertical velocity. Above the supergradient wind region, another weak

subgradient wind region appears due to radial outflow above the top of the inflow boundary layer.

3.1.2 Sensitivity to surface drag coefficient

Figure 3.1 shows the radius-height cross-sections of the steady-state response of tangential and radial winds as well as vertical relative vorticity and vertical motion with different C_D in the simple boundary layer model. Since surface friction is proportional to C_D, as inferred from the bulk formula (22), the results in Figure 3.1 demonstrate that the boundary layer inflow is stronger and deeper with larger C_D (around 30 km to 40 km in radius). The upward motion in the boundary layer is also stronger, and is located more inward with larger C_D (around 25 km to 35 km in radius). This is consistent with results in previous studies, namely larger C_D can lead stronger boundary layer inflow and upward motion at the top of the inflow boundary layer. The stronger and more inwardly penetrated inflow contributes to larger contraction of the RMW and displays a larger radial gradient of tangential wind slightly inside the RMW, leading to a stronger and more inwardly displaced vorticity ring (below 1500 m) due to larger shear vorticity (around 30 km in radius). The maximum upward motion (and the vorticity ring) is located more inward with larger C_D. These features may result in the contraction of the eyewall and thus the eyewall convective heating, and increasing the heating efficiency and intensification rate of the storm, as will be discussed in the next section.

Note that the maximum tangential wind in the boundary layer, namely the supergradient wind,

is stronger in the experiment with larger C_D. Consistent with the continuity equation, the stronger boundary layer inflow is accompanied by the stronger shallow outflow layer immediately above the inflow boundary layer in the experiment with larger C_D. This can be also explained in terms of a large agradient force (Figure 3.1f) in the larger C_D experiment. This outflow would spin down the tangential wind or thus will reduce the supergradient wind and bring the flow back to gradient wind balance. Also, since the solution is a steady-state response of the boundary layer flow to surface friction under a given radial distribution of gradient wind at the top of the boundary layer model, the net time tendency of tangential wind and radial wind disappears. This means that the spin-down of tangential wind due to the outflow is balanced by the spin-up of tangential wind by upward advection of supergradient wind from below.

3.1.3 Sensitivity to the initial tropical cyclone vortex structure and intensity

Figure 3.2, Figure 3.3, and Figure 3.4 show the radius-height cross-sections of the steady-state response of tangential and radial winds, vertical relative vorticity and velocity, and agradient force for the storm with a larger RGW (b = 0.4), a larger RMW (R_m = 60 km), and a higher intensity (V_m = 30 m s^{-1}) at the top of the boundary layer model. The boundary layer inflow is weaker and shallower in the larger RGW vortex (Figure 3.2b) than that in the smaller RGW vortex (Figure 3.2a). This means that a storm with larger inertial stability outside the RMW due to larger RGW has a greater resistance to the frictionally induced inflow. This is very similar to the case with

smaller C_D, shown in Figure 3.1. As a result, the boundary layer inflow in the larger RGW TC vortex is weaker and extends more broadly to outer radii 80-km from the storm center (Figure 3.2b), leading to the reduction of the radial gradient of both tangential and radial winds, and thus weaker vertical relative vorticity and vertical motion (Figure 3.2d). These results are consistent with those of Kepert and Wang (2001), who showed that the AAM of a storm with larger RGW increases with radius, leading to an inertially more stable condition to resist the radial inflow in the boundary layer. Note that the vertical relative vorticity in the larger RGW TC vortex is more broadly distributed and shows a monopole rather than a ring structure in the boundary layer. The vertical motion is much weaker in the larger RGW TC vortex, implying the reduced contribution of boundary layer dynamics to diabatic heating in the eyewall (see results in the next section). This is consistent with the results of Rogers et al. (2013), who compared the intensifying TC group with the steady-state TC group. They found that the storms in the steady-state group have a monopole vorticity distribution inside the RMW and larger RGWs outside the RMW.

The boundary layer inflow in the storm with a larger RMW is weaker (around 60 km in radius), and both the vertical motion and vertical relative vorticity are smaller (Figure 3.3b and Figure 3.3d) than those in the vortex with a smaller RMW. An interesting result is the more inward shift of upward motion and relative vorticity ring relative to the RMW in the vortex with the larger RMW (from 60 km to 40 km) than in the vortex with the smaller RMW (from 40 km to 25 km)

(Figure 3.3d and Figure 3.3c). This dependence of frictionally induced upward motion on the RMW is consistent with the findings of Kepert (2017) using a similar TC boundary layer model. Kepert (2017) hypothesized that this dependence may explain why TCs with a larger RMW may contract more rapidly during their early intensification stage, while the contraction of the RMW in the later intensification stage will slow down after the RMW becomes smaller. How this dependence would affect TC intensification will be discussed in the next subsection with the interactive model.

Finally, the secondary circulation in a TC often depends on the intensity of the TC itself. The boundary layer response to a stronger TC vortex (V_m = 30 m s^{-1}) is shown in Figure 3.4. As expected, the storm with a higher intensity shows a stronger and deeper boundary layer inflow (Figure 3.4b) as well as stronger and more inwardly displaced upward motion and vertical relative vorticity (Figure 3.4d). These are similar to those in a TC with larger C_D or with a smaller RGW. Interestingly, the dependence of boundary layer response on TC intensity here is very similar to the dependence of the balanced response of the secondary circulation to eyewall heating documented in earlier studies (e.g., Schubert and Hack 1982; Pendergrass and Willoughby 2009). The dependence of the balanced response on eyewall heating has been understood based on inertial stability. Namely, a stronger TC vortex has higher inner core inertial stability and thus higher efficiency of eyewall heating in spinning up tangential winds, thus the intensification of

the TC vortex. Since the boundary layer model shows a steady-state response, the boundary layer response shows a balance between the larger spinning up of tangential wind due to the stronger storm and the larger spinning down due to greater surface frictional dissipation. This strongly suggests that caution must be taken when attributing TC intensification to diabatic heating and boundary layer dynamics.

3.1.4 Dependence of the boundary layer response to various parameter spaces

To give an overall description of the dependences of the boundary layer response on the various parameter spaces, more cases for the given parameters with reasonable ranges for C_D, RGW, RMW, and intensity of the TC vortex were calculated, with the results shown in Figure 3.5. It can be seen that storms with larger C_D, smaller RGW, smaller RMW, and higher intensity correspond to stronger boundary layer inflow along with stronger upward motion at the top of the inflow boundary layer. Quantitatively, the consequence of surface friction is similar to the effect of the storm RGW and RMW, while the intensity of the storm has a more significant impact. Note that the radial inflow increases linearly with all parameters except for C_D (thus surface friction). The radial inflow increases slowly with increase C_D when C_D is relatively high. Similarly, the upward motion also increases slowly with C_D when the C_D is relatively high (i.e., larger than 1.5 times of the default value (Figure 3.5a). This can be interpreted as that while increasing C_D is conducive to enhancing boundary layer inflow and vertical motion, surface friction does not

substantially increase when C_D is very large because surface layer wind speed is also largely reduced. As a result, if diabatic heating in the eyewall is parameterized using the vertical motion at the top of the boundary layer, the results discussed in this section would imply that the indirect effect depends strongly on not only C_D, but also the intensity and structure of the TC vortex. This is further demonstrated by results from the interactive model discussed in the next section.

3.2 Results from the interactive model

3.2.1 Overview of the boundary layer response and gradient wind evolution

The issue how the boundary layer response may lead to changes in the gradient wind distribution above the boundary layer and thus the intensification of the TC vortex is examined in this subsection based on results from the interactive model introduced in Section 2.2. In this regard, the boundary layer dynamics are coupled with the gradient wind in the middle layer through diabatic heating (mass sink in the shallow water equation system) in the eyewall. That is, the boundary layer response to gradient wind above the boundary layer in the middle layer determines the strength and radial location of eyewall heating, thus modifying the gradient wind distribution in the middle layer. In turn, the modified gradient wind distribution may modify diabatic heating in the eyewall again through the boundary layer dynamics. All sensitivity calculations discussed in Section 3.1 were repeated using the time-dependent interactive model instead of the steady-

state solution of the boundary layer model. Since the vertical motion at the top of the boundary layer considerably determines diabatic heating in the eyewall and the gradient wind distribution reflects the intensification and structure change of the TC vortex above the boundary layer, this section mainly examines the radius-time evolutions in both the boundary layer and in the middle layer in all sensitivity experiments.

3.2.2 Sensitivity to surface drag coefficient

Figure 3.6 shows the radius-time evolutions of vertical motion at the top level of the boundary layer (at the 944-m height) and the gradient wind in the middle layer, which is close to the gradient wind balance, in the experiments with halved and doubled C_D (Figure 3.6b and Figure 3.6c respectively). Because the maximum gradient wind in the middle layer can be proportional (and reflects) as the storm intensity, the increasing rate in the maximum gradient wind speed can be regarded as the intensification rate of the storm. In all intensifying experiments, both the maximum upward motion and the maximum gradient wind speed started to shift inward (contract) and increase with time. More importantly, the strong upward motion was always located inside the RMW. This inward shift of vertical motion (eyewall updraft) relative to the RMW indicates that the boundary layer dynamics contributes to the contraction of the RMW (and also the eyewall), as recently inferred from the simple boundary layer model by Kepert (2017). In particular, boundary layer inflow induced by surface friction can penetrate into the eye region and determine

the strength and radial location of mass convergence and upward motion inside the RMW, leading to the contraction of the RMW and the intensification of the gradient wind. This would further enhance the inward penetration of boundary layer inflow and diabatic heating and thus dynamical efficiency and the storm intensification. This indirect effect of surface friction can be described as a positive feedback among inwardly shifted eyewall updraft, the contraction of the eyewall and intensification of the TC vortex.

Consistent with the results discussed in Section 3.1, the storm with a larger C_D shows stronger and more inwardly shifted upward motion and thus larger diabatic heating through the boundary layer dynamics. As a result, the storm with a larger C_D contracted faster and showed a higher intensification rate than the storm with a smaller C_D (Figure 3.6a and Figure 3.6b, or Figure 3.6c and Figure 3.6a). This means that the positive feedback associated with the indirect effect mentioned above is stronger in the storm with larger C_D. That is, the storm with larger C_D can contract its radius of maximum gradient wind at a higher rate with larger upward motion inside the RMW, as in the simple boundary layer model, eventually displaying a more rapid intensification.

3.2.3 Sensitivity to the initial tropical cyclone vortex structure and intensity

As expected, similar to the storm with a larger C_D, the smaller RGW storm showed stronger upward motion, faster contraction of the RMW, and more rapid intensification (Figure 3.6a and

Figure 3.6d). The larger RGW storm (with b = 0.4) did not show strong upward motion in the boundary layer and thus intensified very slowly, with little contraction of the RMW through the first 18-h integration (Figure 3.6d). This is consistent with the results of Rogers et al. (2013), who showed that steady-state TCs often had larger RGW with relatively stronger tangential winds outside the RMW, that is, a slower radial decay rate of tangential wind outside the RMW.

Since the boundary layer inflow and vertical motion at the top of the boundary layer were both larger in the storm with a smaller RMW than in the storm with a larger RMW in the simple boundary layer model (Figure 3.5c), the storm with a smaller RMW would be expected to intensify more rapidly. However, this was not true in the interactive model. As illustrated in Figure 3.6a and Figure 3.6e, the storm with a larger RMW intensified more rapidly with a larger contraction rate of the RMW than the storm with a smaller RMW. This can be explained by the fact that the upward motion in the larger RMW storm shifted more inside the RMW than the smaller RMW storm, favoring an initially faster contraction and rapid intensification of the storm. However, as will be shown soon later, the intensification rate is not linearly dependent on the initial RMW.

Consistent with what was inferred from the simple boundary layer model, the storm with an initially higher intensity intensified more rapidly with much stronger eyewall updraft (Figure 3.6f). The rapid intensification occurred much earlier for the initially stronger storm than for the initially

weaker storm. Nevertheless, the differences in intensification rate at a similar intensity (but different times) between the weak and strong storms (Figure 3.6a, Figure 3.6c, and Figure 3.6f) were relatively small (the differences in the RMW also contribute to the difference in intensification rate). Since the intensification in the interactive model is driven considerably by diabatic heating parameterized using the mass-flux at the top of the boundary layer, this result is consistent with findings based on balanced dynamics (Schubert and Hack 1982; Pendergrass and Willoughby 2009) as mentioned in Section 3. Namely, the stronger storm has higher inner-core inertial stability and thus higher dynamical efficiency of eyewall heating in spinning up tangential wind near the RMW and thus more rapid intensification of the storm.

3.2.4 Dependence of intensification rate on various parameter spaces

In the above subsections, only limited cases for the dependences of TC intensification rate on several parameters have been highlighted. Figure 3.7 shows the dependences of the average intensification rate of the storm together with the contraction rate of the RMW on the reasonable parameter spaces based on all sensitivity experiments to provide a complete picture. Comparing Figure 3.7 with Figure 3.5, it is demonstrated that the overall intensification rate of the storm and contraction rate of the RMW are proportional to the strength of the boundary layer inflow and upward motion at the top of the boundary layer in the steady-state response to boundary layer dynamics, except for the case of the dependence on the initial RMW (Figure 3.7c). The storms

with larger C_D, smaller RGW, and higher intensity display higher intensification rate and faster contraction of the RMW. The intensification rate increases initially with the increase of storm intensity, but the increasing trends decrease gradually after the storm intensity is close to 20 m s^{-1} (Figure 3.7d). Similarly, the intensification rate shows little change when the decaying parameter b is close to 0.9 (i.e., a smaller RGW) (Figure 3.7b). These phenomena occur primarily because the mimicked diabatic heating rate is controlled by the nondimensional entrainment parameter η in the interactive model [see equations (30) and (33)]. That is, even though larger C_D can induce stronger boundary layer inflow and stronger vertical motion at the top of the boundary layer, the mimicked diabatic heating rate is not allowed to increase when η is close to unit, leading to an asymptotic intensification rate for further increase in C_D. Note that a too low C_D could not induce sufficiently large upward motion in the eyewall to lead to the intensification of the storm through the boundary layer dynamics. In this sense, a minimum threshold of C_D is indispensable to storm intensification in the interactive model (as well as in the full-physics models mentioned in the introduction). Note also that compared to the sensitivity of the intensification rate to C_D, RMW, and intensity (around 20 m s^{-1} 12 hr^{-1}) (Figure 3.7a, c, and d), the sensitivity to RGW is marginal (around 5 m s^{-1} 12 hr^{-1}) (Figure 3.7b). This point will be addressed in the next chapter.

As opposed to the monotonic change of the storm intensification rate with C_D, the initial RGW, and intensity of the TC vortex, the storm intensification rate increases with the initial RMW,

reaches a maximum when the initial RMW is around 80 km, and then decreases with the increase of the initial RMW (Figure 3.7c). This nonmonotonic dependence of intensification rate on the initial RMW can be explained by a balance between the availability of AAM to spin up the storm and the increase of inertial stability outside the RMW in the near-core environment of the storm as the storm evolves. That is, when the initial RMW is too small, the boundary layer inflow will come from relatively small radii with relatively small AAM. There is no room for any significant contraction of the RMW and intensification of the storm. In this case, the intensification rate will increase with the initial RMW of the storm. In contrast, when the initial RMW is too large, as the storm intensifies and the RMW contracts, relatively large circulation and thus inertial stability outside the contracting RMW will pose considerable resistance to the boundary layer inflow. In this regime, the intensification rate will decrease as the initial RMW increases. A full understanding of the sensitivity to the initial RMW could be evaluated further using full-physics model simulations. Nevertheless, all results discussed here are physically consistent. Therefore, it is concluded that the simple interactive model can not only take into account contributions of the boundary layer dynamics to the organized eyewall convection, but also reproduce the primary balanced dynamics of TC intensification that have been well studied and documented in previous studies.

3.3 Concluding remarks on results from the two simplified models

In Sections 3.1 and 3.2, the role of boundary layer dynamics in TC intensification was studied using a multi-level boundary layer model and an interactive model that included an upper layer, a shallow water equation model as the middle layer, and a multi-level boundary layer. The coupling between the boundary layer and the free troposphere above is achieved in terms of the upward mass-flux at the top of the boundary layer to mimic diabatic heating in the TC eyewall. A possible indirect pathway was examined to explain how the boundary layer dynamics contributes to eyewall contraction and TC intensification, which is schematically summarized in Figure 3.8. There are four sequential interactive processes: (1) the boundary layer inflow in response to the given radial distribution of gradient wind above the boundary layer in the presence of surface friction; (2) the boundary layer inflow, as a function of surface friction and radial distribution of gradient wind above the boundary layer, determines the strength and radial location of the boundary layer convergence and thus the eyewall updraft; (3) the upward mass-flux at the top of the boundary layer determines both the strength and radial location of diabatic heating in the eyewall; and (4) the responses to gradient wind above the boundary layer to diabatic heating (represented as a mass sink in the middle layer shallow water equation system) are the contraction of the RMW and intensification of the TC vortex.

The first and second processes were studied as a forced response problem for a given radial distribution of gradient wind above the boundary layer using a simple multi-level boundary layer model. This helps quantify the dependence of boundary layer responses on the given radial distribution of gradient wind above the boundary layer on the C_D and the structure and intensity of the TC vortex. The results demonstrate that storms with larger C_D, smaller RGW, smaller RMW, and higher intensity correspond to stronger and deeper boundary layer inflow along with larger radial mass convergence and stronger upward motion inside the RMW, and a stronger and more inwardly shifted vorticity ring inside the RMW. The third and fourth processes (Figure 3.8) were examined using the interactive model. Unlike the simple boundary layer model, the interactive model can realize how the gradient wind distribution above the boundary layer is influenced by the boundary layer response through diabatic heating (parameterized using the upward mass-flux at the top of the boundary layer) in the eyewall. The storms with larger C_D, smaller RGW, and higher intensity experience faster contraction of the radius of maximum gradient wind with a larger upward motion inside the RMW, similar to the results in the simple boundary layer model, thus displaying more rapid intensification. These four sequential processes can be regarded as the indirect effect of surface friction on TC intensification. In short, the storm with larger C_D, smaller RGW, moderate RMW, and higher intensity can have more rapid intensification if only the indirect effect of surface friction is mainly considered.

CHAPTER 4. RESULTS FROM A FULL-PHYSICS MODEL

In this chapter, the full-physics TC model (TCM4) is used to perform sensitivity experiments to evaluate the combined dissipation and indirect effects of boundary layer dynamics on TC intensification. It is hypothesized that the positive indirect and negative dissipation effects of surface friction largely offset each other, resulting in insensitivity of the simulated TC intensification rate to change in surface drag coefficient (C_D).

4.1 Overview of the control experiment

The total wind field evolution of the simulated TC in CTRL from the TCM4 model is shown in Figure 4.1. After a 24-h spin-up, the TC circulation and eye gradually appeared together with a clear contraction of the RMW, although the intensity had not reached 17 m s^{-1} (Tropical Storm). Then, the TC kept intensifying, and the eye became compact with a radius of around 50 km. The TC intensity reached 17 m s^{-1} at 36 h, 34 m s^{-1} (Typhoon) at 60 h, and 63 m s^{-1} (Supertyphoon) at 96 h (Figure 4.2a). Overall, the TC intensity did not increase until 24 h, then increased for 84 h, and was sustained in the last 72 h. Therefore, the storm's evolution can be classified into three different stages: the initial spin-up stage, the primary intensification stage, and the quasi-steady stage. The initial spin-up stage is defined as the period from the initial time to the time when the storm intensity (maximum 10-m height tangential wind speed) becomes higher than its average intensity during the past 12 h. The primary intensification stage is defined from the end of the

initial spin-up stage to the time when the storm intensity is no longer higher than the average intensity in the past 12 h. The last stage, namely the quasi-steady stage or the mature stage, is defined as the time period from the end of the primary intensification stage to the end of the model simulation. The time evolution of the RMW also similarly demonstrates these three stages (Figure 4.2b). The RMW in the initial spin-up stage had substantial fluctuation since the TC structure was not yet well developed. Afterwards, the RMW contracted rapidly during the primary intensification stage and was sustained at around 15-20 km in the quasi-steady stage. Figure 4.3 shows the radius-height cross-section of both azimuthal mean radial wind and tangential winds at 12-h interval. The tangential wind, inflow in the boundary layer, and outflow in the upper troposphere increased and contracted as the storm intensified. The radial inflow showed a deepening trend until the quasi-steady stage was reached, and the maximum tangential wind appeared inside the maximum radial inflow in the boundary layer. The corresponding radius-height cross-sections of the azimuthal mean vertical velocity and relative humidity are shown in Figure 4.4. The azimuthal mean upward motion was quite weak (less than 0.5 m s^{-1}) prior to 36 h of integration during the initial spin-up stage. The azimuthal mean relative humidity was also relatively low during this stage due to insufficient moisture convergence in the boundary layer. However, both upward motion and relative humidity increased in the eyewall region and became well-organized during the primary intensification stage. In contrast, in the eye region, the relative

humidity was very low due to strong compensating downdraft, in particular by around 60 h of simulation, when the convection well developed in the eyewall. The corresponding radius-height cross-sections of the azimuthal mean vertical vorticity and condensational heating rate are shown in Figure 4.5. Since the upward motion is the primary source of condensational heating in the eyewall, the distribution and time evolution of condensational heating are very similar to those of the azimuthal mean vertical motion (Figure 4.4). For the azimuthal mean vertical vorticity, a clear vorticity ring is shown slightly inside the eyewall convection. These behaviors of the simulated TC in CTRL by TCM4 can be regarded as representative of a typical TC vortex in the real world.

4.2 Sensitivity to surface drag coefficient

Figure 4.6 shows the time evolution of the maximum 10-m height azimuthal mean tangential wind speed and the corresponding intensification rate defined as the 12-h intensity change before the time given in the axis in the five experiments with different C_Ds from the beginning of all simulations. In CTRL, the TC vortex experienced an initial spin-up stage for about 24 h and then started to intensify until about 108 h. This was followed by a quasi-steady stage until the end of 180-h simulation (Figure 4.6a). After about 108 h of simulation, the TC vortex in CTRL reached a quasi-steady intensity evolution, with a maximum 10-m height wind speed of around 75 m s^{-1} at a RMW of around 15-20 km. It can be considered that the period from 24 h to 108 h of the

simulation was the primary intensification stage of the simulated TC in CTRL as defined in section 4.1. In the following discussion, the storm intensity evolution is also divided into three different stages as defined in Section 4.1: the initial spin-up stage, the primary intensification stage, and the quasi-steady stage.

From Figure 4.6a, one can see that the storm with a larger C_D (CT20) intensified 12 h earlier than the storm with a smaller C_D (CT05). Actually, the initial spin-up stage was shorter in the former (about 24 h) than in the latter (about 36 h). This suggests that a larger C_D and thus greater surface friction corresponded to greater moisture convergence into the core region in the boundary layer and thus larger Ekman pumping, providing faster moistening of the inner core and initiation and organization of convection near and inside the initial RMW, as recently demonstrated by Xu and Wang (2018a, b). In contrast, the overall intensity of the simulated storm with a larger C_D was weaker than that with the smaller C_D during the quasi-steady stage. Namely, surface friction contributes negatively to the final intensity of the simulated storm. This is consistent with the theoretical maximum potential intensity (MPI), which is inversely proportional to the square root of C_D (Emanuel 1988, 1989). However, the simulated storms with different C_Ds had similar intensification rates during the primary intensification stage (Figure 4.6b). For example, the 12-h intensification rates of the storms in CT05, CTRL, and CT20 were similar to each other and were all around 10 m s^{-1} 12 hr^{-1} before 72-h of the simulations. The intensification rate in CT20

decreased after reaching a maximum, while a high intensification rate remained in other experiments even after 48 h of simulations. This is mainly due to the fact that the storm with larger C_D in CT20 had the lowest quasi-steady intensity and reached its quasi-steady stage earlier than storms in other experiments because it intensified at a similar intensification rate. This led to the storm in CT20 having the shortest primary intensification stage. Figure 4.7 compares the scatter diagrams of the subsequent 12-h intensification rate against the instantaneous maximum tangential wind speed during the primary intensification stage. All three experiments have a similar inverted "U" curve in the scatter diagram. The only difference is that the inverted "U" curve becomes smaller as C_D increases, since the quasi-steady intensity is weaker as C_D increases. This is consistent with the results from an observational study by Xu and Wang (2015), who found that the intensification rate is positively (negatively) correlated with the maximum tangential wind speed when the storm is weaker (stronger) than some intermediate intensity. This is to say, the intensification rate of a TC during its primary intensification stage is insensitive to C_D as found in many earlier studies. However, surface friction (with larger C_D) does play a significant role in both the initial spin-up stage and the final intensity in quasi-steady.

The duration of the initial spin-up stage in the simulated storm is closely related to the initial moistening and saturation of the inner core, which is accomplished predominantly by moisture convergence in the boundary layer and Ekman pumping associated with surface friction and

vertical mixing (Xu and Wang 2018a, b). As a result, a large C_D corresponds to stronger boundary layer inflow and moisture convergence and greater Ekman pumping (Figure 4.8), leading to earlier saturation and initiation of convection in the inner core and thus the onset of the primary intensification stage. This can be clearly seen in Figure 4.9, which shows the radius-time cross-sections of relative humidity at a height of 1331 m near the top of the boundary layer for the storms in CT05 and CT20. Comparing Figure 4.9a with Figure 4.9b, it can be seen that the air in the boundary layer was more rapidly moistened in CT20 than in CT05, indicating that a larger C_D favored greater moisture convergence and stronger Ekman pumping and moistening of the inner core of the storm in the simulation. Greater Ekman pumping in response to larger C_D (and thus surface friction) can transport more moisture from the underlying ocean surface layer upward and outward the boundary layer, and moistening the inner core of the TC vortex. This suggests that boundary layer dynamics is key to the initial moistening and initiation of convection in the inner core of the TC vortex, thus shortening the initial spin-up stage of the simulated storm. Note that the storm started to intensify after the averaged relative humidity in the boundary layer within the RMW reached about 90% in both CT05 and CT20 (Figure 4.10). This is consistent with findings from earlier studies that once relative humidity in the inner core is high enough, convection can be initiated and organized, leading to the intensification of a TC (Riehl 1950; Kleinschmidt 1951; Malkus and Riehl 1960; Charney and Eliassen 1964; Ogura 1964; Ooyama 1969; Rotunno and

Emanuel 1987; Emanuel 1995). The onset time of the primary intensification stage in the experiment with a smaller C_D was considerably delayed. This is consistent with the results of Kilroy et al. (2017), who showed that surface friction plays a key role in organizing deep convection in the inner core and shortening the initial spin-up stage when compared with an experiment without surface friction in a numerical simulation.

4.3 Sensitivity to surface drag coefficient after the eyewall convection well organized

To isolate the impact of C_D on the initial spin-up stage and the primary intensification stage, experiments CT05 and CT20, renamed as CT05-R and CT20-R, were repeated. In these repeated runs, C_D was multiplied by 50% and 200% after the initial 36-h spin-up of the simulated storm in CTRL. Figure 4.11 compares the evolutions of the simulated storm intensity and intensification rates in CT05-R, CTRL, and CT20-R. Results show that both the storm intensity and intensification rate during the primary intensification stage were very close to each other in the three experiments, confirming that the TC intensification rate during the primary intensification stage is insensitive to C_D. A notable result was that the storm intensity in the quasi-steady stage in CT05-R and CT20-R was largely similar to that in the corresponding experiments CT05 and CT20 (cf. Figure 4.6a). This implies that the quasi-steady intensity is independent of the duration of the initial spin-up stage of the storm. Note that the duration of the primary intensification stage

is different among experiments with different C_Ds because the quasi-steady intensity is a function of C_D. Since the storm in CT20-R approached its quasi-steady stage after about 54 h of simulation (Figure 4.11a), the intensification rate decreased afterward (Figure 4.11b). However, the storm in CT05-R was still in its primary intensification stage after 54 h of simulation (Figure 4.11a). Correspondingly, the intensification rate in CT05-R showed an increase between 54 h and 72 h (Figure 4.11b). These results demonstrate that enhanced surface friction can shorten the duration of both the initial spin-up stage and the primary intensification stage, but reduces the quasi-steady TC intensity. However, the intensification rate of a TC during the primary intensification stage is insensitive to C_D and surface friction. Note that although both intensity and intensification rates were fairly similar in CT05-R and CT20-R during the primary intensification stage, the storm size in CT05-R was larger due to relatively weaker contraction associated with reduced surface friction than in CT20-R (Figure 4.12).

One of the main objectives in this study is to understand why the simulated TC intensification rate during the primary intensification stage is insensitive to C_D. As mentioned in the introduction, it is hypothesized that this insensitivity results mainly from an offset of the direct dissipation and the indirect effects of surface friction on TC intensification. Chapter 3 focuses on the indirect effect of surface friction on TC intensification. The results demonstrated that greater surface friction not only enhances the boundary layer response in terms of boundary layer inflow and

upward motion at the top of the boundary layer but also accelerates the contraction of the radius of maximum gradient wind by enhancing the strength and more inwardly penetrated radial location of diabatic heating inside the RMW, thus leading to more rapid intensification. However, the dissipation effect of surface friction, which is roughly included in the simplified dynamical framework, has an inverse relationship to TC intensification, as demonstrated by Stern et al. (2015), Heng and Wang (2016a, b, 2017). Here, both the indirect effect and the direct dissipation effect of surface friction in the full-physics model simulations will be examined and compared with the results from the simplified dynamical framework discussed in Chapter 3.

To understand the role of the indirect effect of surface friction in TC intensification, first, the boundary layer response to surface friction resulting from different C_Ds in the simulated storms was examined. Figure 4.13 illustrates the radius-height cross-sections of the azimuthal mean radial wind in the simulated storms in CT05-R and CT20-R from 37 h to 40 h of simulation at hourly interval during the primary intensification stage. Note that surface drag coefficient was modified after a 36-h spin-up (in CTRL) in both CT05-R and CT20-R. This means that the question of how radial wind responds to a modified C_D and, therefore, surface friction in the initial four hours was the focus for the analysis of the primary intensification stage. Both the azimuthal mean boundary layer inflow and vertical motion became stronger and penetrated further inward in CT20-R than in CT05-R. As a result, the azimuthal mean condensational heating rate (Figure

4.14) also became higher and penetrated further inward in CT20-R than in CT05-R. These results are consistent with the findings in Chapter 3, which suggested that larger C_D can induce stronger and more inwardly penetrated boundary layer inflow, and thus larger radial mass convergence and stronger vertical motion and diabatic heating through the boundary layer dynamics. Note that changes in both boundary layer inflow and condensational heating took place only a few hours after the change of C_D, implying that response of the boundary layer dynamics to surface friction is a fast process that plays a significant role in modifying the eyewall updraft/convection and thus affecting TC structure and intensification. However, although considerable differences in diabatic heating rate in the inner core region occurred shortly after the change in C_D (Figure 4.14), radial wind above the boundary layer showed little difference between the experiments CT05-R and CT20-R (Figure 4.13), suggesting that the response of the transverse circulation above the boundary layer to diabatic heating is slower than that in the boundary layer.

Second, the evolution of diabatic heating and the inner core structure of the storms simulated with different C_Ds are compared with those discussed in Chapter 3. Figure 4.15 shows the radius-time cross-sections of the azimuthal mean tangential wind speed and the condensational heating rate at the 1781-m height above the boundary layer in CT05-R and CT20-R respectively. Consistent with the findings in Chapter 3, the RMW of the storm with a larger C_D in CT20-R contracted at a higher rate than that in CT05-R with smaller C_D, leading to a more compact inner-

core structure of the storm in CT20-R than in CT05-R. Larger C_D in CT20-R induced a higher condensational heating rate in the eyewall and shifted the eyewall convection further inside the RMW than in CT05-R. These behaviors are in agreement with the indirect effect of surface friction on TC intensification identified in Chapter 3 (cf. Figure 3.6). It can be concluded that the indirect effect of surface friction to TC intensification is consistent in the simplified interactive dynamical model discussed in Chapter 3 and in the full-physics model discussed in this section. Nevertheless, the intensity evolutions of the simulated storms in the two models were completely different. Results from the interactive model in Chapter 3 demonstrated that the storm with a larger C_D intensified more rapidly. In contrast, results from the full-physics model here suggest that the intensification rate of the simulated TC is not sensitive to C_D. Note that the primary difference between the two models lies in the fact that the full-physics model includes the dissipation effect of surface friction on the gradient wind in the free troposphere through a full turbulent parameterization scheme and also radiative cooling, while the simplified dynamical model in Chapter 3 only included the contribution of the positive indirect effect of boundary layer dynamics to TC intensification and the effect of surface friction on the middle layer is very roughly and incompletely considered. This implies that the increased positive contribution by the indirect effect of surface friction in CT20-R was largely offset by the increased negative contribution by the dissipation effect of surface friction. Hence, it is necessary to compare the

indirect and direct dissipation effects of surface friction in the full-physics model simulations.

Figure 4.16 shows the time evolutions of the differences in the vertically integrated condensational heating rate averaged within a radius of 1.5 times of the RMW in the simulated TCs and surface wind stress at the RMW between experiments CT20-R and CT05-R. The difference in condensational heating rate between the two storms can be regarded as the indirect effect of surface friction to TC intensification (black slashed area). Similarly, the difference in surface wind stress between the two storms can be regarded as the dissipation effect of surface friction to TC intensification (green slashed area). Although the storm intensities in CT05-R and CT20-R were quite similar to each other until 66 h of simulation, the differences in both the condensational heating rate (Figure 4.16a) and surface wind stress (Figure 4.16b) were increasingly larger in CT20-R than in CT05-R. Since the storms in both experiments intensified synchronously, this again supports the idea that the increase in the positive indirect effect of surface friction is largely offset by the increase in the negative dissipation effect of surface friction in the experiment with a larger C_D (CT20-R). This also strongly suggests that the TC intensification rate could not simply be considered as a function of the diabatic heating rate in the eyewall alone, as was inferred from balanced dynamics (e.g., Schubert and Hack 1982; Pendergrass and Willoughby 2009). Caution should also be given to surface frictional dissipation. This is because greater surface friction can, on one hand, induce stronger and more inwardly

penetrated eyewall updraft and condensational heating due to the positive indirect effect of surface friction. However, on the other hand it also induces larger frictional dissipation resulting from the dissipation effect of surface friction in the TC system. This explains why the simulated TC intensification rate during the primary intensification stage is insensitive to C_D in numerical simulations of TCs.

4.4 Sensitivity to surface wind dependent surface drag coefficient

In this section, two new dependences of C_D on surface wind speed, which is widely used in current state-of-the-art numerical models, are used to perform sensitivity experiments to further evaluate the effect of different dependences of C_D on TC intensification. The results in Section 4.3 suggested that the intensification rate of the simulated TC in the full-physics model during the primary intensification stage is insensitive to C_D. Therefore, the hypothesis here is that although given different dependencies of C_D on surface wind speed, the intensification rates of the simulated TCs with different dependencies during the primary intensification stage are similar because the positive indirect and negative dissipation effects of surface friction largely offset, resulting in insensitivity of the simulated TC intensification rate to the wind-dependency of C_D.

The sensitivity experiments are conducted to examine the effect of different dependences of C_D on surface wind speed on TC intensification rate in the full-physics model. Based on the results

in Section 4.3, if the simulated TC intensification rate during the primary intensification stage is insensitive to C_D in the full-physics model, the intensification rate should be similar during the primary intensification stage even if different dependences of C_D on surface wind speed are used. The dependence of C_D on surface wind speed mainly determines the duration of the initial spin-up stage and the quasi-steady intensity. Figure 4.17 shows the time evolution of the maximum 10-m height azimuthal mean tangential wind speed and the corresponding intensification rate (defined as the 12 h intensity change before the time given in the axis) in the experiments with different wind speed dependences of C_D from the beginning of the simulations. The dependences of C_D in the three experiments – CTRL (black), CTDO (magenta), and CTD1 (blue) – are illustrated in Figure 2.6. The main difference in the dependence between CTRL and CTDO is that C_D is larger in the low-wind regime (below 15 m s^{-1}) and smaller in the moderate-wind regime (from 15 m s^{-1} to 40 m s^{-1}). It becomes larger again in the high-wind regime (above 40 m s^{-1}). On the other hand, the dependence of CTD1 is exactly the same as that of CTDO when the 10-m height wind speed is below 30 m s^{-1}, and afterwards remains larger than CTDO. Results show that both storm intensity and intensification rate during the primary intensification stage are very close to each other in the three experiments, confirming the results in Section 4.3 are robust. Namely, the TC intensification rate during the primary intensification stage is insensitive not only to the C_D but also to the dependence of C_D on surface wind speed. In contrast, the duration of the initial

spin-up stages in both CTDO and CTD1 are longer than that in CTRL. This is because the smaller C_D in the low-wind regime in both CTDO and CTD1 resulted in slower initial moistening and delayed the saturation of the inner core. These results are consistent with the results in Section 4.2, namely, the TC with smaller C_D had the longer initial spin-up stage. An interesting result is that the blue curve and magenta curve split when their intensity reaches 30 m s^{-1}, which is the turning point in Figure 2.6. The C_D decreases with surface wind speed in the magenta curve, and becomes a constant in the blue curve. Nevertheless, their intensification rates are still similar to each other, again supporting the result that the intensification rate is insensitive to C_D during the primary intensification stage. Note that the overall intensity of the simulated storm in CTD1 is less than that in CTRL and CTDO during the quasi-steady stage. This is mainly due to the fact that C_D in CTD1 is always larger than that in CTRL and CTDO in the high-wind regime.

Figure 4.18 shows the time evolution of relative humidity and vertical velocity averaged within the radius of 1.5 times RMW in all three experiments. As expected, the results were similar to those in Section 4.2, a deep moist layer in the lower-middle troposphere in the inner-core region is key to the initial spin-up stage of the simulated TC. It took about 24 h for the TC vortex in CTRL to become moistened at a height of about 8 km, from which the storm intensified. In contrast, it took about 30 h for the TC vortices in CTDO and CTD1 to complete the initial moistening of the inner-core region. These results are also consistent with the results of sensitivity

to C_D in Section 4.3, while it is more marginally due to the smaller difference of C_D between CTRL and CTDO in the low-wind regime. Figure 4.19 shows the radial distribution of radial wind, vertical velocity, condensational heating rate, and inertial stability in CTRL and CTDO when the intensity is over 20 m s^{-1} during the primary intensification stage. It is shown that both vertical velocity and condensational heating were stronger and more concentrated inside of the RMW in CTDO. This is mainly because C_D in CTDO was larger than that in CTRL in the moderate-wind regime, leading to stronger upward motion and higher condensational heating rate inside the RMW of the storm. However, the intensification rate of the storm in CTDO was still very close to that in CTRL during the primary intensification stage. As discussed in Section 4.3, greater surface friction not only enhances the condensational heating rate inside the RMW through the boundary layer dynamics (indirect effect), but also increases the frictional dissipation to the simulated TC (dissipation effect). Figure 4.20 shows the vertically integrated condensational heating rate and surface wind stress near the RMW in both experiments when the storms had similar intensities, showing that the storm in CTDO had higher condensational heating rate and wind stress during the primary intensification stage. Indeed, C_D was larger in CTDO when the surface wind speed was moderate (Figure 2.6). Thus, the positive effect due to higher heating rate is largely offset by the negative effect resulting from larger surface wind stress, leading to a similar intensification rate of the simulated storms.

Figure 4.21 presents the same comparison between CTDO and CTD1 during the primary intensification stage when they had similar intensity. Similarly, since C_D in CTD1 was larger than that in CTDO in high-wind regime, both vertical motion and condensational heating rate were higher in CTD1, even if they had similar intensities. On the other hand, this larger C_D also causes greater wind stress, as shown in Figure 4.22b. These results are consistent with the hypothesis of this study that different dependencies of C_D on surface wind speed (or different C_D) can only change the duration of the initial spin-up stage of the simulated TC. The intensification rates of the simulated TCs during the primary intensification stage were similar because the positive indirect and negative direct dissipation effects of surface friction largely offset each other, resulting in insensitivity of the simulated TC intensification rate to the change in C_D. Note that both vertical motion and condensational heating were very sensitive but responded very quickly in a short time period to the change of C_D, implying that the boundary layer dynamics can significantly affect the TC structure in the inner core of a simulated TC.

CHAPTER 5. THE INFLUENCE OF INITIAL VORTEX STRUCTURE ON TROPICAL CYCLONE INTENSIFICATION

Since the results in Chapter 4 demonstrate that the intensification rate of the simulated TC during the primary intensification stage is insensitive to surface drag coefficient (C_D), a question naturally arises as to what determines the intensification rate of a TC given favorable environmental conditions, including sea surface temperature. It is hypothesized in this study that the indirect effect of boundary layer dynamics on TC intensification depends considerably on the storm structure, as indicated in Chapter 3 (see Figure 3.7), while the dissipation effect of boundary layer dynamics depends mainly on TC intensity but very weakly depends on the storm structure. As a result, the intensification rate of a TC during its primary intensification stage is largely determined by the structure of the initial TC vortex (for the tropical storm intensity). In Chapter 3, in addition to C_D, it was shown that the indirect effect of boundary layer dynamics on TC intensification rate strongly depends on the initial vortex structure and intensity, such as the initial RMW and RGW. The results showed that the storm initially with a smaller RMW, smaller RGW (higher radial decay rate of tangential wind outside the RMW), and higher intensity can induce stronger radial inflow and upward motion through the boundary layer dynamics, leading to more inwardly penetrated radial locations of diabatic heating inside the RMW, and thus to more rapid intensification. In this chapter, the full-physics model is used again to clarify how the TC structure determines the intensification rate through the boundary layer dynamics.

5.1 Sensitivity to the initial vortex radius of maximum wind

First, the sensitivity to the RMW of the initial TC vortex is investigated to address the importance of the initial RMW to TC intensification. The radial distributions of the initial tangential wind speed and inertial stability in all three TC vortices with different RMWs are shown in Figure 5.1. It can be seen that the storm with a larger RMW also has a larger RGW, implying stronger tangential wind in the outer radii compared to the storm with a smaller RMW. In addition, the storm with a smaller RMW has much higher inertial stability in the inner-core region, but has relatively lower inertial stability outside the RMW (Figure 5.1b). The total wind field evolution of the simulated TCs in R041, R061, and R101 are shown in Figure 5.2, Figure 5.3, and Figure 5.4 respectively. After the first 24-h simulation, a clear and compact TC eye (with a radius of around 10 km) appeared as a result of the eyewall contraction in R041. However, by this time, the TC circulation had not organized well yet in R101. While the TC intensity reached 30 m s^{-1} in R041, the TC intensity in R101 was still weak with the maximum tangential wind less than 20 m s^{-1}. After that, the storm in R041 had a rapid intensification (35 m s^{-1} in 24 h) and reached its maximum intensity at 48 h. The maximum intensity was sustained for about 24 h and then weakened. The outer storm size did not significantly change (RGW of around 50 km) from 24 h to 108 h of the simulation. On the other hand, the storm intensified slowly (15 m s^{-1} in 24 h) in

R101 with a sustained large eye (with a radius of around 30 km). Overall, these results suggest that the initial RMW of the TC vortex largely determines the intensity and structure evolution of the simulated TC. Note that the initial intensity was 20 m s^{-1} in all three experiments, which was higher than the initial intensity of 15 m s^{-1} in the sensitivity experiments for C_D in the last chapter. This was chosen to highlight the impact of the initial RMW on the intensification rate of the simulated storm.

Figure 5.5 compares the time evolutions of maximum 10-m height tangential wind speeds and RMWs in all sensitivity experiments. It took about 12 h for the storm with an initially smaller RMW in R041 to spin up, while the storms with an initially larger RMW had a longer spin-up stage about 18 h in R061 and 24 h in R101. Indeed, the duration of the initial spin-up stage is considerably sensitive to the initial RMW. After the initial spin-up stage, the storm with a smaller RMW intensified more rapidly than the others during the primary intensification stage. The RMWs in the three experiments experienced contraction during the spin-up stage and the primary intensification stage, but did not change significantly during the quasi-steady stage. The steady-state RMW was about 10 km in R041 (R_m = 40 km), about 15 km in R061 (R_m = 60 km), and about 30 km in R101 (R_m = 100 km). In other words, the mature TC size also depends on the initial TC inner-core size. An interesting result is that the steady-state intensities of the three simulated TCs were also different. The storm with an initially larger RMW had the strongest

steady-state intensity. Nevertheless, the MPI theory (Emanuel 1988, 1989, 1995, 1997) does not include any explicit TC size parameters, implying that the initial TC structure may also affect the steady-state intensity or the MPI. This result is consistent with the results recently reported in Xu and Wang (2018b), and this issue needs to be investigated in future studies. Figure 5.6 shows that the storm with the initially smallest RMW in R041 had a substantially higher intensification rate (about 25 m s^{-1} 12 hr^{-1}) than the storms in either R061 or R101 (about 15 and 10 m s^{-1} 12 hr^{-1} respectively). Note that the storm with the initially largest RMW in R101 took about 60 h to reach its maximum intensification rate, while those took about 36 h and 30 h in R061 and R041 respectively. These results suggest that the initial RMW of the TC vortex can determine not only the duration of the initial spin-up stage but also the intensification rate during the primary intensification stage, as well as the quasi-steady state intensity.

The results in Chapter 3 suggest that the storm with an initially smaller RMW induced stronger inflow and upward motion inside the RMW through the boundary layer dynamics. This is mainly because the storm with an initially larger RMW had a greater resistance to the frictionally induced inflow into the inner core region. Figure 5.7 shows that the faster initial moistening/saturation of the inner core in R041 is associated with stronger upward motion largely due to stronger boundary layer inflow and larger moisture convergence and Ekman pumping. Greater Ekman pumping can transport more moisture from the underlying ocean surface layer

upward out of the boundary layer, and moistening the inner core of the TC vortex. On the other hand, the storm with a smaller RMW has a smaller volume in the inner core, which could be moistened in a shorter time. These results are consistent with the results of Rotunno and Emanuel (1987), Emanuel (1989, 1995), and Xu and Wang (2018b). After the initial spin-up stage, the storms started their primary intensification stage after the averaged relative humidity in the inner-core region reached about 90% in all three experiments, which is consistent with the results in Chapter 4. During the primary intensification stage, averaged vertical motion in the inner-core region was the strongest (about 50 cm s^{-1}) in R041, compared with about 30 cm s^{-1} in R061 and 20 cm s^{-1} in R101. Compared with the effects of boundary layer dynamics in the initial spin-up stage, which can accelerate moistening in the inner-core region, the effects of boundary layer dynamics during the primary intensification stage may primarily enhance condensational heating in the region with high inertial stability inside the RMW.

Figure 5.8 compares the radial inflow and condensational heating rate together with the inertial stability prior to the primary intensification stage in all three experiments. As expected, the storm with an initially smaller RMW induced stronger radial inflow and upward motion inside the RMW (Figure 5.8a) and had a higher condensational heating rate in the region with higher inertial stability (Figure 5.8b). On the other hand, both the condensational heating rate and inertial stability were lower inside the RMW in R101 (Figure 5.8f). This can be explained based on the

balanced vortex dynamics (Schubert and Hack 1982; Pendergrass and Willoughby 2009), which predicts that heating inside the RMW with higher inertial stability has higher dynamical efficiency in spinning up the low-level tangential wind and thus the intensification of the storm. During the corresponding primary intensification stage in all three experiments, distribution of condensational heating and inertial stability in all three experiments (Figure 5.9) were also similar to those in the period prior to the primary intensification stage. Note that although the condensational heating rate occurred in a much narrower ring inside the RMW in R041 than in others, it still can enhance the intensification of the storm due to the higher dynamical efficiency. Indeed, heating outside of the RMW has a lower efficiency in spinning up the low-level tangential wind. As a result, even though condensational heating occurred in a much wider area in R101, its contribution to the spinning up of the storm is likely limited. Figure 5.10 presents the rain rate in all three experiments during the primary intensification stage. The vertically-integrated condensational heating rate is wider but smaller in R101 than in other two experiments.

In short, the storm with an initially smaller RMW could induce higher condensational heating rate inside the RMW compared to the storm with an initially larger RMW. As a result, the duration of the initial spin-up stage was shorter and the intensification rate during the primary intensification stage was higher for the storm with an initially smaller RMW. Note that the differences in azimuthal mean radial wind, vertical motion, and condensational heating between

R041 and R101 were very similar to those between CT20-R and CT05-R with different C_Ds (cf. Figure 4.13 and Figure 4.14). However, the positive impact of the higher condensational heating rate in CT20-R with a larger C_D was largely offset by the negative impact of greater surface frictional dissipation, resulting in little net contribution to the TC intensification rate. In sharp contrast, since the two storms in R041 and R101 in the given time period had a similar intensity and thus similar surface friction, the higher condensational heating rate in R041 was not offset by the small difference in surface friction, thus directly contributing to a higher intensification rate of the simulated storm. These results are consistent with the results in Chapter 3, and also demonstrate that the RMW in the initial TC vortex is key to the duration of the initial spin-up stage and the actual intensification rate of TCs during their primary intensification stage.

5.2 Sensitivity to the initial vortex radius of gale wind

The radius of gale wind (RGW) is another important parameter that may affect the intensification rate of TCs, as documented in Chapter 3 and also studied by Xu and Wang (2018a, b). To examine this effect, three sensitivity experiments with initially different RGWs were performed to demonstrate the importance of TC structure to the intensification rate during the initial spin-up stage and the primary intensification stage of the simulated TC. The larger RGW TC vortex (b055) had a slower radial decay rate of tangential wind (Figure 5.11a), that is, stronger

tangential winds in the outer radii and represented by a smaller decaying shape parameter *b* (0.5) in equation (40). All three vortices in the three experiments (b055, b075, and b105) had the same inertial stability in the inner-core region inside the RMW, while the storm with a larger RGW had relatively higher inertial stability outside the RMW like a skirt (Figure 5.11b). The evolutions of total wind speed of the simulated TCs in b055, b075, and b105 are shown in Figure 5.12, Figure 5.13, and Figure 5.14 respectively. After the first 24-h of simulation, all three vortices developed a clear eye with similar intensities, while the RMW was larger and about 40 km in b055 (35 km in b075 and 30 km in b105). By about 48 h, the initially smaller RGW TC vortex (b105) was slightly stronger than the other two TCs. Both the RMW and RGW were always smaller in b105 than in either b055 or b075 throughout the simulation. Overall, these results suggest that the initial RGW of a simulated TC can also affect its structure and intensity evolution. Note that the initial TC intensity was set at 25 m s^{-1} in all three experiments, which is higher than the initial intensity20 m s^{-1} in the sensitivity experiments to the initial RMW discussed in last section. This is intended to allow the difference in the effect of the initial outer core tangential winds on the simulated TC among the three experiment to be more obvious.

Figure 5.15 compares the time evolutions of the maximum 10-m height tangential wind speed and the RMW in the three sensitivity experiments. Similar to the evolution of the initially smaller RMW TC in the sensitivity experiments to the initial storm RMW, the initially smaller RGW TC

(b105) intensified a few hours earlier than the other two TCs, that is, the initial spin-up stage was shorter. The storm in b105 experienced slightly more rapid intensification during the primary intensification stage than the initially larger RGW TC in b055. Compared with the storm initially with a smaller RMW in Section 5.1, the initially smaller RGW storm behaved similarly to the TC with the initially smaller RMW and had a higher quasi-steady intensity but a smaller intensity difference among the TCs in this group. Figure 5.16 shows that the maximum intensification rate was higher in b105 during the early primary intensification stage (24 to 36 h), but the difference was considerably small. This is because the difference between the inner-core inertial stability and the outer-core inertial stability among the storms in the RGW experiments was significantly smaller than those in the sensitivity experiment to the initial storm RMW. For example, the difference between the inertial stability at the RMW and at two times of the RMW was 5×10^{-4} s^{-2} in b055, 5.2×10^{-4} s^{-2} in b075, and 6×10^{-4} s^{-2} in b105 (shown in Figure 5.11b). On the other hand, the difference was 10×10^{-4} s^{-2} in R041, 6×10^{-4} s^{-2} in R061, and 3.5×10^{-4} s^{-2} in R101 respectively (shown in Figure 5.1b). Note that the azimuthal mean tangential wind in the outer region is still stronger in b105 than b055 and b075 by 10 h of the simulation (Figure 5.17), indicating that the initial storm RGW difference can be sustained during the initial spin-up stage mainly because an initially stronger TC vortex was used in these experiments.

Figure 5.18 shows the time evolution of the relative humidity and the vertical motion averaged

within the radius of 1.5 times of the RMW in all three experiments. Based on results in Chapter 3, which suggested that the storm with a smaller RGW induces stronger boundary layer inflow and upward motion inside the RMW through the boundary layer dynamics, the initial moistening of the inner core is slower largely due to weaker upward motion in experiment b055, which in turn resulted from weaker boundary layer inflow and smaller boundary layer moisture convergence and weaker Ekman pumping. These results are consistent with those recently reported by Xu and Wang (2018a, b), who also found that an initially larger RGW TC vortex had a longer initial spin-up stage and intensified less rapidly than the one with an initially smaller RGW. They attributed the difference in intensification rate of the simulated storms to higher inertial stability outside the RMW in the initially larger RGW TC vortex because high inertial stability outside the RMW may have a large resistant effect on boundary layer inflow. This would reduce boundary layer mass and moisture convergence and eyewall updraft, and thus unfavorable for rapid intensification.

Figure 5.19 compares the azimuthal mean radial wind, vertical motion, condensational heating rate, and inertial stability averaged in three hours prior to the corresponding primary intensification stage in the three experiments. It is shown that the initially smaller RGW TC developed stronger and deeper boundary layer inflow in the inner core region within a radius of 75 km, leading to stronger and more inwardly penetrated upward motion in the early primary

intensification stage. Meanwhile, although condensational heating distributed wider in b055 than in b105, the condensation heating rate was higher inside the RMW in b105. As discussed in the last section, heating near a region of higher inertial stability is more effective to the intensification of a TC. These results thus are consistent with those discussed in Chapter 3, where it was shown that an initially smaller RGW TC vortex could induce stronger and more inwardly penetrated inflow and upward motion in the boundary layer in response to the boundary layer dynamics. The inner-core inertial stability distribution is very similar in all three experiments. This might explain why the differences in both the duration of the initial spin-up stage and the intensification rate during the primary intensification stage among the three sensitivity experiments for the initial RGW (Figure 5.15) are smaller than those in the sensitivity experiments for the initial RMW (cf. Figure 5.5). In addition, during the corresponding primary intensification stage in the three experiments, the vertical motion and condensational heating distributions (Figure 5.20) are also similar to those in the time period prior to their corresponding primary intensification stage. The vertically integrated condensational heating rate (Figure 5.21) is wider but lower in b055.

Finally, the intensification rate of the storm with a smaller RMW is higher than that of the storm with a larger RMW during the primary intensification stage because the smaller RMW storm can induce higher condensational heating rate inside the RMW through the boundary layer dynamics, namely, through the indirect effect of surface friction. Therefore, the storm with an

initially smaller RGW can induce stronger condensational heating inside the RMW than the storm with an initially larger RGW, the duration of the initial spin-up stage is shorter and the intensification rate during the primary intensification stage is higher. Once again, the differences in vertical motion and condensational heating between b055 and b105 are very similar to those between CT05-R and CT20-R with different C_Ds (cf. Figure 4.13). However, the positive effect of the higher condensational heating rate in CT20-R with larger C_D was largely offset by the negative effect of greater surface frictional dissipation, resulting in little net contribution to the TC intensification rate. In sharp contrast, since the two storms in b055 and b105 in the given time period had a similar intensity and thus similar surface friction, the higher condensational heating rate in b105 than in b055 was not offset by the small difference in surface friction. As a result, the higher condensational heating rate directly contributed to a higher intensification rate of the simulated storm in b105. It should be pointed out that compared with the sensitivity to the initial RMW, the sensitivity of the intensification rate to the initial RGW is marginal, as the difference in inertial stability between the inner core and outer core is much smaller, leading to a smaller difference in the radial inflow and condensational heating rate through the boundary layer dynamics among these experiments. These results are consistent with the results in Chapter 3, and demonstrate that the radial distribution of tangential wind outside the RMW in the initial TC

vortex can also affect the duration of the initial spin-up stage and the intensification rate during the primary intensification stage of a simulated TC.

CHAPTER 6. CONCLUSIONS

6.1 Key findings

The role of boundary layer dynamics in tropical cyclone intensification is studied using three models with different complexities. Figure 6.1 summarizes the major processes in this study. The indirect effect of boundary layer dynamics is key to both the initial spin-up and the subsequent primary intensification of a TC. First, surface friction contributes to the initial moistening of the inner core through moisture convergence in the inflow boundary layer and Ekman pumping, and thus to the initiation of convection and the initial spin-up of the TC vortex. Second, surface friction together with its associated unbalanced boundary layer dynamics induces strong boundary layer inflow, leading to inward penetration of boundary layer inflow into the eye region, and thus an inward displacement of upward motion and eyewall convection inside the RMW. This contributes to eyewall contraction and intensification of the TC through a quasi-balanced response of the secondary circulation to diabatic heating inside the RMW (red arrows in Figure 6.1). However, for a given initial TC vortex, the intensification rate during the primary intensification stage is insensitive to surface drag coefficient (C_D) in a reasonable range. This is because the enhanced/reduced indirect effect due to an increased/reduced C_D is often largely offset by the enhanced/reduced negative effect due to surface frictional dissipation (green arrows in Figure 6.1) in the TC system, leading to a similar intensification rate.

Next, if the intensification rate of the simulated TC during the primary intensification stage is insensitive to C_D, what determines the intensification rate of a TC under favorable environmental conditions? It is shown that the indirect effect of boundary layer dynamics on TC intensification depends considerably on the storm structure, while the dissipation effect of boundary layer dynamics depends little very weakly on the storm structure. Therefore, the intensification rate of a simulated TC during its primary intensification stage can be largely determined by the structure of the initial TC vortex. The higher and more inward condensational heating rate inside the RMW, namely the positive indirect effect of surface friction in the storm with the initially smaller RMW and/or smaller RGW, is not offset by the small difference in dissipation effect of surface friction, thus directly contributing to a higher intensification rate of the simulated storm. As a result, it is concluded that a storm with an initially smaller RMW or a smaller RGW has a shorter initial spin-up stage and more rapid intensification during the primary intensification stage through boundary layer dynamics (yellow arrows in Figure 6.1).

6.2 Summary and discussion

In this study, first, the role of boundary layer dynamics in TC intensification was investigated using a multi-level boundary layer model and an interactive model including an upper layer, a middle layer governed mainly by a shallow water equation model with a mass sink to mimic

diabatic heating in the eyewall, and a multi-level boundary layer below. The mass-flux at the top of the boundary layer is used to parameterize diabatic heating in the TC eyewall. A possible indirect pathway related to surface friction has been examined and used to explain how the boundary layer dynamics contributes to eyewall contraction and TC intensification, which is schematically summarized in Figure 3.8. There are four sequential interactive processes: (1) the boundary layer inflow in response to the given radial distribution of gradient wind above the boundary layer in the presence of surface friction; (2) the boundary layer inflow, as a function of C_D (surface friction) and radial distribution of gradient wind above the boundary layer, determines the strength and radial location of the boundary layer mass/moisture convergence and thus the eyewall updraft; (3) the upward mass-flux at the top of the boundary layer determines both the strength and radial location of diabatic heating in the eyewall; and (4) the contraction of the RMW and intensification of the TC vortex are in response to gradient wind above the boundary layer to diabatic heating, represented as a mass sink in the shallow water equation system and parameterized using the upward flux at the top of the boundary layer.

The first and second processes in Figure 3.8 were investigated as a forced response problem to a given radial distribution of gradient wind above the boundary layer using a simple multi-level boundary layer model. This helps quantify the dependence of the boundary layer response on the given radial distribution of gradient wind above the boundary layer on C_D and the structure and

intensity of the TC vortex. The results demonstrate that storms with larger C_D (and thus surface friction), smaller RGW, smaller RMW, and higher intensity correspond to stronger and deeper boundary layer inflow as well as larger radial mass convergence and stronger upward motion inside the RMW and a stronger and more inwardly shifted vorticity ring at low-levels inside the RMW. This implies a faster contraction of the RMW and a higher diabatic heating rate inside the RMW, and thus a higher intensification rate of the TC vortex. Nevertheless, since the results from the simple boundary layer model are steady-state solutions, the larger spinning-down due to surface friction exactly offsets the implied larger spinning-up of the TC vortex induced by the indirect effect. Therefore, the results from the simple forced boundary layer model could not be directly used to infer the intensification of the TC vortex. Furthermore, although the stronger supergradient wind with a larger C_D is presented, the spin-up of tangential wind by the upward advection of supergradient wind from below is often balanced by the spin-down of tangential wind due to the outflow induced by the agradient force immediately above the inflow boundary layer. Therefore, caution needs to be given when attributing TC intensification to boundary layer dynamics discussed with the simple boundary layer model although most of the results are very informative.

The third and fourth processes in Figure 3.8 have been examined using the interactive model. As opposed to the simple boundary layer model, the interactive model can simulate how the

gradient wind distribution above the boundary layer is influenced by the boundary layer response through diabatic heating (parameterized using mass-flux at the top of the boundary layer) in the eyewall. The results suggest that storms with larger C_D, smaller RGW, and higher intensity can experience faster contraction of the radius of maximum gradient wind with larger upward motion inside the RMW, similar to the results in the simple boundary layer model, and thus display more rapid intensification. An interesting finding that differs from that implied by the simple boundary layer model is the nonlinear dependence of the TC intensification rate on the initial RMW of the TC vortex. That is, the TC intensification rate initially increases with the increase in the initial RMW, reaches a maximum when the initial RMW is around 80 km, and then decreases with further increases in the initial RMW. This nonmonotonic dependence on the initial RMW can be explained by a balance between the availability of AAM to spin up the storm and the increase in inertial stability outside of the RMW in the near-core environment of the storm. This nonlinear dependence on the initial RMW is a very interesting phenomenon and will be further evaluated using full-physics model simulations in a future study. Moreover, too small C_D could not induce sufficiently large upward motion at the top of the boundary layer, and thus diabatic heating in the eyewall to lead to intensification of the TC vortex through the boundary layer dynamics. In this regard, a minimum threshold of C_D is vital to storm intensification in the interactive model developed in this study. Thus, it is concluded that although dynamically surface friction is an

energetic sink for a TC system, it can contribute positively to intensification of a TC vortex through an indirect effect by modifying the strength and radial location of eyewall updraft/convection. This means that surface friction plays a dual role in TC intensification through the boundary layer dynamics.

The full-physics model TCM4 was used to include both the direct dissipation effect and the indirect effect of surface friction and help understand the individual and combined effects of boundary layer dynamics on TC intensification. Results show that large C_D can considerably shorten both the initial spin-up stage and the primary intensification stage of a simulated storm. It reduces the intensity of the simulated storm in the quasi-steady stage, and has dual opposite effect on the intensification rate during the primary intensification stage. The duration of the initial spin-up stage is determined by the rate of moistening in the inner core region, which is largely controlled by moisture convergence in the inflow boundary layer and Ekman pumping due to surface friction and vertical mixing. During the primary intensification stage, larger C_D can induce stronger radial inflow together with higher condensational heating rate in the eyewall and shift the eyewall convection further inside the RMW. However, larger C_D (and thus surface friction) also induces larger frictional dissipation resulting from greater surface wind stress in the TC system. This explains why the simulated TC intensification rate during the primary intensification stage is insensitive to C_D in numerical simulations of TCs in this and also in some earlier studies.

For the steady-state stage, the weaker final intensity of the simulated storm with larger C_D is consistent with the MPI theory, which predicts an inverse proportion of the maximum wind speed of the storm to the square root of C_D. Thus, since the intensification rate of the simulated storm is insensitive to C_D, a storm with a larger C_D would experience a shorter primary intensification stage with a weaker steady-state intensity. In addition, results from the sensitivity experiments to surface wind speed dependent C_D also support the idea that different dependencies of C_D on surface wind speed (or different C_D) can only change the duration of the initial spin-up stage and the steady-state intensity of the simulated TC. The intensification rate of the simulated TC during the primary intensification stage is similar since the positive indirect and negative direct dissipation effects of surface friction largely offset, resulting in insensitivity of the simulated TC intensification rate to change in C_D.

The hypothesis that it is the initial vortex structure that substantially determines the intensification rate of a TC through the boundary layer dynamics given all other favorable environmental conditions is also tested. Because the positive indirect effect of boundary layer dynamics on TC intensification depends considerably on the storm structure, while the negative dissipation effect of boundary layer dynamics depends heavily on TC intensity but very weakly on the storm structure, it is strongly suggested that the intensification rate of a TC during its primary intensification stage is mainly determined by the structure of the initial TC vortex. The

dependence of the intensification rate on the RMW and RGW of the initial TC vortex has been demonstrated using sensitivity experiments with the different initial vortex structure in TCM4. The results show that the both initially smaller RGWs and smaller RMWs TC vortices have a shorter initial spin-up stage and more rapid intensification during the primary intensification stage. This results mainly from stronger and more inwardly penetrated boundary layer inflow and updraft, and thus diabatic heating, in response to the boundary layer dynamics. During the spin-up stage, the stronger boundary layer inflow associated with faster moisture convergence induced by an initially smaller RGW or smaller RMW TC vortex through the boundary layer dynamics can shorten the duration of the initial spin-up stage of the simulated TC. After the initial spin-up stage, the indirect effect of surface friction can lead to more rapid intensification due to higher condensational heating rate inside the RMW. Indeed, although the indirect effect of surface friction is exactly the same as in the storm with larger C_D, where the positive contribution induced by larger C_D is largely offset by the negative contribution of surface frictional dissipation, given the low net contribution to the TC intensification rate. In contrast, the higher condensational heating rate in storms with an initially smaller RGW or a smaller RMW is not offset by the frictional dissipation since the negative dissipation effect of surface friction depends very weakly on the storm structure, thus directly contributing to a higher intensification rate of the simulated storm. It should be pointed out that compared with the sensitivity to the initial RMW, the

sensitivity of the TC intensification rate to the initial RGW is marginal. This is because the difference in inertial stability between the inner core and outer core is smaller, leading to a smaller difference in radial inflow and condensational heating through the boundary layer dynamics among the initial RGWs examined in this study.

Results from this study strongly suggest that the initial structure of the TC vortex is critical to the intensification rate of the storm through boundary layer dynamics in numerical models, and thus more attention needs to be given to the analysis of TC structure in observations and accurate representation of TC structure in the initial condition of numerical prediction models used for TC forecasts.

6.3 Some remaining issues and future work

Some scientific issues need to be further addressed. First, whether the differences among all sensitivity experiments are physical and significant. To address this issue, three ensemble groups' simulations with the given initial moisture perturbations in the innermost domain – CTRL-E_n, CT05-E_n, and CT20-E_n – were conducted (Table 6.1). Each simulation has seven ensemble members. Figure 6.2 demonstrates the time evolution of the maximum 10-m height tangential wind speed in the experiments with different C_D and each members and their ensemble mean. It can be seen that although some fluctuations appear among members in each simulation, the basic

TC behaviors in the three ensemble means (Figure 6.3) are very similar to those in the experiments (CTRL, CT05, and CT20) discussed earlier in Chapter 5. The evolution of both the intensity and intensification rate are similar, as shown in Figure 3.1. The intensification rates in all ensemble simulations are similar during the primary intensification stage, and the duration of the initial spin-up stage decreases with increasing C_D. Also, the steady-state intensity is the highest in the experiments with smaller C_D. The variability is much smaller during the initial spin-up stage in all simulations. This is consistent with the results of many previous studies (e.g., Miyamoto and Nolan 2018).

Second, results from this study suggest that surface friction can determine the duration of the initial spin-up stage through its impact on moisture convergence in the boundary layer. Lower surface friction lengthens the initial spin-up stage due to weaker boundary layer moisture convergence. In other words, the initial moisture of a TC can also determine the duration of the spin-up stage. Therefore, by reducing the moisture to 90% in the inner domain as in CTRL, a sensitivity experiment (Q090) with less initial moisture was performed in TCM4 to understand TC behavior during the initial spin-up stage (Table 6.2). Figure 6.4 compares the intensity evolutions in CTRL and Q090.The storm in Q090 had a longer initial spin-up stage than that in CTRL, while the intensification rates during the primary intensification stage and the quasi-steady intensities were similar in the two experiments. As seen from Figure 6.5, the inner core became

well moistened after the first 24 h of simulation in CTRL. In contrast, due to less initial moisture, the inner core spent more time to become moistened until 30-36 h of simulation in Q090. The results in Section 3.4.2 suggest that the storm starts to intensify after the averaged moisture in the boundary layer within the RMW reaches 90%. The storm in Q090 shows a very similar feature (cf. Figure 4.9), indicating that the moisture in the inner core plays an important role in the duration of the initial spin-up stage. However, the intensification rate during the primary intensification stage and the quasi-steady intensity in Q090 are very similar to those in CTRL. This implies that the initial moisture of a TC can only determine the duration of the initial spin-up stage of the simulated TC, while has little impact on the intensification rate and the quasi-steady state intensity. This result is consistent with results discussed in Chapter 4.2.

Lastly, more experiments with smaller C_D (and thus surface friction) were also conducted to further understand the TC behavior after the initial spin-up stage (Table 6.2 and Figure 6.6). Figure 6.6 demonstrates that the intensification rate of the simulated TC is also insensitive to C_D between 36 h and 72 h, even in the experiment with 5% C_D in CTRL. On the other hand, the quasi-steady state intensity of the simulated storms with a smaller C_D are strongest, but the results here suggest that the storm with 20% C_D (blue) has the highest steady-state intensity, rather than the storm with 5% C_D (yellow). This seems to suggest that, when C_D decreases further, no significant changes occur to the intensification rate. Nevertheless, the quasi-steady intensity increases until a

threshold of approximately 4.8×10^{-4}, beyond which the quasi-steady intensity decreases. Furthermore, when C_D is reduced to a much smaller value such as 1% C_D, 1.5×10^{-5}, or even zero (Figure 6.7), the storms can still intensify but with a much reduced intensification rate. This also leads to the weaker quasi-steady intensity. The results thus suggest that the indirect effect of surface friction is key to eyewall heating and the working of the balanced dynamics, which can largely explain TC intensification once diabatic heating in the eyewall is given through the boundary layer dynamics. Note that the simulation results are consistent with those in Montgomery et al. (2010), Zhang and Emanuel (2016), and Kilroy et al. (2017), but with different explanation in this study. Note also that although this study has suggested that the intensification rate is insensitive to C_D during the primary intensification stage in TCM4, the C_D should be in the observational and reasonable range, namely not too small and not too large.

Finally, most results from this study have been based on TCM4, only one SST, and also the use of the standard vertical diffusivity (K_m) parameterized in the model, it is unclear whether the main conclusions would be altered if different boundary layer schemes, or other model physics, or different SSTs are used. It is our hypothesis that the main conclusions from this study should not be altered qualitatively but mainly quantitatively. A last issue is the use of the atmospheric model only in this study. With the ocean coupling, larger C_D would impose larger surface stress curl and stirring to the ocean and induce stronger upwelling and mixing in the upper ocean, leading

to cooling in SST. This extra negative effect has not been considered in this study. Since numerical experiments with a coupled ocean-atmospheric model need to be conducted to address the issue, this will be a topic for a future study.

REFERENCES

Anthes, R. A., and S. W. Chang, 1978: Response of the hurricane boundary layer to changes of sea surface temperature in a numerical model. *J. Atmos. Sci.*, **35**, 1240–1255.

Black, P. G., and Coauthors, 2007: Air–sea exchange in hurricanes: Synthesis of observations from the coupled boundary layer air–sea transfer experiment. *Bull. Amer. Meteor. Soc.*, **88**, 357–374.

Bryan, G. H., and J. M. Fritsch, 2002: A benchmark simulation for moist nonhydrostatic numerical models. *Mon. Wea. Rev.*, **130**, 2917–2928.

Callaghan, A., G. de Leeuw, and L. Cohen, 2007: Observations of oceanic whitecap coverage in the North Atlantic during gale force winds, *Nucleation and Atmospheric Aerosols*, **9**, 1088-1092.

Carrasco, C. A., C. W. Landsea, and Y. Lin, 2014: The influence of tropical cyclone size on its intensification. *Wea. Forecasting*, **29**, 582–5900.

Charney, J. G. and A. Eliassen, 1964: On the growth of the hurricane depression. *J. Atmos. Sci*., **21**, 68-75.

Chen, H., D.-L. Zhang, J. Carton, and R. Atlas, 2011: On the rapid intensification of Hurricane Wilma (2005). Part I: Model prediction and structural changes. *Wea. Forecasting*, **26**, 885–901.

Craig, G. C. and S. L. Gray, 1996: CISK or WISHE as the mechanism for tropical cyclone intensification. *J. Atmos. Sci.*, **53**, 3528–3540.

DeMaria, M., and W. H. Schubert, 1984: Experiments with a spectral tropical cyclone model. *J. Atmos. Sci.*, **41**, 901–924.

____, M., M. Mainelli, L. K. Shay, J. A. Knaff, and J. Kaplan, 2005: Further improvements to the statistical hurricane intensity prediction Scheme (SHIPS). *Wea. Forecasting*, **20**, 531–543.

____, 2009: A simplified dynamical system for tropical cyclone intensity prediction. *Mon. Wea. Rev.*, **137**, 68–82.

Donelan, M. A., B. K. Haus, N. Reul, W. J. Plant, M. Stiassnie, H. C. Graber, O. B. Brown, and E. S. Saltzman, 2004: On the limiting aerodynamic roughness of the ocean in very strong winds. *Geophys. Res. Lett.*, **31**, L18306.

____, 2018: On the decrease of the oceanic drag coefficient in high Winds. *Journal of Geophysical Research: Oceans*, **123**, 1485–1501.

Durran, D. R. and J. B. Klemp, 1983: A compressible model for the simulation of moist mountain waves. *Mon. Wea. Rev.*, **111**, 2341–2361.

Eliassen, A. and M. Lystad, 1977: The Ekman layer of a circular vortex. A numerical and theoretical study. *Geophysica Norvegica*, **7**, 1–16.

Emanuel, K. A. 1986: An air-sea interaction theory for tropical cyclones. Part I: Steady state maintenance. *J. Atmos. Sci.*, **43**, 585-604.

____, 1988: The maximum intensity of hurricanes. *J. Atmos. Sci.*, **45**, 1143-1155.

____, 1989: The finite-amplitude nature of tropical cyclogenesis. *J. Atmos. Sci*., **46**, 3431-3456.

____, 1995: Sensitivity of tropical cyclones to surface exchange coefficients and a revised steady-state model incorporating eye dynamics. *J. Atmos. Sci.*, **52**, 3969–76.

____, 1997: Some aspects of hurricane inner-core dynamics and energetics. *J. Atmos. Sci.*, **54**, 1014–26.

Fairall, C. W., E. F. Bradley, J. E. Hare, A. A. Grachev, and J. B. Edson, 2003: Bulk parameterization of air–sea fluxes: Updates and verification for the COARE algorithm. *J. Climate*, **16**, 571–591.

Frisius, T. and M. Lee, 2016: The impact of gradient wind imbalance on tropical cyclone intensification within Ooyama's three-layer model. *J. Atmos. Sci.*, **73**, 3659–3679.

Fudeyasu, H. and Y. Wang, 2011: Balanced contribution to the intensification of a tropical cyclone simulated in TCM4: Outer-core spinup process. *J. Atmos. Sci.*, **68**, 430–449.

Garratt, J. R., 1992: The atmospheric boundary layer. *Cambridge University Press*.

Golbraikh, E., and Y. M. Shtemler, 2016: Foam input into the drag coefficient in hurricane conditions. *Dynamics of Atmospheres and Oceans*, **73**, 1–9.

Gopalakrishnan, S. G., F. Marks, J. A. Zhang, X. Zhang, J. Bao, and V. Tallapragada, 2013: A study of the impacts of vertical diffusion on the structure and intensity of the tropical cyclones using the high-resolution HWRF system. *J. Atmos. Sci.*, **70**, 524–541.

Gray, W. M., E. Ruprecht, and R. Phelps, 1975: Relative humidity in tropical weather systems. *Mon. Wea. Rev.*, **103**, 685–690.

Hendricks, E. A., M. T. Montgomery, and C. A. Davis, 2004: The role of "102ertical" hot towers in the formation of Tropical Cyclone Diana (1984). *J. Atmos. Sci.*, **61**, 1209–1232.

Heng, J., and Y. Wang, 2016a: Nonlinear response of a tropical cyclone vortex to prescribed eyewall heating with and without surface friction in TCM4: Implications for tropical cyclone intensification. *J. Atmos. Sci.*, **73**, 1315–1333.

____, and ____, 2016b: Reply to ‘‘Comments on ‘Nonlinear response of a tropical cyclone vortex to prescribed eyewall heating with and without surface friction in TCM4: Implications for tropical cyclone intensification.’’’ *J. Atmos. Sci.*, **73**, 5105–5109.

____, ____, and W. Zhou, 2017: Revisiting the balanced and unbalanced aspects of tropical cyclone intensification. *J. Atmos. Sci.*, **74**, 2575–2591.

Jordan, C. L., 1958: Mean soundings for the West Indies area. *J. Meteor.*, **15**, 91–97.

Kaplan, J., M. DeMaria, and J. A. Knaff, 2010: A revised tropical cyclone rapid intensification index for the Atlantic and Eastern North Pacific basins. *Wea. Forecasting*, **25**, 220–241.

Kepert, J. D., 2001: The dynamics of boundary layer jets within the tropical cyclone core. Part I:

Linear theory. *J. Atmos. Sci.*, **58**, 2469–2484.

____, and Y. Wang, 2001: The dynamics of boundary layer jets within the tropical cyclone core. Part II: Nonlinear enhancement. *J. Atmos. Sci.*, **58**, 2485–2501.

____, 2010a: Slab- and height-resolving models of the tropical cyclone boundary layer. Part I: Comparing the simulations. *Quart. J. Roy. Meteor. Soc.*, **136**, 1686–1699.

____, 2010b: Slab- and height-resolving models of the tropical cyclone boundary layer. Part II: Why the simulations differ. *Quart. J. Roy. Meteor. Soc.*, **136**, 1700–1711.

____, 2017: Time and space scales in the tropical cyclone boundary layer, and the location of the eyewall updraft. *J. Atmos. Sci.*, **74**, 3305–3323.

Kilroy, G., M. T. Montgomery, and R. K. Smith, 2017: The role of boundary-layer friction on tropical cyclogenesis and subsequent intensification. *Quart. J. Roy. Meteor. Soc.*, **143**, 2524–2536.

Kimball, S. K. and M. S. Mulekar, 2004: A 15-year climatology of North Atlantic tropical cyclones. Part I: Size parameters. *J. Climate*, **17**, 3555–3575.

Kleinschmidt, E., Jr., 1951: Grundlagen einer theorie der tropischen zyklonen. Arch. *Meteor. Geophys. Bioklimatol.*, **4A**, 53–72.

Kurihara, Y., and R. E. Tuleya, 1974: Structure of a tropical cyclone developed in a three-dimensional numerical simulation. *J. Atmos. Sci.*, **31**, 893–919.

Li, T.-H., and Y. Wang 2018a: The role of boundary layer dynamics in tropical cyclone intensification. Part I: Results from a simplified framework. *J. Atmos. Sci.*

Li, T.-H., and Y. Wang 2018b: The role of boundary layer dynamics in tropical cyclone intensification. Part II: Results from a full-physics model. *J. Atmos. Sci.*

Langland, R. H., and C.-S. Liou, 1996: Implementation of an E–ε parameterization of vertical subgrid-scale mixing in a regional model. *Mon. Wea. Rev.*, **124**, 905–918.

Large, W. G. and S. Pond, 1981: Open ocean momentum flux measurements in moderate to strong winds. *J. Phys. Oceanogr.*, **11**, 324–336.

Makin, V. K. 2005: A note on drag of the sea surface at hurricane winds. *Boundary Layer Meteorology*, **115**(1), 169–176.

Malkus, J. S., H. Riehl, 1960: On the dynamics and energy transformations in steady-state hurricanes. *Tellus*, **12**, 1–20.

Miyamoto, Y. and D. S. Nolan, 2018: Structural changes preceding rapid intensification in tropical cyclones as shown in a large ensemble of idealized simulations. *J. Atmos. Sci.,* **75**, 555–569.

Molinari, J. and D. Vollaro, 1990: External influences on hurricane intensity. Part II: Vertical structure and response of the hurricane vortex. *J. Atmos. Sci.*, **47**, 1902–1918.

____, ____, and S. Skubis, 1993: Application of the Eliassen balanced model to real-data tropical cyclones. *Mon. Wea. Rev.*, **121**, 2409–2419.

Möller, J. D., and L. J. Shapiro, 2002: Balanced contributions to the intensification of Hurricane Opal as diagnosed from a GFDL model forecast. *Mon. Wea. Rev.*, **130**, 1866–1881.

Monahan, E. C. and I. Muircheartaigh, 1980: Optimal power-law description of oceanic whitecap coverage dependence on wind speed. *J. Phys. Oceanogr.*, **10**, 2094–2099.

Monahan, E. C. and D. K. Woolf, 1989: Comments on "Variations of whitecap coverage with wind stress and water temperature. *J. Phys. Oceanogr.*, **19**, 706–709.

Monin, A. S., and A. M. Obukhov, 1954: Basic laws of turbulent mixing in the surface layer of the atmosphere. *Tr. Akad. Nauk. SSSR Geophiz. Inst.* **24** (151), 163–187.

Montgomery, M. T., M. E. Nicholls, T. A. Cram, and A. B. Saunders, 2006: A vertical hot tower route to tropical cyclogenesis. *J. Atmos. Sci.*, **63**, 355–386.

____, R. K. Smith, and S. V. Nguyen, 2010: Sensitivity of tropical cyclone models to the surface drag coefficient. *Quart. J. Roy. Meteor. Soc.*, **136**, 1945-1953.

____, and ____, 2014: Paradigms for tropical-cyclone intensification. *Aust. Meteorol. Ocean*, Bruce Morton Memorial Volume, **64**, 37-66.

Moon, I.-J., T. Hara, I. Ginis, S. E. Belcher, and H. Tolman, 2004a: Effect of surface waves on air–sea momentum exchange. Part I: Effect of mature and growing seas. *J. Atmos. Sci.*, **61**, 2321–2333.

____, I. Ginis, and T. Hara, 2004b: Effect of surface waves on air–sea momentum exchange. Part II: Behavior of drag coefficient under tropical cyclones. *J. Atmos. Sci.*, **61**, 2334–2348.

Newell, A. C., and V. E. Zakharov, 1992: Rough sea foam. *Physical Review Letters*, **69**(8), 1149-1151.

Nolan, D. S., Y. Moon, and D. P. Stern, 2007: Tropical cyclone intensification from asymmetric convection: Energetics and efficiency. *J. Atmos. Sci.*, **64**, 3377–3405.

Ogura, Y., 1964: Frictionally controlled, thermally driven circulations in a circular vortex with application to tropical cyclones. *J. Atmos. Sci.*, **21**, 610–621.

Ooyama, K. V. 1969: Numerical simulation of the life cycle of tropical cyclones. *J. Atmos. Sci.*, **26**, 3–40

Pendergrass, A. G. and H. E. Willoughby, 2009: Diabatically induced secondary flows in tropical cyclones. Part I: Quasi-steady forcing. *Mon. Wea. Rev.*, **137**, 805–821.

Peng, K., R. Rotunno, and G. H. Bryan, 2018: Evaluation of a time-dependent model for the intensification of tropical cyclones. *J. Atmos. Sci.*

Persing, J., M. T. Montgomery, and R. E. Tuleya, 2002: Environmental interactions in the GFDL hurricane model for Hurricane Opal. *Mon. Wea. Rev.*, **130**, 298–317.

Powell, M. D., P. J. Vickery, and T. Reinhold, 2003: Reduced drag coefficient for high wind

speeds in tropical cyclones. *Nature*, **422**, 279–283.

Reul, N., and B. Chapron (2003): A model of sea-foam thickness distribution for passive microwave remote sensing applications, *J. Geophys. Res.*, **108**, 3321.

Riehl, H., 1950: A model for hurricane formation. *J. Appl. Phys.*, **21**, 917–925.

Rogers, R., P. Reasor, and S. Lorsolo, 2013: Airborne Doppler observations of the inner-core structural differences between intensifying and steady-state tropical cyclones. *Mon. Wea. Rev.*, **141**, 2970–2991.

Rosenthal, S. L., 1962: '*A theoretical analysis of the field of motion in the hurricane boundary layer*', National Hurricane Research Project Report No. 56, U. S. Department of Commerce.

____, 1971: The response of a tropical cyclone model to variations in boundary layer parameters, initial conditions, lateral boundary conditions, and domain size. *Mon. Wea. Rev.*, **99**, 767–777.

Rotunno, R., and K. A. Emanuel, 1987: An air-sea interaction theory for tropical cyclones. Part II: Evolutionary study using a nonhydrostatic axisymmetric Model. *J. Atmos. Sci.*, **44**, 542–561.

Schecter, D. A., 2011: A method for diagnosing the sources of infrasound in convective storm simulations. *J. Appl. Meteor. Climatol.*, **50**, 2526–25423

Schubert, W. H. and J. J. Hack, 1982: Inertial stability and tropical cyclone development. *J. Atmos. Sci.*, **39**, 1687–1697.

Shapiro, L. J. and H. E. Willoughby, 1982: The response of balanced hurricanes to local sources of heat and momentum. *J. Atmos. Sci.*, **39**, 378–394.

____, 1983: The asymmetric boundary layer flow under a translating hurricane. *J. Atmos. Sci.* **40**: 1984–1998.

Smith, R. K., 1968: The surface boundary layer of a hurricane. *Tellus*, **20**, 473–483.

____, and M. T. Montgomery, 2015: Towards clarity on understanding tropical cyclone intensification. *J. Atmos. Sci.*, **72**, 3020–3031.

____, ____, and S. V. Nguyen, 2009: Tropical-cyclone spin up revisited. *Quart. J. Roy. Meteor. Soc*., **135**, 1321–35.

Soloviev, A. V., R. Lukas, M. A. Donelan, B. K. Haus, and I. Ginis, 2014: The air–sea interface and surface stress under tropical cyclones. *Scientific Reports*, **4**, 5306.

Stern, D. P., J. L. Vigh, D. S. Nolan, and F. Zhang, 2015: Revisiting the relationship between eyewall contraction and intensification. *J. Atmos. Sci.*, **72**, 1283–1306.

Stogryn A. 1972: The emissivity of sea foam at microwave frequencies. *J Geophys Res*, **77,** 1658–1666.

Thomsen, S., C. Eden, and L. Czeschel, 2014: Stability analysis of the Labrador Current. *J. Phys. Oceanogr.*, **44**, 445–463.

Tuleya, R. E., and Y. Kurihara, 1978: A numerical simulation of the landfall of tropical cyclones. *J. Atmos. Sci.*, **35**, 242–257.

Vigh, J. L. and W. H. Schubert, 2009: Rapid development of the tropical cyclone warm core. *J. Atmos. Sci.*, **66**, 3335–3350.

Wang, Y., 1999: A triply-nested movable mesh tropical cyclone model with explicit cloud microphysics-TCM3. BMRC report No.74. Bureau of Meteorology Research Center, Australia.

____, 2001: An explicit simulation of tropical cyclones with a triply nested movable mesh primitive equation model: TCM3. Part I: Model description and control experiment. *Mon. Wea. Rev.*, **129**, 1370–1394.

____, 2007: A multiply nested, movable mesh, fully compressible, nonhydrostatic tropical cyclone model—TCM4: Model description and development of asymmetries without

explicit asymmetric forcing. *Meteor. Atmos. Phys.*, **97**, 93–116.

____, 2008a: Structure and formation of an annular hurricane simulated in a fully compressible, nonhydrostatic model—TCM4. *J. Atmos. Sci.*, **65**, 1505–1527.

____, 2008b: Rapid filamentation zone in a numerically simulated tropical cyclone. *J. Atmos. Sci.*, **65**, 1158–1181.

____, 2009: How do outer spiral rainbands affect tropical cyclone structure and intensity? *J. Atmos. Sci.*, **66**, 1250–1273.

____, and J. Xu, 2010: Energy production, frictional dissipation, and maximum intensity of a numerically simulated tropical cyclone. *J. Atmos. Sci.*, **67**, 97–116

Wood, V. T., and L. W. White, 2011: A new parametric model of vortex tangential-wind profiles: Development, testing, and verification. *J. Atmos. Sci.*, **68**, 990–1006.

____, ____, H. E. Willoughby, and D. P. Jorgensen, 2013: A new parametric tropical cyclone tangential wind profile model. *Mon. Wea. Rev.*, **141**, 1884–1909.

Xu, J., and Y. Wang, 2010a: Sensitivity of tropical cyclone inner core size and intensity to the radial distribution of surface entropy flux. *J. Atmos. Sci.*, **67**, 1831–1852.

____, and ____, 2010b: Sensitivity of the simulated tropical cyclone inner-core size to the initial vortex size. *Mon. Wea. Rev*., **138**, 4135–4157.

____, and ____, 2015: A statistical analysis on the dependence of tropical cyclone intensification rate on the storm intensity and size in the North Atlantic. *Wea. Forecasting*, **30**, 692–701.

____, and ____, 2018a: Dependence of tropical cyclone intensification rate on sea surface temperature, storm intensity, and size in the Western North Pacific. *Wea. Forecasting*, **33**, 523–537.

____, and ____, 2018b: Effect of the initial vortex structure on intensification of a numerically simulated tropical cyclone. *J. Meteor. Soc. Japan*, **96**(2), 111–126.

Yamasaki, M., 1968: Numerical simulation of tropical cyclone development with the use of primitive equations. *J. Meteor. Soc. Japan*, **46**, 202–214.

Zhang, F. and K. Emanuel, 2016: On the role of surface fluxes and WISHE in tropical cyclone intensification. *J. Atmos. Sci.*, **73**, 2011–2019.

Zhang, J. A. and M. T. Montgomery, 2012: Observational estimates of the horizontal eddy diffusivity and mixing length in the low-level region of intense hurricanes. *J. Atmos. Sci.*, **69**, 1306–1316.

Table 1.1. Results of the role of surface friction in TC formation and subsequent intensification in previous studies using numerical models.

Intensification rate is sensitive to surface drag coefficient	Intensification rate is insensitive to surface drag coefficient	Surface friction is indispensable to TC formation and subsequent intensification
Rosenthal (1971)		Rosenthal (1971)
	Graig and Gray (1996)	Graig and Gray (1996)
Montgomery et al. (2010)		Montgomery et al. (2010)
		Schecter (2011)
Emanuel (2012)		Emanuel (2012)
	Thomsen et al. (2014)	Thomsen et al. (2014)
	Peng et al. (2018)	Peng et al. (2018)
	Li and Wang (2018b)	Li and Wang (2018b)

Table 1.2. Summary of the main purpose of each model in this study.

Models	Indirect effect of surface friction	Dissipation effect of surface friction
Simple boundary layer model	The effect of gradient wind on boundary layer responses	Only in boundary layer
Interactive model	The effect of boundary layer responses on gradient wind	Only in boundary layer
Full-physics model	Both of above	Both boundary layer and free atmosphere

Table 2.1. Values of the parameters used in the interactive model.

Parameter	Values
α	0.95
ε	0.88
H_b	1000 m
H_1, H_2	5000 m
f	3.6×10^{-5} s^{-1}
θ_{e1}	332 K
$\overline{\theta_{e2}^*}$	342 K
$\overline{\theta_{es}^*}$	372 K
a, b	10, 2

Table 2.2. Summary of the model physical processes in TCM4.

Physical process	Scheme and reference
Surface flux	Bulk scheme (Fairall et al. 2003)
Vertical mixing	*E*-ε turbulence closure scheme (Langland and Liou 1996)
Horizontal diffusion	Deformation-dependent fourth-order (Wang 2001)
Cloud microphysics	Bulk mixed-phase cloud microphysics (Wang 2001)
Radiation	Newtonian cooling (Rotunno and Emanuel 1987)
Dissipative heating	Turbulent kinetic energy dissipation rate ε

Table 2.3. Summary of numerical sensitivity experiments for C_D performed using TCM4. The maximum tangential wind speed V_m is 15 m s^{-1} at the radius of maximum wind R_m of 75 km with the decaying parameter b = 1 for the initial TC vortex in all experiments.

Experiment	C_D	Time to change C_D
CTRL	100% C_D	In the beginning
CT05	50% C_D	In the beginning
CT07	70% C_D	In the beginning
CT13	130% C_D	In the beginning
CT20	200% C_D	In the beginning
CT05-R	50% C_D	At 36 h
CT20-R	200% C_D	At 36 h
CTDO	Donelan (2018)	In the beginning
CTD1	Modified Donelan	In the beginning

Table 2.4. Summary of numerical sensitivity experiments for the initial TC structure performed using TCM4.

Experiment	*b*	Maximum tangential wind speed (m s^{-1})	RMW (km)
R041	1.0	20	40
R061	1.0	20	60
R101	1.0	20	100
b055	0.5	25	75
b075	0.7	25	75
b105	1.0	25	75

Table 6.1. Summary of ensemble numerical sensitivity experiments of surface friction performed using TCM4. The maximum tangential wind speed V_m is 15 m s^{-1} at the radius of maximum wind R_m of 75 km with the decaying parameter b = 1 for the initial TC vortex in all experiments.

Experiment	C_D	Initial moisture
CTRL	100% C_D	Tropical sounding
CTRL-E_n (six experiments in total)	100% C_D	100$\pm$0.5×n% as CTRL (n = +1, +2, +3, -1, -2, -3)
CT05	50% C_D	Same as CTRL
CT05-E_n (six experiments in total)	50% C_D	100$\pm$0.5×n% as CT05 (n = +1, +2, +3, -1, -2, -3)
CT20	200% C_D	Same as CTRL
CT20-E_n (six experiments in total)	200% C_D	100$\pm$0.5×n% as CT20 (n = +1, +2, +3, -1, -2, -3)

Table 6.2. Summary of numerical experiments performed using TCM4. The maximum tangential wind speed V_m is 15 m s^{-1} at the radius of maximum wind R_m of 75 km with the decaying parameter b = 1 for the initial TC vortex in all experiments.

Experiment	C_D	Time to change C_D	Initial moisture
CTRL	100% C_D	In the beginning	Tropical sounding
C001-R	1% C_D	At 36 h	Same as in CTRL
C005-R	5% C_D	At 36 h	Same as in CTRL
C010-R	10% C_D	At 36 h	Same as in CTRL
C020-R	20% C_D	At 36 h	Same as in CTRL
C030-R	30% C_D	At 36 h	Same as in CTRL
C040-R	40% C_D	At 36 h	Same as in CTRL
CC5-R	1.5×10^{-5}	At 36 h	Same as in CTRL
CC0-R	0	At 36 h	Same as in CTRL
Q090	100% C_D	In the beginning	90% as in CTRL

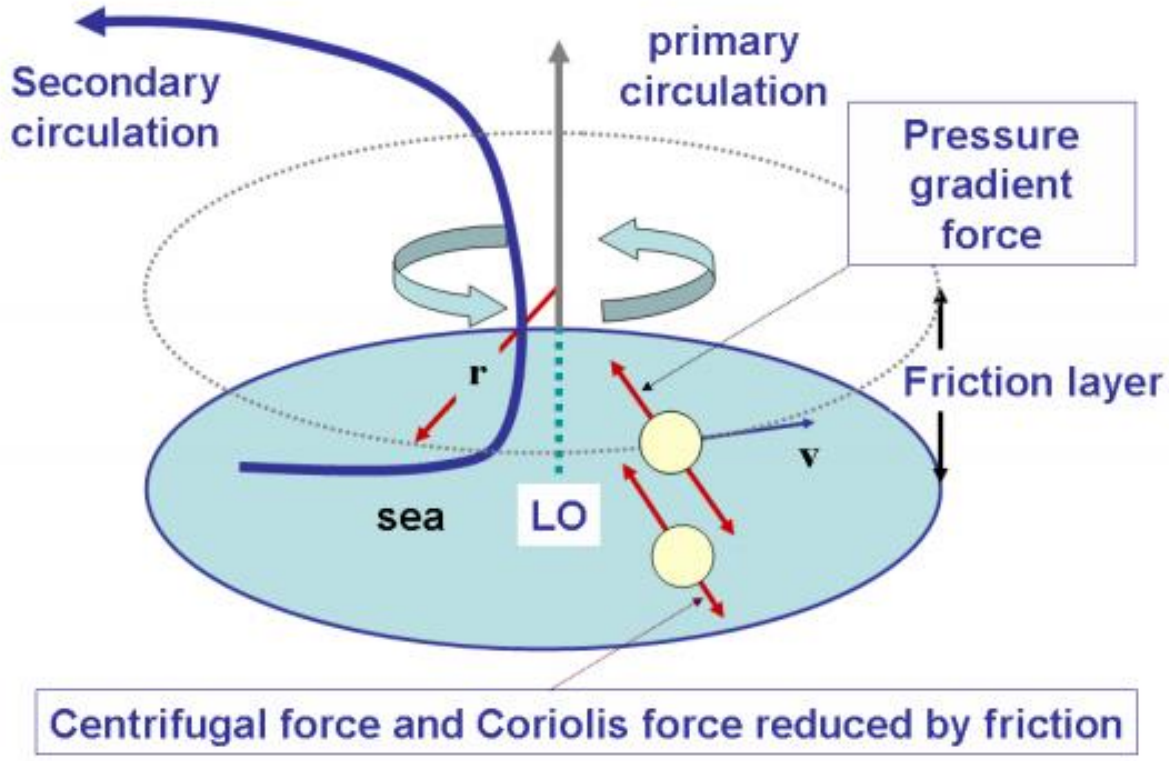

Figure 1.1. Schematic diagram illustrating the agradient force imbalance in the friction layer of a tropical cyclone and the secondary circulation that it generates (quoted from Montgomery and Smith 2014).

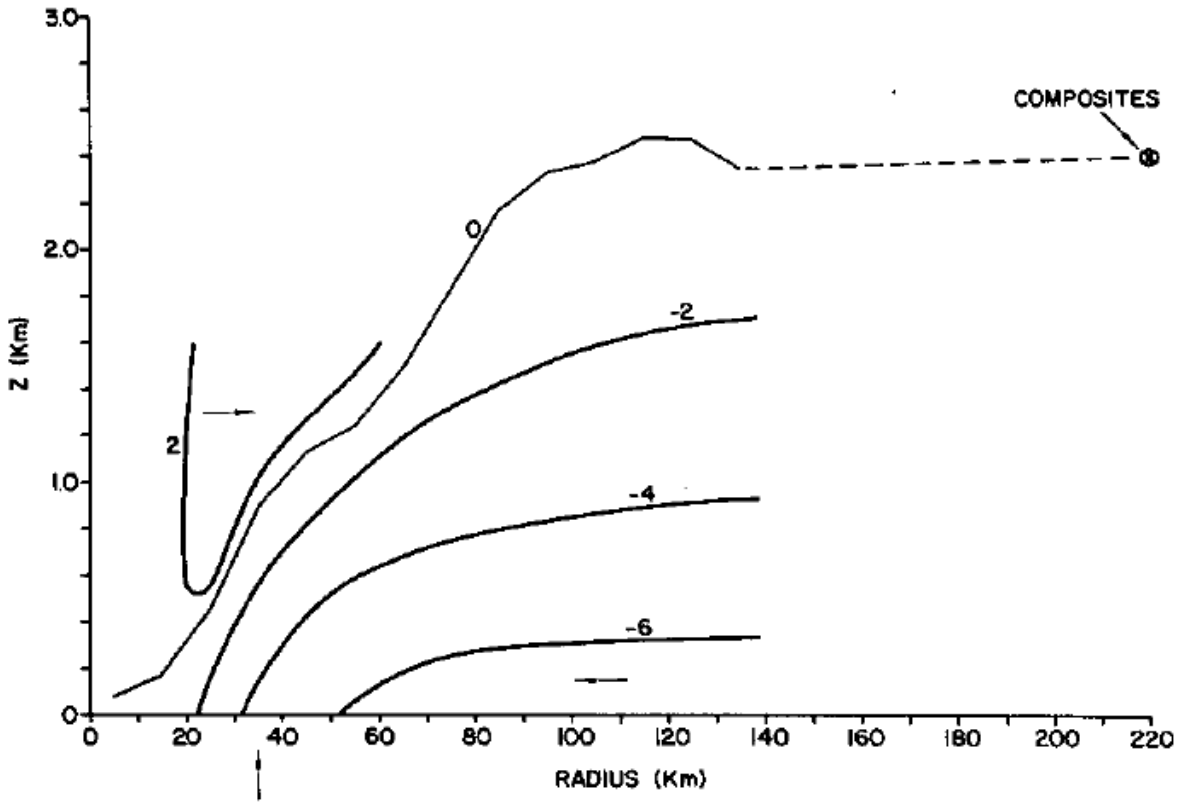

Figure 1.2. Vertical cross section of the mean radial wind (m s^{-1}). The zero contour (vertically interpolated, then radially smoothed) corresponds to the top of the inflow layer. Other contours were drawn subjectively. Also shown is the V_r = 0 level at R = 2° (222 km) from Frank's (1977) composite analysis of typhoons. The arrow on the abscissa denotes the radius of maximum winds and mean upward motion at 560 m; the other arrows illustrate the flow (quoted from Frank 1984).

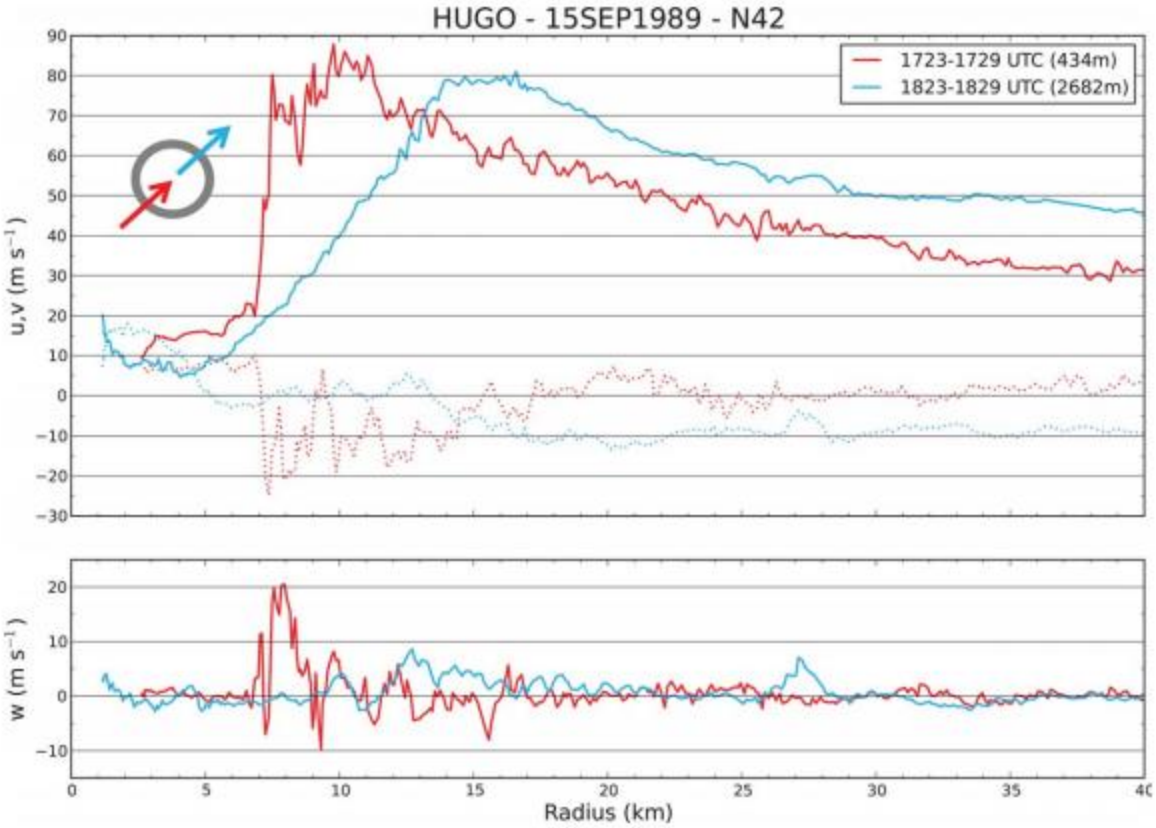

Figure 1.3. The aircraft data from an inbound leg in the southwest quadrant (red, 434 m average height) and an outbound leg in the northeast quadrant (blue, 2682 m average height) of Hurricane Hugo on 15 September 1989. The solid curves show the tangential wind component, while the dotted curves show the radial wind component (top). The vertical component of the velocity (bottom) (quoted from William et al. 2013).

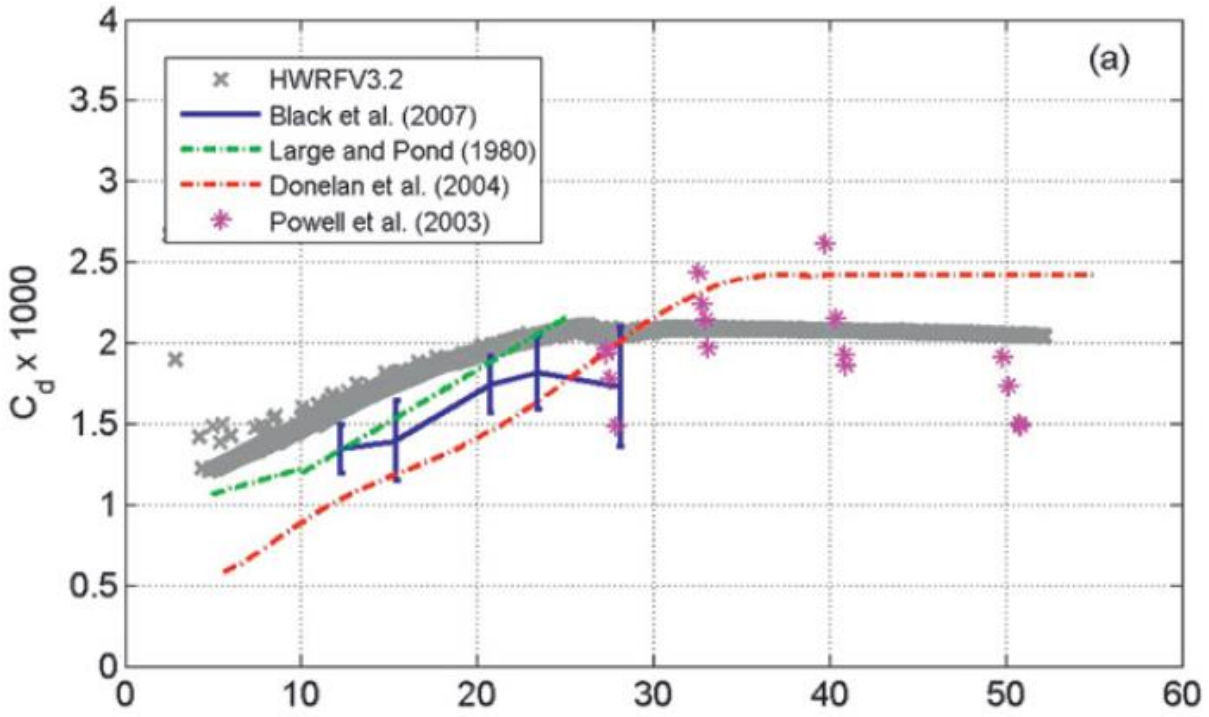

Figure 1.4. The variation of C_D with 10-m height wind speed from Gopalakrishnan (2013) (gray), Black et al. (2007) (blue), Large and Pond (1981) (green), Donelan et al. (2004) (red), and Powell et al. (2003) (pink) (quoted from Gopalakrishnan 2013).

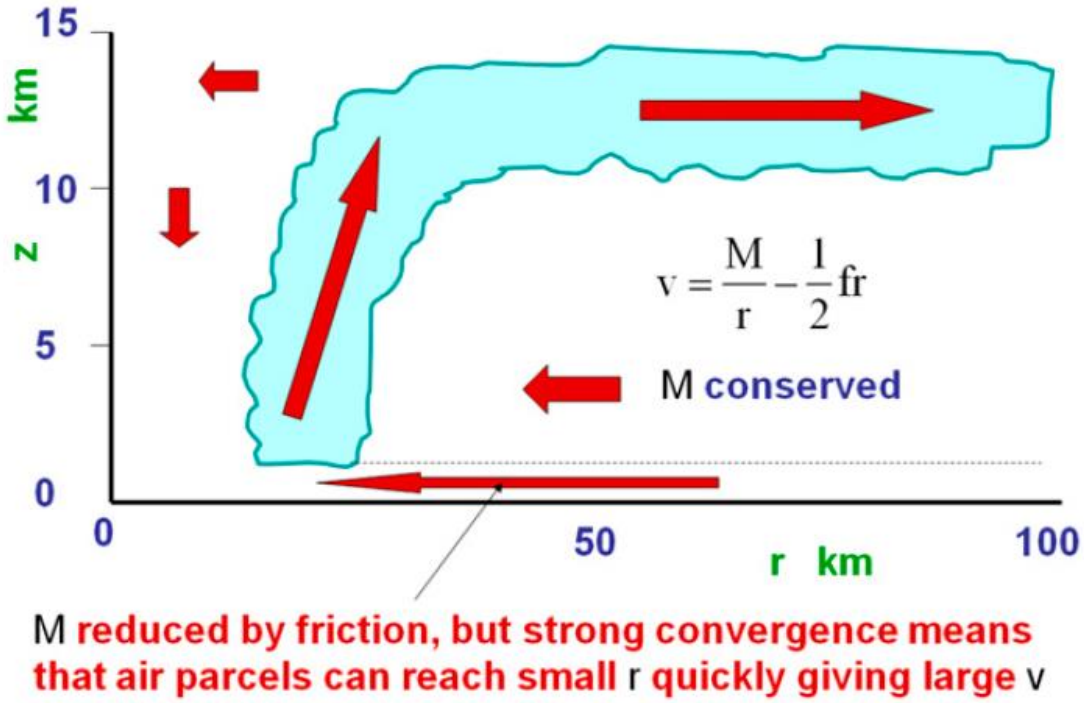

Figure 1.5. Schematic of the axisymmetric view of tropical cyclone intensification in the new paradigm. Above the boundary layer, spinup of the vortex occurs as air parcels are drawn inward by the inner-core convection at levels where absolute angular momentum is approximately conserved. Air parcels spiraling inward in the boundary layer may reach small radii quickly (minimizing the loss of absolute angular momentum during spiral circuits) and acquire a larger tangential wind speed than that above the boundary layer (quoted from Smith and Montgomery 2015).

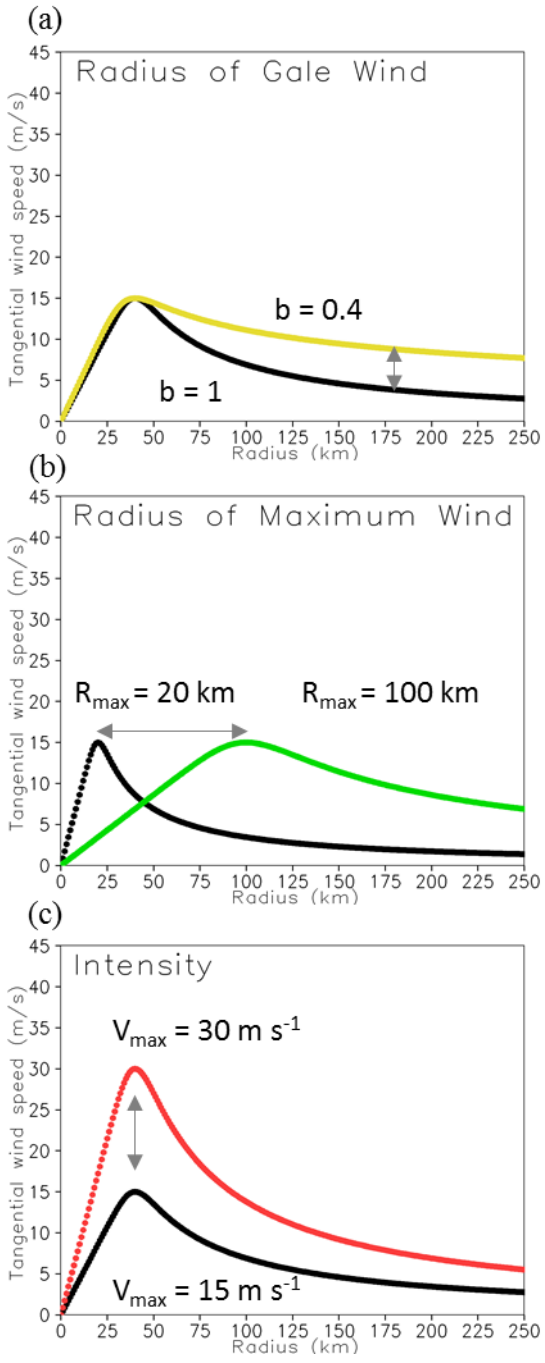

Figure 2.1. Radial profiles of the initial tangential wind speed used in the sensitivity experiments in the simple boundary layer model for (a) storm RGW [b = 1 (black) and b = 0.4 (yellow)], (b) storm RMW [R_m = 20 km (black) and R_m = 100 km (green)], and (c) storm intensity [V_m = 15 m s^{-1} (black) and V_m = 30 m s^{-1} (red)].

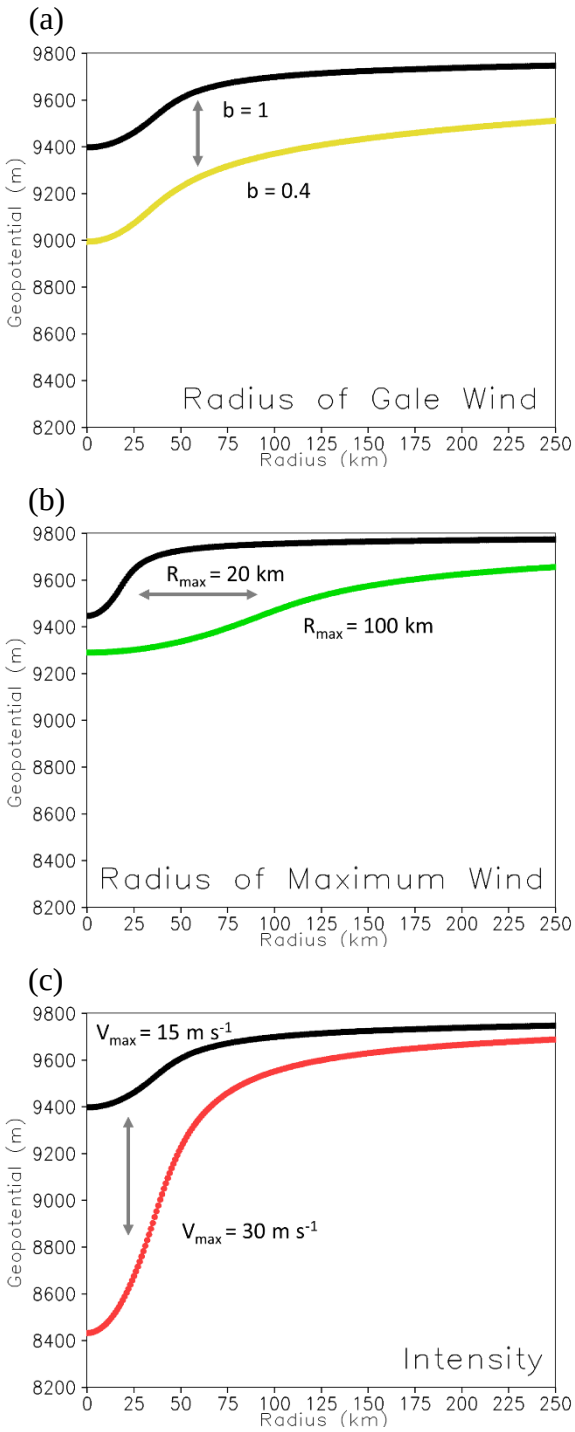

Figure 2.2. As in Figure 2.1, but for geopotential field.

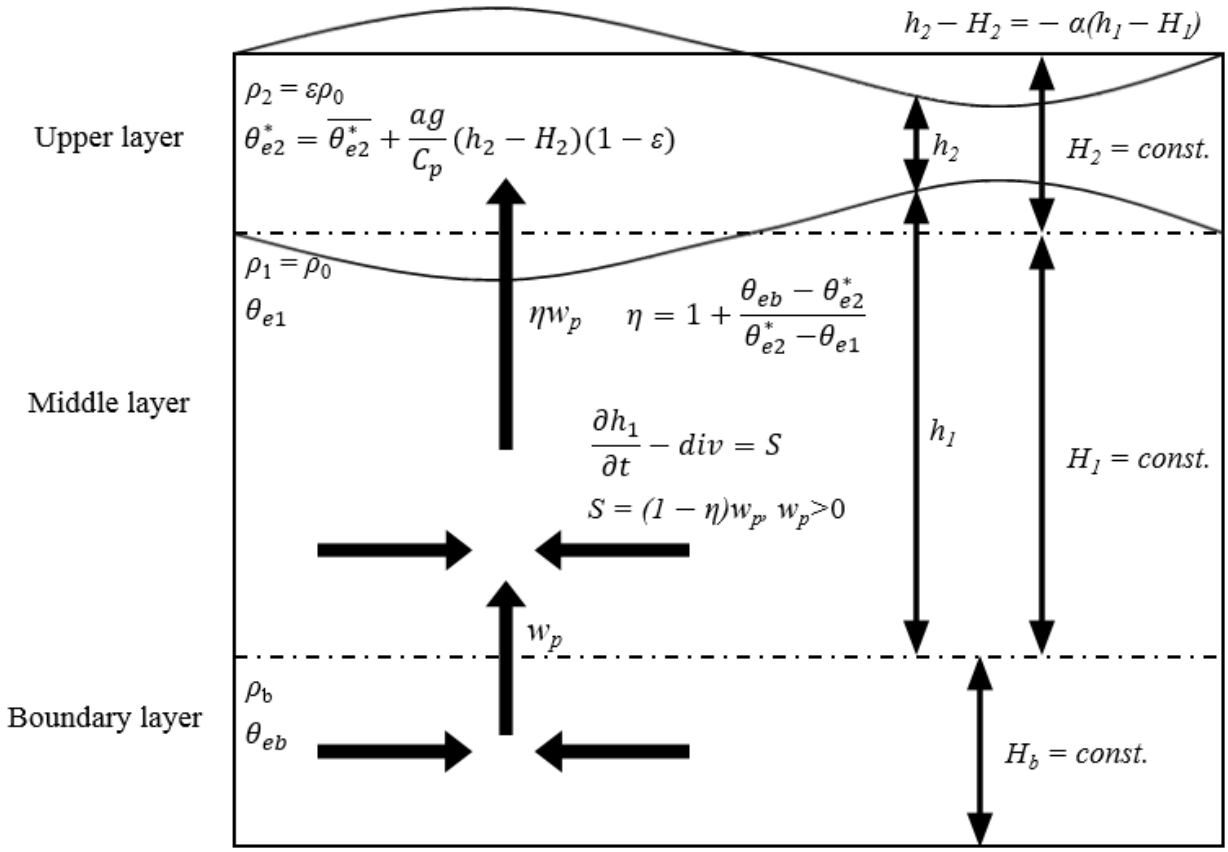

Figure 2.3. Schematic showing the design of the interactive model.

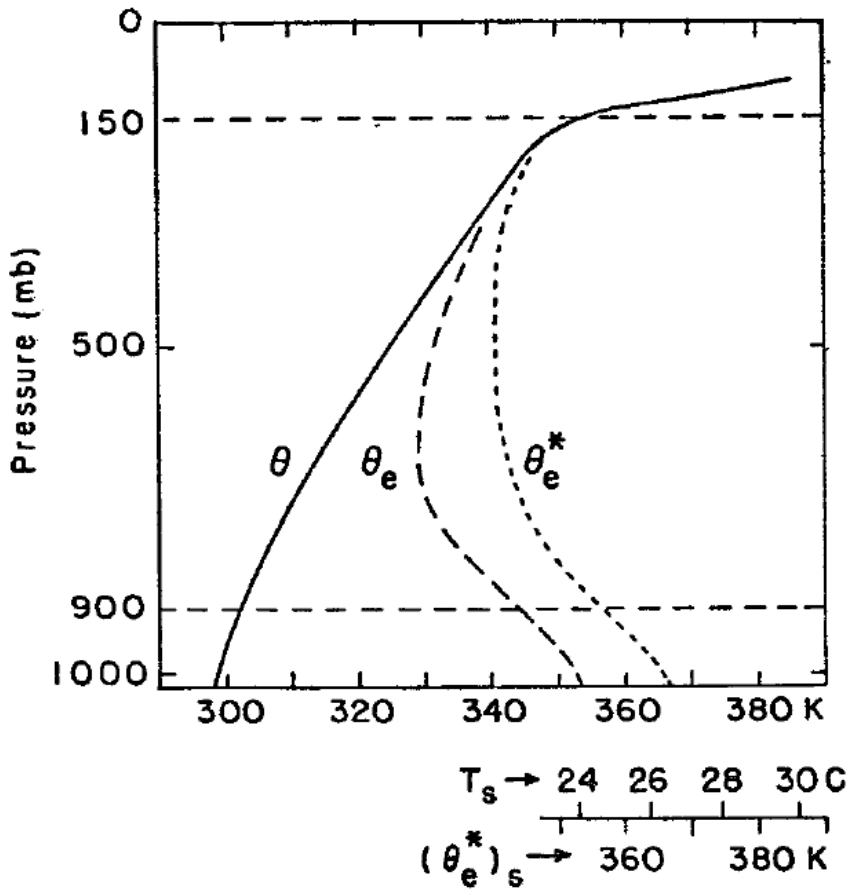

Figure 2.4. Typical stratification of the tropical atmosphere (after Jordan, 1958) where θ is the potential temperature, θ_e the equivalent potential temperature, θ_e^* the equivalent potential temperature of the hypothetically saturated air of the same temperature at each level. Correspondence between the sea surface temperature T_s and the saturated equivalent potential temperature, $(\theta_e^*)_s$ at the sea surface, is shown on the additional scale below the diagram (quoted from Ooyama 1969).

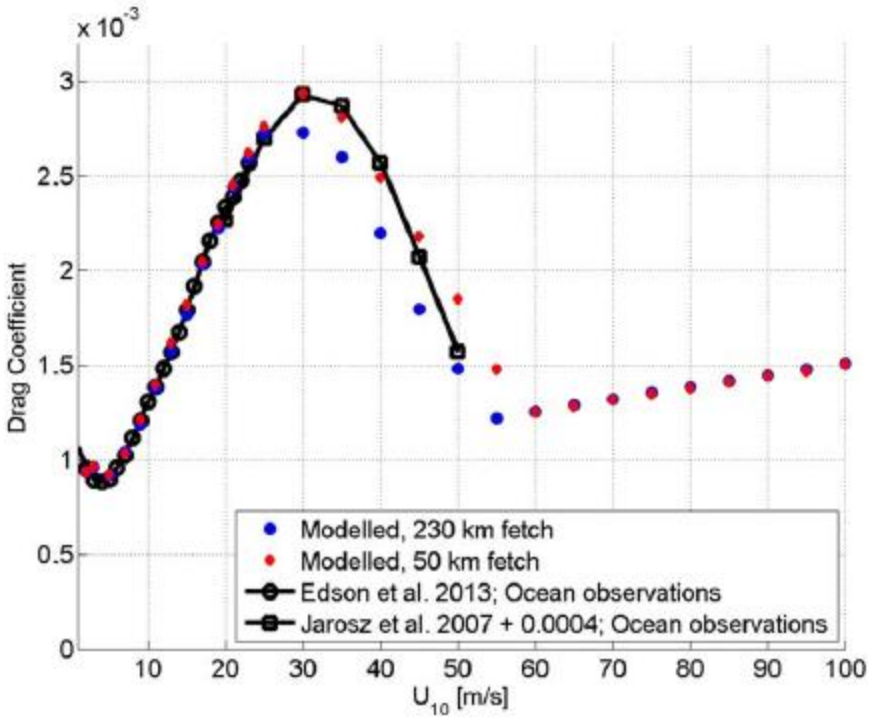

Figure 2.5. Modeled (with Reynolds number dependent sheltering coefficient) and observed surface drag coefficients versus wind speed. Note the fetch dependence of the modeled surface drag coefficient between 30 and 55 m s^{-1} (quoted from Donelan 2018).

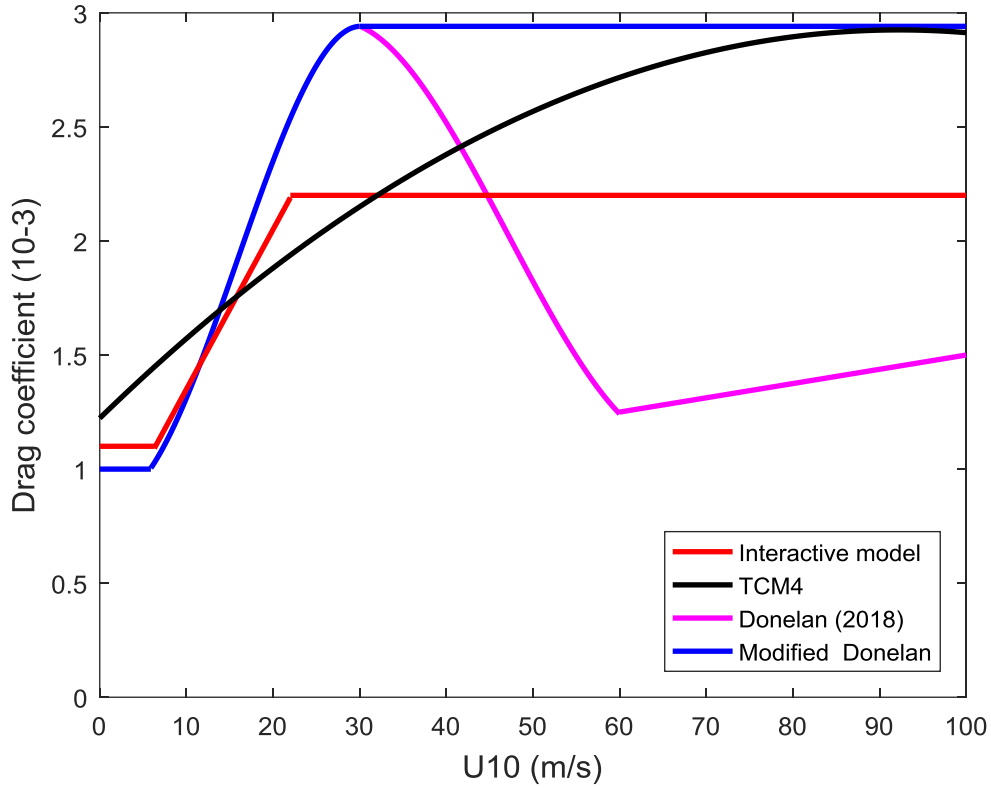

Figure 2.6. The dependence of surface drag coefficients (10^{-3}) on surface wind speed (m s^{-1}) in the interactive model (red), TCM4 (black), Donelan (2018) (magenta), and modified Donelan (blue).

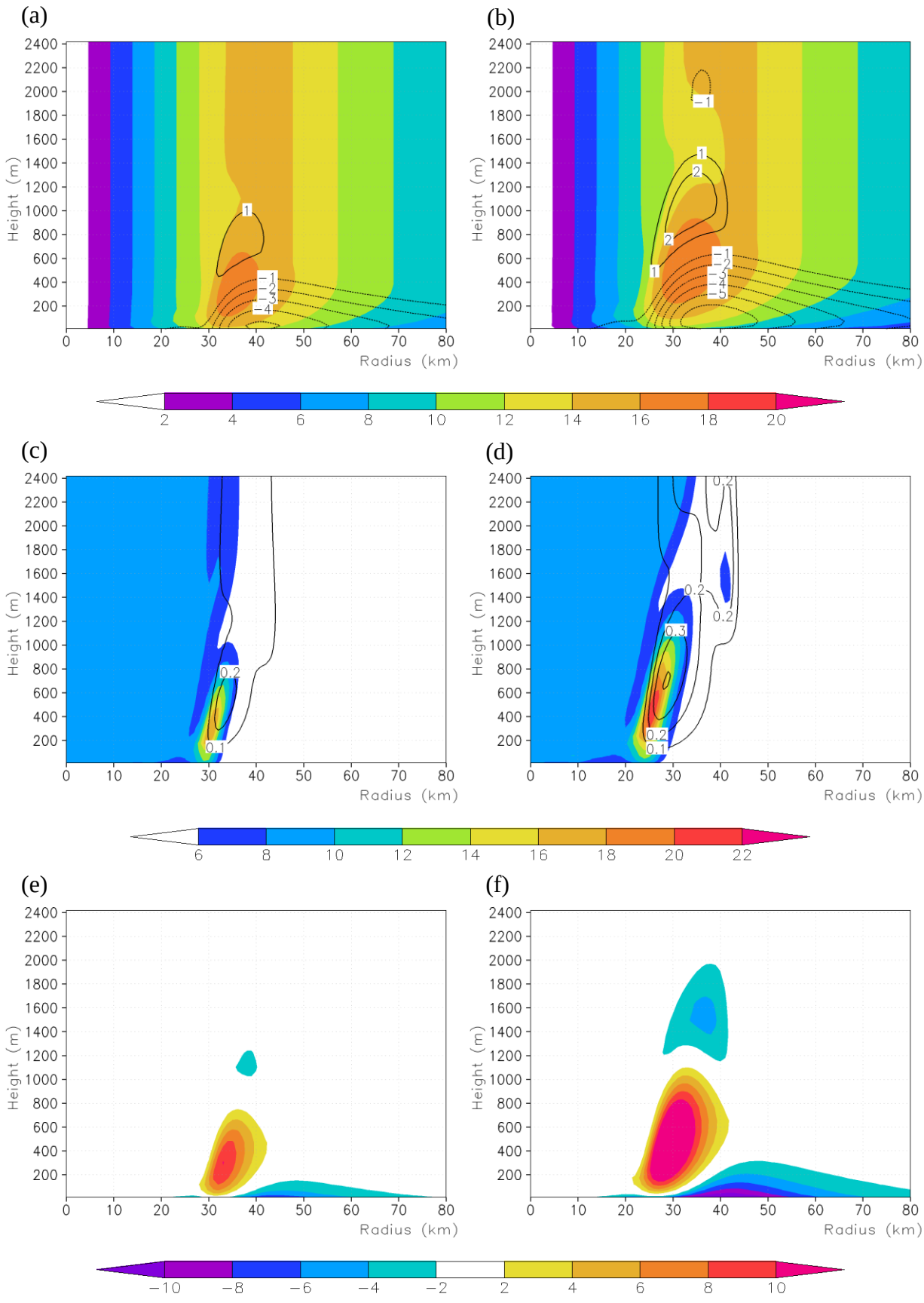
(a)
(b)
(c)
(d)
(e)
(f)
Height (m)
Radius (km)
2400
2200
2000
1800
1600
1400
1200
1000
800
600
400
200
0
10
20
30
40
50
60
70
80
2
4
6
8
10
12
14
16
18
20
22
−10
−8
−6
−4
−2

Figure 3.1. Radius-height cross-sections of tangential wind speed (shaded; m s^{-1}) and radial velocity (contours; m s^{-1}) for (a) 50% C_D and (b) 200% C_D; vertical vorticity (shaded; 10^{-4} s^{-2}) and vertical velocity (contours; m s^{-1}) for (c) 50% C_D and (d) 200% C_D; agradient force (shaded; m s^{-2}) for (e) 50% C_D and (f) 200% C_D in the steady-state response in the simple boundary layer model.

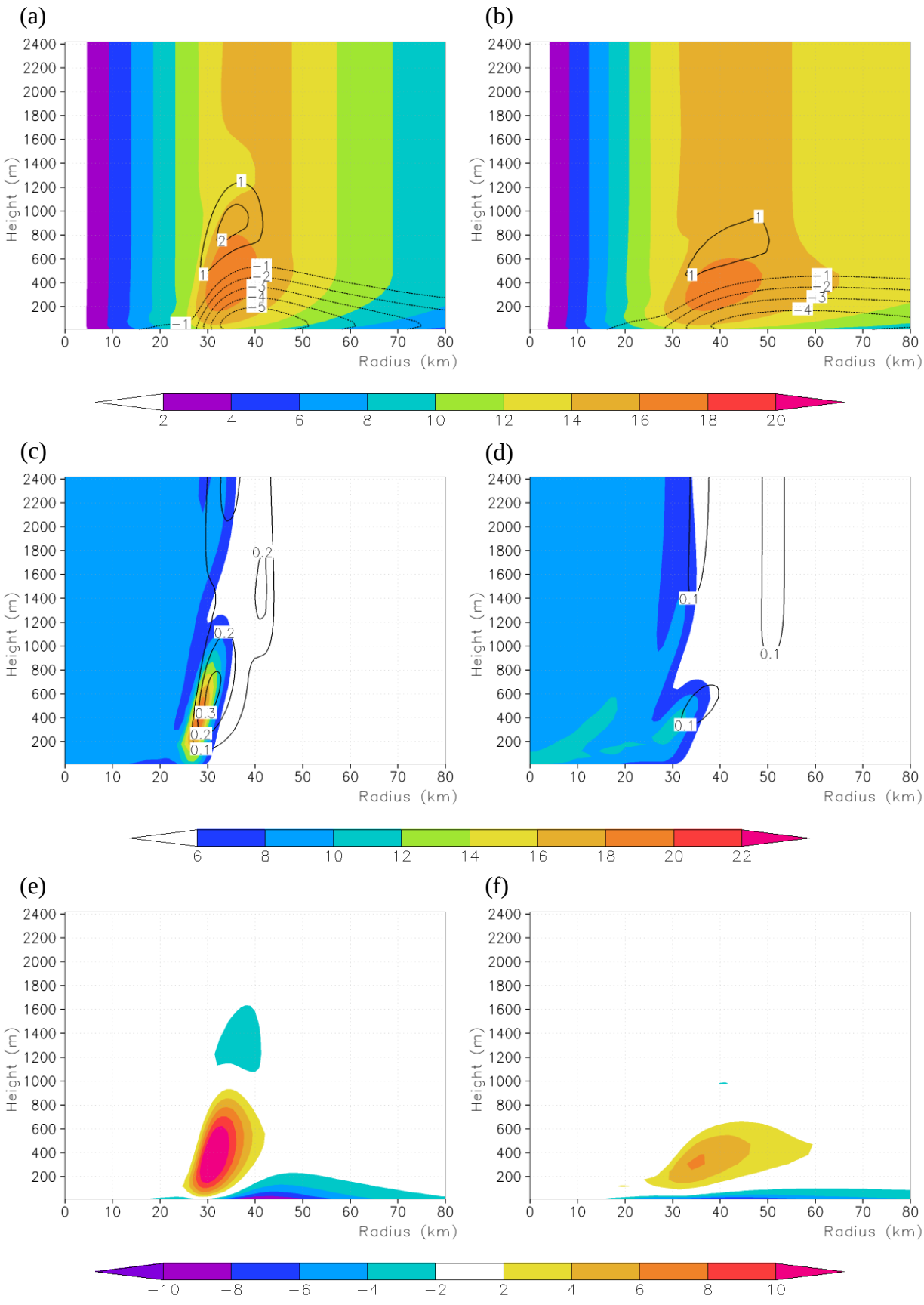
(a)
(b)
(c)
(d)
(e)
(f)
Height (m)
Radius (km)
2400
2200
2000
1800
1600
1400
1200
1000
800
600
400
200
0
10
20
30
40
50
60
70
80
2 4 6 8 10 12 14 16 18 20
6 8 10 12 14 16 18 20 22
−10 −8 −6 −4 −2 2 4 6 8 10

Figure 3.2. As in Figure 3.1, but (a), (c), (e) for the storm with a smaller RGW (b = 1) and (b), (d), (f) for the storm with a larger RGW (b = 0.4).

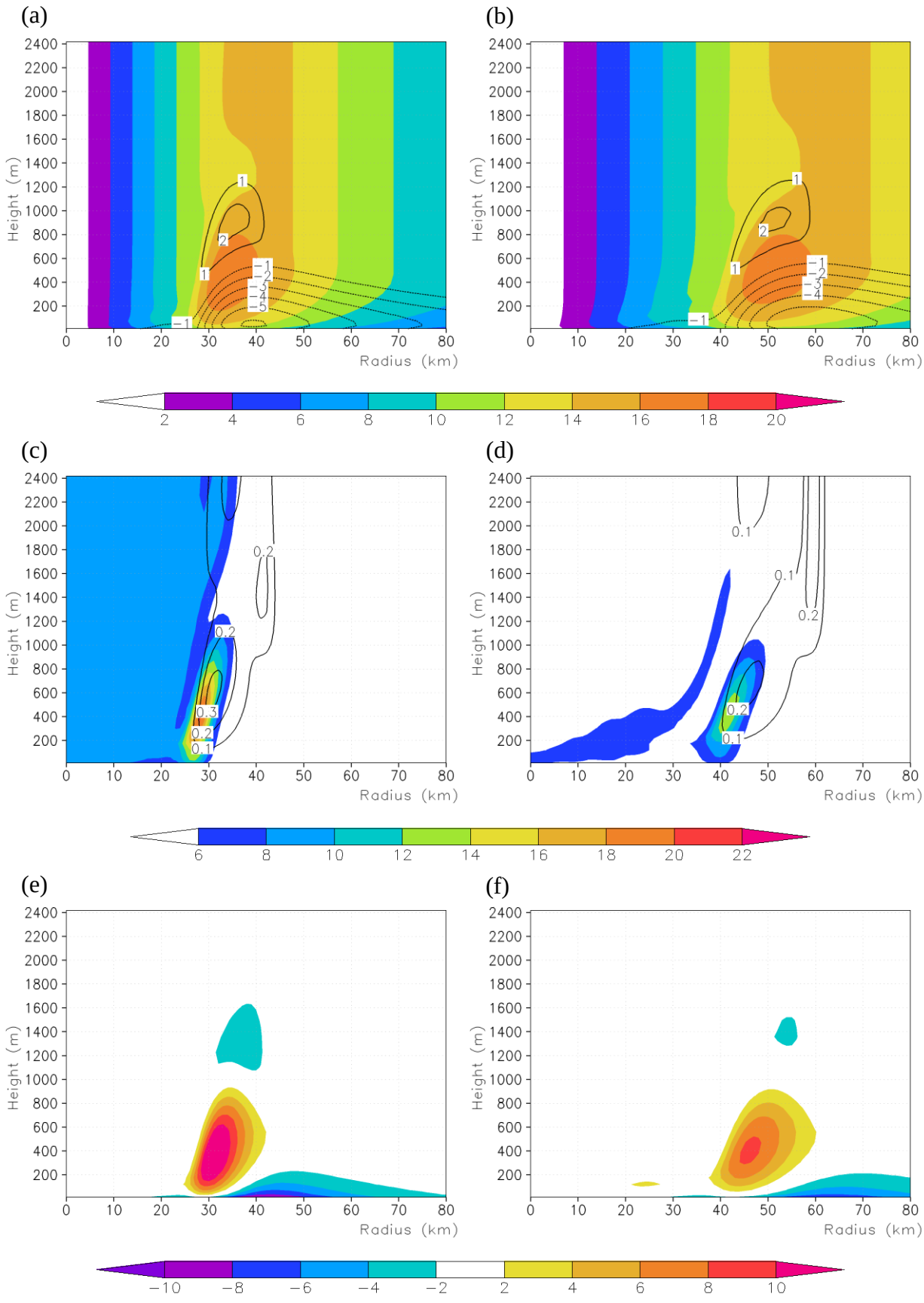
(a)
(b)
(c)
(d)
(e)
(f)
Height (m)
Radius (km)
2400
2200
2000
1800
1600
1400
1200
1000
800
600
400
200
0
10
20
30
40
50
60
70
80
1
2
−1
−2
−3
−4
−5
0.1
0.2
0.3
2
4
6
8
10
12
14
16
18
20
22
−10
−8
−6
−4
−2

Figure 3.3. As in Figure 3.1, but (a), (c), (e) for the storm with a smaller RMW (R_m = 40 km) and (b), (d), (f) for the storm with a larger RMW (R_m = 60 km).

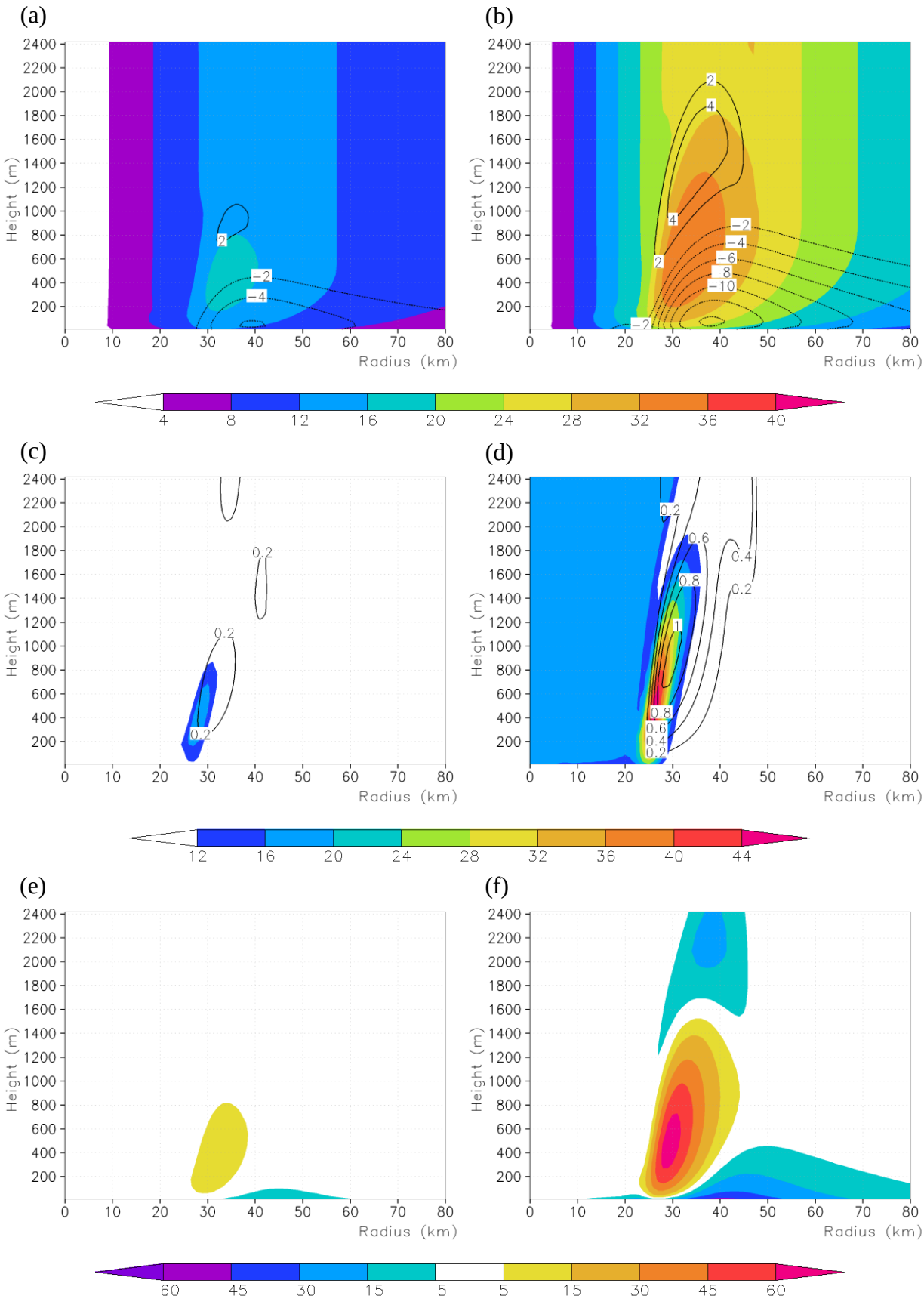
(a)
(b)
(c)
(d)
(e)
(f)
Height (m)
Radius (km)
4 8 12 16 20 24 28 32 36 40
12 16 20 24 28 32 36 40 44
−60 −45 −30 −15 −5 5 15 30 45 60

Figure 3.4. As in Figure 3.1, but (a), (c), (e) for the storm with a lower intensity (V_m = 15 m s^{-1}) and (b), (d), (f) for the storm with a higher intensity (V_m = 30 m s^{-1}).

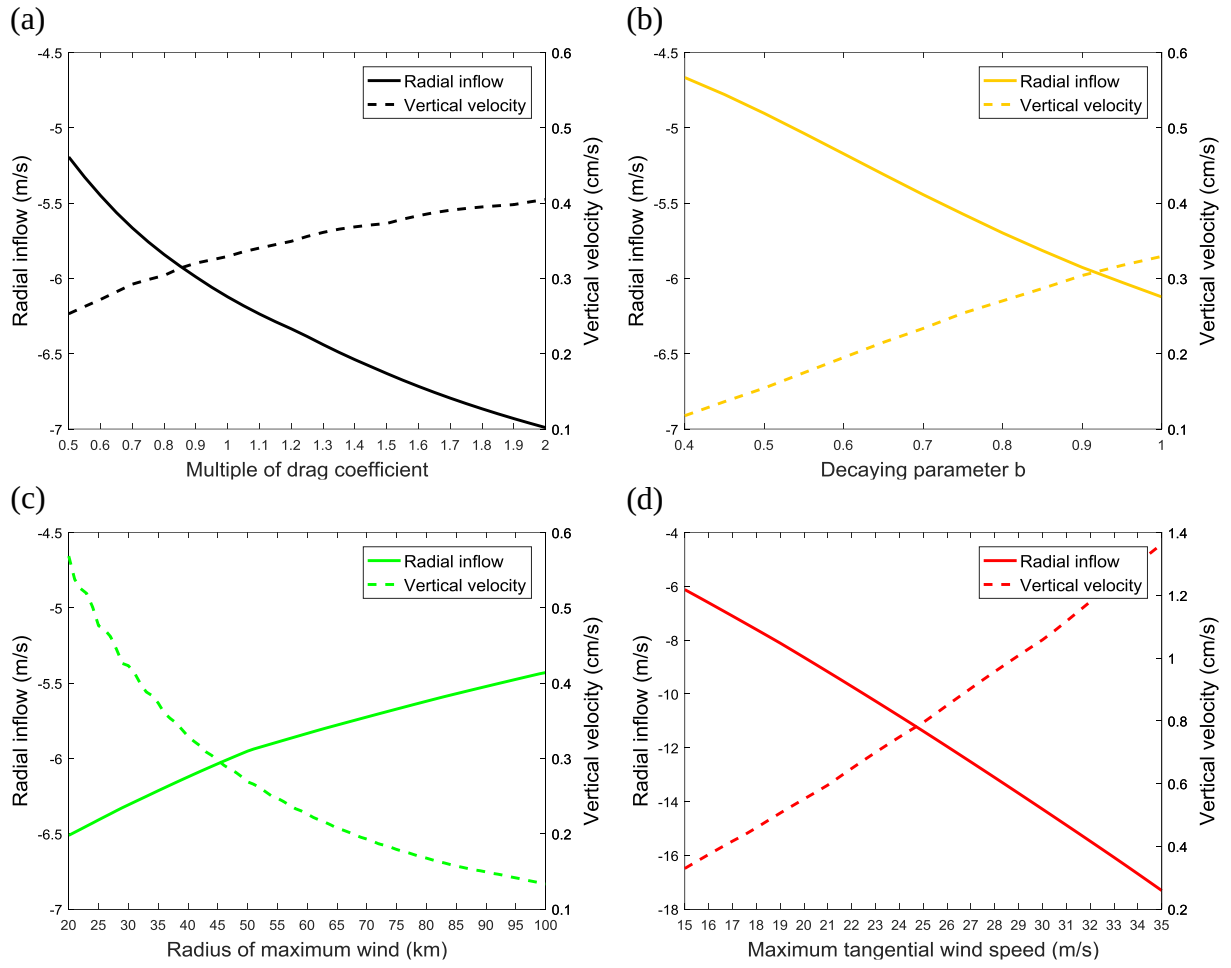

Figure 3.5. Dependence of the maximum radial wind speed (solid, left ordinate, m s^{-1}) and the maximum vertical velocity (dashed, right ordinate, m s^{-1}) near the top of the boundary layer (at the 866-m height) on (a) surface drag coefficient, (b) the initial RGW inferred from the decaying parameter *b*, (c) the initial RMW (km), and (d) the initial storm intensity (m s^{-1}) in the steady-state response in the simple boundary layer model.

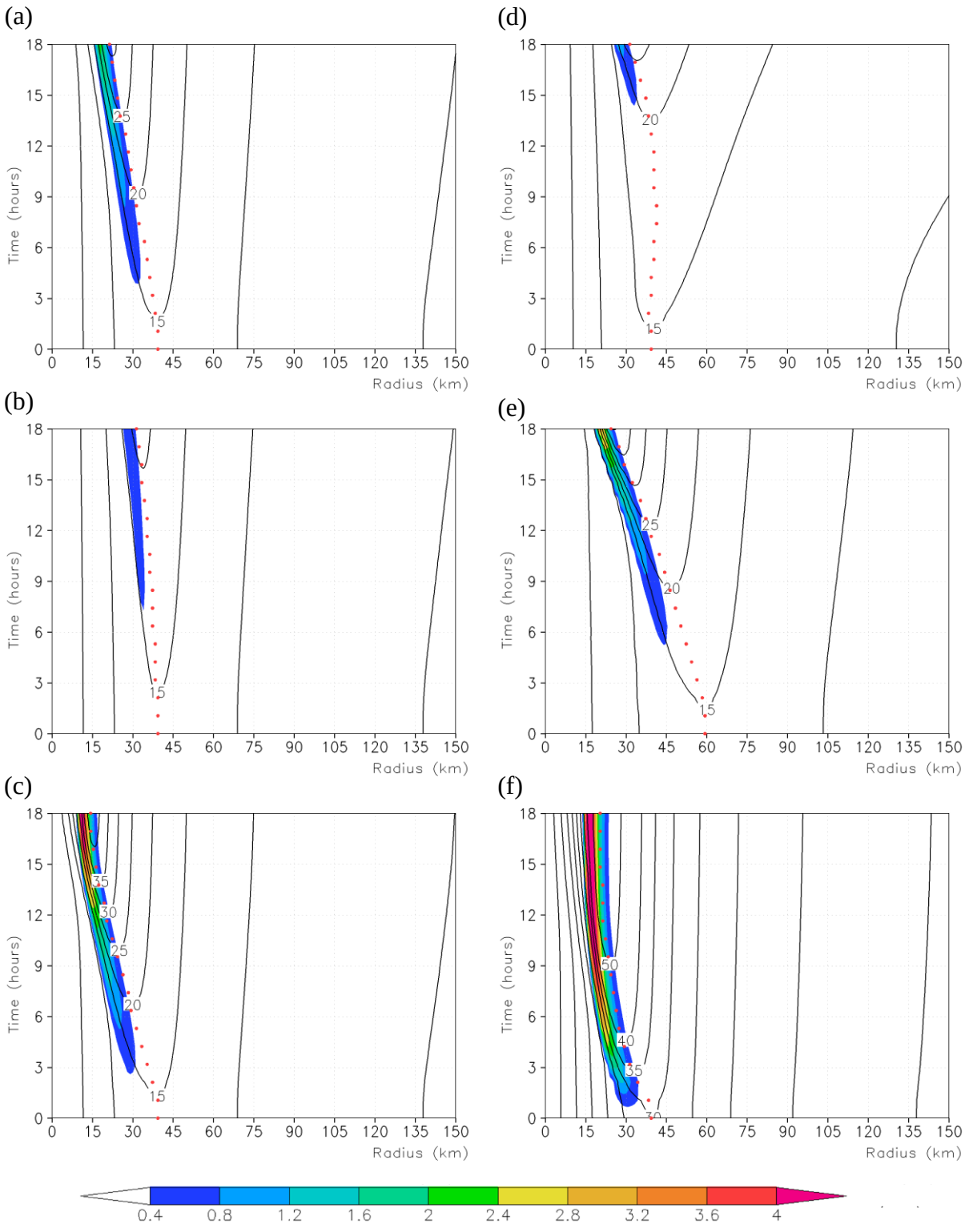

Figure 3.6. Radius-time cross-sections of vertical velocity at the top of the boundary layer (944 m) (m s^{-1}, shaded) and gradient wind speed at the middle layer (m s^{-1}, contours) in the

experiment with (a) 100% C_D and initial b = 1.0, the initial RMW = 40 km, and V_m = 15 m s^{-1}, (b) as in (a) but with 50% C_D, (c) as in (a) but with 200% C_D, (d) as in (a) but for initial b = 0.4, (e) as in (a) but with an initial RMW of 60 km, and (f) as in (a) but with an initially V_m = 30 m s^{-1}. The red dots represent the radius of maximum gradient wind in the middle layer.

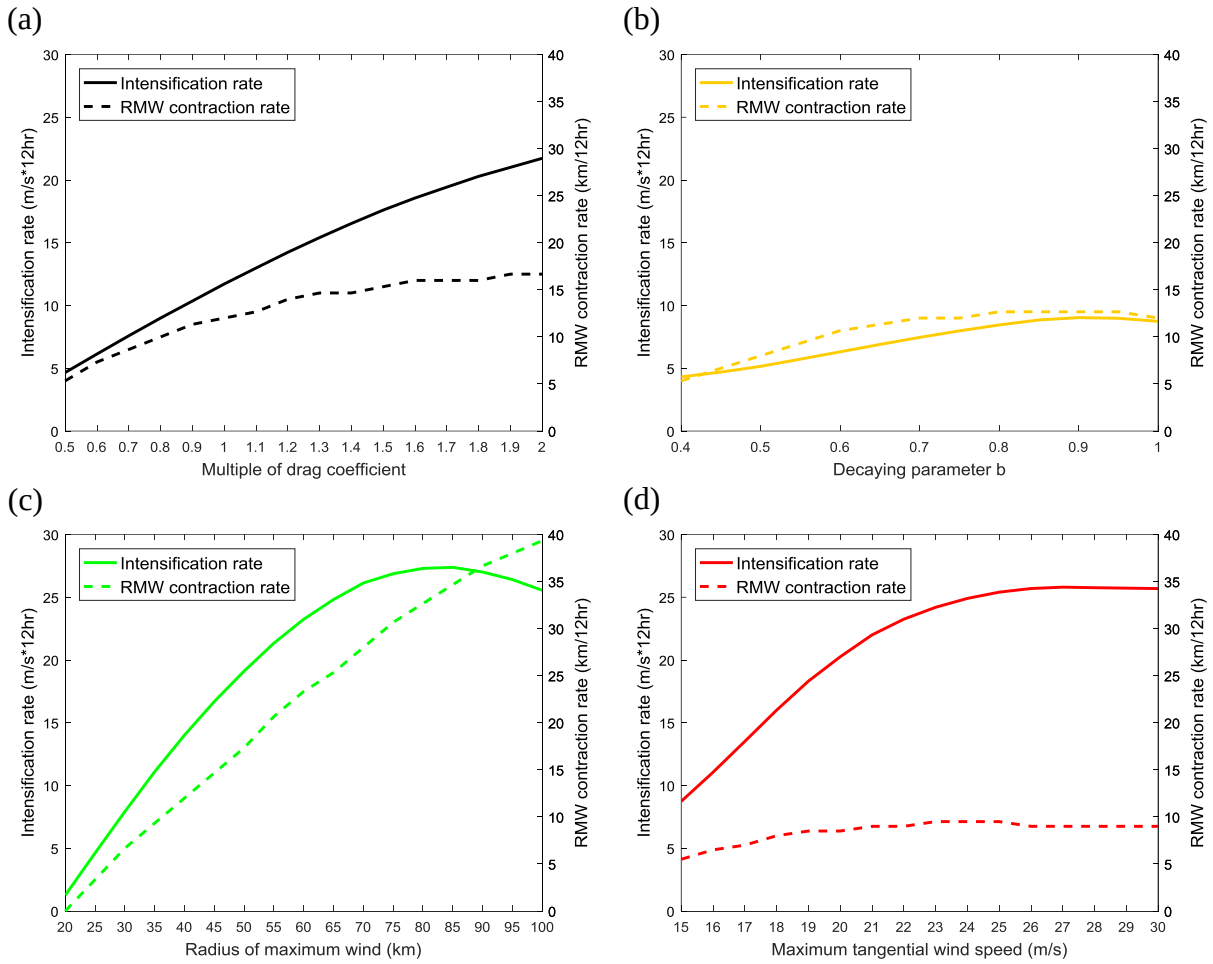

Figure 3.7. Dependence of the averaged intensification rates [solid, left ordinate, m s^{-1} (12 hr)$^{-1}$] and the contraction rates of the RMW [dashed, right ordinate, km (12 hr)$^{-1}$] on (a) surface drag coefficient, (b) the initial RGW inferred from the decaying parameter *b*, (c) the initial RMW (km), and (d) the initial storm intensity (m s^{-1}), all are averaged between 0 h and 18 h of integration in the interactive model.

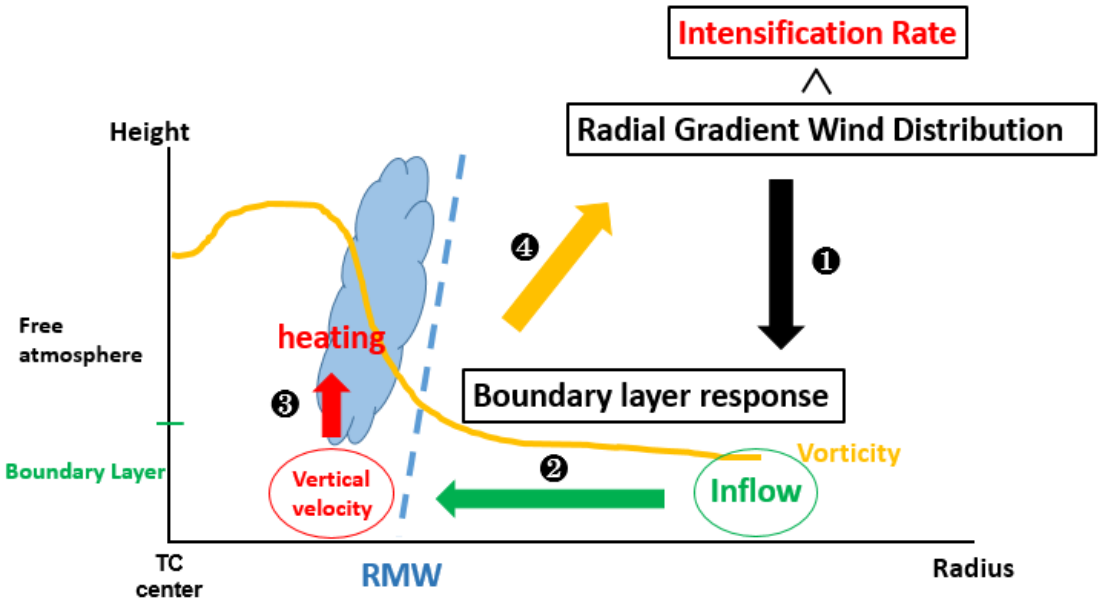

Figure 3.8. Schematic diagram summarizing the role of boundary layer dynamics in TC intensification. The direction of the arrow represents the cause and effect. The thick yellow curve denotes the radial profile of axisymmetric vertical vorticity. The blue dashed line denotes the RMW. The blue scalloped area denotes the predominant radial location of eyewall convection. There are four sequential interactive processes: (1) the boundary layer inflow in response to the given radial distribution of gradient wind above the boundary layer in the presence of surface friction; (2) the boundary layer inflow, as a function of surface friction and radial distribution of gradient wind above the boundary layer, determines the strength and radial location of the boundary layer mass convergence and thus the eyewall updraft; (3) the upward mass-flux at the top of the boundary layer determines both the strength and radial location of diabatic heating in the eyewall; and (4) the contraction of the RMW and intensification of the TC vortex in response to diabatic heating in the eyewall, which is in turn a response to gradient wind above the boundary layer through the boundary layer dynamics.

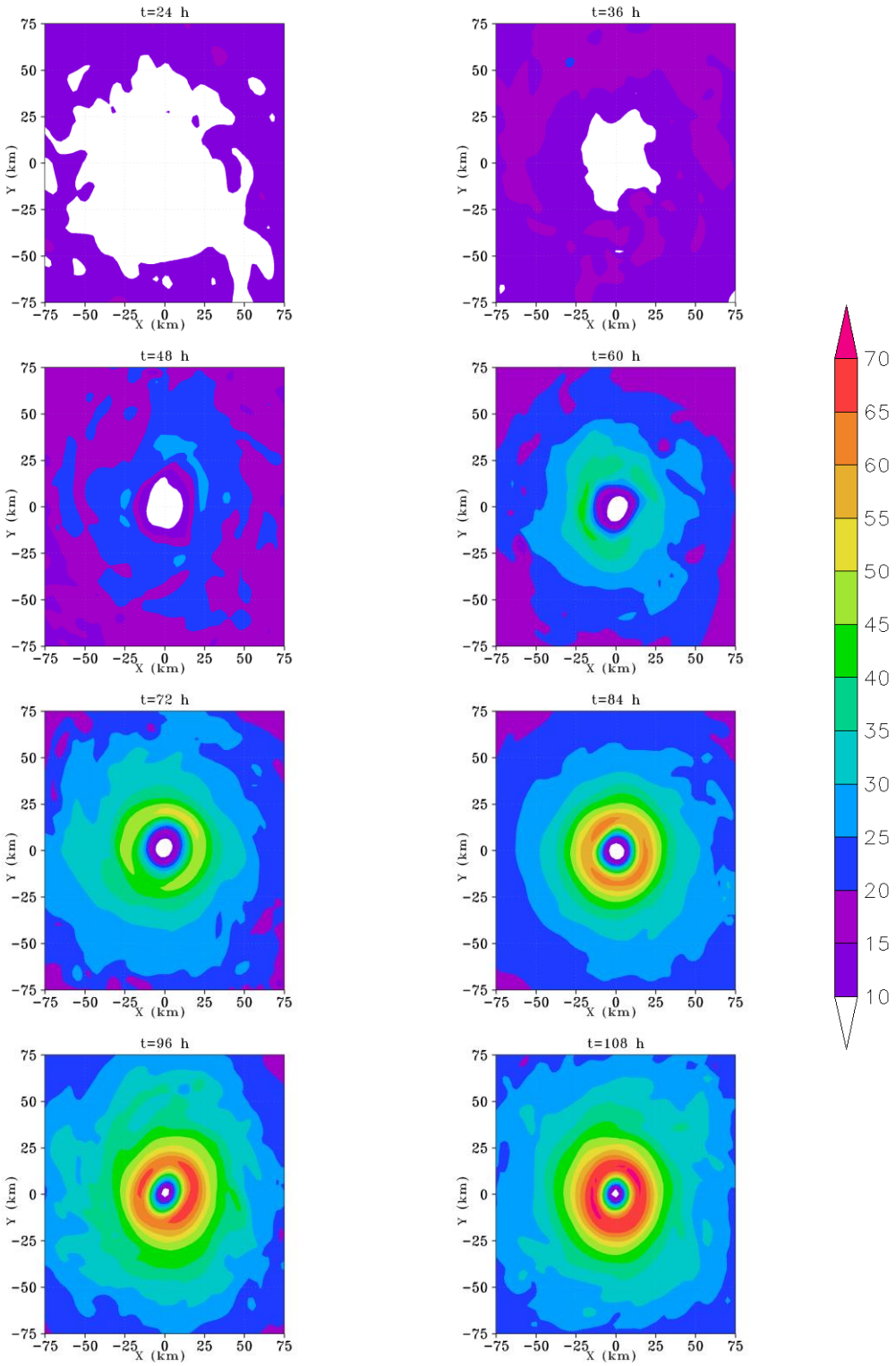

Figure 4.1. The total wind speed (m s^{-1}) at the 2320-m height at every 12-h interval from 24 h to 108 h in CTRL.

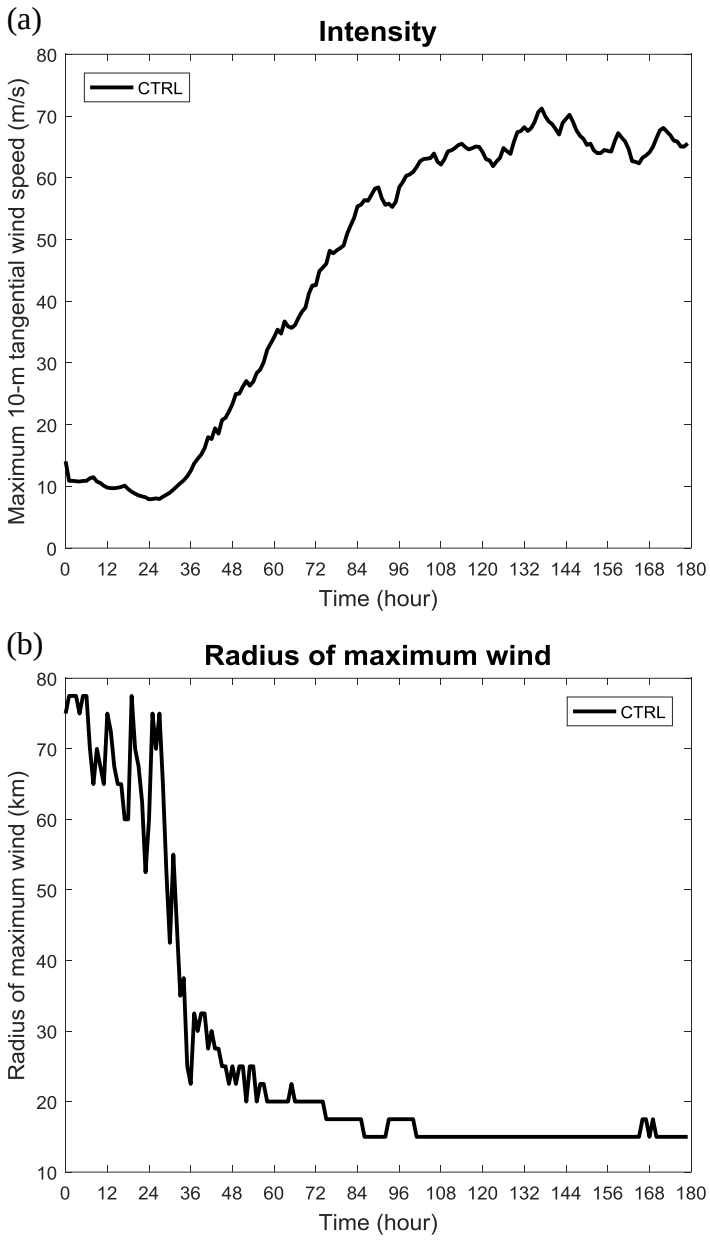

Figure 4.2. Time evolution of (a) the maximum 10-m height tangential wind speed (m s^{-1}) and (b) the radius of maximum wind (km) in CTRL.

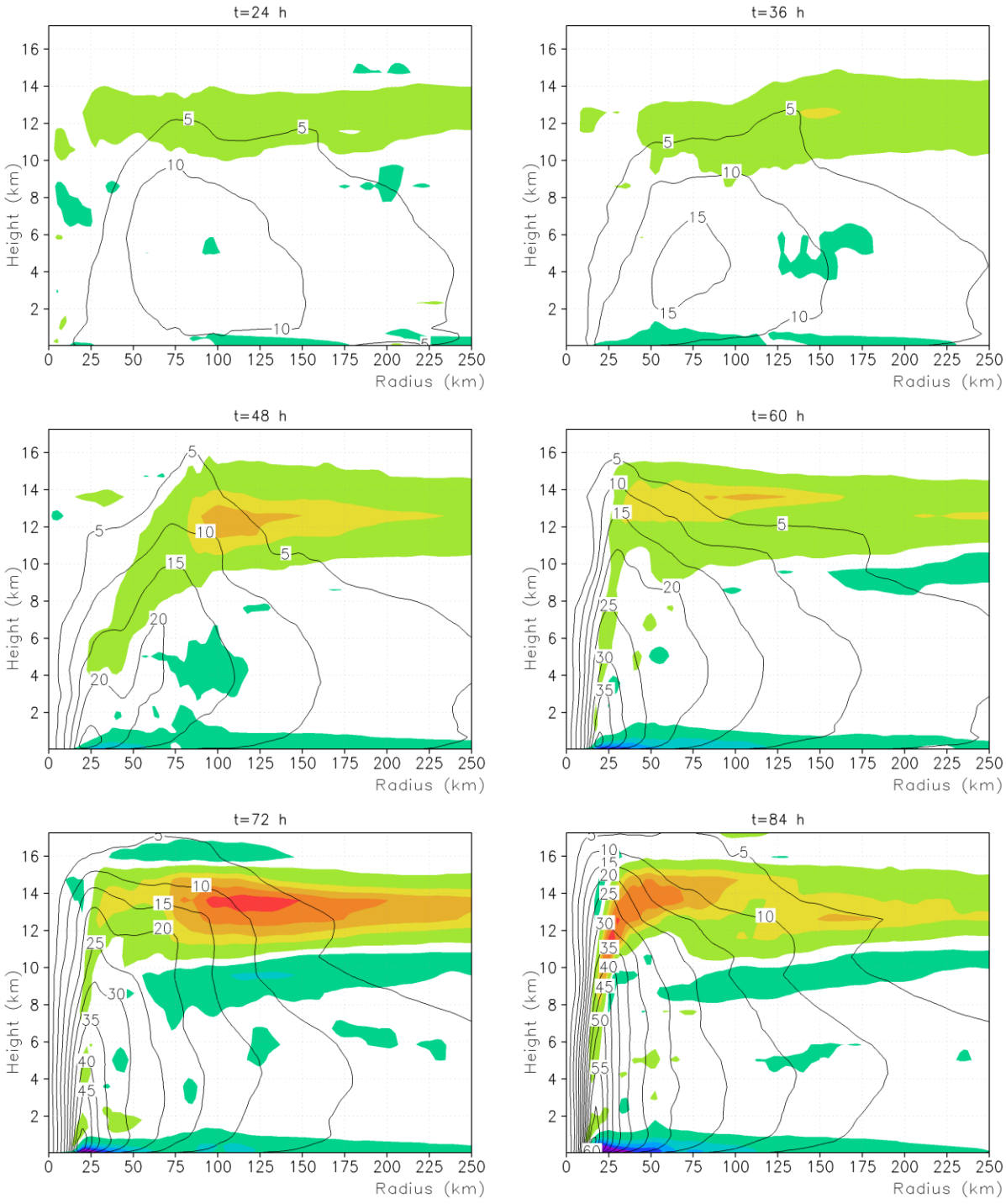
t=24 h
t=36 h
t=48 h
t=60 h
t=72 h
t=84 h
Height (km)
Radius (km)

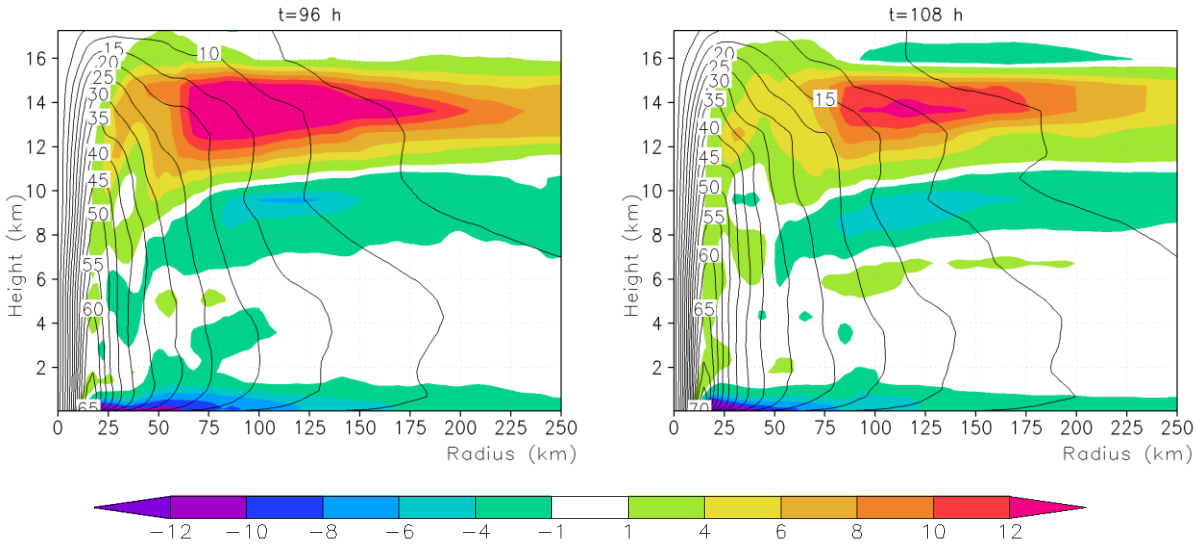

Figure 4.3. Radius-height cross-sections of the azimuthal mean radial wind speed (shaded; m s^{-1}) and tangential wind speed (contours; m s^{-1}) at every 12-h interval from 24 h to 108 h in CTRL.

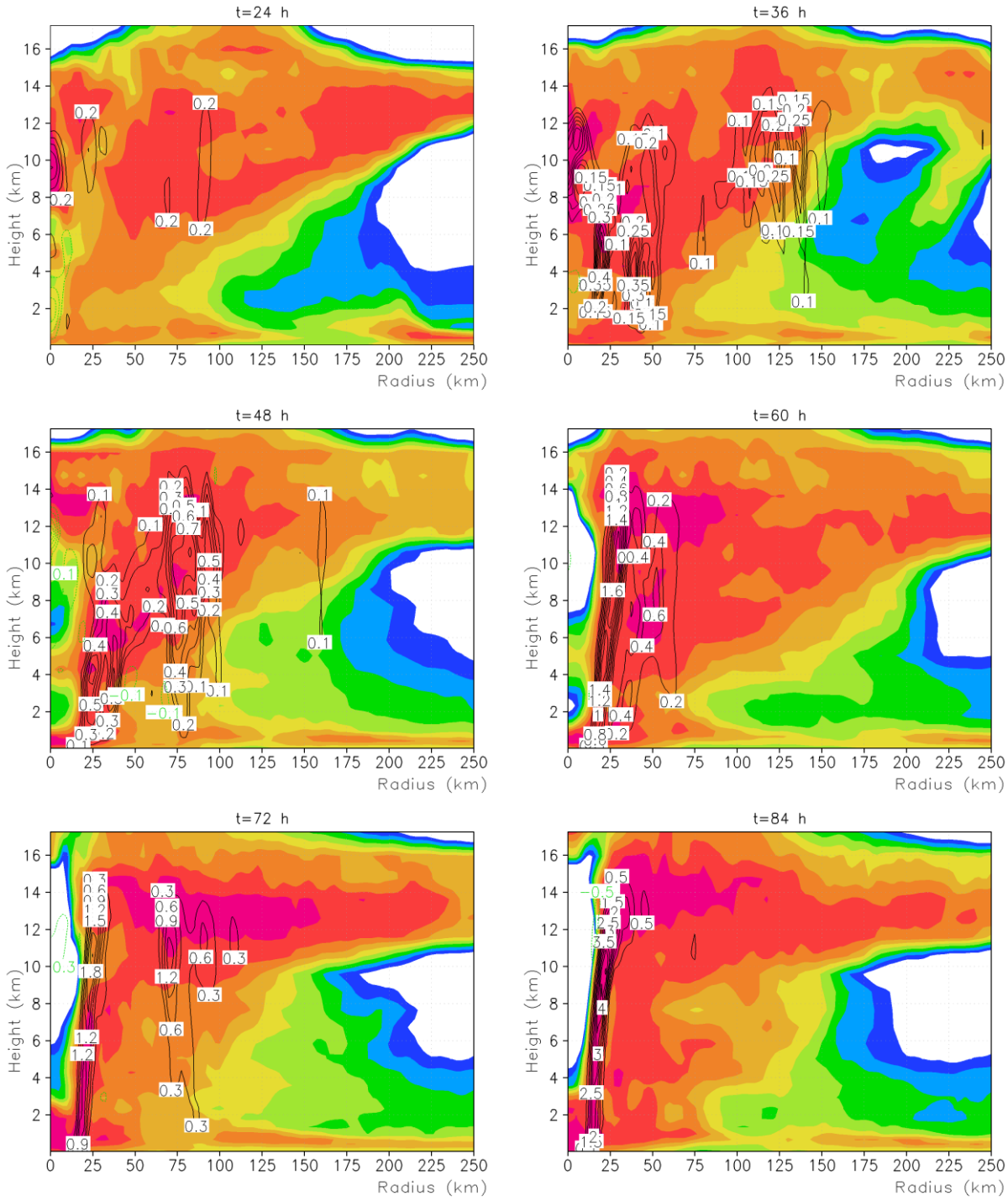
t=24 h
t=36 h
t=48 h
t=60 h
t=72 h
t=84 h
Height (km)
Radius (km)

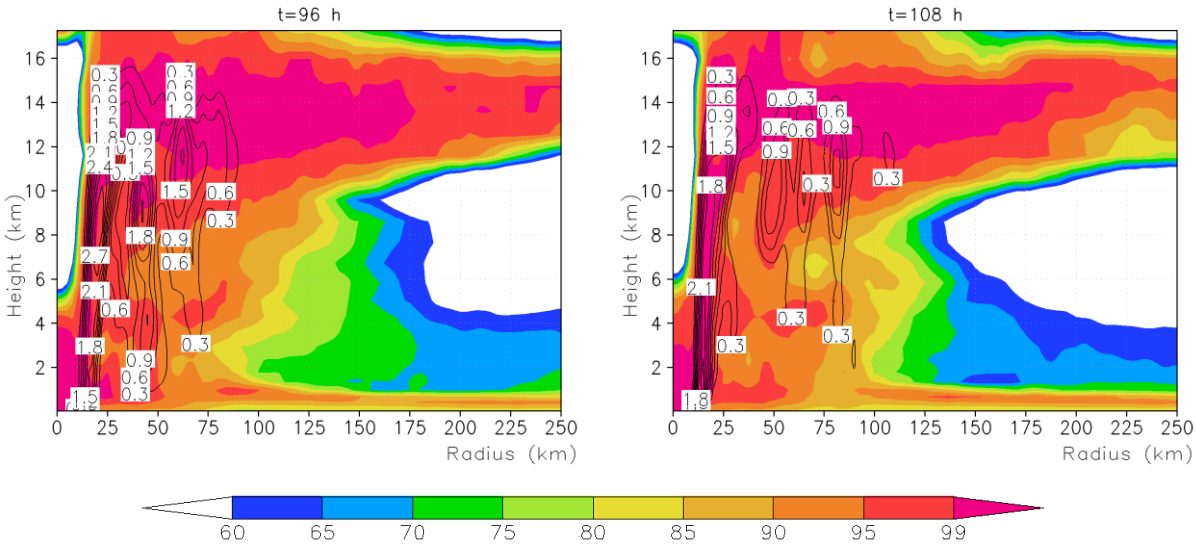

Figure 4.4. As in Figure 4.3, but for the azimuthal mean relative humidity (shaded; %) and vertical velocity (contours; m s^{-1}).

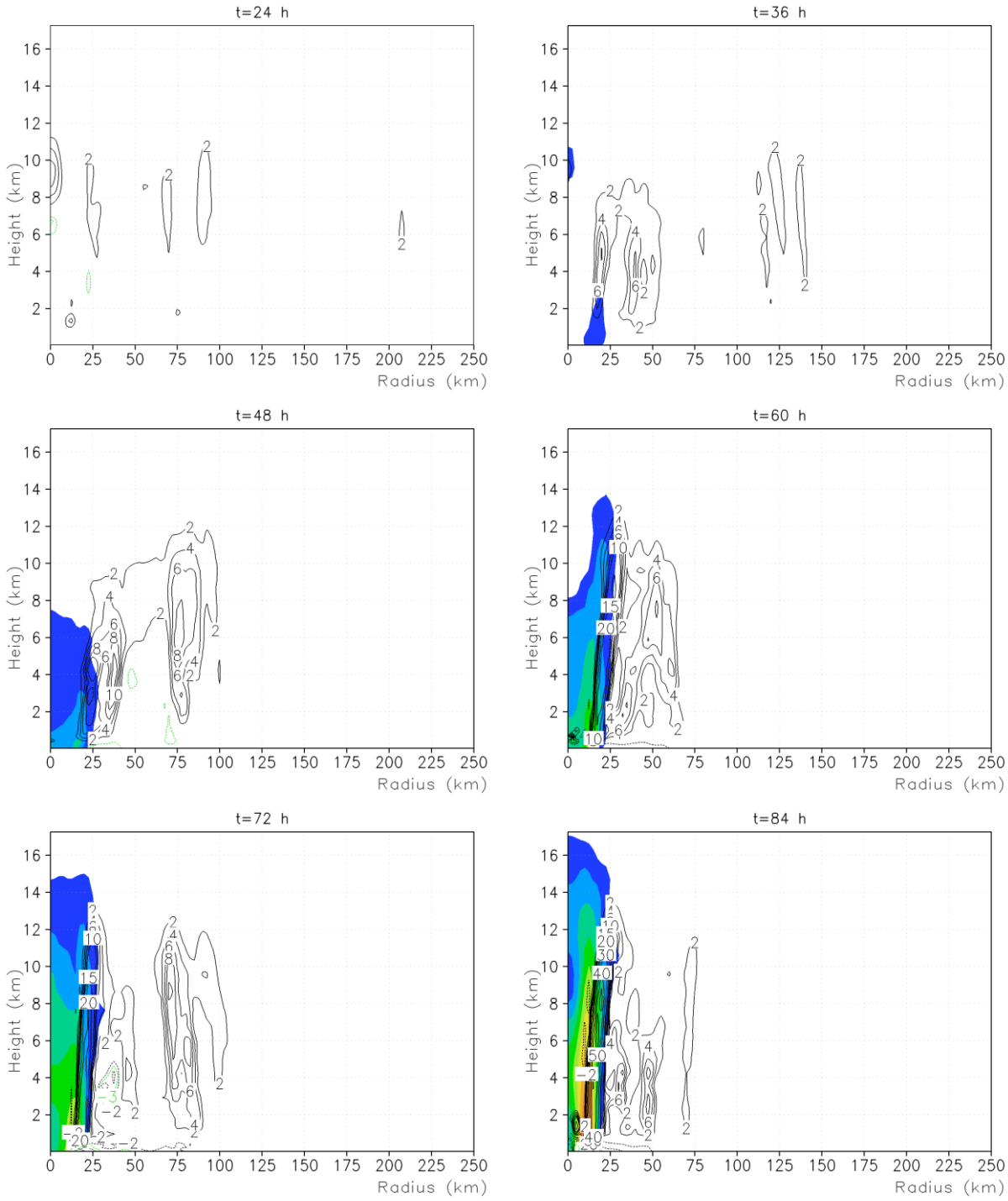
t=24 h
t=36 h
t=48 h
t=60 h
t=72 h
t=84 h
Height (km)
Radius (km)

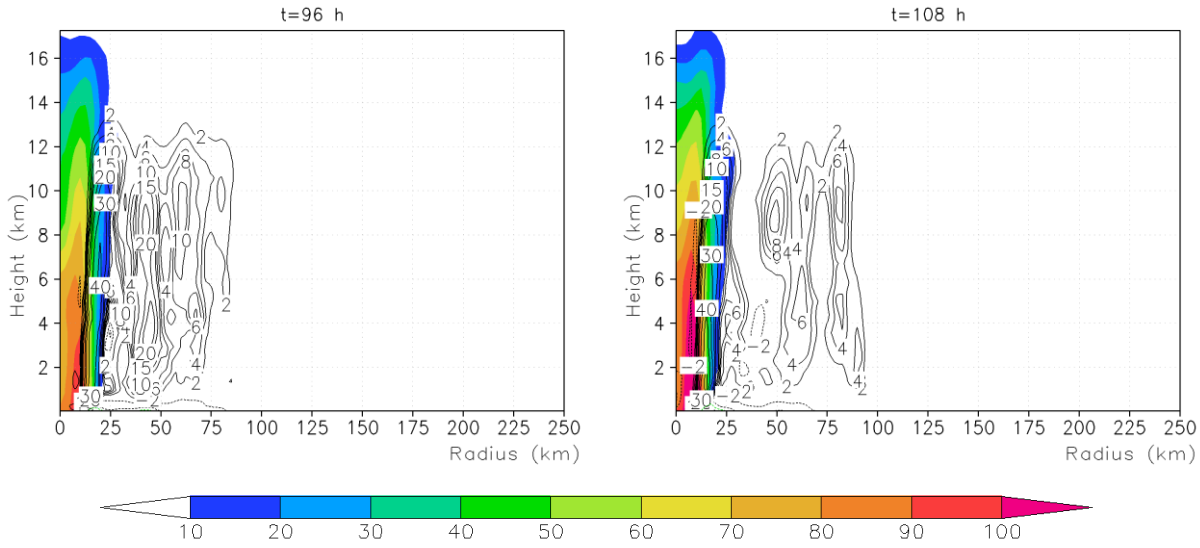

Figure 4.5. As in Figure 4.3, but for the azimuthal mean vertical vorticity (shaded; 10^{-4} s^{-1}) and condensational heating rate (contours; K hr^{-1}).

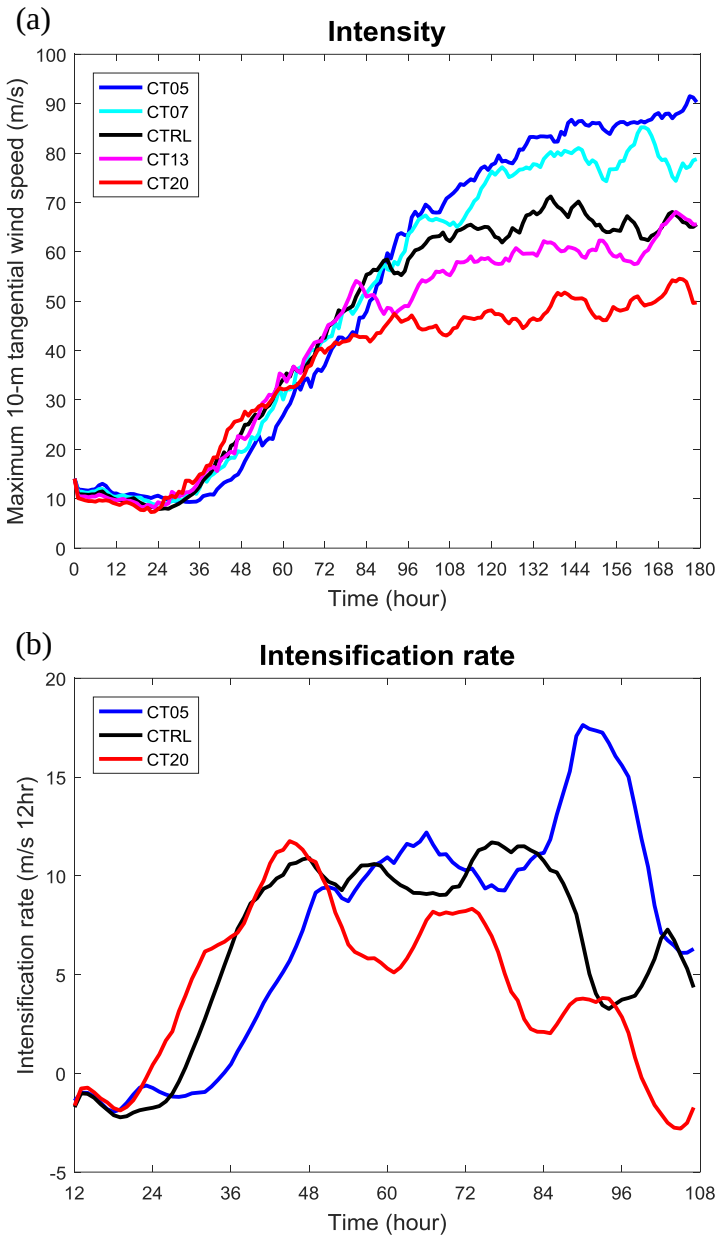

Figure 4.6. Time evolution of (a) the maximum 10-m height tangential wind speed (m s^{-1}) in the control experiment (CTRL, black), 50% C_D experiment (CT05, blue), 70% C_D experiment (CT07, cyan), 130% C_D experiment (CT13, magenta), and 200% C_D experiment (CT20, red). (b) the 12-h intensification rates (m s^{-1} 12 hr^{-1}) with 5-h running mean in CT05 (blue), CTRL (black), and CT20 (red).

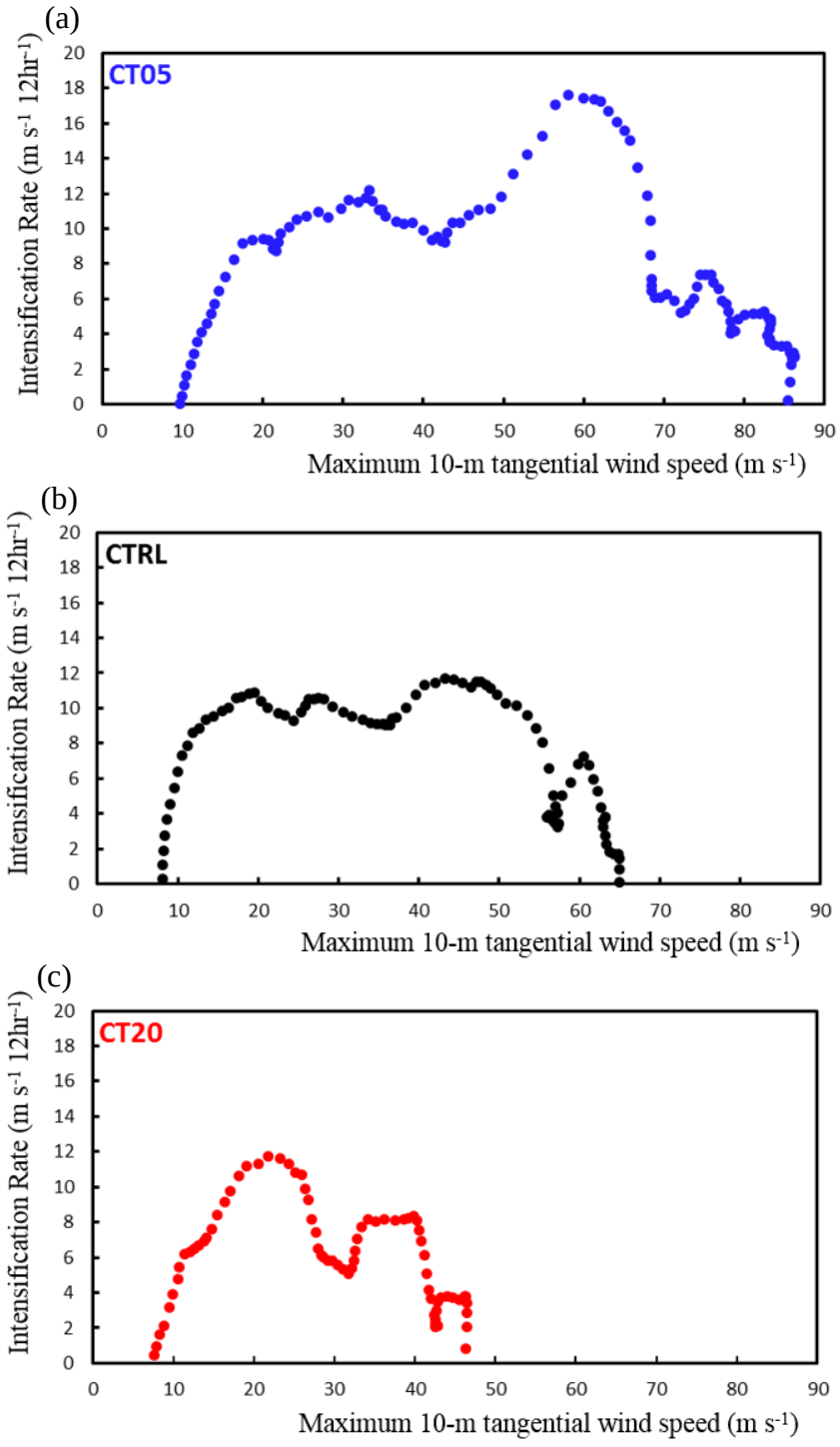

Figure 4.7. Scatter diagrams of the subsequent 12-h intensification rate (m s^{-1} 12 hr^{-1}) against instantaneous maximum tangential wind speed (m s^{-1}) during the intensification stage with 5-h running mean in CT05, CTRL, and CT20.

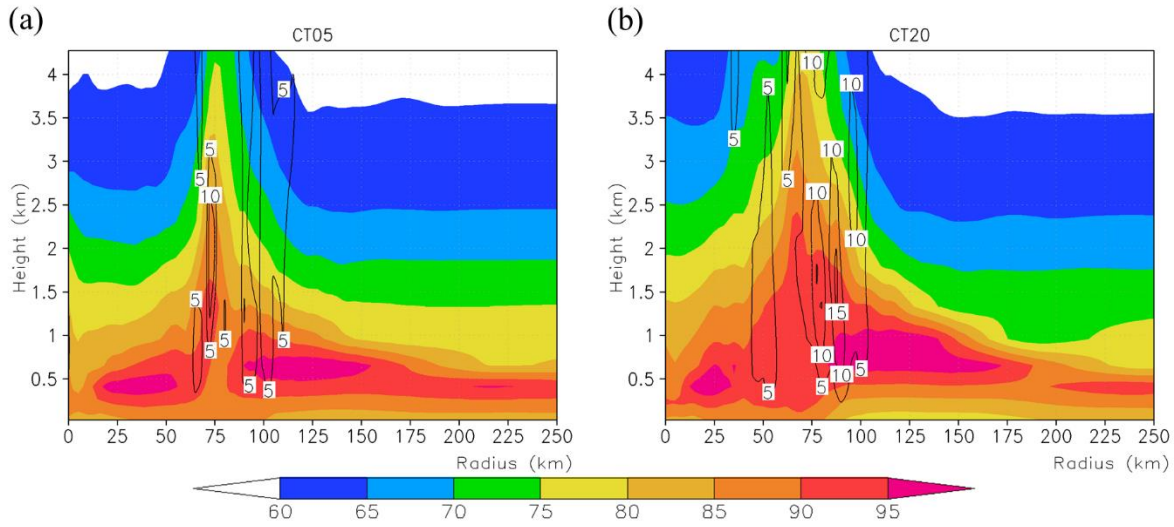

Figure 4.8. Radius-height cross-sections of the azimuthal mean relative humidity (shaded, %) and vertical velocity (contours, cm s^{-1}), both averaged in the first 6-h simulation in (a) CT05 and (b) CT20 respectively.

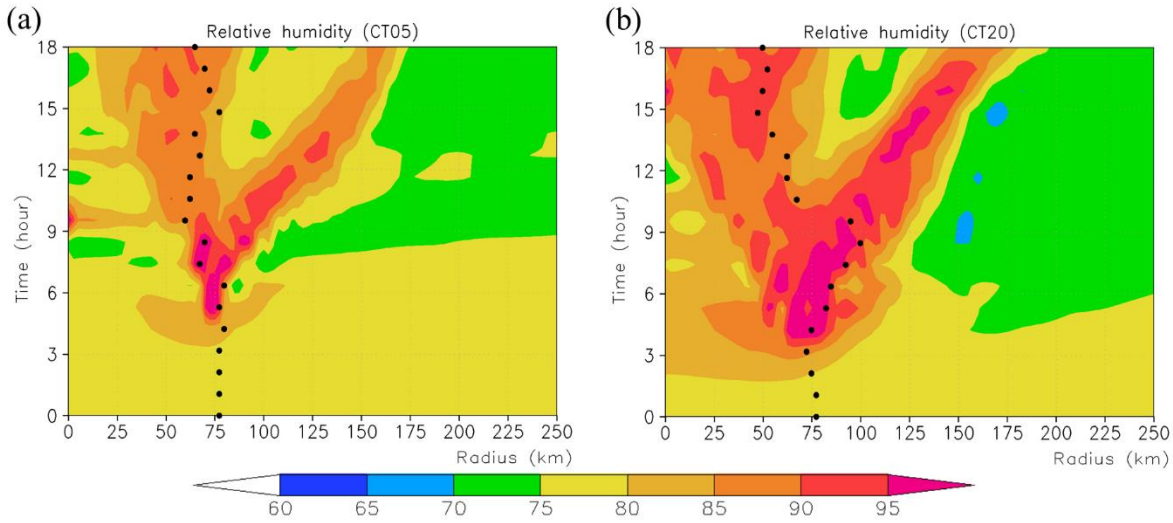

Figure 4.9. Radius-time cross-sections of the azimuthal mean relative humidity (%) at the 1331-m height in (a) CT05, (b) CT20. The black dots represent the radius of maximum tangential wind at the same level.

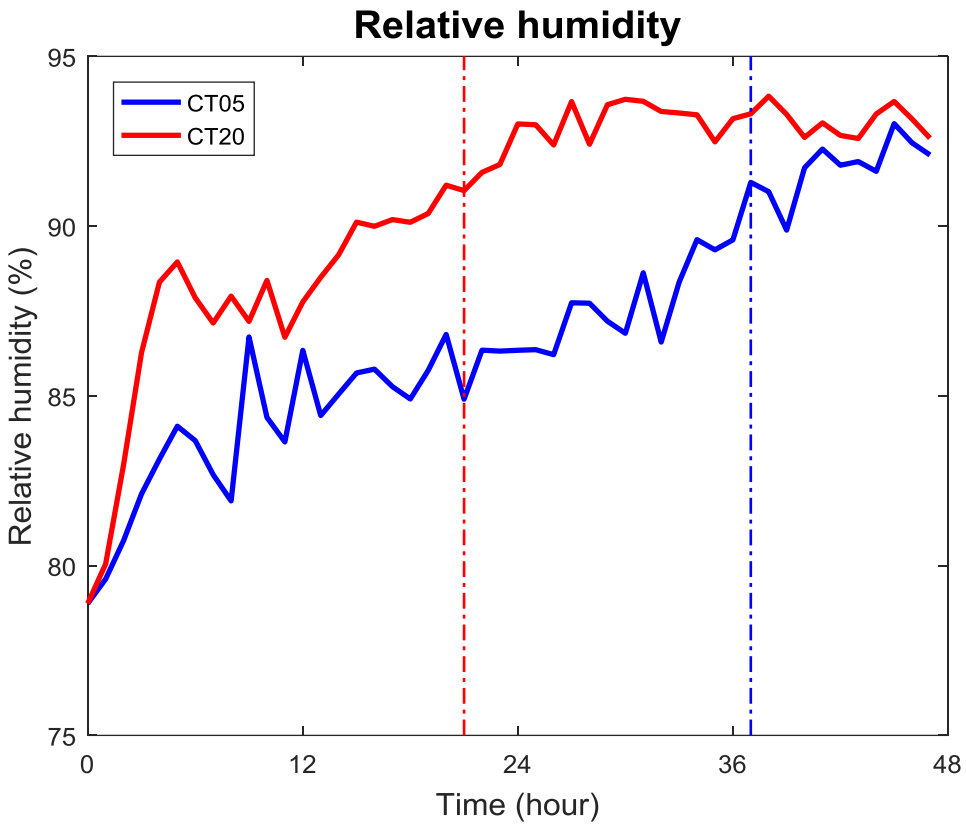

Figure 4.10. Time evolution of relative humidity (%) at the 1331-m height averaged within the RMW in CT05 (blue) and CT20 (red). The blue (red) dashed line denotes the time when the storm starts to intensify in CT05 (CT20).

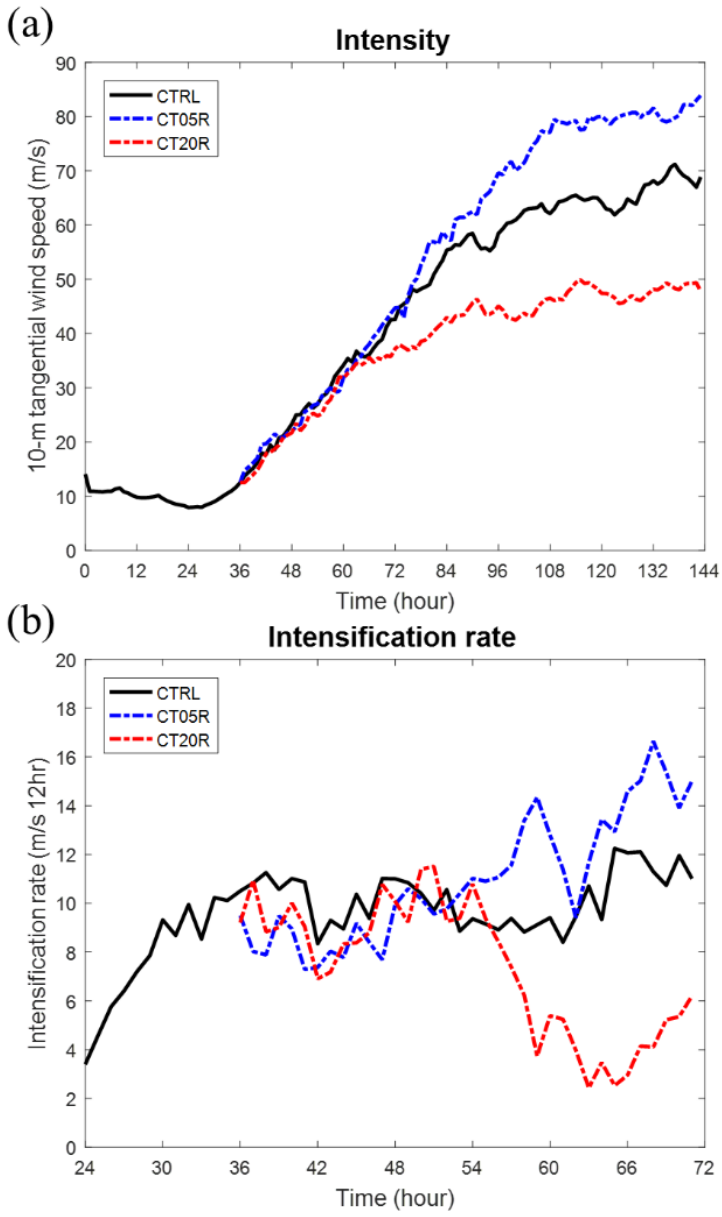

Figure 4.11. (a) Time evolution of the maximum 10-m height tangential wind speed (m s^{-1}) in CTRL (black), 50% C_D experiment but with C_D changed after 36 h (CT05-R, dashed blue) and 200% C_D experiment but with C_D changed after 36 h (CT20-R, dashed red). (b) Time evolution of the 12-h intensification rate (m s^{-1} 12 hr^{-1}) in CTRL (black), CT05-R (dashed blue), and CT20-R (dashed red).

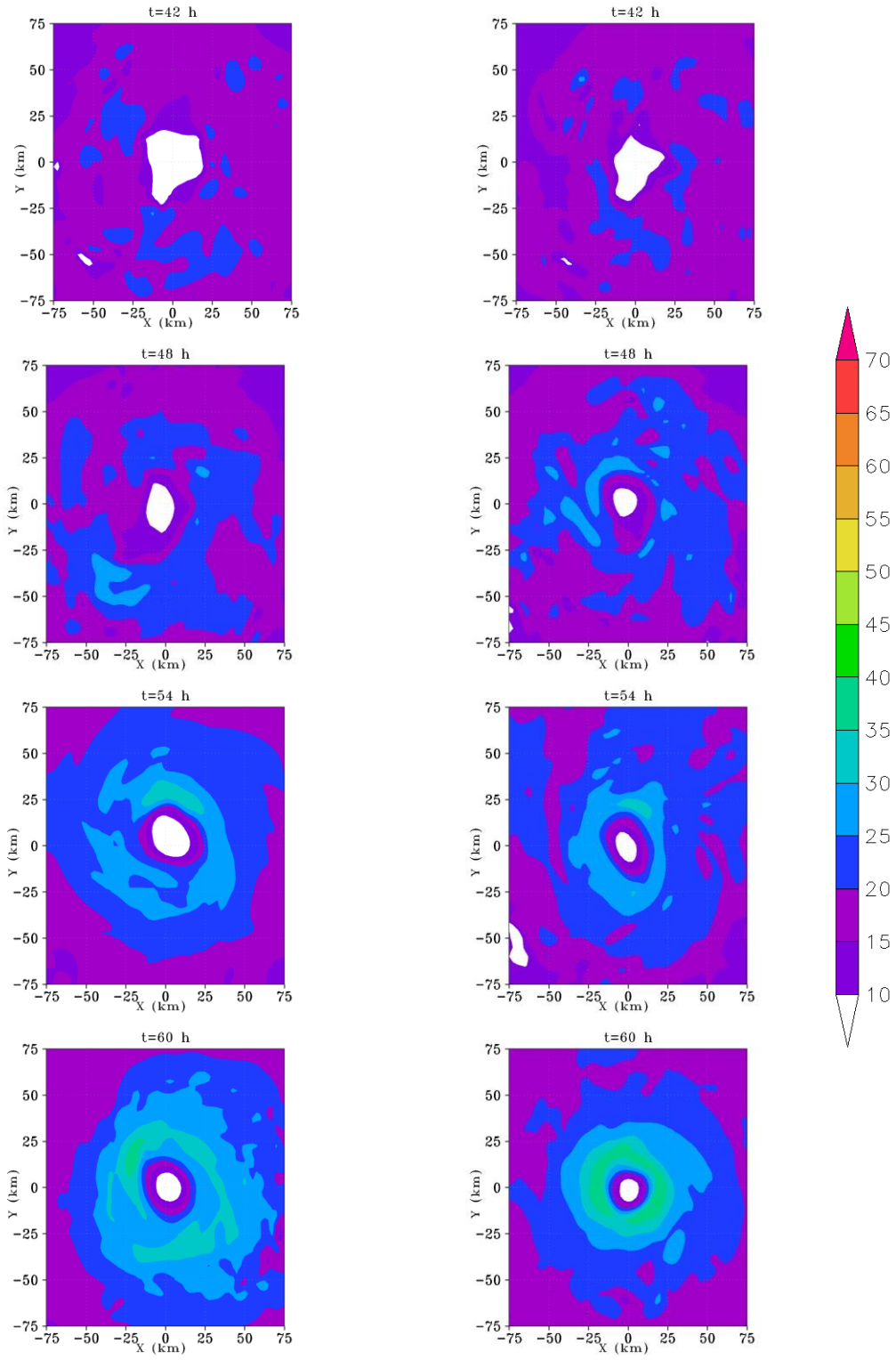

Figure 4.12. The total wind speed (m s^{-1}) at the 2320-m height at every 6-h interval from 42 h to 60 h in CT05-R (left) and CT20-R (right).

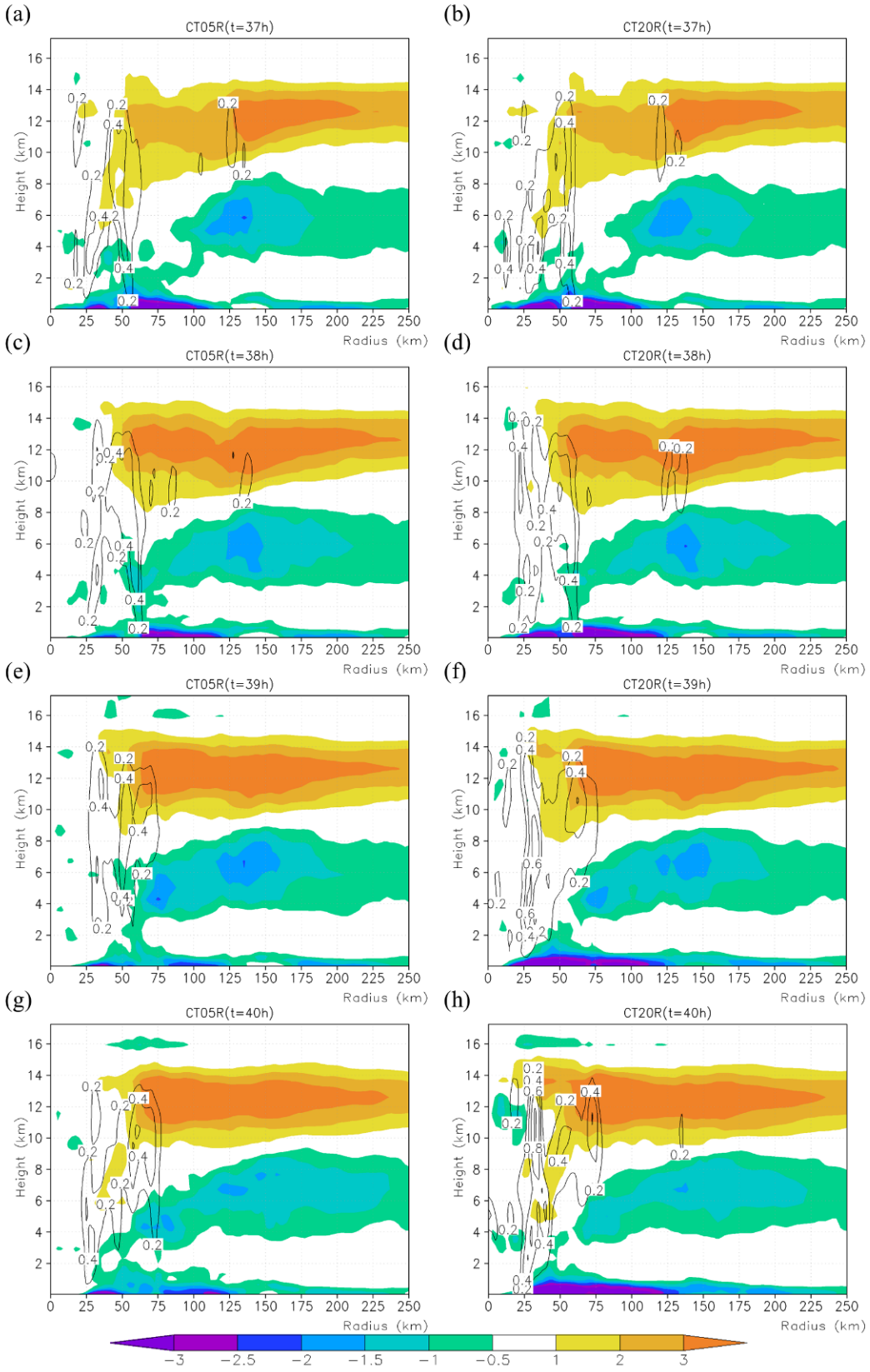
(a)
CT05R(t=37h)
(b)
CT20R(t=37h)
(c)
CT05R(t=38h)
(d)
CT20R(t=38h)
(e)
CT05R(t=39h)
(f)
CT20R(t=39h)
(g)
CT05R(t=40h)
(h)
CT20R(t=40h)
Height (km)
Radius (km)
−3 −2.5 −2 −1.5 −1 −0.5 1 2 3

Figure 4.13. Radius-height cross-sections of the azimuthal mean radial wind speed (m s^{-1}) and vertical velocity (contours, m s^{-1}) at (a) 37 h, (c) 38 h, (e) 39 h, and (g) 40 h in CT05-R and (b) 37 h, (d) 38 h, (f) 39 h, and (h) 40 h in CT20-R. C_D was modified after the first 36 h of integration in CTRL in both CT05-R and CT20-R.

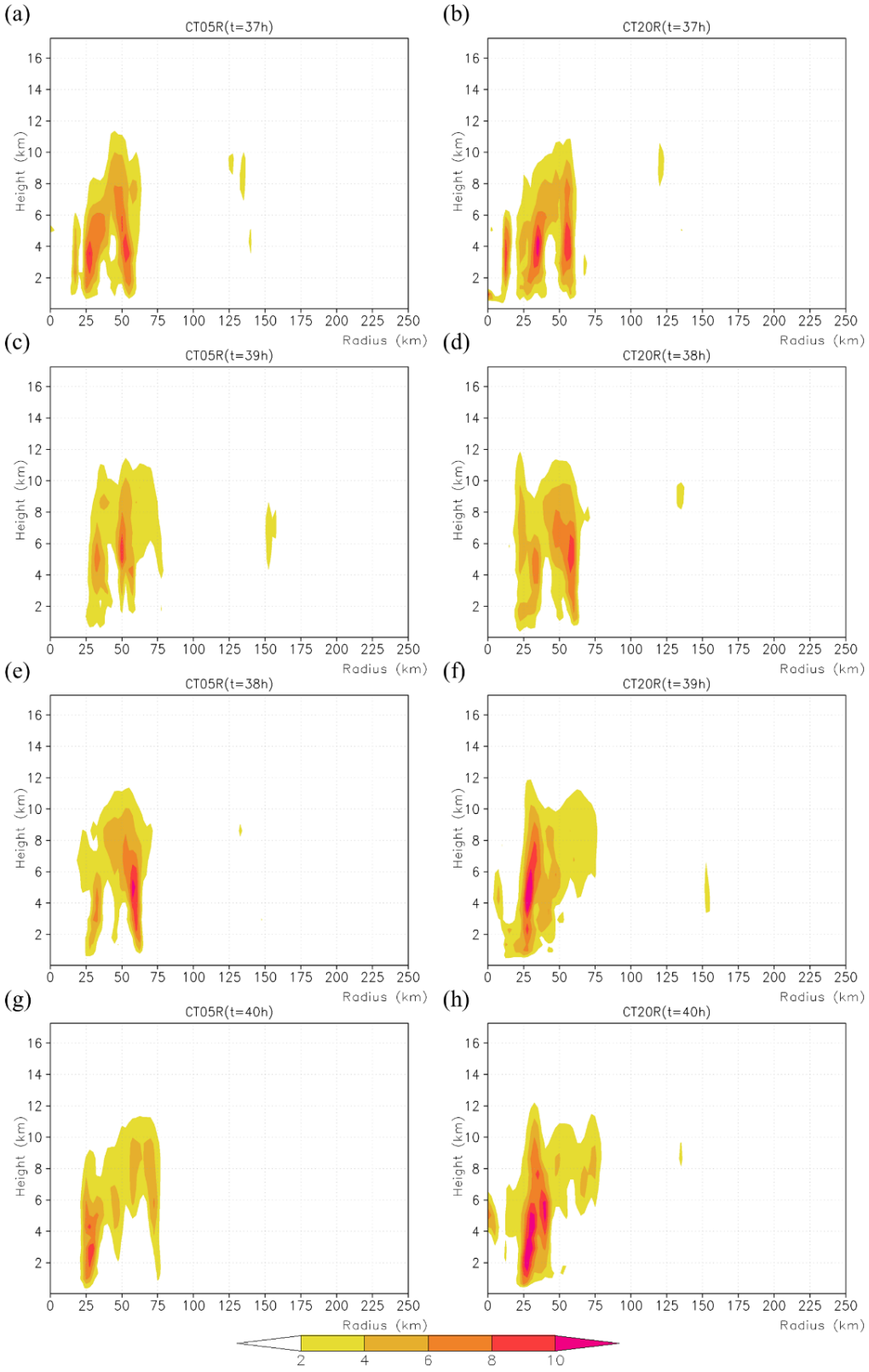

Figure 4.14. As in Figure 4.13, but for condensational heating rate (K hr^{-1}).

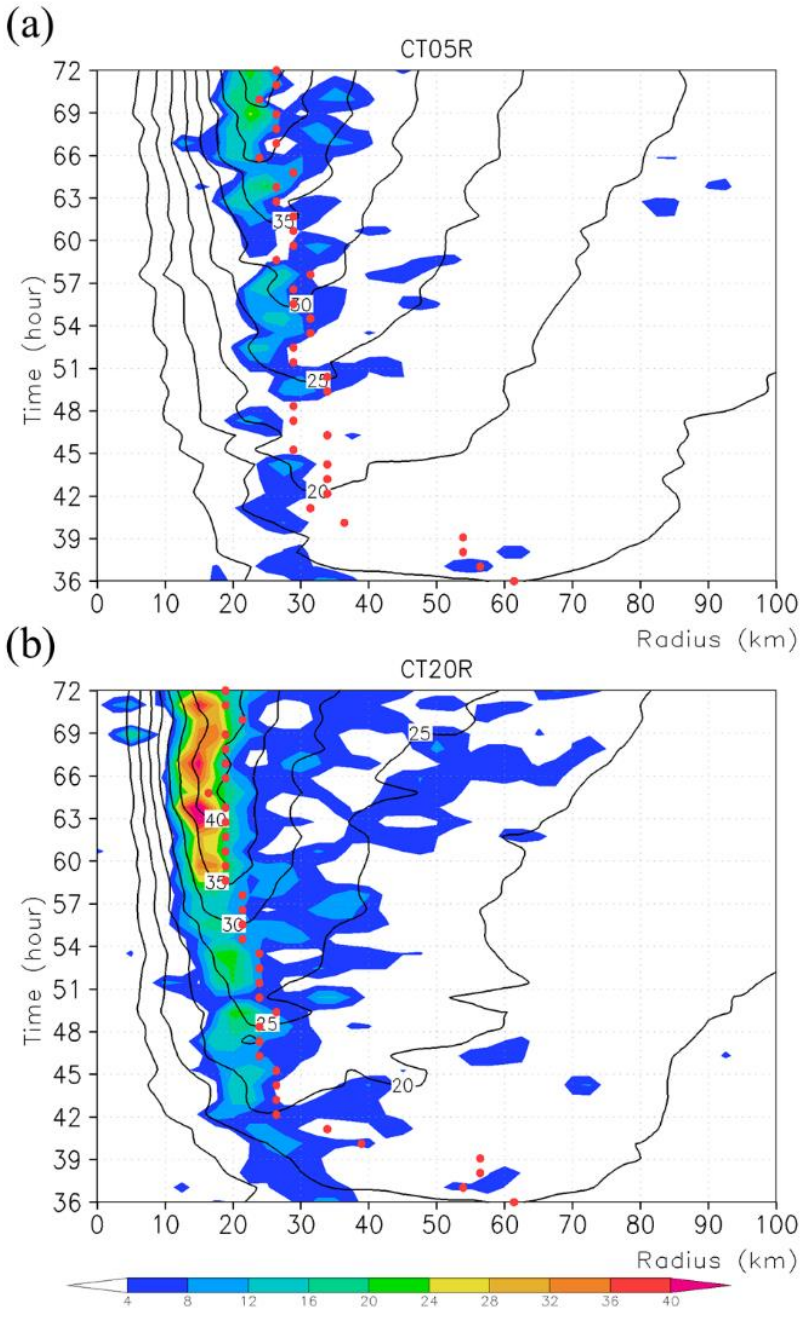

Figure 4.15. Radius-time cross-sections of the azimuthal mean condensational heating rate (shaded, K hr^{-1}) and tangential wind speed (contours, m s^{-1}) at the 1781-m height in (a) CT05-R and (b) CT20-R from 36 h. The red dots represent the radius of maximum tangential wind at the same level.

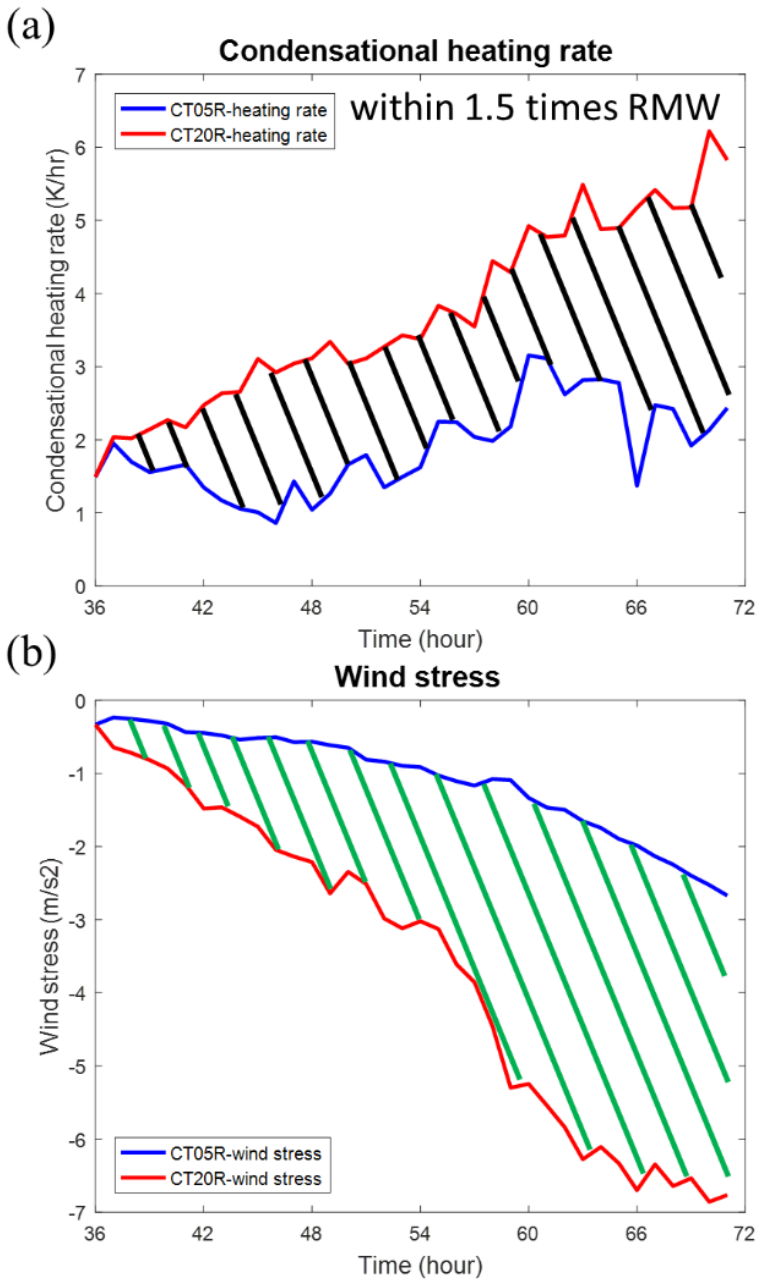

Figure 4.16. Time evolution of (a) the vertically integrated condensational heating rate (K hr^{-1}) averaged within 1.5 times of the RMW (K hr^{-1}) and (b) surface wind stress at the RMW (m s^{-2}) in CT05-R (blue) and CT20-R (red) from 36-h of simulation after C_D was modified in the two experiments. The black (green) slashed area can be considered as the difference in the indirect (dissipation) effect of surface friction.

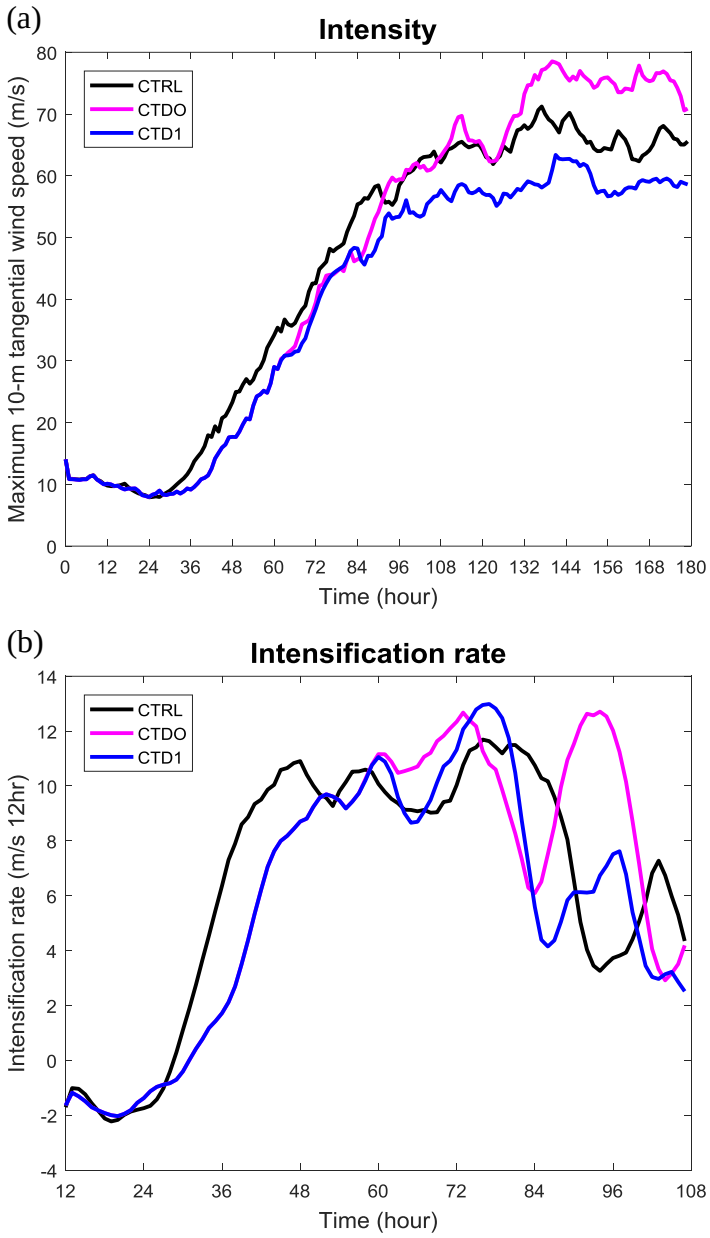

Figure 4.17. Time evolution of (a) the maximum 10-m height tangential wind speed (m s^{-1}) in the control experiment (CTRL, black), the experiment with new dependence of surface drag coefficient on surface wind speed (CTDO, magenta), and the experiment with modified dependence of surface drag coefficient on surface wind speed (CTD1, blue). (b) the 12-h intensification rate (m s^{-1} 12 hr^{-1}) with 5-h running mean in CTRL (black), CTDO (magenta), and CTD1 (blue).

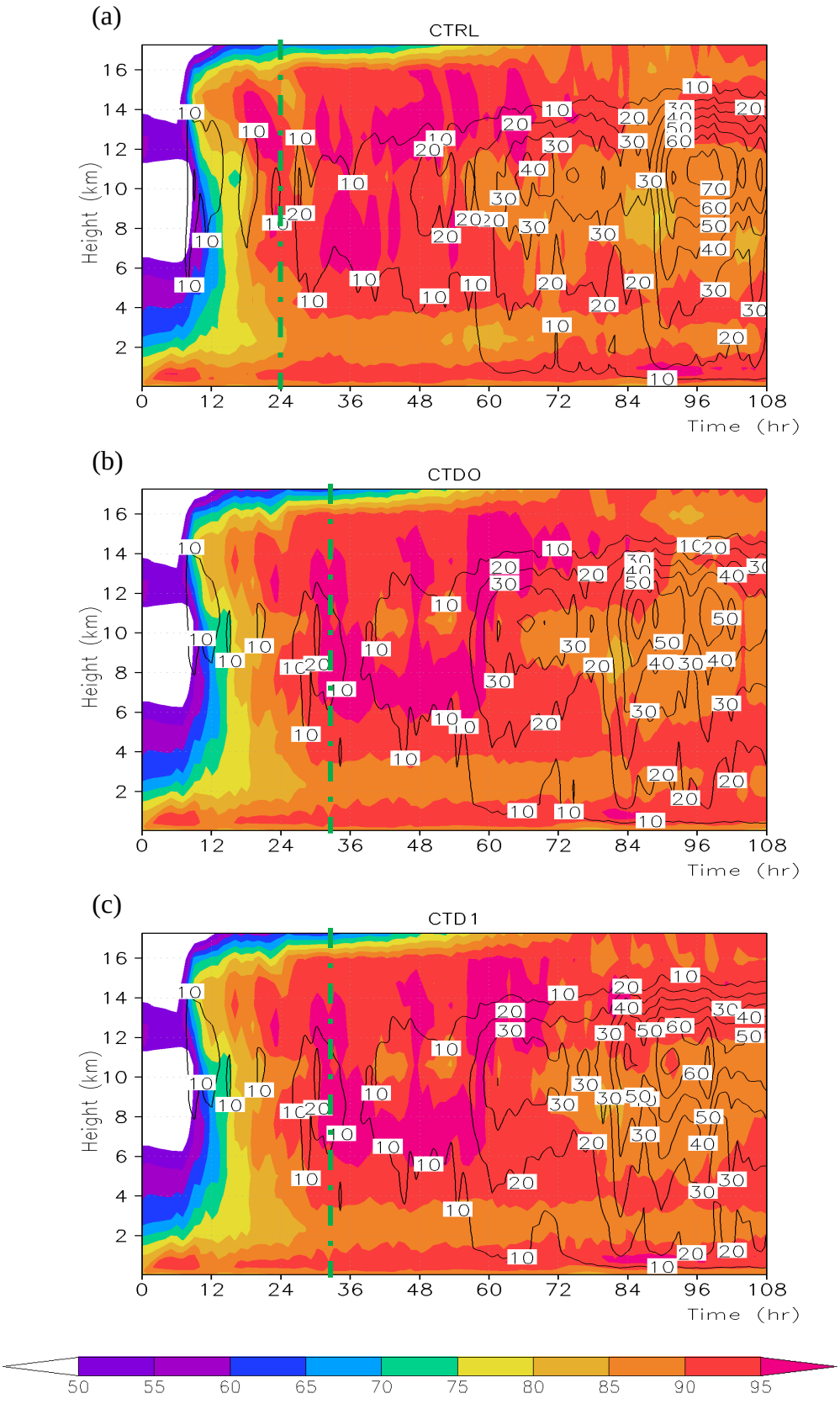
(a)
CTRL
Height (km)
Time (hr)
(b)
CTDO
Height (km)
Time (hr)
(c)
CTD1
Height (km)
Time (hr)
50 55 60 65 70 75 80 85 90 95

Figure 4.18. Time-height cross-sections of relative humidity (shaded, %) and the vertical velocity (contours, cm s^{-1}), both averaged within the radius of 1.5 times of the RMW in (a) CTRL, (b) CTDO, and (c) CTD1, respectively. The vertical green dashed line in each panel shows the time when the initial spin-up stage ends in the corresponding experiments.

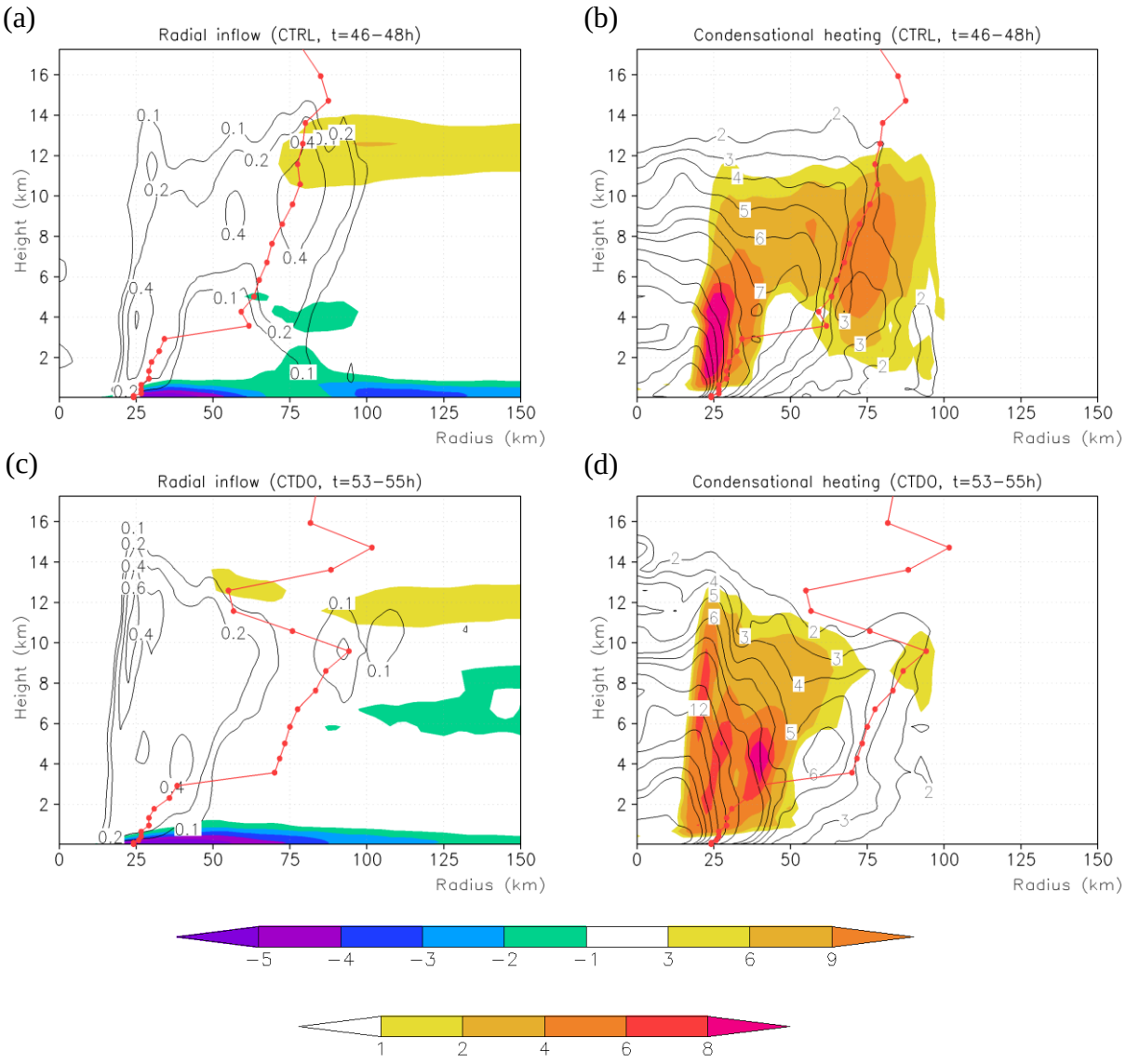

Figure 4.19. Radius-height cross-sections of azimuthal mean radial wind (left shaded, m s^{-1}) and vertical velocity (left contours, m s^{-1}), together with the condensational heating rate (right shaded, K hr^{-1}) and inertial stability (right contours, 10^{-4} s^{-1}) for (a), (b) CTRL and (c), (d) CTDO, all averaged 3-h interval when the intensity is over 20 m s^{-1}, respectively. The red solid curve shows the radius of maximum wind in the corresponding experiments.

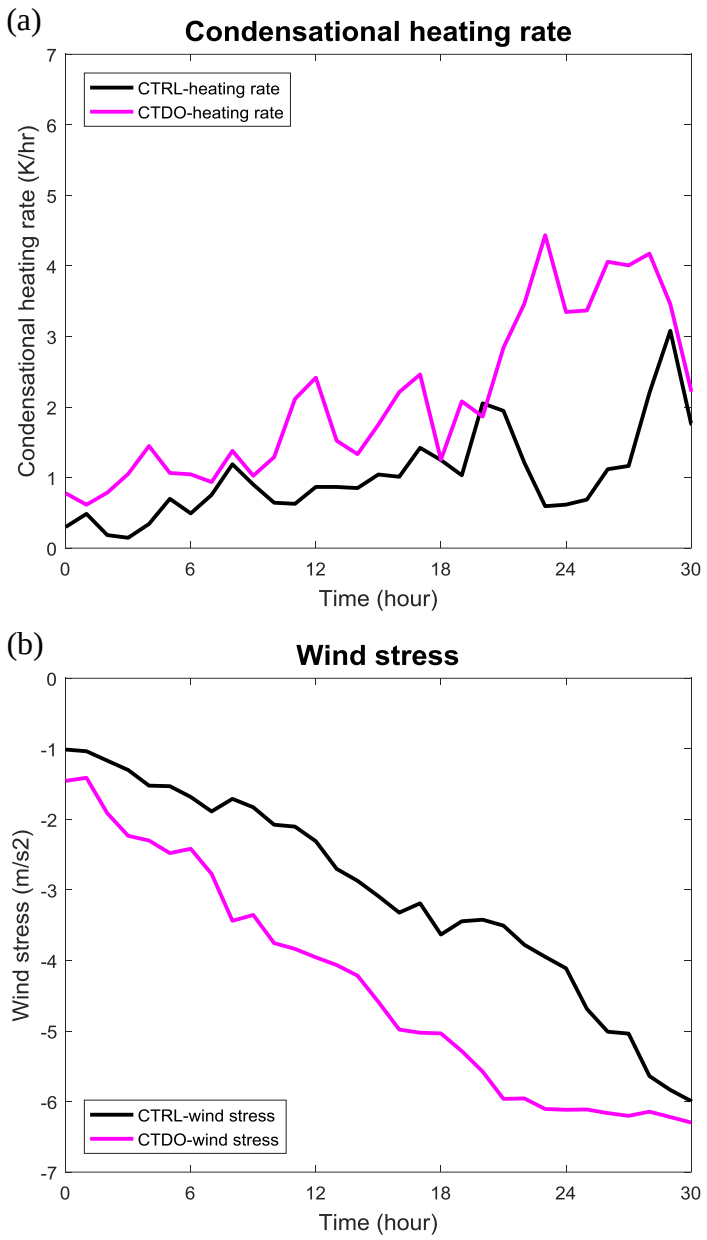

Figure 4.20. Time evolution of (a) the vertically integrated condensational heating rate (K hr^{-1}) averaged within 1.5 times of the RMW and (b) surface wind stress at the RMW (m s^{-2}) in CTRL (black) and CTDO (magenta) from 46 h and 53 h when the intensity is over 20 m s^{-1}, respectively.

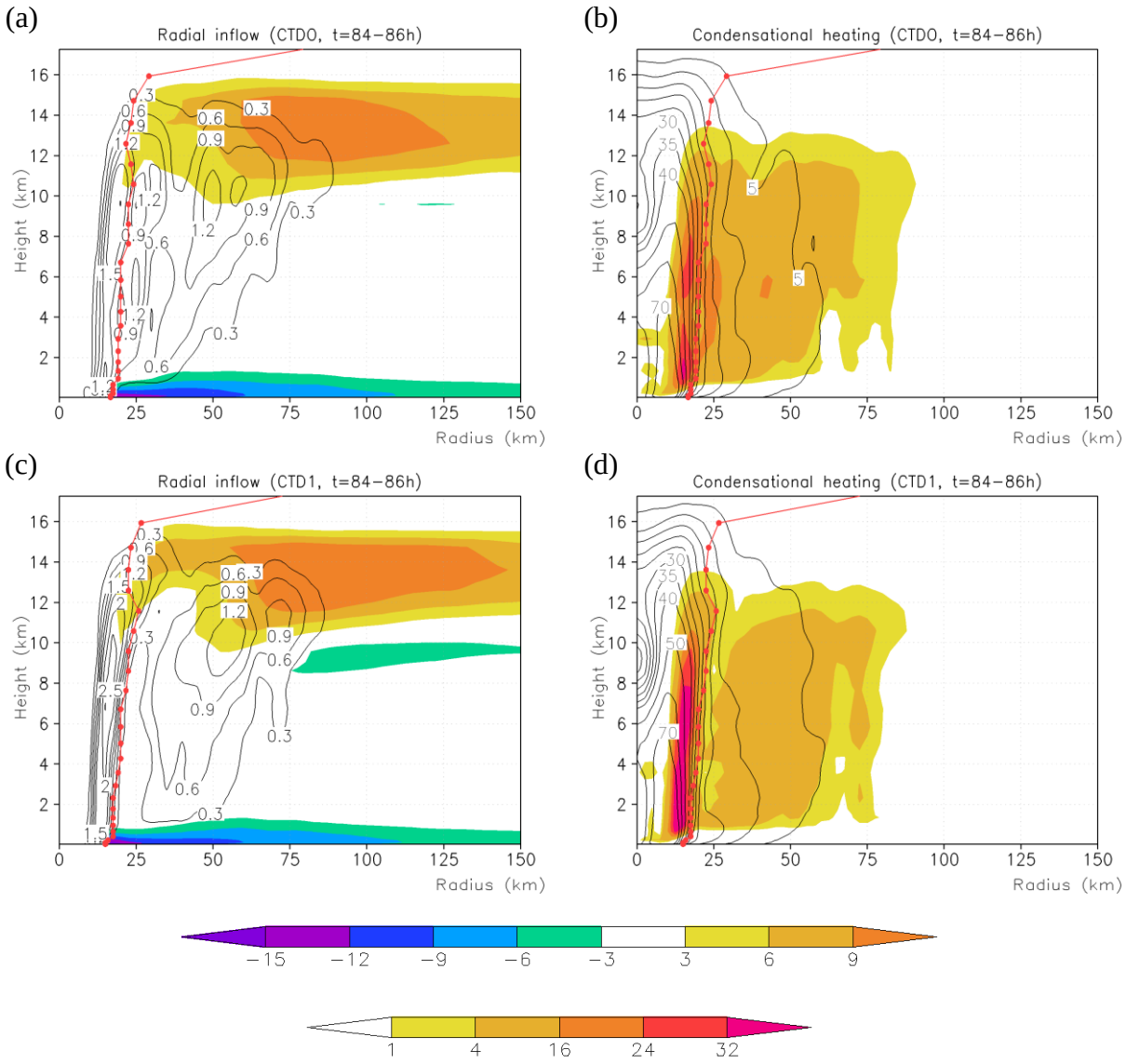

Figure 4.21. As in Figure 4.19, but for (a), (b) CTDO and (c), (d) CTD1, all averaged in 3-h interval when the intensity is over 48 m s^{-1} respectively.

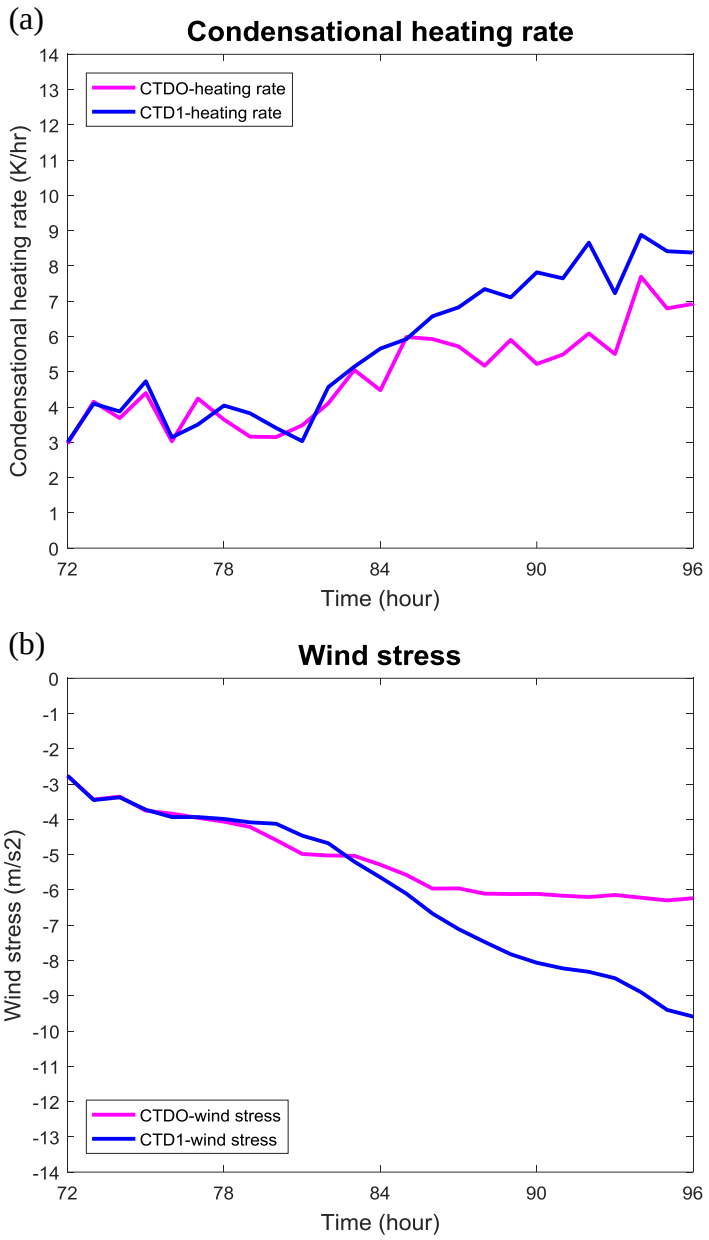

Figure 4.22. As in Figure 4.20, but for CTDO (magenta) and CTD1 (blue) from 72 h to 96 h.

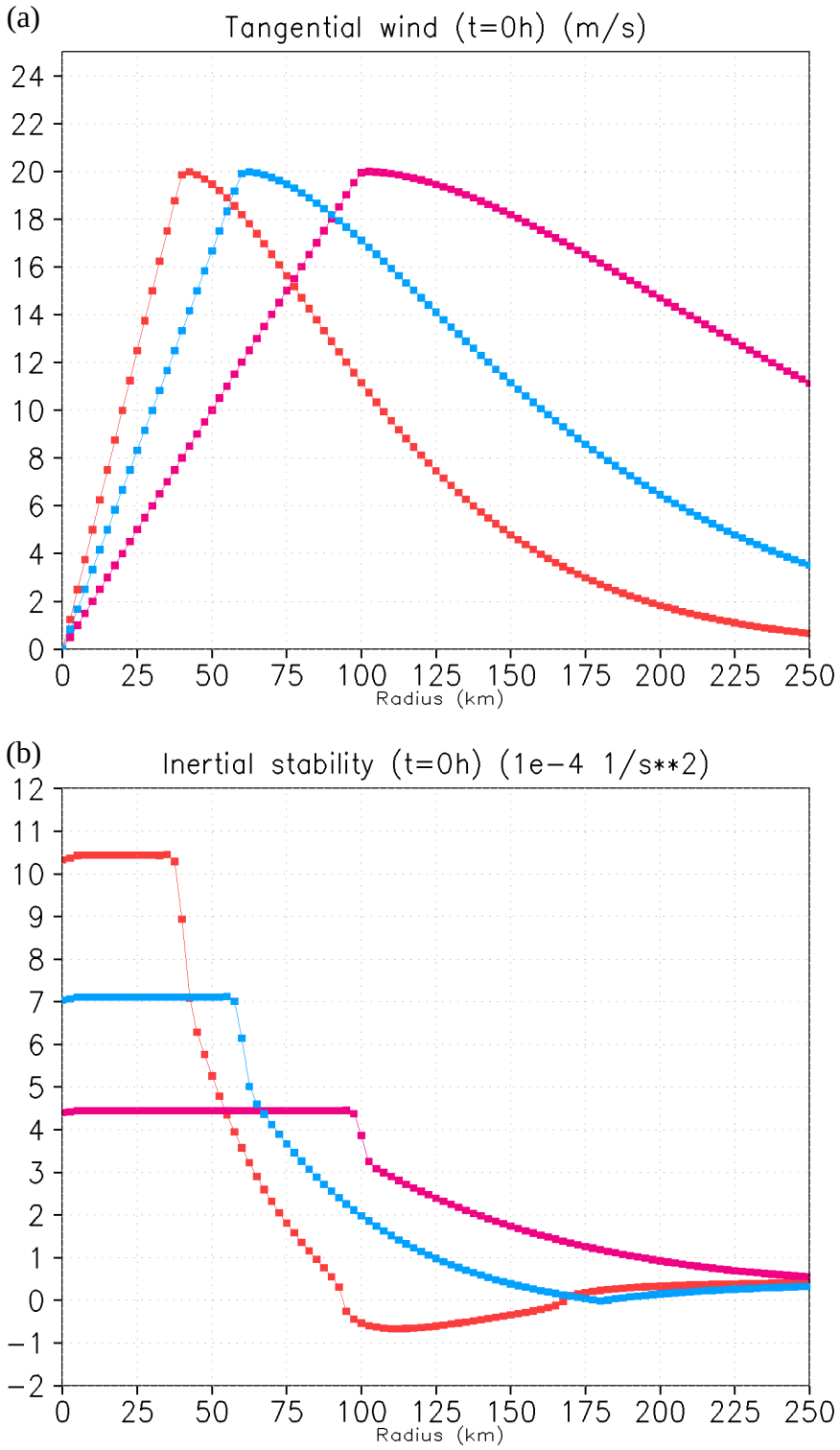

Figure 5.1. Radial distribution of (a) initial tangential wind speed (m s^{-1}) and (b) inertial stability (10^{-4} s^{-2}) in R041 (R_m = 40 km, red), R061 (R_m = 60 km, blue), and R101 (R_m = 40 km,

magenta).

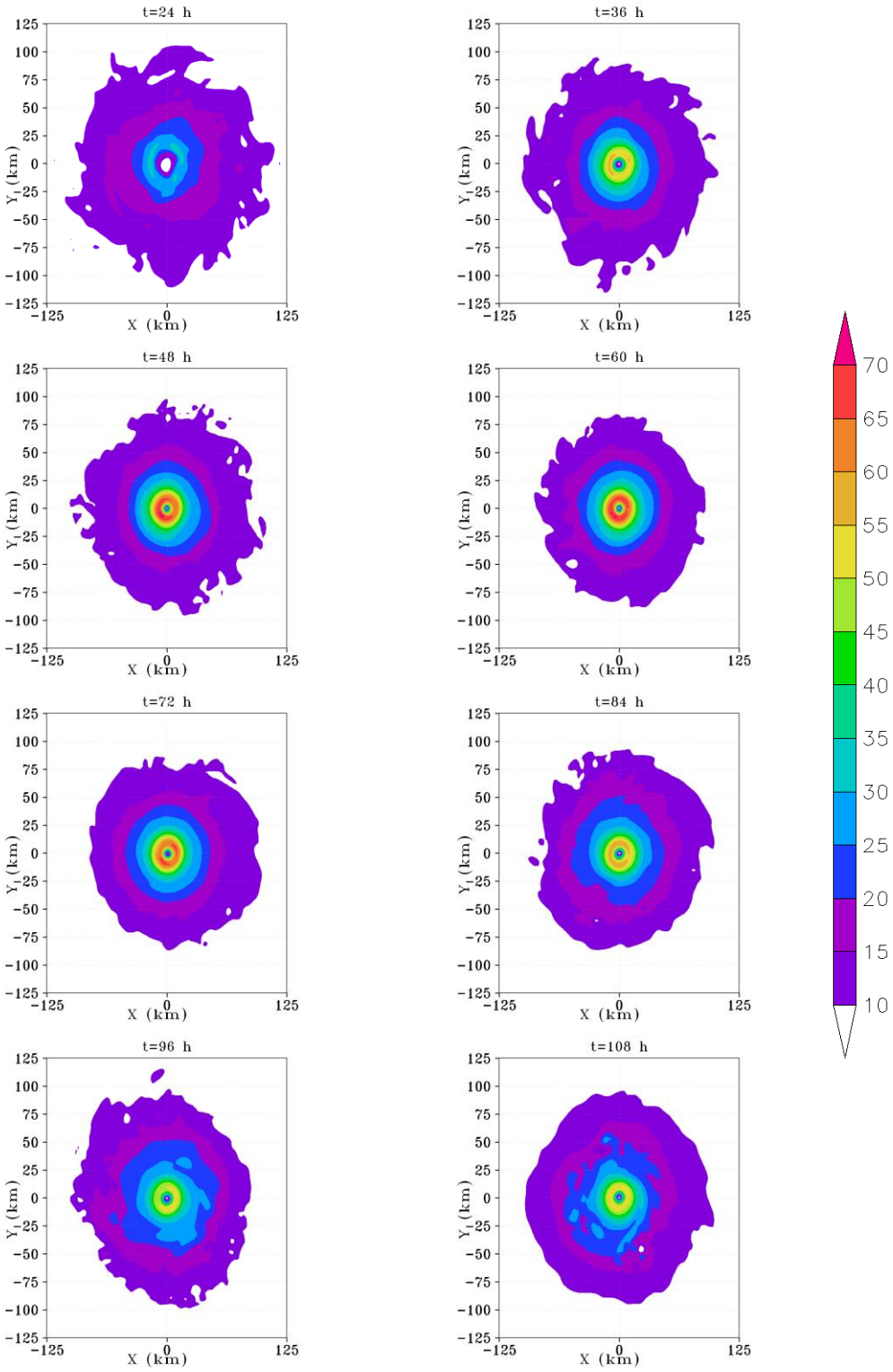

Figure 5.2. The total wind speed (m s^{-1}) at the 2320-m height at every 12-h interval from 24 h to 108 h in R041.

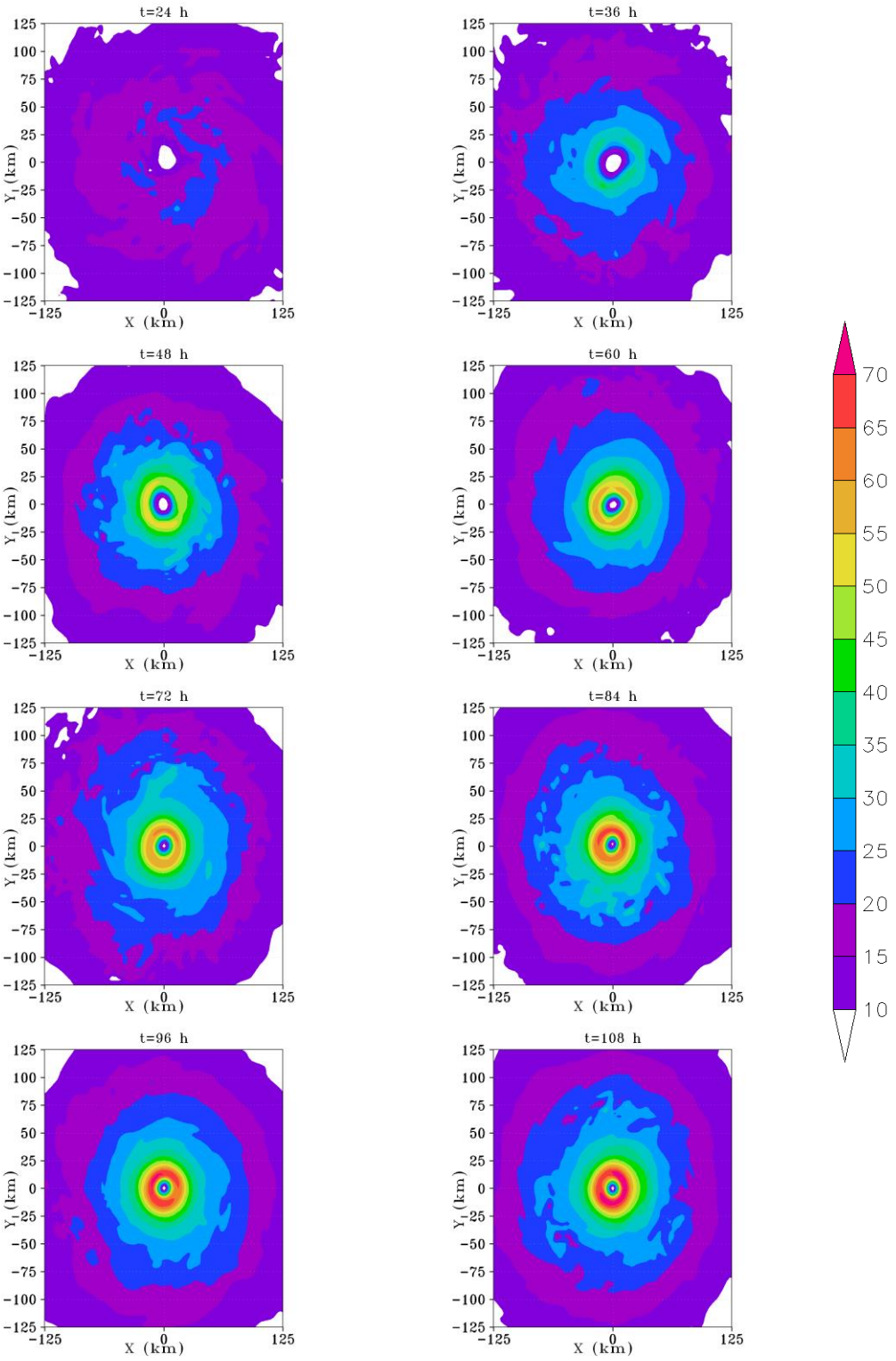

Figure 5.3. As in Figure 5.2, but for R061.

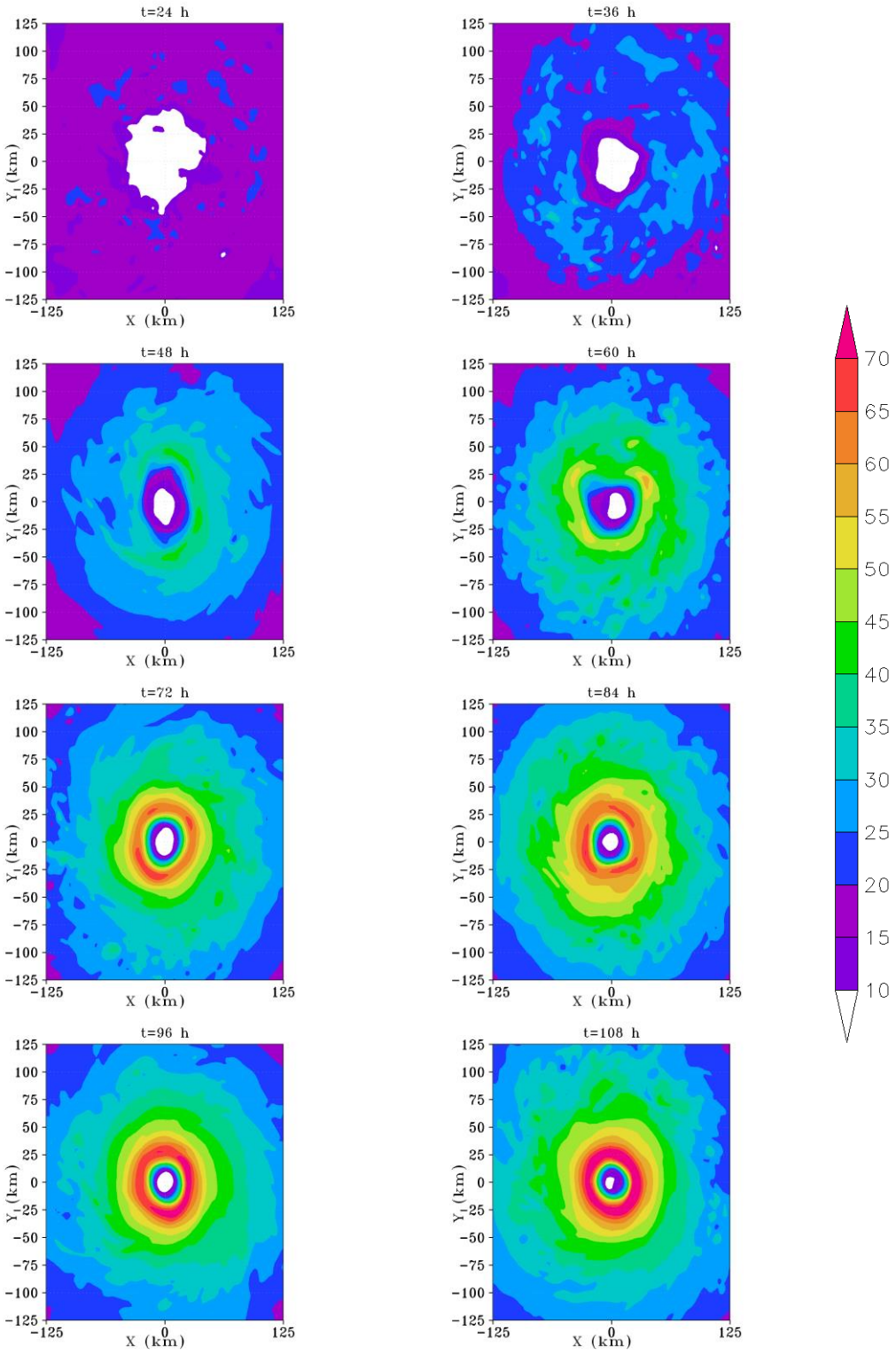

Figure 5.4. As in Figure 5.2, but for R101.

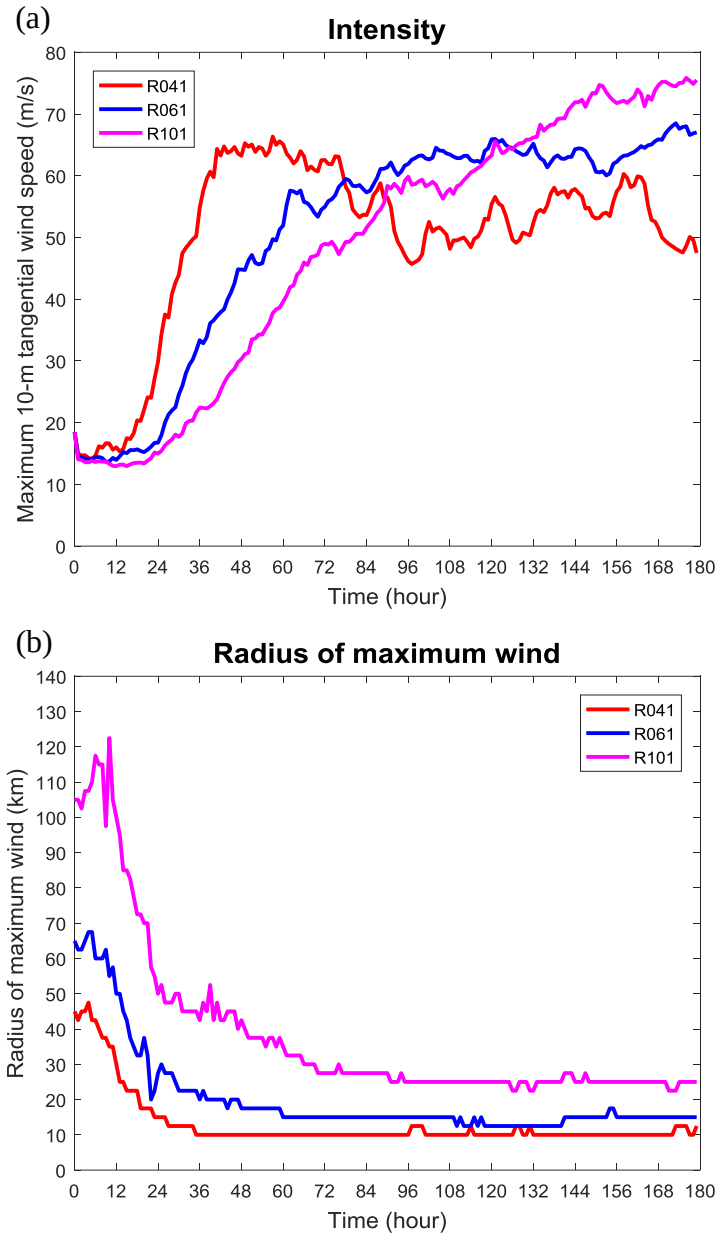

Figure 5.5. Time evolution of (a) the maximum 10-m height tangential wind speed (m s^{-1}) and (b) the radius of maximum wind (km) in R041 (R_m = 40 km, red), R061 (R_m = 60 km, blue), and R101 (R_m = 100 km, magenta).

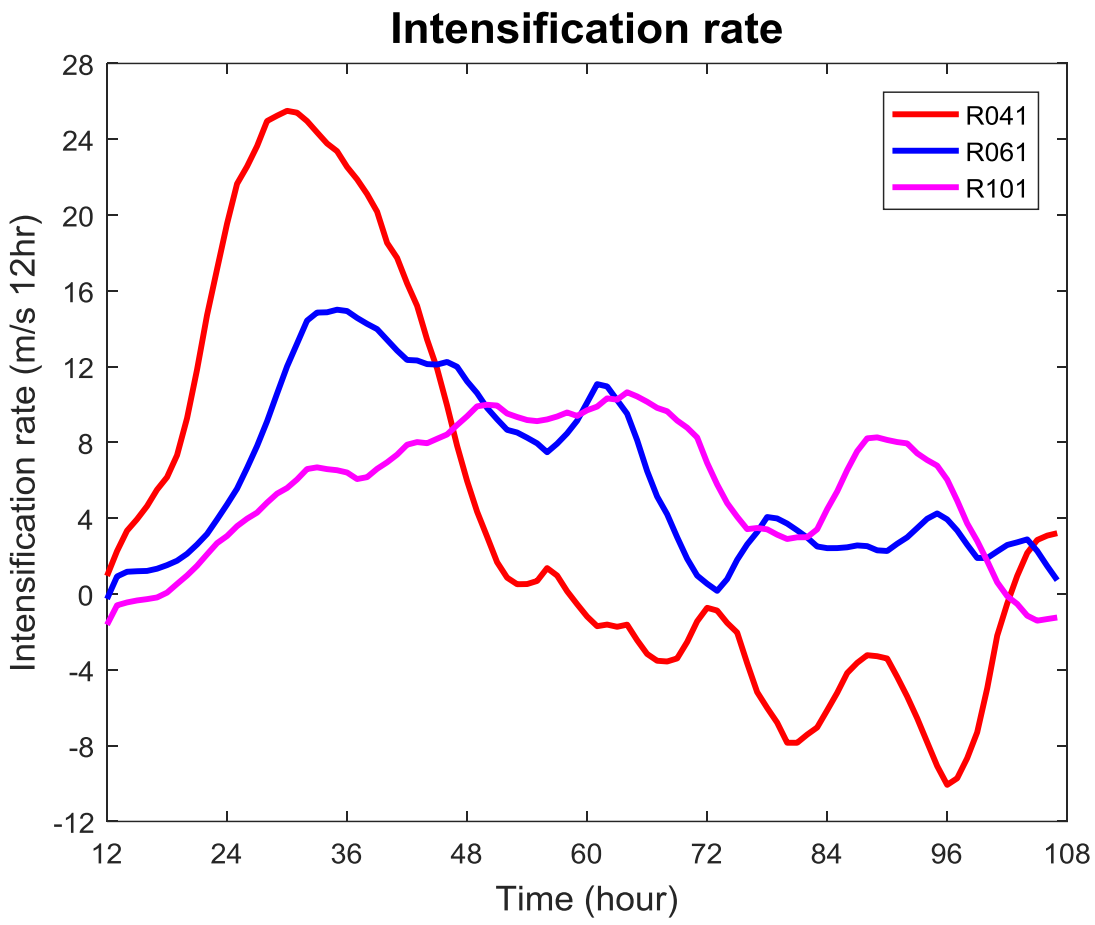

Figure 5.6. Time evolution of the intensification rate (m s^{-1} 12 hr^{-1}) with 5-h running mean in R041 (R_m = 40 km, red), R061 (R_m = 60 km, blue), and R101 (R_m = 100 km, magenta).

(a)

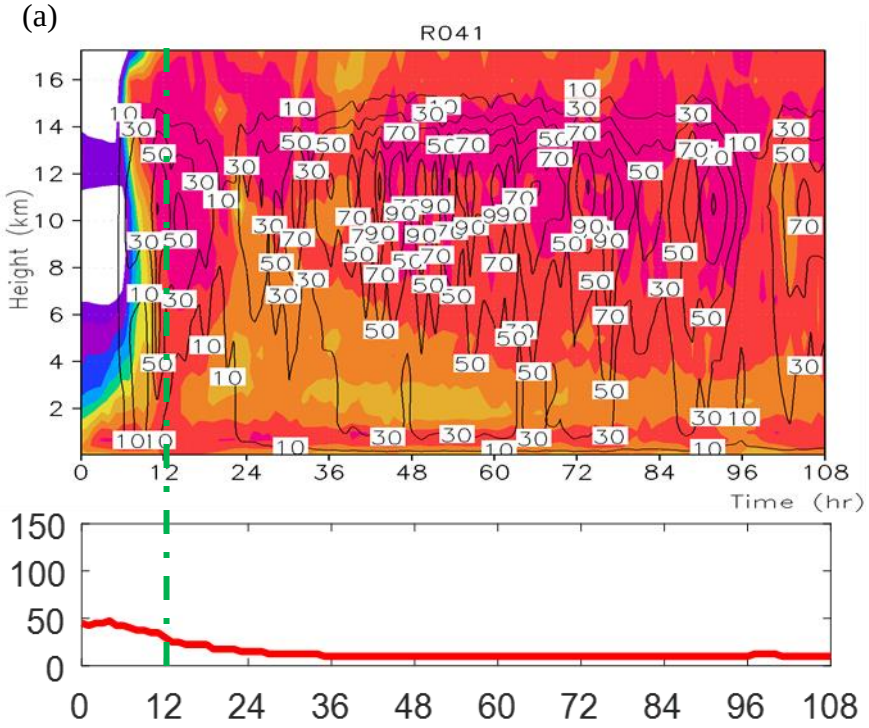
R041
Height (km)
Time (hr)
0 12 24 36 48 60 72 84 96 108
2 4 6 8 10 12 14 16
150
100
50
0

(b)

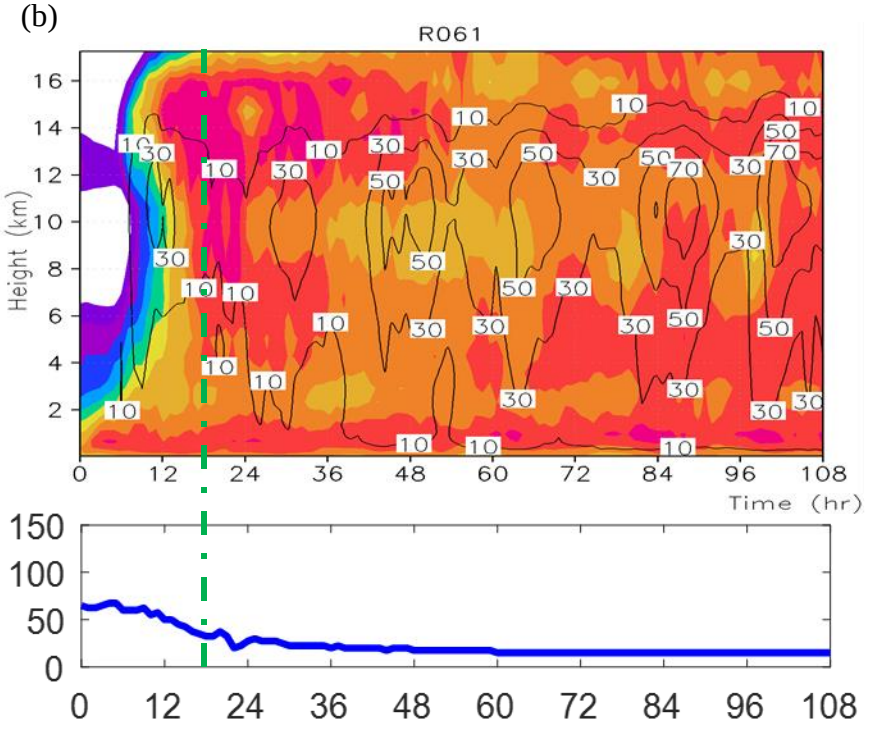
R061
Height (km)
Time (hr)
0 12 24 36 48 60 72 84 96 108
2 4 6 8 10 12 14 16
150
100
50
0

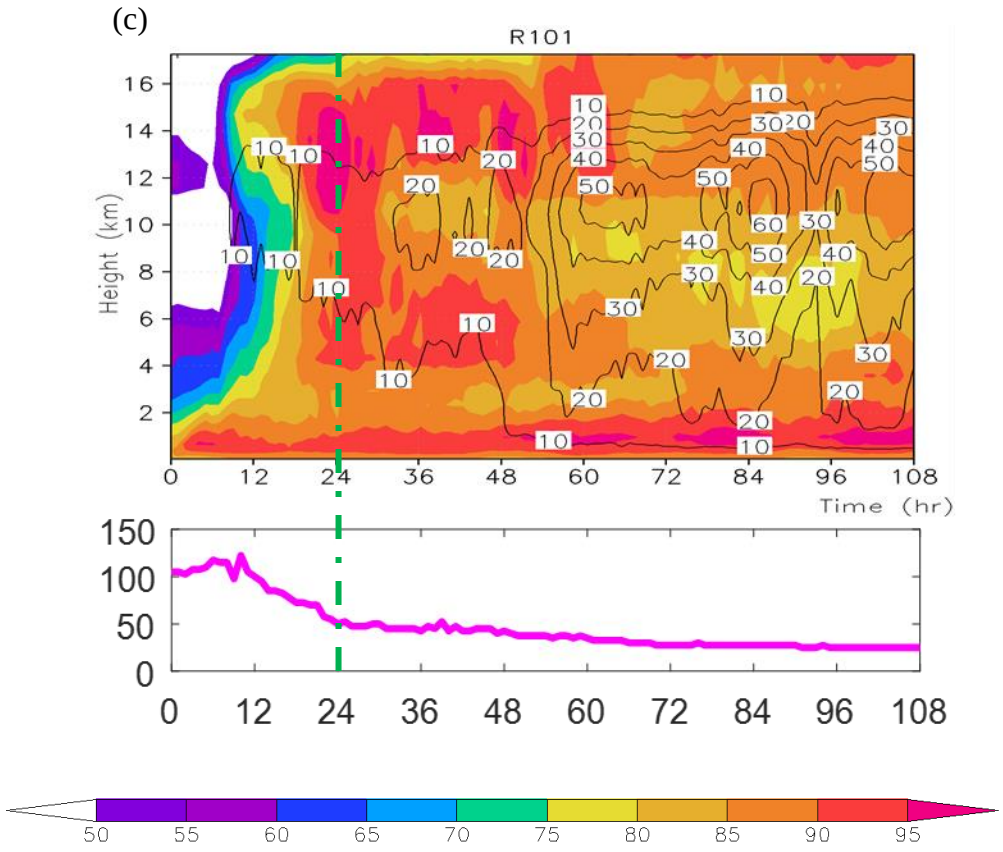

Figure 5.7. Time-height cross-sections of relative humidity (shaded, %) and vertical velocity (contours, cm s^{-1}), both averaged within the radius of 1.5 times of the RMW, together with the time evolution of the RMW (km) shown at the bottom of each panel in (a) R041 (R_m = 40 km), (b) R061 (R_m = 60 km), and (c) R101 (R_m = 100 km). The vertical green dashed line in each panel shows the time when the initial spin-up stage ends in the corresponding experiment.

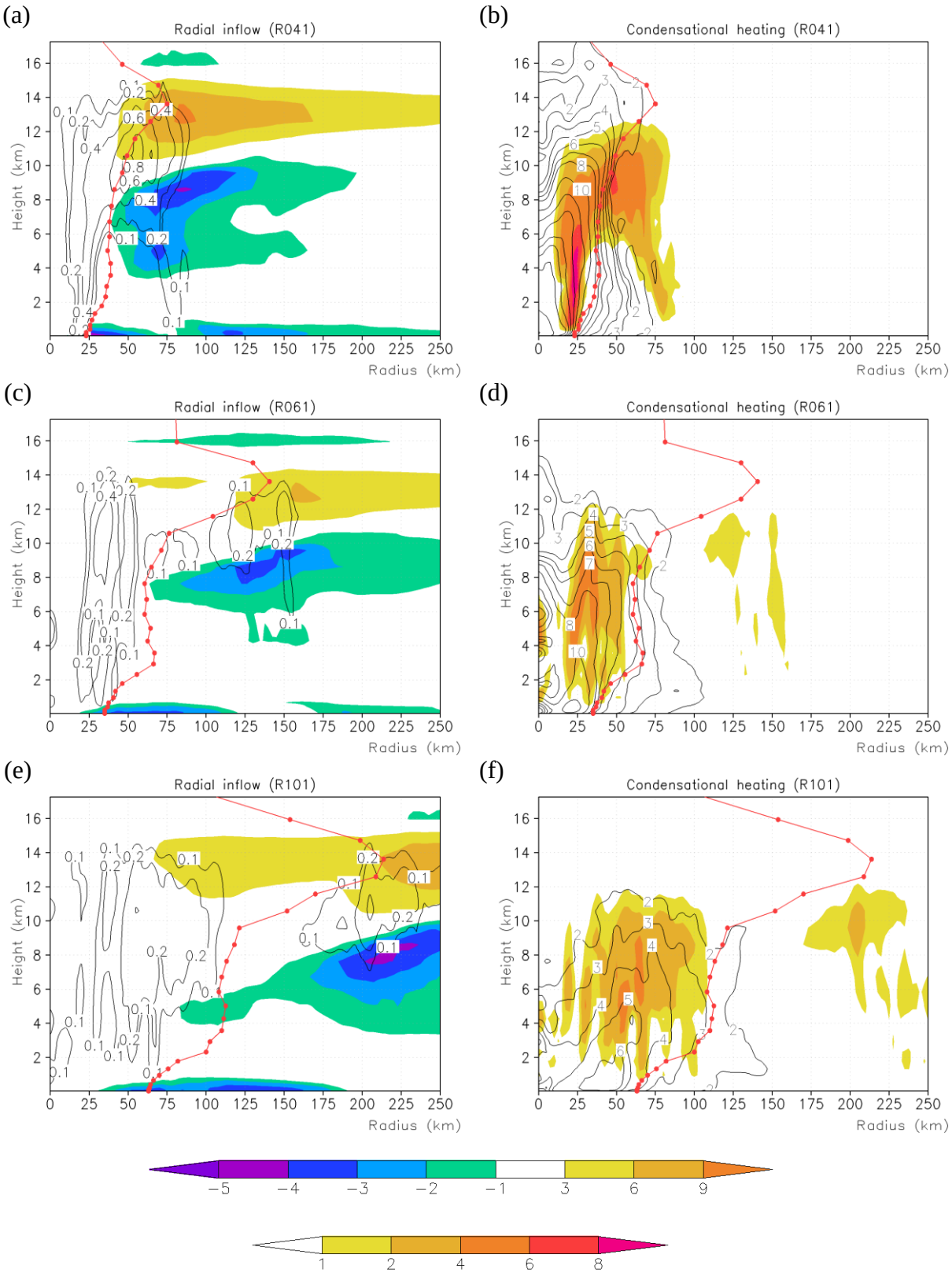

Figure 5.8. Radius-height cross-sections of the azimuthal mean radial wind (left shaded, m s^{-1})

and vertical velocity (left contours, m s^{-1}), together with the condensational heating rate (right shaded, K hr^{-1}) and inertial stability (right contours, 10^{-4} s^{-1}) for (a), (b) R041 (R_m = 40 km), (c), (d) R061 (R_m = 60 km), and (e), (f) R101 (R_m = 100 km), all averaged in 3-h interval prior to the corresponding primary intensification stage. The red solid curve shows the radius of maximum wind in the corresponding experiment.

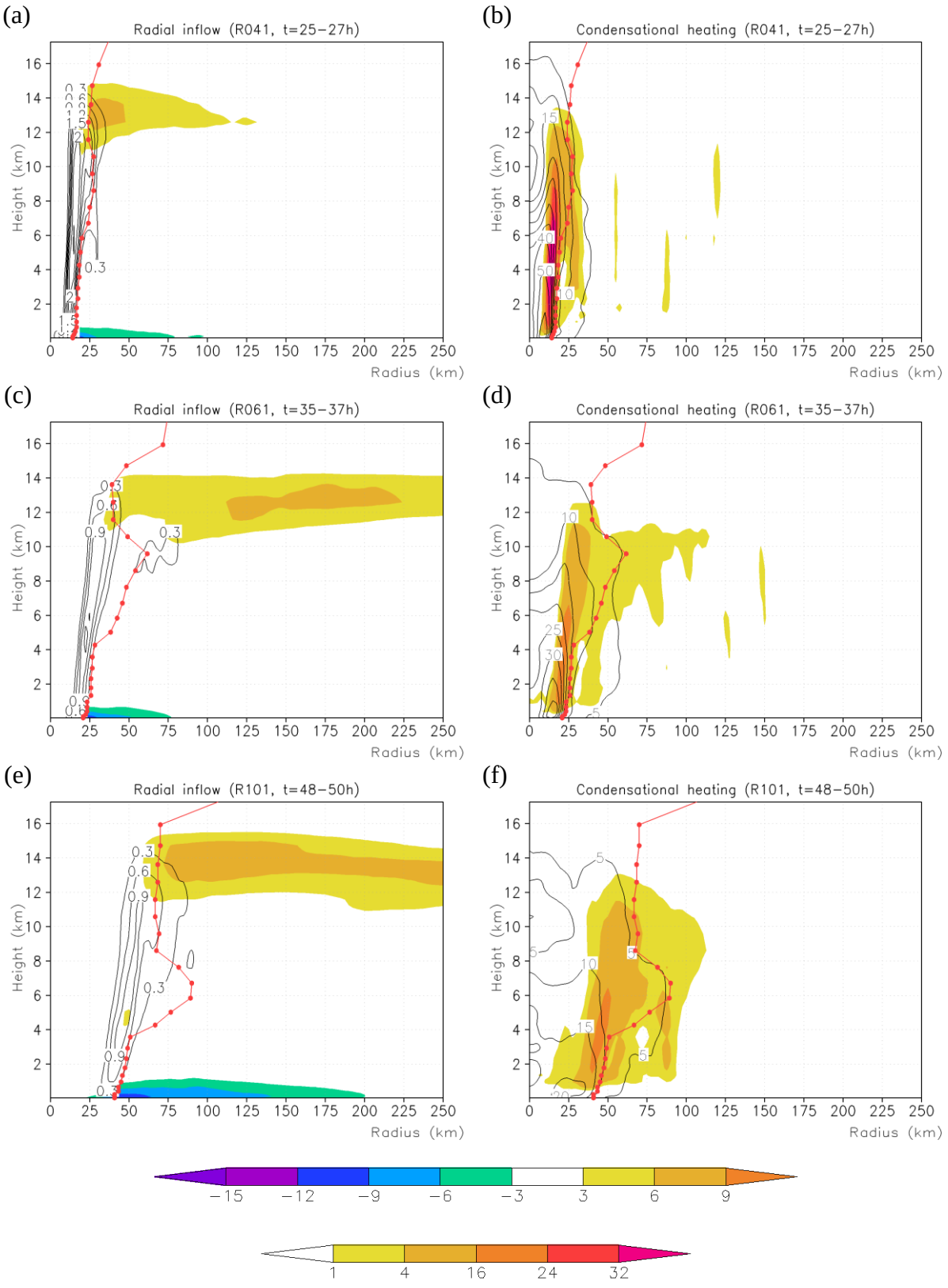

Figure 5.9. As in Figure 5.8, but for 3-h average when the intensity is over 30 m s^{-1} respectively.

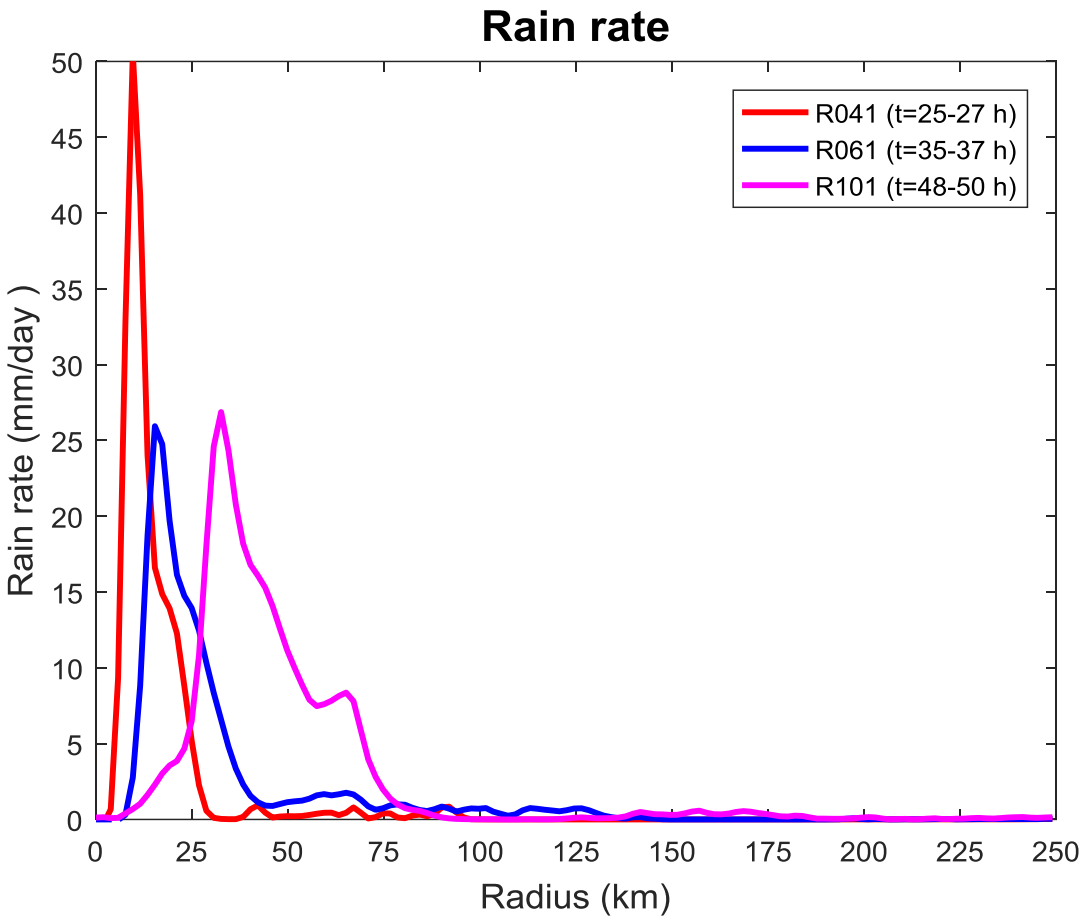

Figure 5.10. Radial distribution of the azimuthal mean rain rate (mm day^{-1}) in R041 (R_m = 40 km, red), R061 (R_m = 60 km, blue), and R101 (R_m = 100 km, magenta), all averaged in 3-h interval when the intensity is over 30 m s^{-1} respectively.

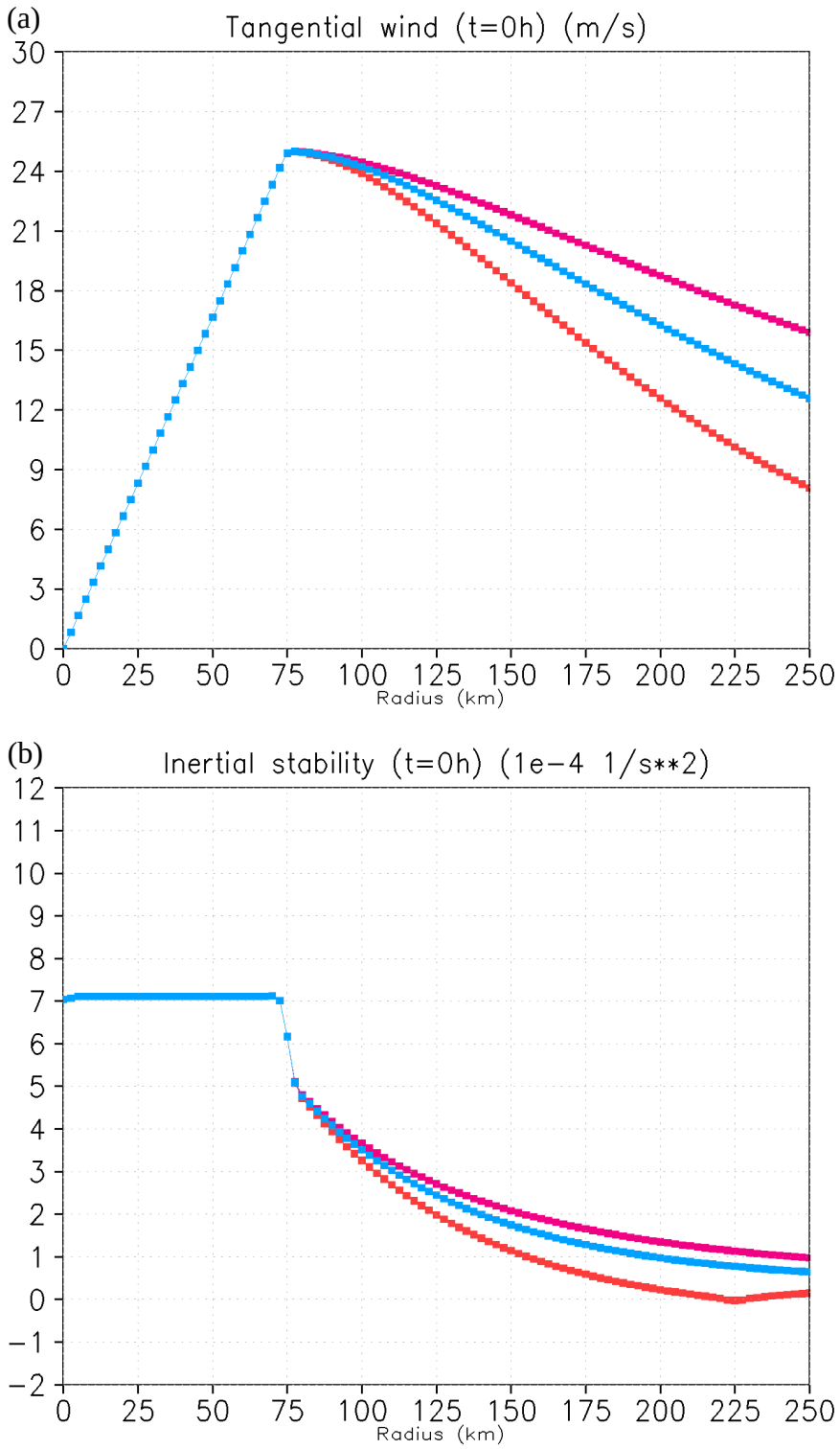

Figure 5.11. Radial distribution of (a) initial tangential wind speed (m s^{-1}) and (b) inertial stability (10^{-4} s^{-2}) in b055 (b = 0.5, magenta), b075 (b = 0.7, blue), and b105 (b = 1, red).

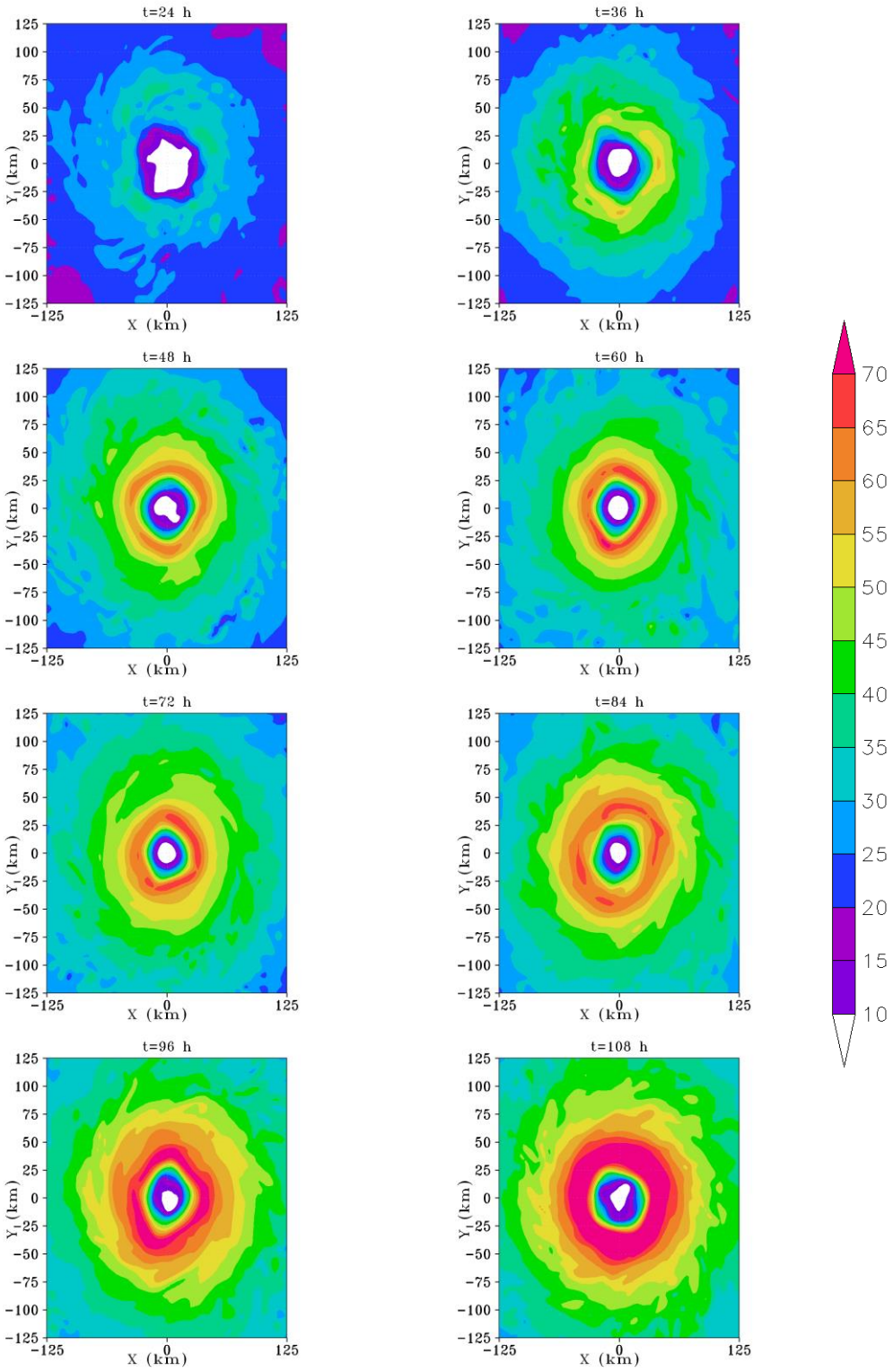

Figure 5.12. The total wind speed (m s^{-1}) at the 2320-m height at every 12-h interval from 24 h to 108 h in b055.

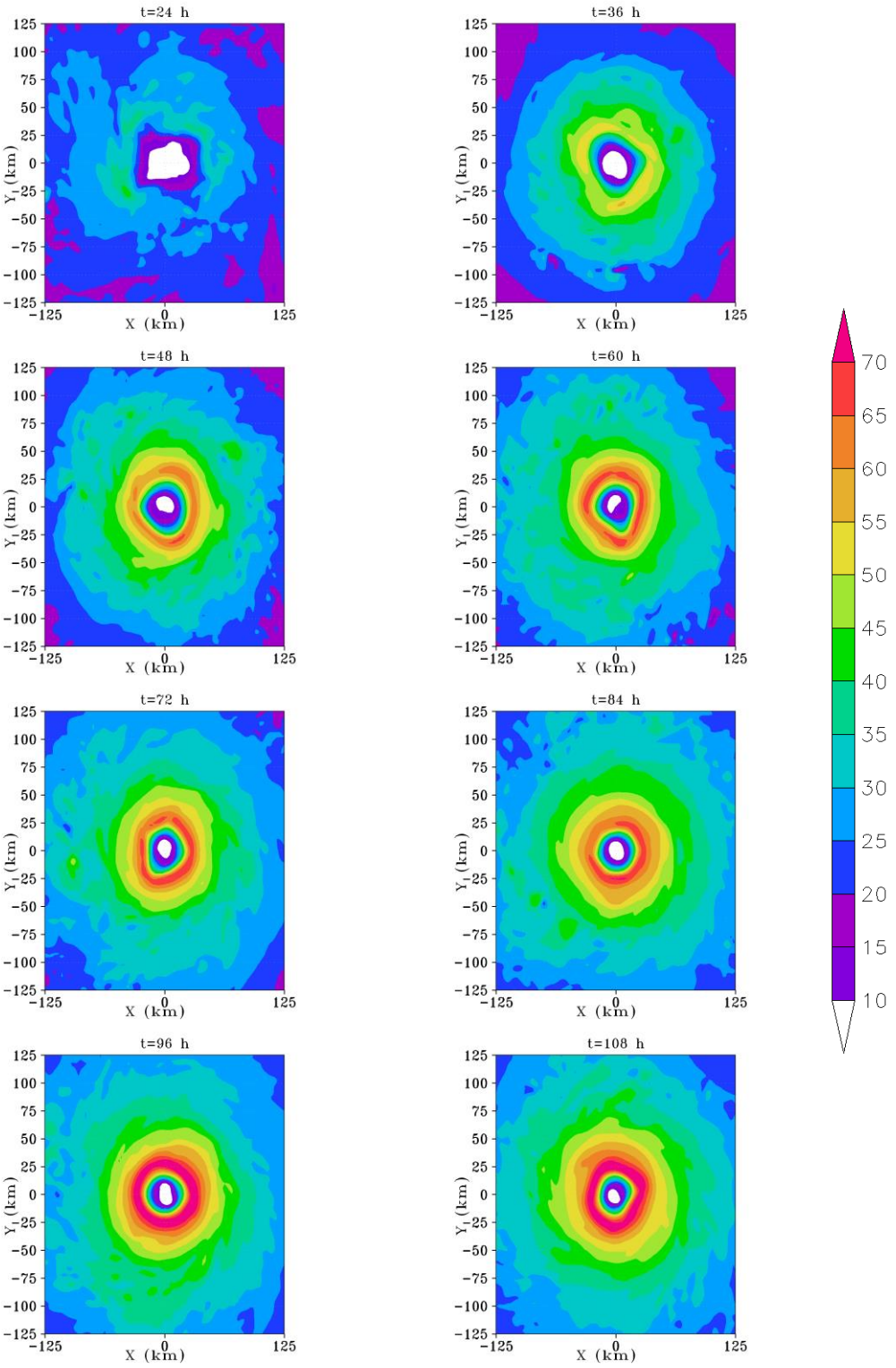

Figure 5.13. As in Figure 5.12, but for b075.

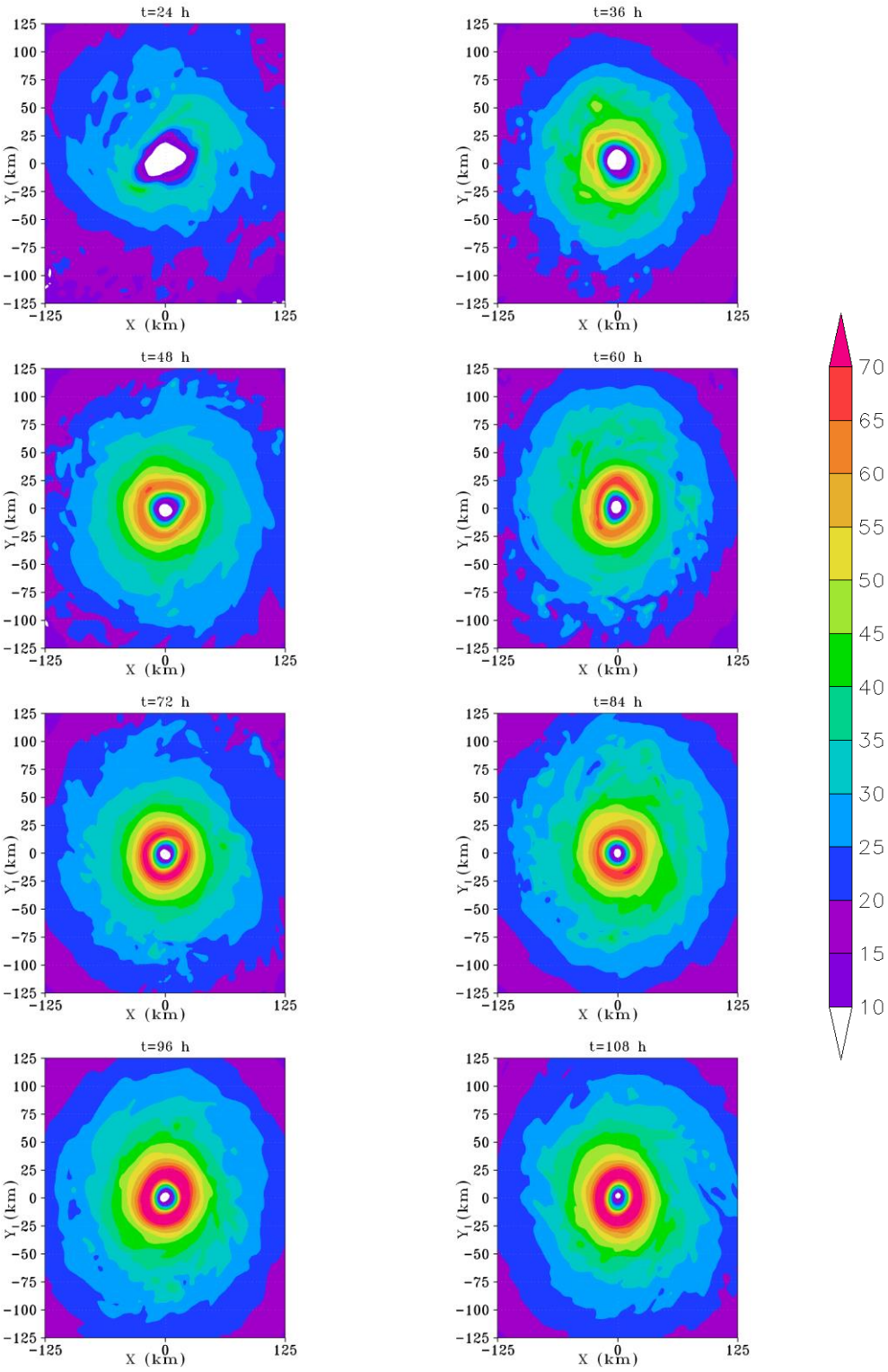

Figure 5.14. As in Figure 5.12, but for b105.

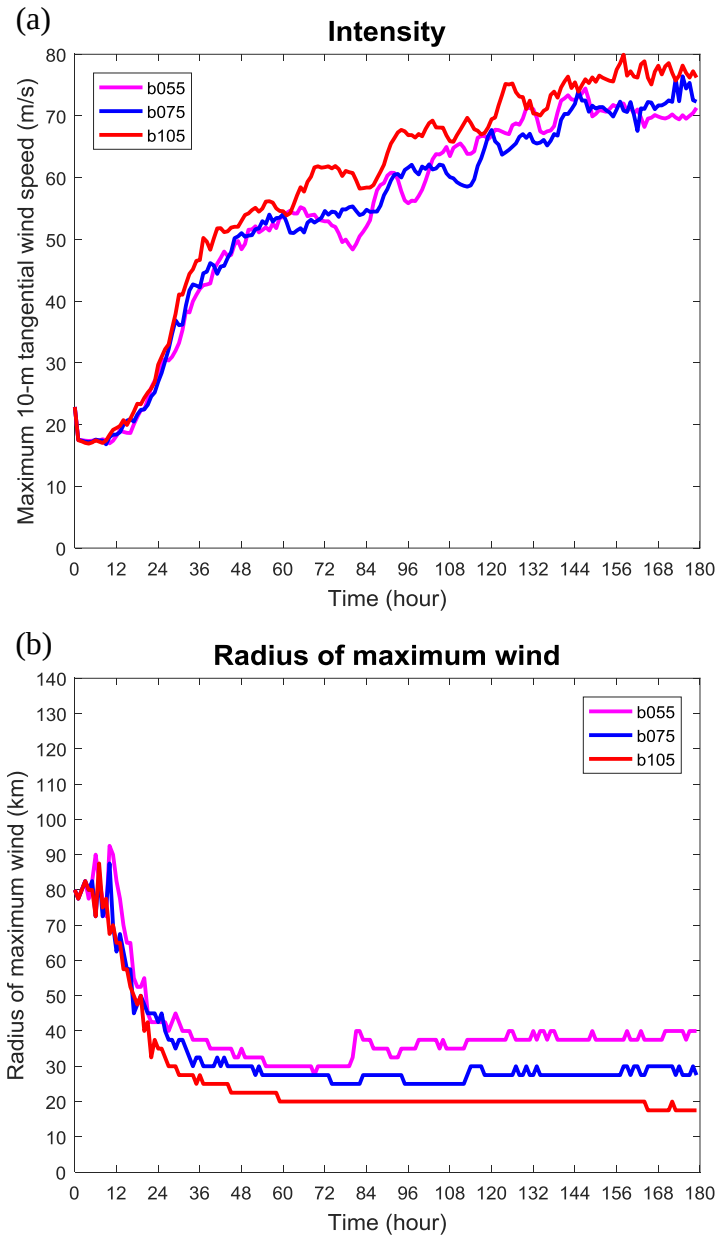

Figure 5.15. Time evolution of (a) the maximum 10-m height tangential wind speed (m s^{-1}) and (b) the radius of maximum wind (km) in b055 (b = 0.5, magenta), b075 (b = 0.7, blue), and b105 (b = 1, red).

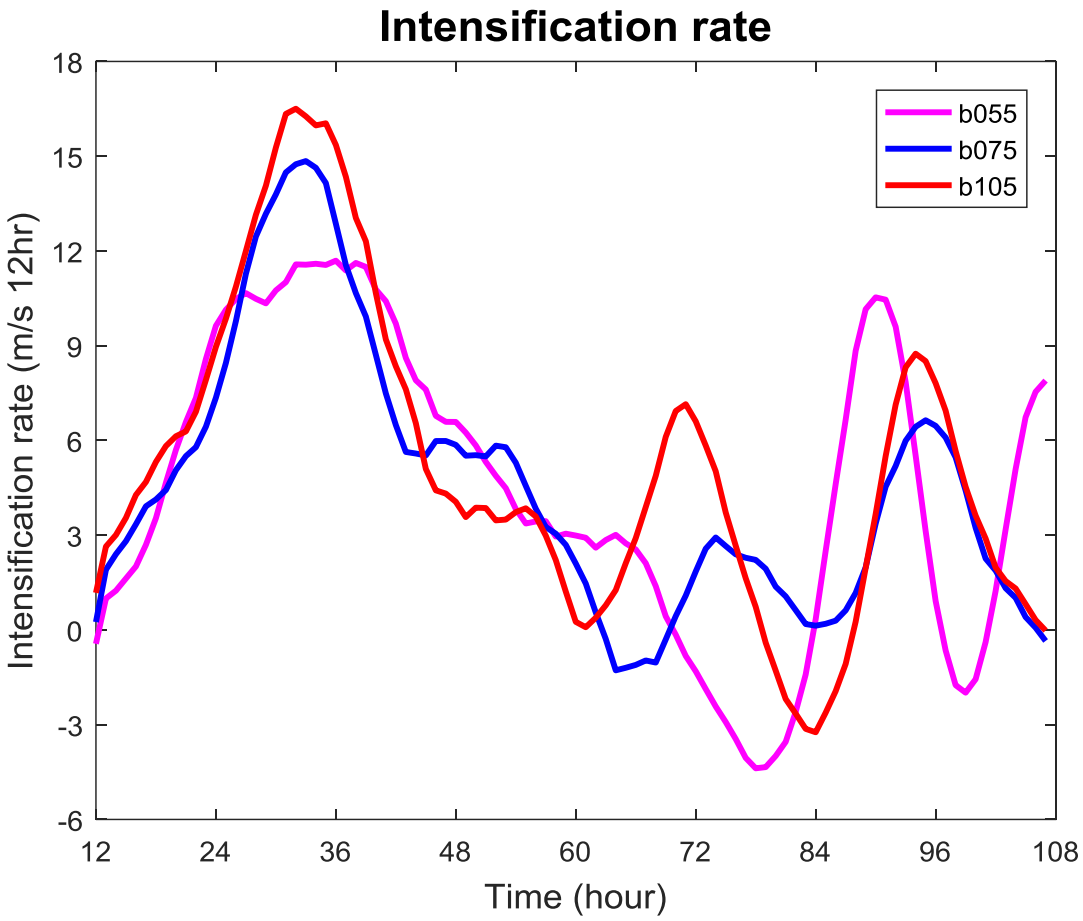

Figure 5.16. Time evolution of the intensification rate (m s^{-1} 12 hr^{-1}) with 5-h running mean in b055 (b = 0.5, magenta), b075 (b = 0.7, blue), and b105 (b = 1, red).

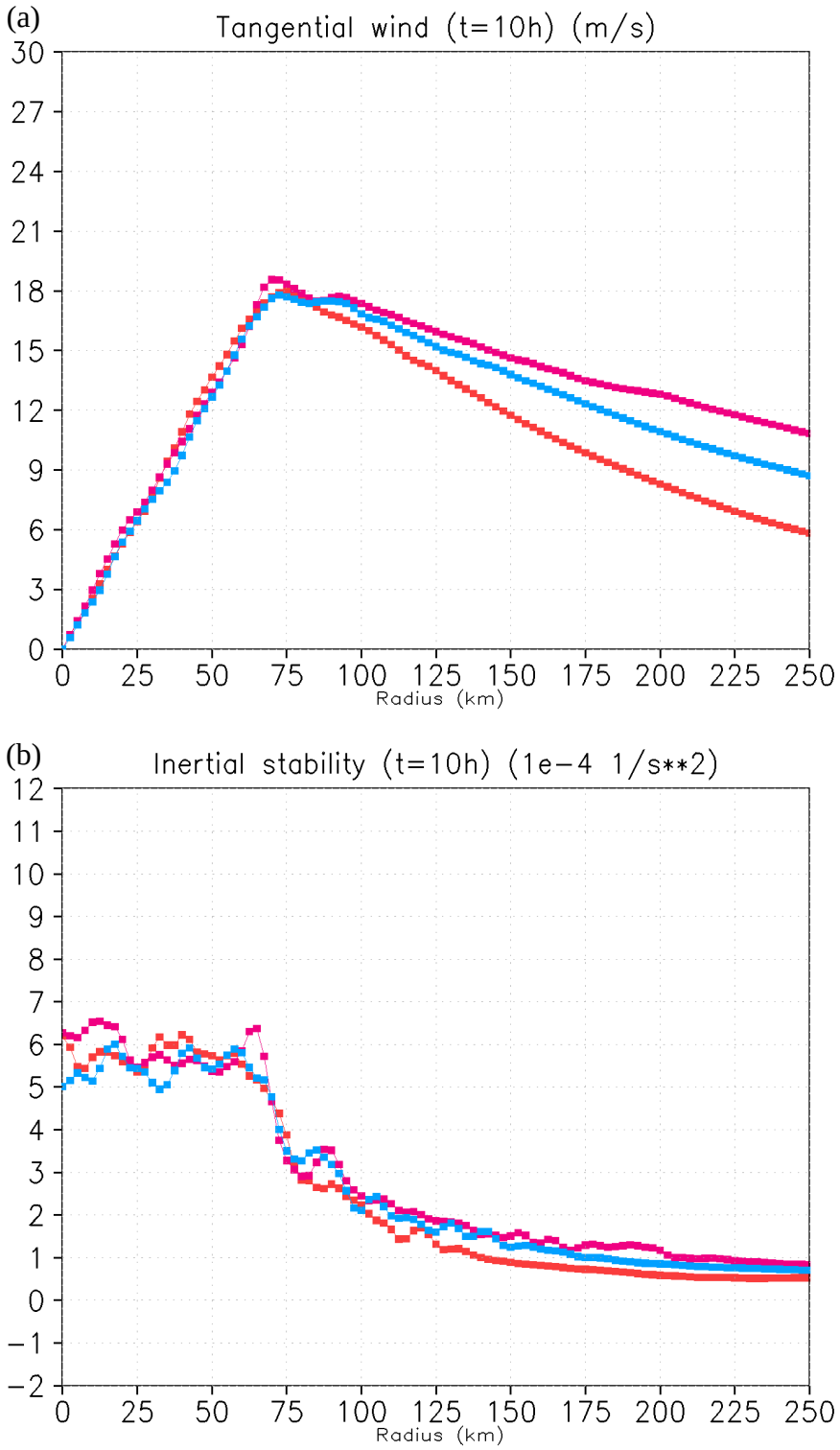

Figure 5.17. As in Figure 5.11, but at 10 h of simulation before the primary intensification stage.

(a)

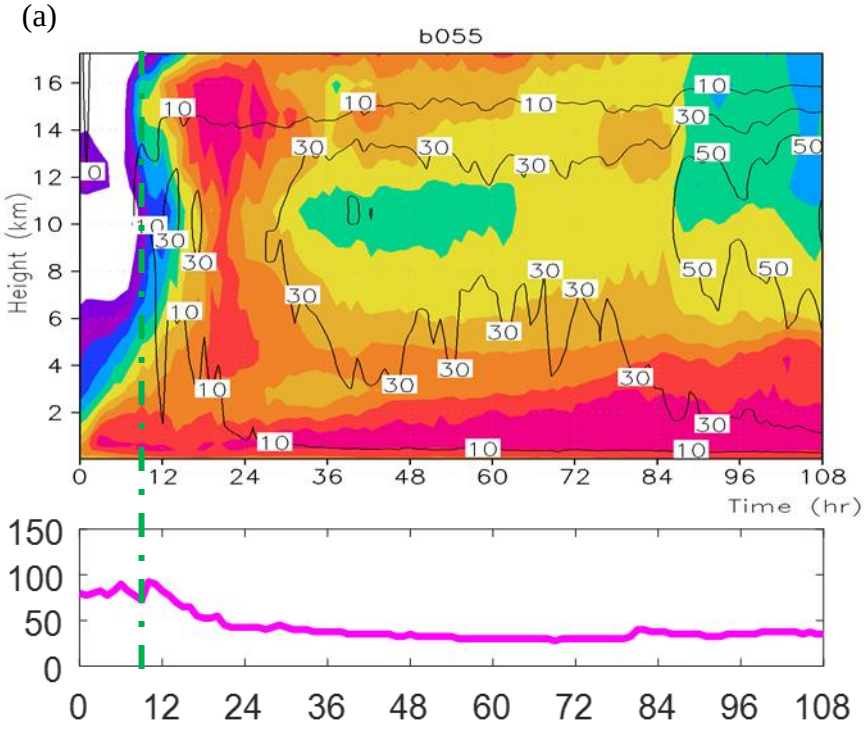
b055
Height (km)
Time (hr)
0 12 24 36 48 60 72 84 96 108
2 4 6 8 10 12 14 16
10 30 50
150
100
50
0

(b)

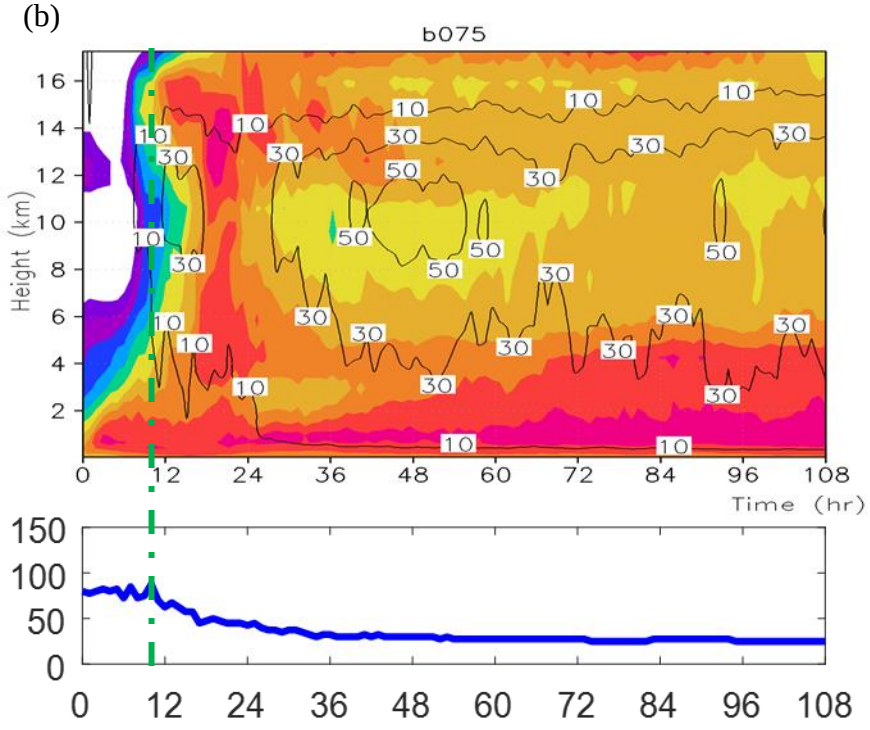
b075
Height (km)
Time (hr)
0 12 24 36 48 60 72 84 96 108
2 4 6 8 10 12 14 16
10 30 50
150
100
50
0

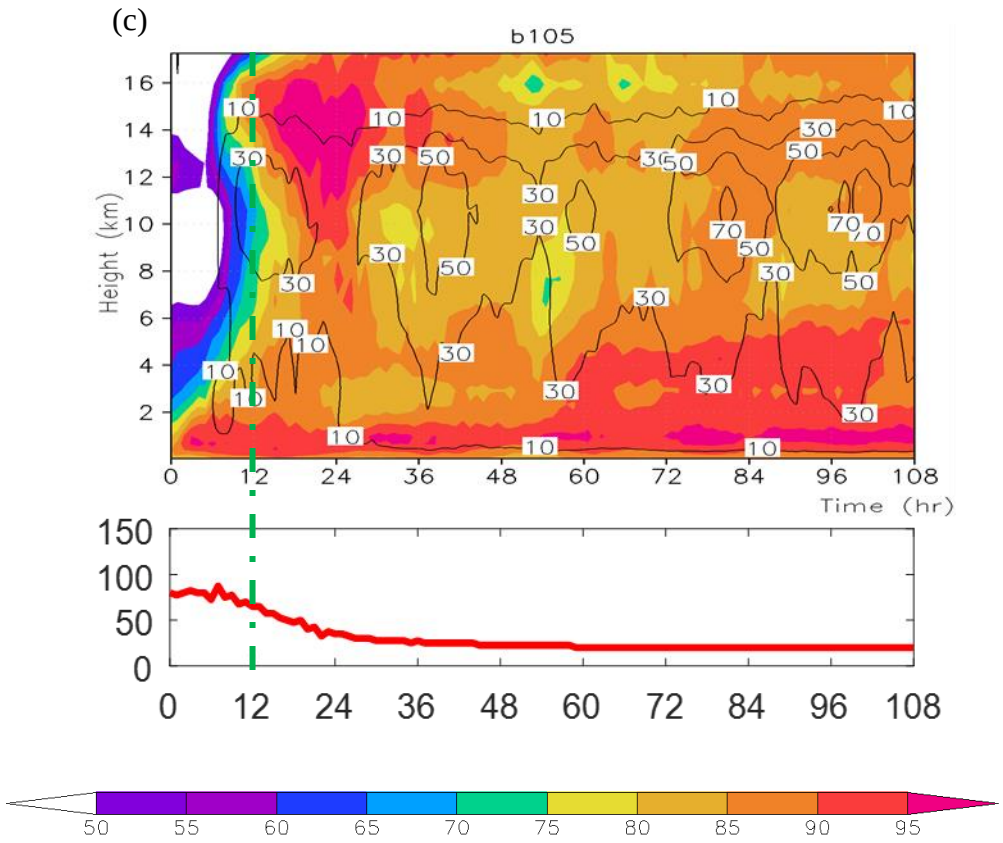

Figure 5.18. Time-height cross-sections of relative humidity (shaded, %) and vertical velocity (contours, cm s^{-1}), both averaged within the radius of 1.5 times of the RMW, together with the time evolution of the RMW (km) shown at the bottom of each panel in (a) b055 (b = 0.5), (b) b075 (b = 0.7), and (c) b105 (b = 1). The vertical green dashed line in each panel shows the time when the initial spin-up stage ends in the corresponding experiment.

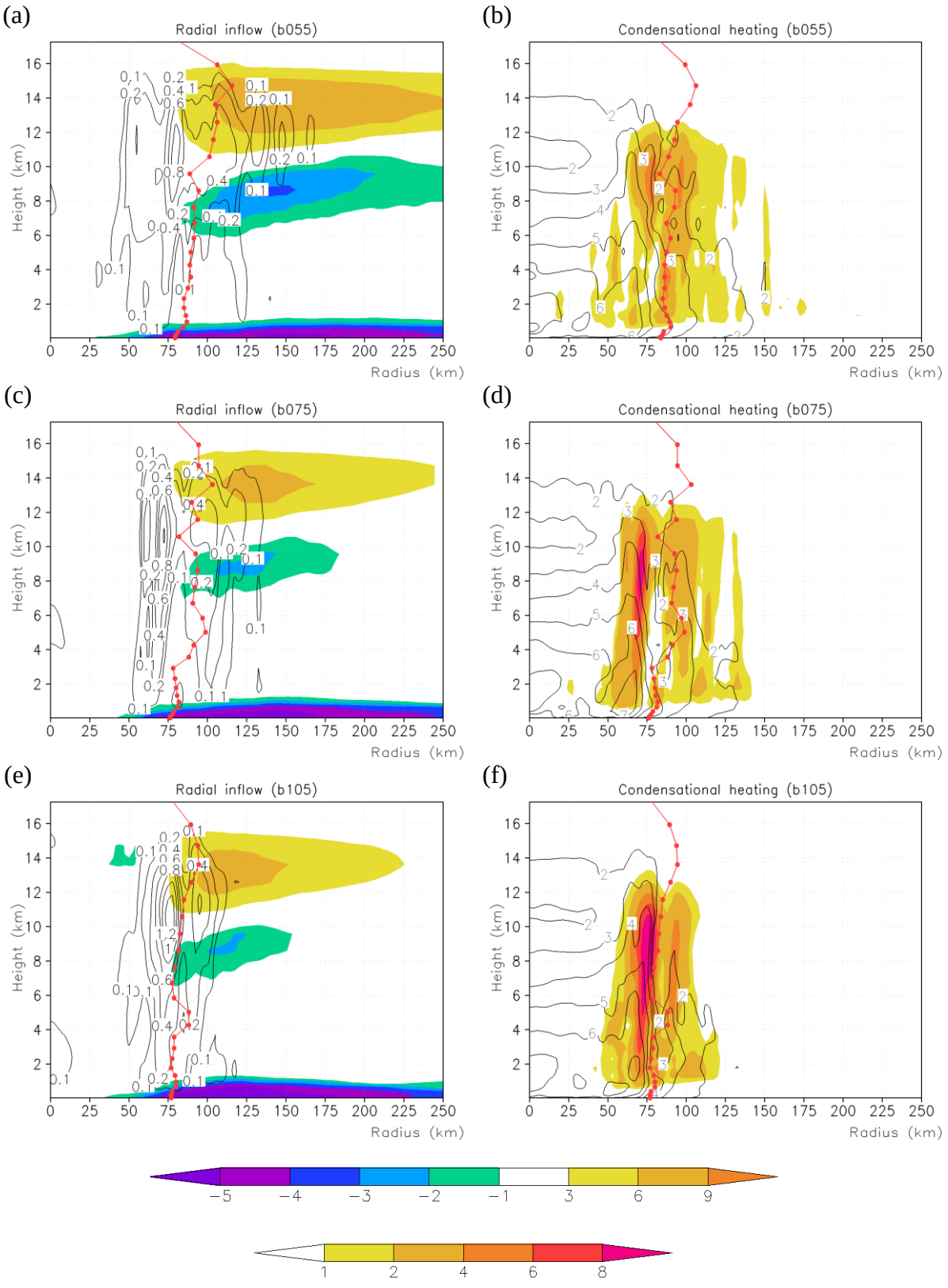

Figure 5.19. Radius-height cross-sections of the azimuthal mean radial wind speed (left shaded,

m s^{-1}) and vertical velocity (left contours, m s^{-1}), together with the condensational heating rate (right shaded, K hr^{-1}) and inertial stability (right contours, 10^{-4} s^{-1}) for (a), (b) b055 (b = 0.5), (c), (d) b075 (b = 0.7), and (e), (f) b105 (b = 1), all averaged in 3-h interval prior to the corresponding primary intensification stage. The red solid curve shows the RMW in the corresponding experiment.

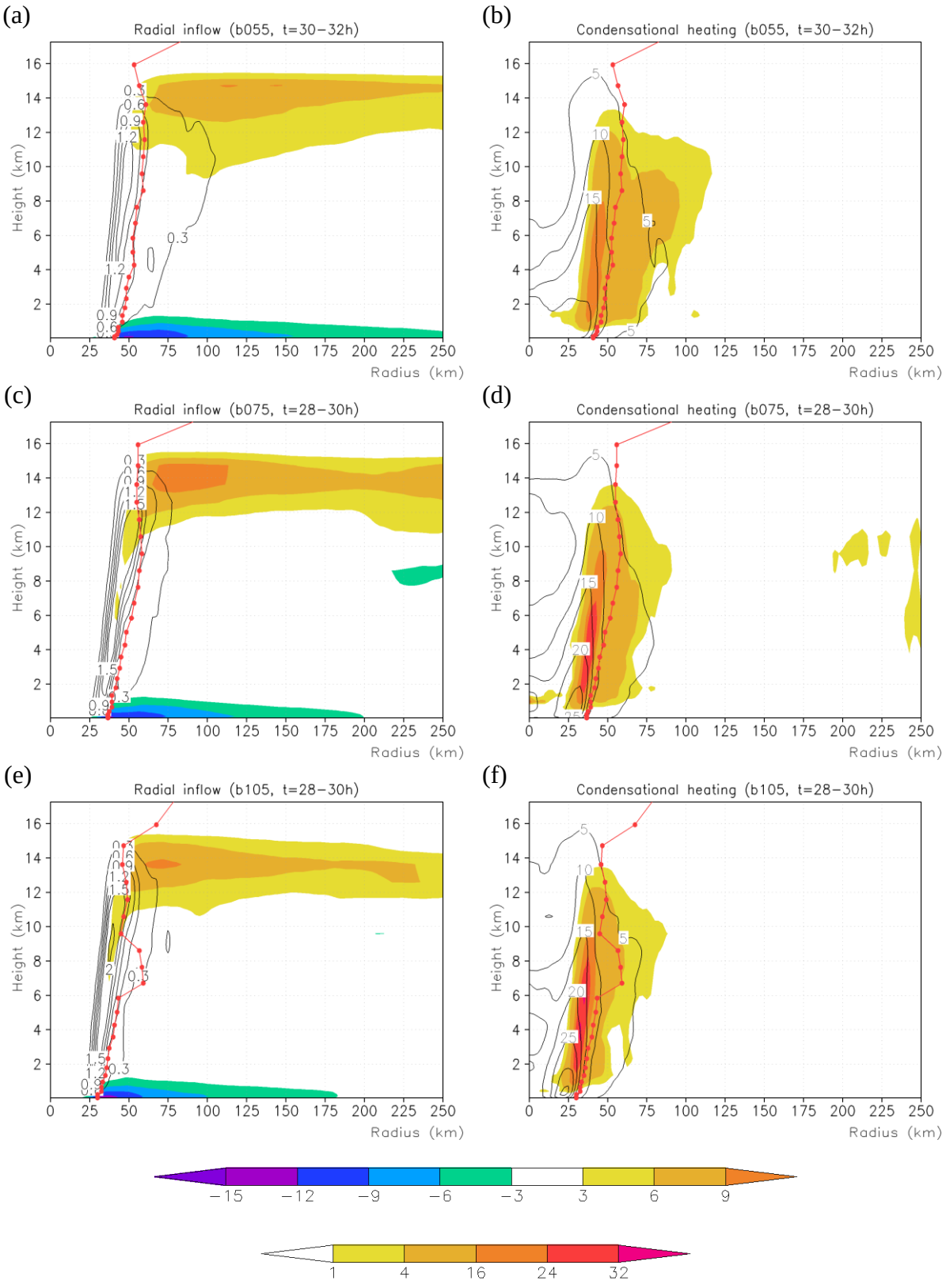

Figure 5.20. As in Figure 5.19, but for 3-h average when the intensity is over 35 m s^{-1} respectively.

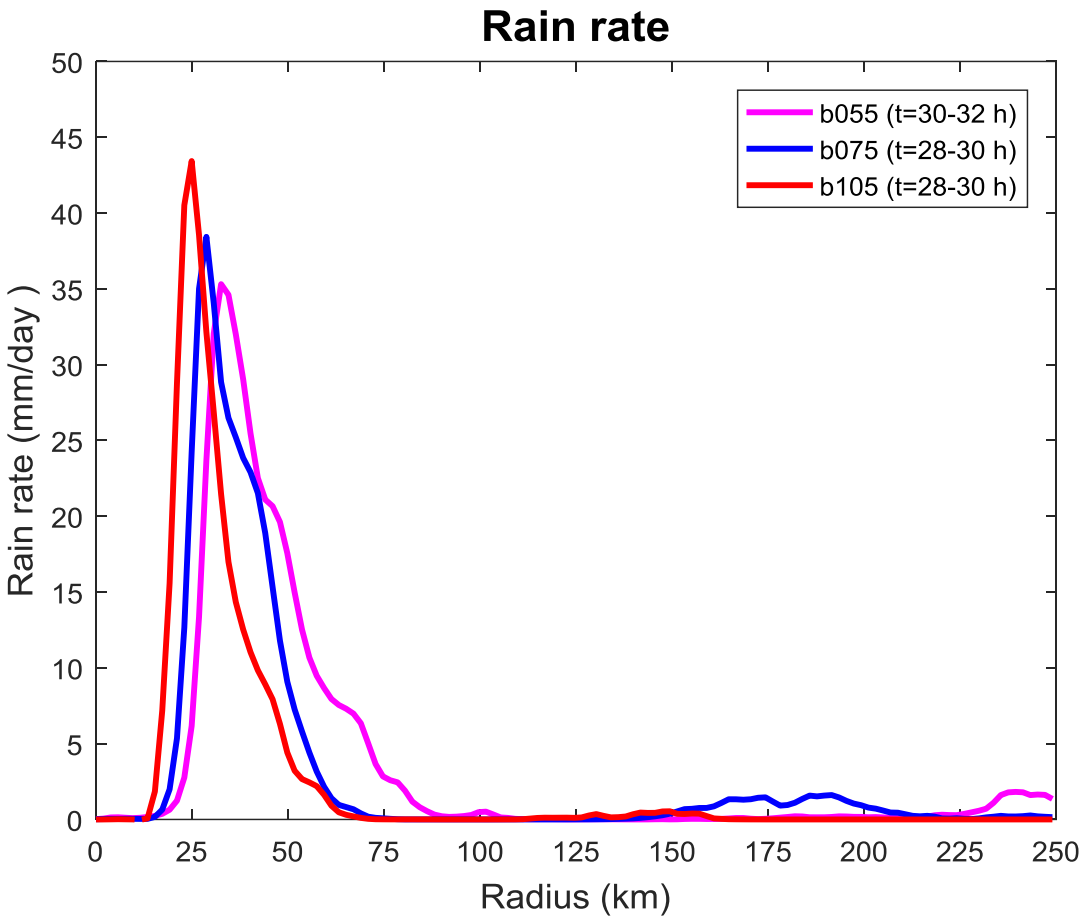

Figure 5.21. Radial distribution of the azimuthal mean rain rate (mm day^{-1}) in b055 (b = 0.5, magenta), b075 (b = 0.7, blue), and b105 (b = 1, red), all averaged in 3-h interval when the intensity is over 35 m s^{-1} respectively.

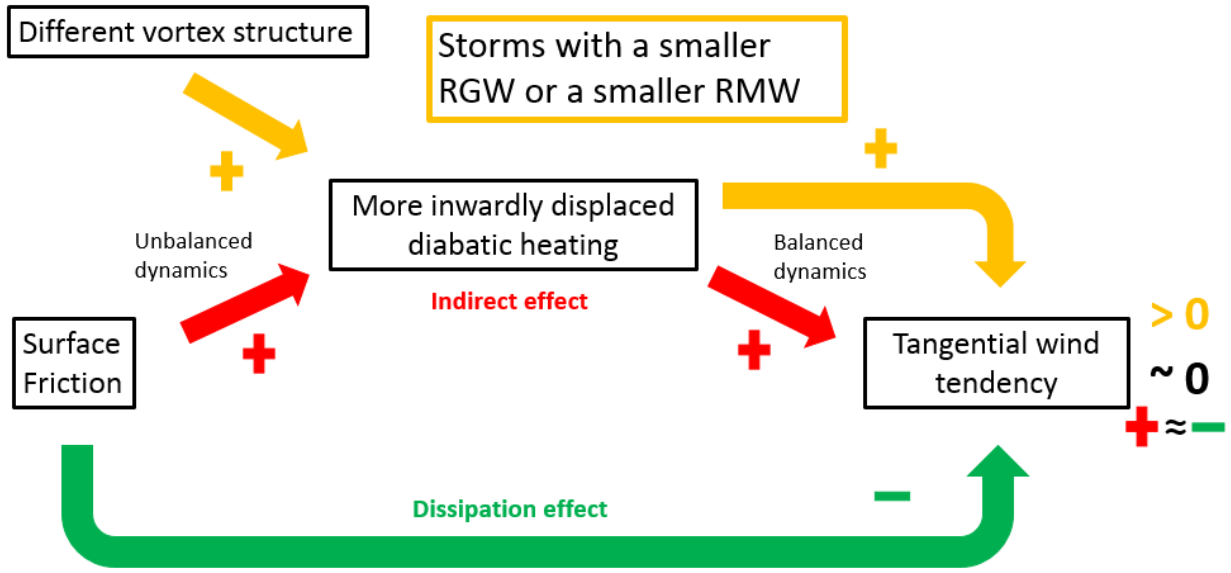

Figure 6.1. Schematic diagram showing the indirect effect and the direct dissipation effect of boundary layer dynamics in the presence of surface friction to the TC intensification rate. The plus (minus) sign denotes the positive (negative) contribution to TC intensification.

(a)

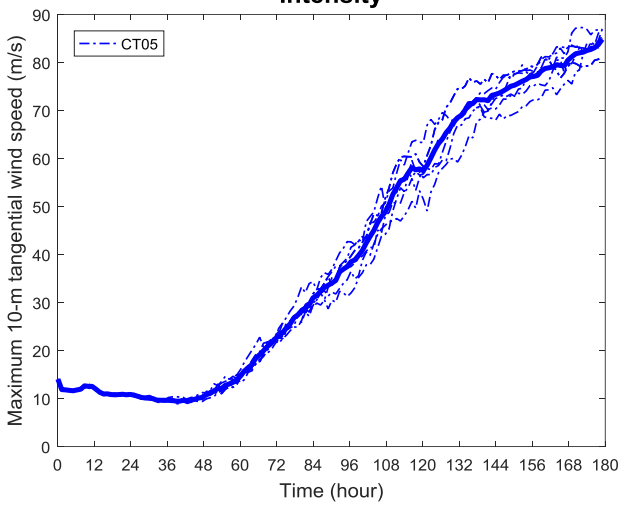
Intensity
CT05
Maximum 10-m tangential wind speed (m/s)
Time (hour)
0 10 20 30 40 50 60 70 80 90
0 12 24 36 48 60 72 84 96 108 120 132 144 156 168 180

(b)

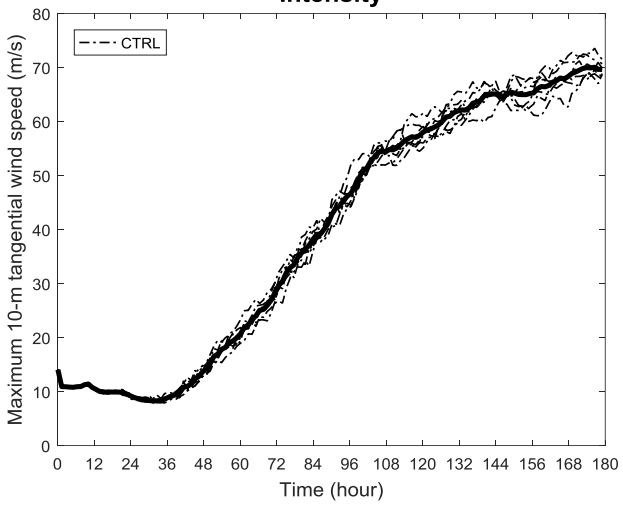
Intensity
CTRL
Maximum 10-m tangential wind speed (m/s)
Time (hour)
0 10 20 30 40 50 60 70 80
0 12 24 36 48 60 72 84 96 108 120 132 144 156 168 180

(c)

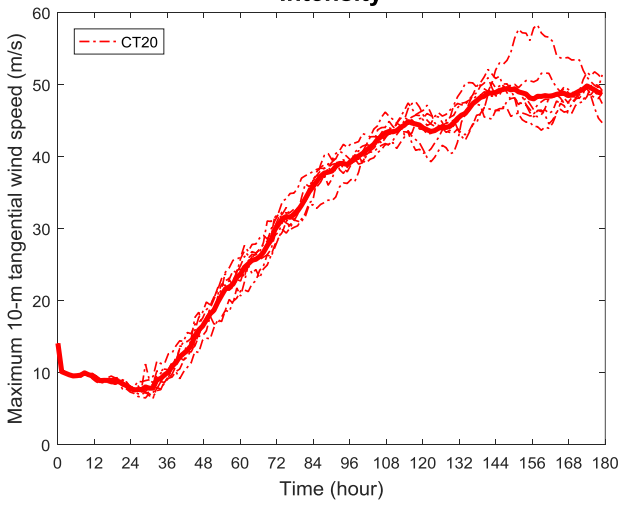
Intensity
CT20
Maximum 10-m tangential wind speed (m/s)
Time (hour)
0 10 20 30 40 50 60
0 12 24 36 48 60 72 84 96 108 120 132 144 156 168 180

Figure 6.2. Time evolution of the maximum 10-m height tangential wind speed (m s^{-1}) for (a) CT05 and its ensemble members (b) CTRL and its ensemble members (c) CT20 and its ensemble members.

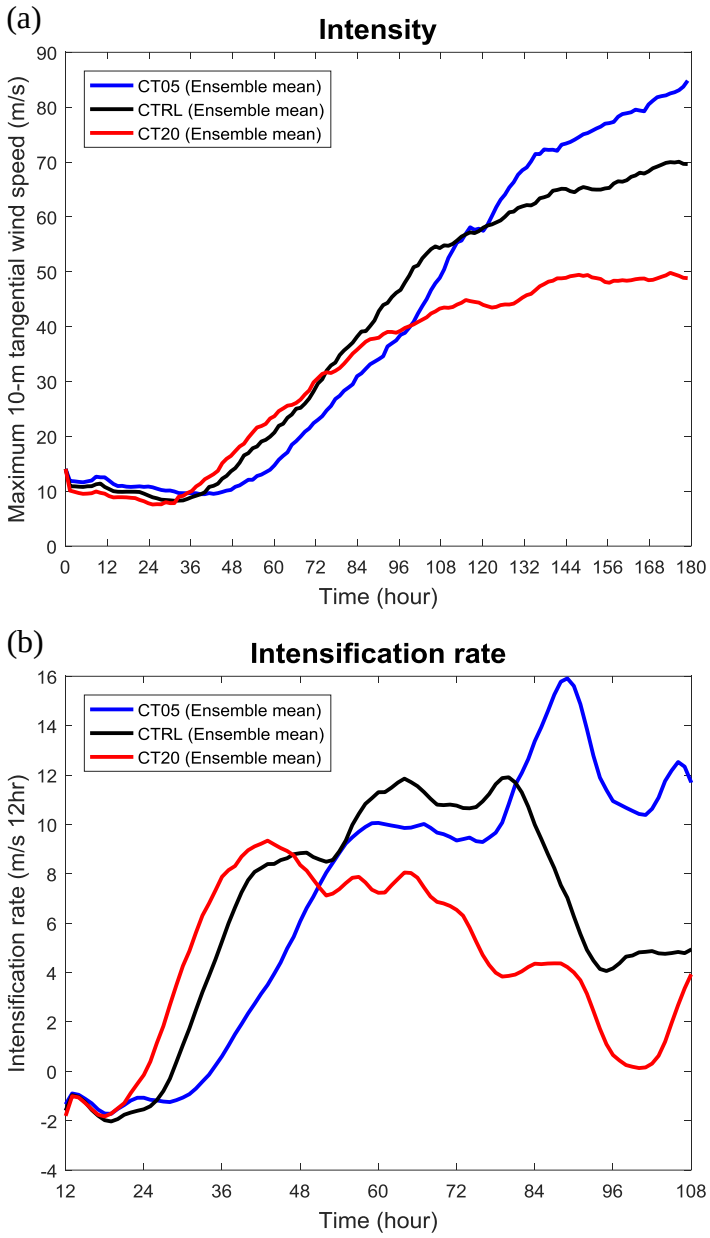

Figure 6.3. (a) Time evolution of the maximum 10-m height tangential wind speed (m s^{-1}) of the ensemble means (eight members) in CT05-E (blue), CTRL-E (black), and CT20-E (red). (b) Time evolution of the 12-h intensification rate (m s^{-1} 12 hr^{-1}) with 5-h running mean of ensemble means (eight members) in CT05-E (blue), CTRL-E (black), and CT20-E (red).

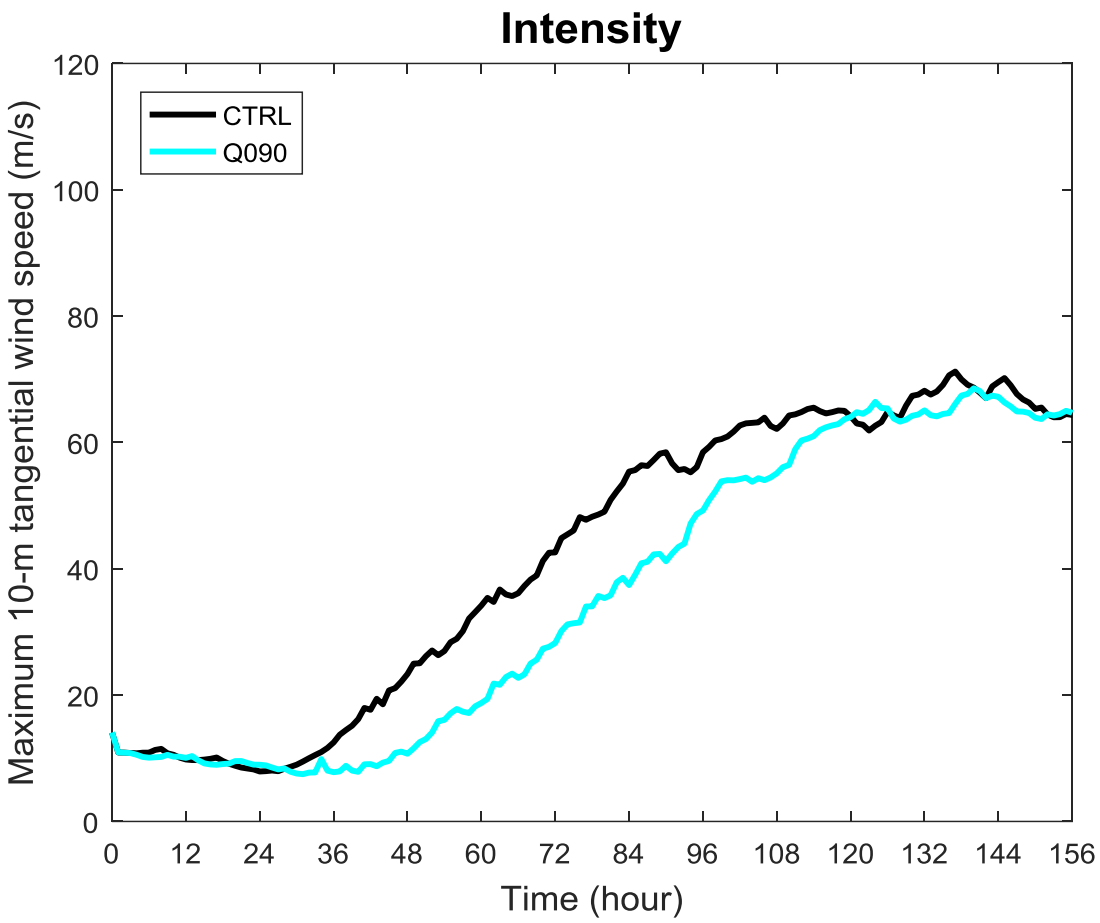

Figure 6.4. Time evolution of the maximum 10-m height tangential wind speed (m s^{-1}) in the control experiment (CTRL, black) and the experiment with 90% initial moisture in CTRL (Q090, cyan).

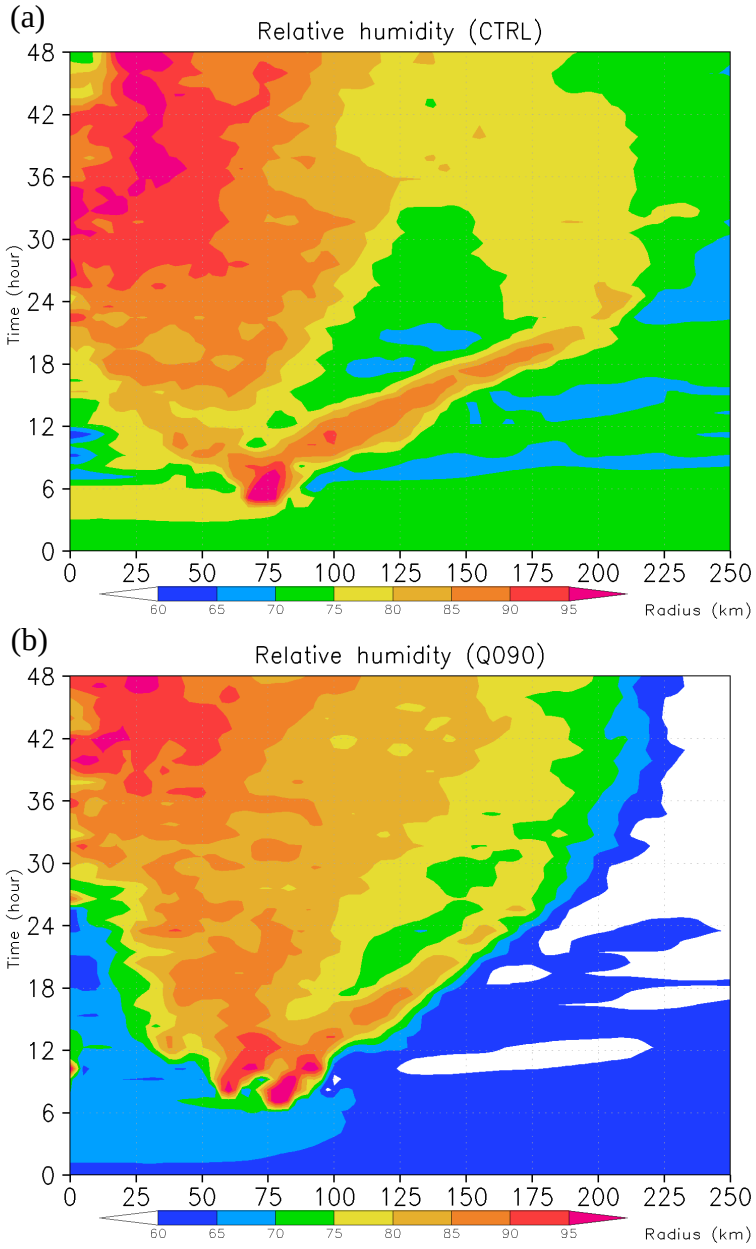

Figure 6.5. Hovmoller plots of the azimuthal mean relative humidity (%) at the 1781-m height in (a) CTRL and (b) Q090.

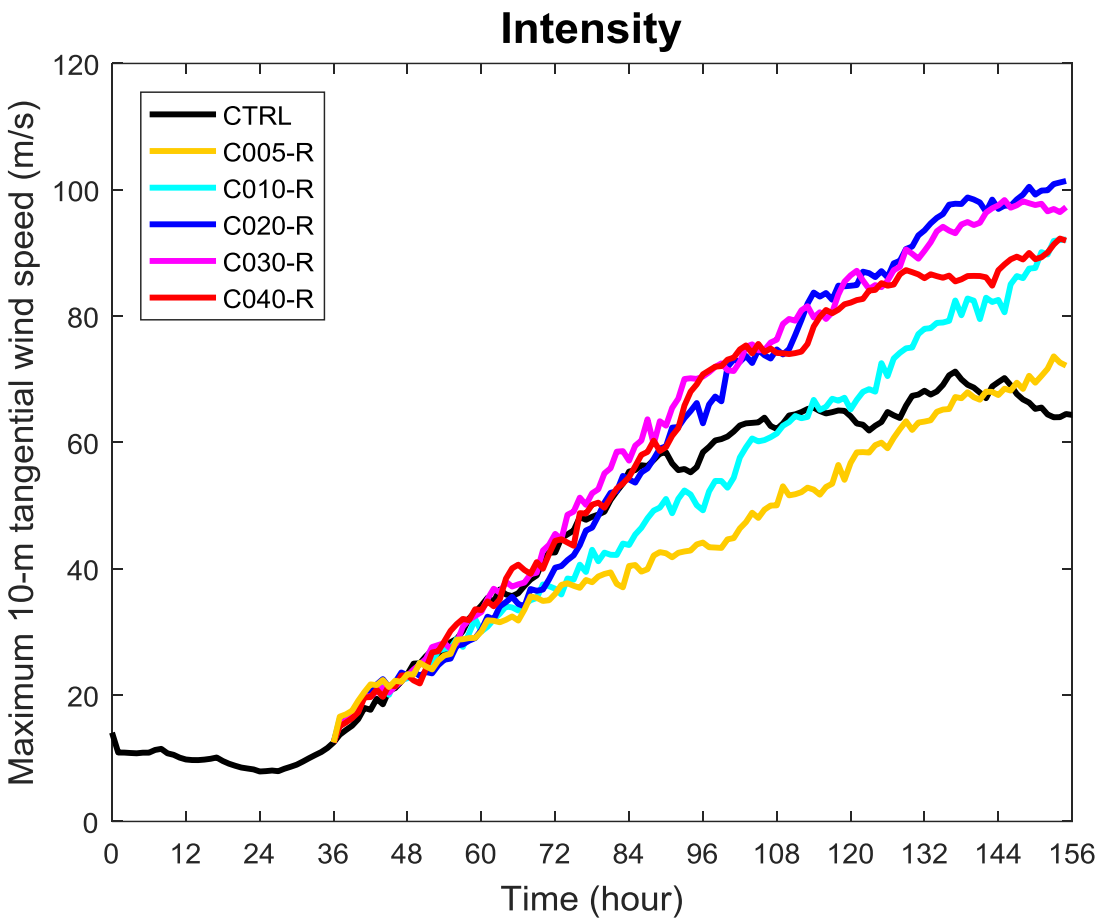

Figure 6.6. As in Figure 6.4, but for the control experiment (CTRL, black), 5% C_D experiment (C005-R, yellow), 10% C_D experiment (C010-R, cyan), 20% C_D experiment (C020-R, blue), 30% C_D experiment (C030-R, magenta), and 40% C_D experiment (C040, red).

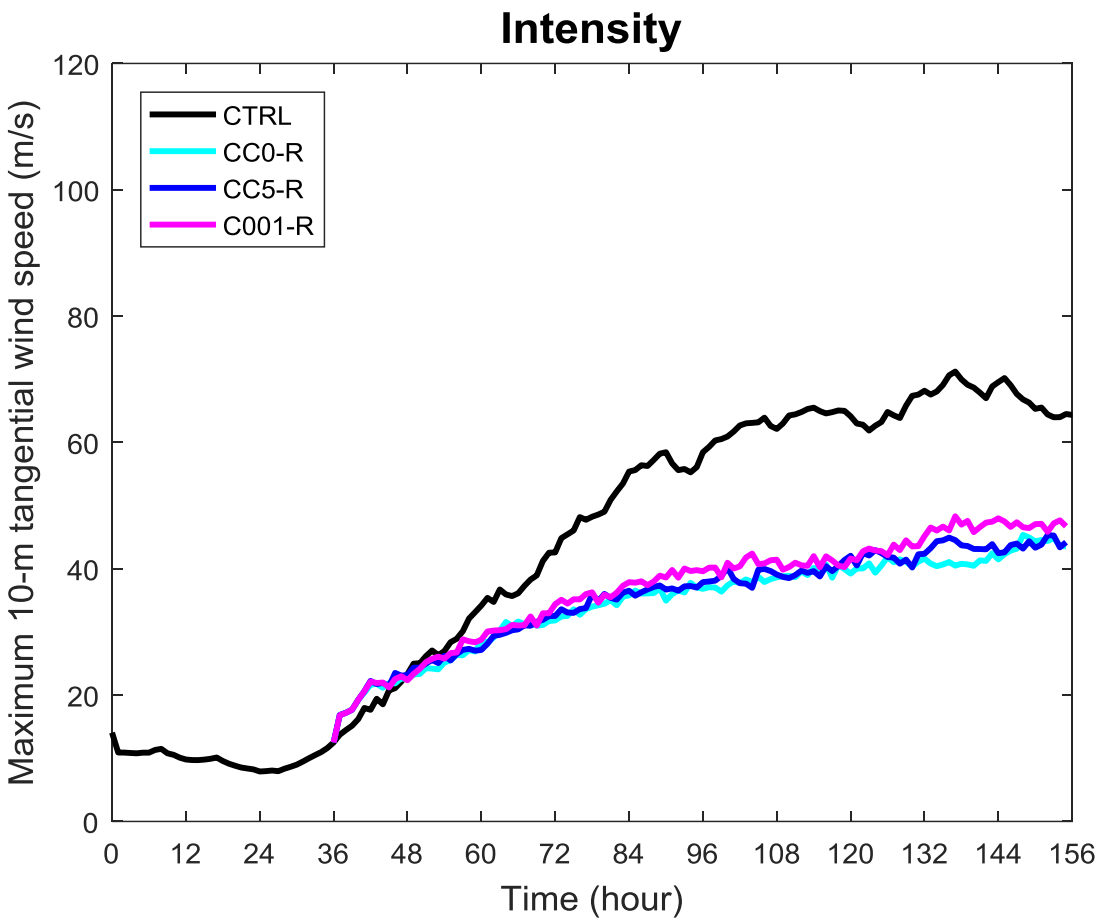

Figure 6.7. As in Figure 6.4, but for the control experiment (CTRL, black), the experiment C_D = 0 (CC0-R, cyan), the experiment $C_D = 1.5\times10^{-5}$ (CC5-R, blue), and 1% C_D experiment (C001-R, magenta).